2020

The Sheeted Dyke-Gabbro Transition Zone: the Key to Unravelling the Palaeomagnetic Record of the Oman Ophiolite

Koornneef, Louise Maria Theresia

UNIVERSITY OF
PLYMOUTH

The Sheeted Dyke-Gabbro Transition Zone: the Key to Unravelling the Palaeomagnetic Record of the Oman Ophiolite

by

LOUISE MARIA THERESIA KOORNNEEF

A thesis submitted to the University of Plymouth
in partial fulfilment for the degree of

DOCTOR OF PHILOSOPHY

School of Geography, Earth, and Environmental Sciences

August 2020

Acknowledgements

The last four years have been a fantastic journey where I got to revisit places that I love and got to explore parts of the world where I had never been before. All of this would not have been possible without my supervisor Prof. Tony Morris, and I would like to thank him for the never-ending support he has given me over the course of this PhD. Thanks for always believing in me and giving me inspiration (scientific and creative!), making me into a better scientist, and for introducing me to some of my now-favourite bands.

Many thanks as well to my external supervisor Prof. Chris MacLeod, who shared his invaluable knowledge of the Oman ophiolite with me. He also never failed to amaze me with his many fieldwork horror stories, in particular the ones involving camel spiders and hundreds of scorpions. Lots of thanks to my second supervisor Dr. Michelle Harris for her great support. She taught invaluable information on hydrothermal alteration and oceanic/continental core logging that could be applied to OmanDP cores and my own surface samples as well. Thanks to my third supervisor Dr. Luca Menegon, who was always available when I needed feedback.

My time spent in the laboratory would have been much less fun without Dr. Anita di Chiara, Dr. Matt Meyer, and Buğra Čavdar; thank you pmag sister and brothers, for the many lab sing-alongs and chats during our countless hours of measurements! Thanks also to Dr. Gustavo Viegas for your assistance in the field. And at the University of Plymouth, thanks to the big PhD and research community for endless motivations and distractions, in particular Dr. Camille Dusséaux, Dr. Grant Cole and Dr. Havananda Ombashi, who started their PhD journey at the same time as me, Francesca Prando, whom I have shared the best office with for years, and Sov Atkinson who introduced me to mountain biking in the UK. Couldn't have done without all our coffee breaks, weekend trips, and barbeques! Also special thanks to Dr. Arjan Dijkstra for always being helpful, Dr. Graeme Taylor for the great times during the Geophysics practicals, and Dr. Hanno Kinkel simply for being Hanno! My time at the university was great with all of you.

Away from the university, I owe a huge thanks to my amazing friends who have always believed one day I would become a "Rock Star". I could not have done without you! A special thanks to my high school lecturer Martin Kamerling for introducing me to geology: my adventure really started here. And to my family;

Aan mijn ouders, heel erg bedankt voor alle steun de afgelopen jaren. Jullie telefoontjes, kaarten, pakketjes, en hagelslag hebben mij ontzettend geholpen! De hagelslag was vaak binnen een week weer op. Lieve grootouders en ooms en tantes, heel erg bedankt voor jullie aanmoedigingen en interesse in geologie, zelfs al was het lastig uit te leggen wat ik voor onderzoek doe. Aan Bingo en Sfinx, bedankt voor alle knuffels en pootjes!

Finally, I would like to dedicate this PhD to my grandfather Levinus 'Louis' Lammers. He always encouraged me to study science and was incredibly proud when he heard I would do a PhD in the UK, the country he loved, lived and worked in for a long time. Thanks for all your knowledge. *La pie niche en haut, le coq niche en bas, l'hibou niche ni haut ni bas.*

Author's Declaration

At no time during the registration for the degree of Doctor of Philosophy has the author been registered for any other University award without prior agreement of the Doctoral College Quality Sub-Committee.

Work submitted for this research degree at the University of Plymouth has not formed part of any other degree either at the University of Plymouth or at another establishment.

Relevant scientific conferences have been regularly attended during the course of this research and findings have been presented at conferences in the form of oral and poster presentations. Various relevant fieldtrips and training courses were also attended, including several postgraduate courses at the University of Plymouth for generic research and academic skills.

During this research extensive fieldwork in the Oman ophiolite, Sultanate of Oman, was undertaken in January/February 2016/2017, which allowed for the collection of samples and the understanding of the geological context of the oceanic crust. In addition, core logging activities for Phase I of the Oman Drilling Project were undertaken in January/February 2017, as well as shipboard activities on board of the *Chikyū* as a palaeomagnetist.

In 2018 a research grant received from EPOS (European Plate Observing System) allowed for a collaboration with the Paleomagnetic Laboratory *Fort Hoofddijk* at the University of Utrecht where

Several manuscripts will be prepared and submitted for publication in peer-reviewed journals upon completion of this Ph.D.

Conferences attended:

- November 2016 – CRES (Centre for Research in Earth Sciences) Postgraduate Conference, Plymouth (UK)
- January 2017 – Magnetic Interactions, Edinburgh (UK)
- November 2017 – CRES Postgraduate Conference, Plymouth (UK)
- January 2018 – Magnetic Moments, Oxford (UK)
- September 2018 – UKIODP 50th Anniversary Event, London (UK)
- November 2018 – CRES Postgraduate Conference, Plymouth (UK)
- December 2018 – AGU (American Geophysical Union) Fall Meeting, Washington (USA)
- January 2019 – Magnetic Interactions, Liverpool (UK)

Presentations given:

- November 2016 – CRES Postgraduate Conference, Plymouth (UK)
  Palaeomagnetic insights into an ancient ocean – Oral presentation
- January 2017 – Magnetic Interactions, Edinburgh (UK)
  Palaeomagnetic insights into an ancient ocean – Oral presentation
- July 2017 – Three minutes thesis competition
  A Journey through Oman's Ancient Ocean – Oral presentation
- January 2018 – Magnetic Moments, Oxford (UK)
  Paleomagnetism of the Oman Ophiolite: New Results from Oman Drilling Project Cores – Poster presentation
- October 2018 – Seminar
  The (re)magnetization of the Oman ophiolite – Oral presentation
- December 2018 – AGU Fall Meeting, Washington (USA)
  Investigating remagnetization of the southern massifs of the Oman ophiolite using rock magnetism – Poster presentation
- January 2019 – Magnetic Interactions, Liverpool (UK)
  Investigating remagnetization of the southern massifs of the Oman ophiolite using rock magnetism – Poster presentation

Word count of main body of thesis: **44504**

Signed

Date

The Sheeted Dyke-Gabbro Transition Zone: the Key to Unravelling the Palaeomagnetic Record of the Oman Ophiolite

Louise Maria Theresia Koornneef

Abstract

The Oman ophiolite is a natural laboratory for the study of processes operating above a nascent subduction zone. It formed in the Late Cretaceous by supra-subduction zone spreading and shortly afterwards was emplaced onto the Arabian continental margin. Twelve massifs in the ophiolite expose complete sections of the Neotethyan oceanic lithosphere, including upper mantle peridotites, lower crustal gabbros, and upper crustal sheeted dykes and lava flows.

Previous palaeomagnetic studies have suggested that the southern massifs of the ophiolite were affected by a large-scale remagnetization event during emplacement, which completely replaced original remanences acquired during crustal accretion. In contrast, primary magnetizations are preserved throughout its northern massifs. This study therefore aims to: (i) apply palaeomagnetic, magnetic fabric and rock magnetic techniques to analyse systematically crustal sections through the southern massifs of the Oman ophiolite to investigate the extent and nature of this remagnetization event; and (ii) to use any primary magnetizations that survived this event to document intraoceanic rotation of the ophiolite prior to emplacement.

Results demonstrate that remagnetization occurred from the base of the ophiolite upwards, and involved the acquisition of a chemical remanence that decreases in intensity up-section, related to upwards expulsion of orogenic fluids during obduction onto the Arabian continent. Magnetic fabrics in layered gabbros and dykes are aligned with macroscopic magmatic structures (layering and dyke margins), indicating that the distribution of new magnetic phases during remagnetization was controlled by existing silicate fabrics. Remagnetization appears to have been pervasive throughout the southern massifs, except at one locality (Wadi Abyad) where primary magnetizations are inferred to be preserved in the sheeted dyke complex at the top of the exposed section. Similar primary remanences were isolated at a control locality in the Salahi massif, outside of the region of remagnetization. Net tectonic rotation analysis at these non-remagnetised sites shows an initial NNE-SSW strike for the supra-subduction zone ridge during spreading, comparable with recently published models for the regional evolution of the ophiolite.

List of Figures and Tables

Figures

Day (1982), S = Shelton (1984), T = Thomas et al. (1988), P = Perrin et al. (1994, 2000), Feinberg et al. (1999), W = Weiler (2000).

Page 26 - Figure 2.12 – Two models proposed by Thomas et al. (1988) for how (re)magnetization events during nappe rotations could lead to the declination anomalies found between the northern and southern massifs of the Oman ophiolite. See text for discussion.

Page 27 - Figure 2.13 – Model of Perrin et al. (1994, 2000) showing a proposed 150° CW rotation of the entire Oman ophiolite in a single movement (see text for discussion). The model is in agreement with Model 1 from Thomas et al. (1988) (Figure 2.12).

Page 28 - Figure 2.15 – Model of Feinberg et al. (1999) for obduction-related remagnetization of the southern massifs, caused by an upwards hydrothermal wave of high-temperature fluids expelled from beneath the ophiolite. Due to more intensive metamorphism beneath the thicker southern massifs the remagnetization was able to affect higher stratigraphic levels than in the northern massifs.

Page 32 - Figure 2.16 – Model of Weiler (2000) in which the Oman ophiolite shows similar behaviour to the Juan Fernandez microplate on the East Pacific Rise (EPR). (a) After back-rotating the mean magnetization orientations in individual massifs to north, the ophiolite is inferred to have a similar geometry to EPR microplate systems (see discussion in text). (b) Simplified model of the Juan Fernandez microplate system (Larson et al. (1992).

Page 34 - Figure 2.17 – Schematic model proposed by Morris et al. (2016) that explains rotation of the Oman ophiolite in a simple way in a suprasubduction zone setting: (a) Formation of the ophiolite along a NE-SW-oriented spreading ridge above a subduction zone; (b) clockwise rotation of the entire ophiolite caused by the northwards movement of Arabia and subduction roll-back; (c) emplacement onto the Arabian continent resulting in remagnetization and then back-rotation of the southern massifs in response to the development of the Saih Hatat structural culmination.

Page 36 - Figure 2.18 – Tectonic model of subduction initiation along the Arabian margin of Oman, proposed by van Hinsbergen et al. (2019). See text for discussion.

Page 37 - Figure 2.19 – Overview of sampling localities.

Page 40 - Figure 2.20 – A simplified geological map of the Wadi Abyad section, showing locations sampled by Meyer (2015) and this study (AB sites) as blue stars. (Modified from Meyer (2015))

Page 41 - Figure 2.21 – Dyke rooting zone of Wadi Abyad (photo credit: M. Harris). Dashed lines indicate the dyke orientations.

Page 41 - Figure 2.22 – Sheeted dyke complex of Wadi Abyad.

Page 43 - Figure 2.23 – An overview map of the southern massifs of the Oman ophiolite, with a zoomed-in geological map of the Wadi Abdah section, showing sample locations as red stars. Maps modified from Nicolas et al. (2000) and (2008).

Page 45 - Figure 2.24 – The Hole GT3 drill site of the Oman Drilling Project

Page 45 - Figure 2.25 – Core from Hole GT3 showing the contact between a dyke from the dyke rooting zone with varitextured gabbro.

Page 47 - Figure 2.26 - An overview map of the southern massifs of the Oman ophiolite, with a zoomed-in geological map of the Al Khadra section, showing the sample location as a blue star. Maps modified from Nicolas et al. (2000) and the geological map from the Sultanate of Oman.

contribute to the bulk susceptibility of a rock, however ferromagnetic minerals will dominate the signal even if present in small concentrations (modified from Tarling and Hrouda, 1993).

Page 85 - Figure 3.9 – Example of a Zijderveld diagram showing the declination through solid black circles, inclination through white circles.

Page 86 - Figure 3.10 – Example of a Zijderveld diagram displaying multiple components of which the coercivities/unblocking temperatures do not overlap (left) and (partially) overlap (right).

Page 95 - Figure 3.11 – Examples of IRM acquisition curves used in CLG analysis; (a) a linear acquisition plot (LAP). SIRM = saturation IRM, (b) the gradient of the acquisition plot (GAP). DP = dispersion parameter that represents one standard deviation, (c) standardised acquisition plot (SAP). On all plots $B_{1/2}$ is the field at which half of the SIRM is reached. Squares in the SAP are measured data from a titanomagnetite. From Kruiver (2001).

Page 96 - Figure 3.12 – Example of linear, gradient, and standardised acquisition plots for a modelled mixture of magnetite (SIRM = 0.1 mA/m, $\log(B_{1/2})$ = 1.76, DP = 0.48) and goethite (SIRM = 0.1 mA/m, $\log(B_{1/2})$ = 3.11, DP = 0.19). Squares represent data points, the short-dashed line represents component 1, the long-dashed line component 2.

Page 99 - Figure 3.13 – Net tectonic rotation for a palaeovertical case (e.g. a dyke) and a palaeohorizontal case (e.g. a layered gabbro or lava). (a-b) Stereographic projections showing the site mean magnetisation vector (SMV), reference magnetisation direction (RMV), present day pole (PDP), initial orientation solutions (IP) (two for palaeovertical case, one for palaeohorizontal case), and rotation poles (RP), (c-d) Histograms of the rotation angles and stereographic projections of 75 calculated solutions for each RP. From Morris et al. (2017).

Page 105 - Figure 4.1 – Alternating field demagnetization curves for a range of magnetite grains. The shape of the curves reflects an increase in magnetite grain size from SD (sigmoidal) to MD (exponential). From Dunlop and Özdemir (1997).

Page 106 - Figure 4.2 – Examples of normalised magnetization intensity curves against field strength for AF demagnetized specimens.

Page 108 - Figure 4.3 – Examples of normalised magnetization intensity curves against temperature for thermally demagnetized specimens.

Page 112 - Figure 4.4 – Examples of normalised thermomagnetic curves per locality. Solid lines represent heating curves up to 700°C, dashed lines represent the cooling curves back to ambient temperature.

Page 114 - Figure 4.5 – Examples of normalised IRM acquisition curves for Wadi Abyad, Wadi Gideah, and the Salahi massif.

Page 119 - Figure 4.6 – Summary of AMS parameters for each locality and lithology sampled in this study. (Left) Corrected anisotropy degree against mean susceptibility, (Right) Corrected anisotropy degree against shape parameter.

Page 120 - Figure 4.7 – AMS data from layered gabbro sites sampled in the Oman ophiolite. The AMS principal axes are shown as blue squares (K_{max}), green triangles (K_{int}), and pink circles (K_{min}), Jelínek (1978) confidence ellipses are plotted for each principal axis, red great circles show the orientation of the gabbro layering.

Page 121 - Figure 4.8 – AMS data from foliated gabbro sites sampled in the Oman ophiolite. The AMS principal axes are shown as blue squares (K_{max}), green triangles (K_{int}), and pink circles (K_{min}),

Jelínek (1978) confidence ellipses are plotted for each principal axis, red great circles show the orientation of the gabbro foliation.

Page 123 - Figure 4.9 – AMS data from varitextured gabbro sites sampled in the Oman ophiolite. The AMS principal axes are shown as blue squares (K_{max}), green triangles (K_{int}), and pink circles (K_{min}), Jelínek (1978) confidence ellipses are plotted for each principal axis.

Page 124 - Figure 4.10 – AMS data from dyke sites sampled in the Oman ophiolite. The AMS principal axes are shown as blue squares (K_{max}), green triangles (K_{int}), and pink circles (K_{min}), Jelinek (1978) confidence ellipses are plotted for each principal axis, red great circles show the orientation of the dykes.

Page 126 - Figure 4.11 – AMS data from lava sites sampled in the Oman ophiolite. The AMS principal axes are shown as blue squares (K_{max}), green triangles (K_{int}), and pink circles (K_{min}), Jelínek (1978) confidence ellipses are plotted for each principal axis, red great circles show the orientation of the lava layering.

Page 127 - Figure 4.12 – Equal area stereographic projections of the AMS K_{max} principal axis for the sheeted dykes, dyke rooting zone, and layered gabbro sites of this study. Great circles show the orientation of the dykes and the layering of the gabbros respectively.

Page 128 - Figure 4.13 – Equal area stereographic projection of the AMS K_{max} principal axis of the layered gabbros of Wadi Gideah against a structural map of the southern massifs of the Oman ophiolite (from Nicholas et al., 2000). Red lines represent the lineation trajectories, black lines the inferred ridge axis. Note how the NE-SW lineation trajectories correlate with the measured K_{max} orientation.

Page 130 – Figure 4.14 - Photomicrographs of thin sections of layered gabbros from Wadi Abyad, showing correlation of Kmax axes (red arrows) with preferred orientations of silicate crystals and of secondary magnetite in olivine crystals (bottom). Yellow scale bars = 1.0 mm. From Morris et al. (2019).

Page 134 - Figure 5.1 – Histograms of the NRM intensities for each pseudostratigraphic level sampled in the Oman ophiolite. SDC = sheeted dyke complex; DRZ = dyke rooting zone; VTG = varitextured gabbros; FG = foliated gabbros; LG = layered gabbros.

Page 137 - Figure 5.2 - Representative Zijderveld diagrams of both alternating field and thermal demagnetization for specimens from Wadi Abyad (geographic coordinates). Steps are shown in °C for thermal demagnetization or mT for alternating field demagnetization.

Page 139 - Figure 5.3 - Representative Zijderveld diagrams of both alternating field and thermal demagnetization for specimens from Wadi Abdah (geographic coordinates). Steps are shown in °C.

Page 141 - Figure 5.4 - Representative Zijderveld diagrams of both alternating field and thermal demagnetization for specimens from Al Khadra (geographic coordinates). Steps are shown in °C for thermal demagnetization or mT for alternating field demagnetization.

Page 142-143 - Figure 5.5 - Representative Zijderveld diagrams of both alternating field and thermal demagnetization for specimens from Wadi Gideah (geographic

coordinates). Steps are shown in °C for thermal demagnetization or mT for alternating field demagnetization.

Page 145 - Figure 5.6 - Representative Zijderveld diagrams of both alternating field and thermal demagnetization for specimens from Salahi massif (geographic coordinates). Steps are shown in °C for thermal demagnetization or mT for alternating field demagnetization.

Page 146 - Figure 5.7 – Equal area stereographic projection in geographic coordinates showing (a) the distribution of secondary components of all combined sites with a NNW declination and mean inclination of 36.5°, close to the Oman IGRF (red dot), (b) TK03 model distribution with a northern mean direction and inclination of 35.8°. Notice how similar the model results are to the measured secondary components.

Page 146 - Figure 5.8 – Equal area stereographic projection in geographic coordinates showing the results of great circle analysis on the sheeted dykes of Wadi Abyad. Notice how the resulting mean direction compares to the calculated means of the measured secondary components and TK03 model results in Figure 5.7, suggesting that these dykes are overprinted by the present day field.

Page 150 - Figure 5.9 – Equal area stereographic projections in both geographic and tilt corrected coordinates showing the site mean magnetisation directions of the Salahi massif. Map modified from Nicolas et al. (2000).

Page 152 - Figure 5.10 – Equal area stereographic projections in geographic coordinates showing the results of great circle analysis on the sheeted dyke site AB06 of Wadi Abyad. The majority of AB06 specimens do not provide stable endpoints, yet their great circle paths migrate towards the two interpretable endpoints. Tilt correction shows a shallow, SE-directed mean ChRM.

Page 153 - Figure 5.11 – Equal area stereographic projection in tilt corrected coordinates showing site mean magnetisation directions of sites of Meyer (2015) and this study combined with their associated α_{95} cones of confidence. Note the progressive change in magnetisation direction from the base to the top of the sequence.

Page 157 - Figure 5.12 - Equal area stereographic projections in both geographic and tilt corrected coordinates showing the site mean magnetisation directions of Wadi Abyad (AB), Wadi Abdah (BD), Al Khadra (KD), and Wadi Gideah (WG) for each sampled lithology (dark green = layered gabbros, light green = foliated gabbros, orange = varitextured gabbros, blue = dyke rooting zone, purple = sheeted dykes, pink = lavas). Map modified from Nicolas et al. (2000).

Page 161 - Figure 5.13 – Positive bootstrap fold-test (Tauxe and Watson, 1994) which demonstrates that remagnetisation in Wadi Abyad, Wadi Abdah, Wadi Gideah, and Khafifah occurred prior to tilting of the Moho at these localities. The red dotted lines contain the trend of the eigenvalues of the eigenvalues of the orientation matrices during progressive untilting. The green line represents the cumulative distribution function of 1000 maxima of the eigenvalues, the dashed blue lines are the bounds that enclose 95% of them.

Page 164 - Figure 5.14 - Model for Late Cretaceous remagnetization of the Oman ophiolite proposed by Feinberg et al. (1999), modified to show variable upper limits of remagnetization in the southern massifs.

Page 165 - Figure 5.15 Schematic diagram illustrating various remagnetization scenarios and resulting demagnetization paths (only N-E horizontal plane shown) predicted for a NNW secondary component (S) and a ESE primary component (P): **A.** a purely thermal event affecting

a single primary population of ferromagnetic grains, resulting in acquisition of a secondary partial thermoremanent (pTRM) overprint with maximum unblocking temperature T_1 (that may be higher than the actual temperature experienced, Pullaiah et al., 1975) and a sharp break point in the demagnetization path at temperature T_1; **B.** Growth of a new assemblage of ferromagnetic grains carrying a secondary chemical remanent magnetization (CRM), whose unblocking temperature spectra may be distinct from that of the primary assemblage (i), partially overlap with it (ii), resulting in a curved demagnetization path over the temperature interval of overlap, or (nearly) completely overlap with that of the primary assemblage (iii-v), resulting in a linear demagnetization path with a direction determined by the relative intensity of the components. Note that CRM due to migration of hot fluids may also be associated with a superimposed pTRM; **C.** Alteration resulting in simultaneous growth of a new ferromagnetic grain assemblage (carrying a CRM) and destruction of the primary grain assemblage, erasing all traces of the original TRM.

Page 166 - Figure 5.16 - Examples of Zijderveld plots through the Wadi Abyad crustal section, showing progressive changes in remanence direction and structure upwards from the base. Specimens from the layered, foliated and varitextured gabbros from Meyer (2015).

Page 169 - Figure 5.17 - Results of forward modelling of Zijderveld diagrams seen in Wadi Abyad.

Page 172 - Figure 5.18 – Equal area projections in tilt corrected coordinates of combined ChRM data from Shelton (1984), Perrin et al. (2000), Weiler et al. (2000) and van Hinsbergen et al. (2019) showing a calculated mean ChRM with an inclination of 21.5° (from van Hinsbergen et al. (2019).

Page 173 - Figure 5.19 – Net tectonic rotation results from dykes in Wadi Abyad and Al Khadra, and layered gabbros from the Salahi massif. Histograms show rotation angles, contoured equal area stereographic projections show the rotation axes.

Page 174 - Figure 5.20 - Permissible initial dyke strikes and associated rotation angles for all sites in the sheeted dyke complex analysed by van Hinsbergen et al. (2019).

Page 181 - Figure 6.1. End-member modelling for specimens from localities Wadi Gideah, Wadi Abyad, and the Salahi massif, combining layered, foliated, and varitextured gabbros, as well as the dyke rooting zone, sheeted dykes, and lava flows. (a) Diagram showing the r^2 distribution against the number of end members. (b-c) End-members for the normalised IRM acquisition curves for three and four end-members. (d-e) End-members displayed as gradients versus the log-field for the normalised IRM acquisition curves for three and four end-members. (f) Relative end-member contributions to each specimen level in a pseudo-stratigraphy for a three end-member model. The black line with red dots represents the IRM_{700mT} intensity (logarithmic scale). The different grey-scale colours represent the three end-members.

Page 183 - Figure 6.2 - IRM component analysis (Kruiver et al., 2001) of the preferred three end-member model. Squares represent the calculated data points from end-member modelling used to fit the IRM components.

Page 186 - Figure 6.3 - End-member modelling for gabbro specimens from localities Wadi Gideah, Wadi Abyad, and the Salahi massif. (a) Diagram showing the r^2 distribution against the number of end members. (b-c) End-members for the normalised IRM acquisition curves for three and four end-members. (d-e) End-members displayed as gradients versus the log-field for the normalised IRM acquisition curves for three and four end-members. (f) Relative end-member contributions to each specimen level in a pseudo-stratigraphy for a three end-member

model. The black line with red dots represents the IRM_{700mT} intensity (logarithmic scale). The different grey-scale colours represent the three end-members.

Page 187 - Figure 6.4 - IRM component analysis (Kruiver et al., 2001) of the end-members of the preferred three end-member model. Squares represent the calculated data points from end-member modelling used to fit the IRM components.

Page 189 - Figure 6.5 - End-member modelling for dyke specimens from localities Wadi Gideah, Wadi Abyad, and the Salahi massif. (a) Diagram showing the r^2 distribution against the number of end members. (b-c) End-members for the normalised IRM acquisition curves for two and three end-members. (d-e) End-members displayed as gradients versus the log-field for the normalised IRM acquisition curves for two and three end-members. (f) Relative end-member contributions to each specimen level in a pseudo-stratigraphy for a two end-member model. The black line with red dots represents the IRM_{700mT} intensity (logarithmic scale). The different grey-scale colours represent the three end-members.

Page 190 - Figure 6.6 - IRM component analysis (Kruiver et al., 2001) of the end-members of the preferred two end-member model. Squares represent the calculated data points from end-member modelling used to fit the IRM components.

Page 196 - Figure 7.1 – Geological map of the southern massifs of the Oman ophiolite, showing the drill site locations of the Oman Drilling Project (modified from Nicolas et al. (2000).

Page 197 - Figure 7.2 – Photographs taken at drill site GT3, showing the drill rig cores in the foreground that are ready to be packed, a group of Phase I scientists describing cores, and the core scanner.

Page 198 - Figure 7.3 – Zijderveld diagrams of those sister samples that were subjected to alternating field and thermal demagnetisation. Note the similarity between the demagnetisation paths.

Page 200 - Figure 7.4 – Downhole plots of (left to right) bulk susceptibility, NRM intensity, Königsberger values (Q), and the olivine mode (%) for hole GT1.

Page 201 - Figure 7.5 – Hole GT1: (a+c) Representative Zijderveld diagrams displaying behaviour of magnetic remanence directions during thermal demagnetisation and alternating field demagnetisation. (b+d) Normalised intensity curves as a function of temperature (b) and applied field (d).

Page 202 - Figure 7.6 – Downhole plots of (left to right) bulk susceptibility, NRM intensity, Königsberger values (Q) for hole GT2.

Page 203 - Figure 7.7 – Hole GT2: (a+c) Representative Zijderveld diagrams displaying behaviour of magnetic remanence directions during thermal demagnetization and alternating field demagnetization. (b+d) Normalised intensity curves as a function of temperature (b) and applied field (d).

Page 205 - Figure 7.8 – Downhole plots of (left to right) bulk susceptibility, NRM intensity, Königsberger values (Q) for hole GT3.

Page 206 - Figure 7.9 – Hole GT3: (a+c) Representative Zijderveld diagrams displaying behaviour of magnetic remanence directions during thermal demagnetisation and alternating field demagnetisation. (b+d) Normalised intensity curves as a function of temperature (b) and applied field (d).

Page 208 - Figure 7.10 – (a) Downhole plots of NRM and ChRM inclinations determined from principal component analysis for the three holes. (b) Stereographic projections of remanence component orientations identified by principal component analysis. Solid black dots represent lower hemisphere directions, open dots represent the upper hemisphere directions.

Page 213 - Figure 7.11 – GT1: (a) Downhole plots of magnetic anisotropy intensity (P'), shape (T), and K_{min} orientation. (b) Anisotropy degree against bulk susceptibility. (c) Shape parameter against anisotropy degree. (d) Stereographic projections of magnetic anisotropy principal axes plotted on the lower hemisphere in a core reference frame.

Page 214 - Figure 7.12 – GT2: (a) Downhole plots of magnetic anisotropy intensity (P'), shape (T), and K_{min} orientation. (b) Anisotropy degree against bulk susceptibility. (c) Shape parameter against anisotropy degree. (d) Stereographic projections of magnetic anisotropy principal axes plotted on the lower hemisphere in a core reference frame.

Page 215 - Figure 7.13 – GT3: (a) Downhole plots of magnetic anisotropy intensity (P'), shape (T), and K_{min} orientation. (b) Anisotropy degree against bulk susceptibility. (c) Shape parameter against anisotropy degree. (d) Stereographic projections of magnetic anisotropy principal axes plotted on the lower hemisphere in a core reference frame.

Page 217 - Figure 7.14 – Examples of: (a) Primary interstitial Fe-oxides occurring in association with Fe-sulphide minerals (reflected light), (b, d, e) Fine-grained oxides in altered olivine grains (reflected light), (c, f) Mesh texture of opaque phases in altered olivine grains (plane-polarised light), (g) Primary Fe-oxide grain containing a modified oxyexsolution texture (reflected light), (h) Pale yellow sulphide grains (reflected light), (i) Opaque mesh texture in an altered olivine grain (plane-polarised light), (j) Fine-grained oxides in the same region as shown in (i) (reflected light).

Page 220 - Figure 7.15 – (a, c, e) Stereographic projections of magnetic anisotropy orientations after azimuthal rotation of ChRM declinations around the core axis to a reference palaeomagnetic declination of 000°. (b, d) Downhole plots of rotated K_{max} declinations.

Page 222 - Figure 7.16 – (a) Example of a continuous borehole image. (b) Core section scans that have been aligned based on their red line and their features (veins and fractures).

Page 223 - Figure 7.17 – Core sections are restored to their initial orientation by aligning features on borehole imagery, such as veins and fractures, with the features on the core sections. We take away 180° from the drawn red lines on the core sections to find a 100° rotation of the core compared to the geographic reference frame of the borehole image.

Page 225 - Figure 7.18 – (Left) Equal area stereographic projection of the GT2 ChRMs in a reoriented geographic reference frame. Open circles represent upper hemisphere, solid circles lower hemisphere. (Right) Equal area stereographic projection of the GT2 AMS data in a reoriented geographic reference frame. Blue squares represent K_{max}, green triangles represent K_{int}, red circles represent K_{min}.

Tables

Table of Contents

Chapter 1 – Introduction

1.1 – Rationale

For as long as research has been conducted, scientists have been interested in the world's oceans and the Earth's crust that lies beneath. And rightly so, for Earth's oceans and their underlying crust make up 70% of the Earth's surface and are of vital importance to us, producing large proportions of the world's oxygen, absorbing greenhouse gases like CO_2, and regulating the world's climate through heat transfer. The oceanic crust is a frontier realm, made largely inaccessible to us by c. 5 km of water. Oceanic crust is formed by seafloor spreading as the lithosphere diverges at constructive plate margins, and this represents one of the most important tectonic processes taking place on Earth. The subseafloor may be accessed via scientific ocean drilling using vessels such as the *Chikyū* and the *JOIDES Resolution*, operated by the International Ocean Discovery Program, or IODP. This represents the longest running and most successful international collaboration in Earth Sciences, and recently celebrated 50 years of scientific discoveries that have revolutionised our understanding of plate tectonics, climate and environmental change and the deep biosphere (Koppers et al., 2019). However, scientific ocean drilling has only recovered cores of oceanic lithospheric rocks to a significant depth (> 100 metres below seafloor) at five localities distributed across the world's oceans, as the majority of drill holes only recover seafloor sediments or the shallowest crustal rocks. Drilling a

complete crustal section remains a long-term ambition, but is technologically challenging and resource intensive.

Ophiolites, ancient remnants of oceanic lithosphere that have been obducted onto continents, are therefore of major importance to understanding the formation of the oceans by seafloor spreading. They provide opportunities to study crust and upper mantle rocks and processes in three-dimensional over large areas, and represent natural laboratories where ideas on magmatic, tectonic and hydrothermal processes developed via analysis of samples collected by ocean drilling may be tested. Ophiolites were first recognised to be fragments of oceanic lithosphere in a study on the Troodos ophiolite (Cyprus) by Gass (1968). Early studies suggested that ophiolites:

(i) most likely form at mid-ocean ridges (MOR) during seafloor spreading and are later emplaced (obducted) onto continental margins (Vine, 1966; Moores and Vine, 1971),

(ii) have the assemblage of a “layer-cake” sequence made up of mafic and ultramafic rocks, commonly consisting of mantle peridotites, gabbros, sheeted dykes, extrusive volcanics, and a sedimentary cover (Anonymous, 1972; Robertson, 2004).

However, more recent research has shown that the majority of ophiolites form by spreading above nascent subduction zones (in so-called supra-subduction zone settings; e.g. Pearce and Robinson (2009)). In addition, not all ophiolites display the complete Penrose (Anonymous, 1972) sequence, most

likely due to differences in oceanic crustal architecture between slow and fast spreading systems (e.g. Cannat (1996)).

1.2 – The Oman ophiolite

The Semail ophiolite in Oman (Figure 1.1) is the best preserved, most well-known, and largest thrust sheet of oceanic crust and upper mantle in the world (with an along-strike length of 550 km and a total area of 10.000 km^2), and for this reason it is also the most extensively studied ophiolite in the world (e.g., Lippard et al., 1986; Thomas et al., 1988; Nicolas et al., 1988). The massif covers the eastern border of the Arabian Peninsula and is generally thought to have formed during the Late Cretaceous at a fast spreading Neotethyan ridge.

Previous palaeomagnetic studies (Luyendyk et al., 1982; Luyendyk and Day, 1982; Shelton, 1984; Thomas et al., 1988; Perrin et al., 1994, 2000; Feinberg et al., 1999; Weiler, 2000; Morris et al., 2016) have shown that the northern and southern massifs of the ophiolite have very different directions of magnetization (Figure 1.1). This led to interpretations invoking large relative rotation in opposing senses, that might have been related to break-up of the ophiolite shortly after formation at a spreading centre above a subduction zone. In the northern massifs, data from lava sequences (Perrin et al., 1994, 2000) show differences in direction between different magmatic phases, suggesting that at least in the north rotation was occurring in an intraoceanic setting rather than during later tectonic emplacement. Interpretation of the ophiolite-wide palaeomagnetic database, however, is made more complex because the southern massifs have

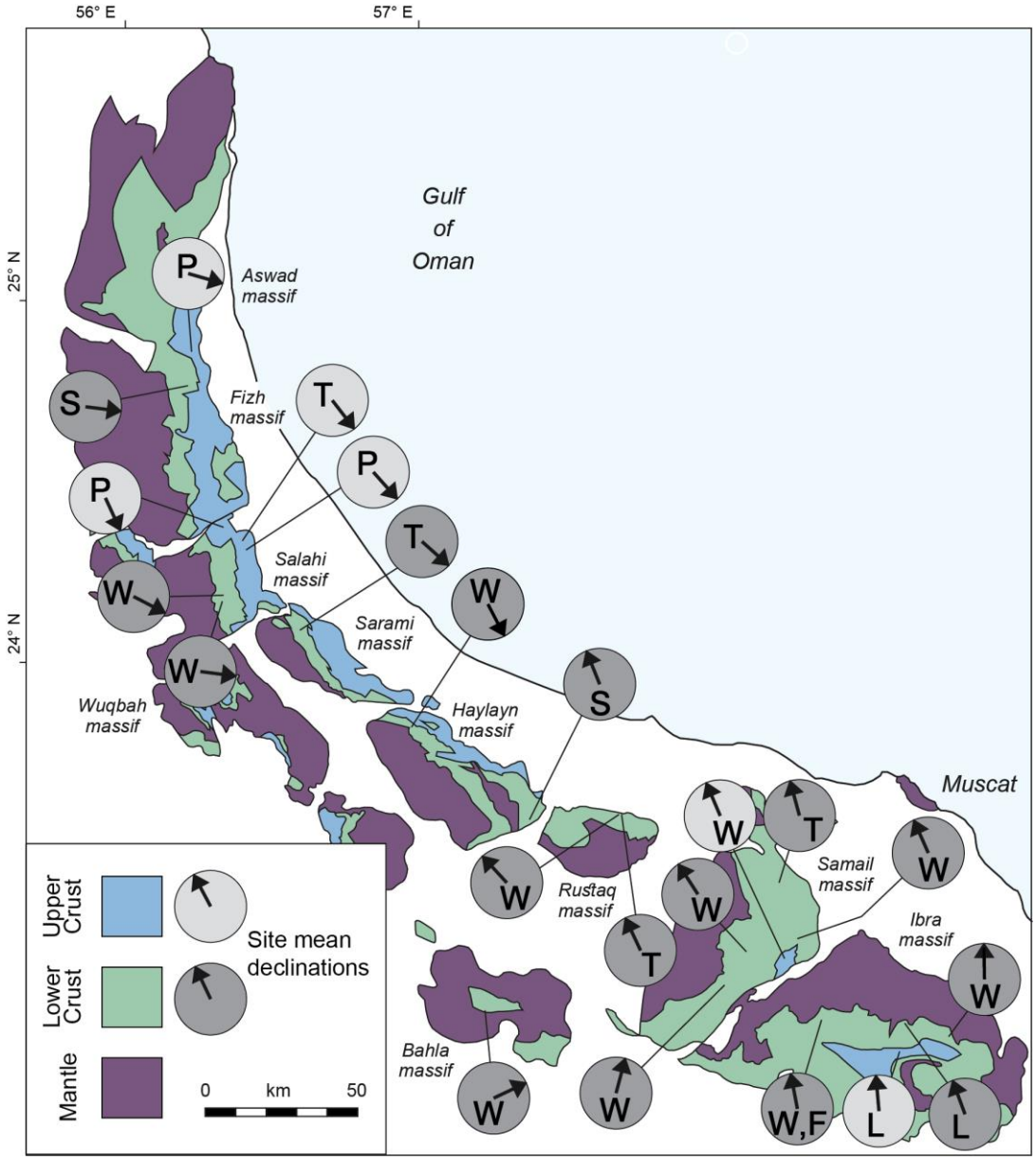

Figure 1.1 – Summary of previously published palaeomagnetic data showing the anomaly between declinations from the northern and southern massifs (modified from Weiler, 2000). Arrow = calculated mean remanence directions (tilt corrected). Sources: L = Luyendyk and Day (1982), S = Shelton (1984), T = Thomas et al. (1988), P = Perrin et al. (1994, 2000), Feinberg et al. (1999), W = Weiler (2000).

undergone an extensive remagnetization event related to obduction of the ophiolite that has completely replaced the original magnetization component (Feinberg et al., 1999), thus leading to confusion over the geodynamic interpretation of the palaeomagnetic data. Recent research from Meyer (2015) shows that the influence of this remagnetization event can be determined by

systematically sampling across the transition zone from lower oceanic crustal gabbros to upper crustal sheeted dykes. In this way it is possible to determine the upper limit of the remagnetization and thus distinguish early acquired magnetic signals, recording the intraoceanic rotation, from overprinted magnetic signals.

In order to better understand how the remagnetization of the ophiolite occurred, a number of aims and objectives have been defined for this research. They are summarised in the next section.

1.3 – Aims and Objectives

The key aim of this study is to apply (palaeo)magnetic techniques to analyse systematically sampled sequences through the southern massifs of the Oman ophiolite in order to investigate an inferred large-scale remagnetization event that has obscured the original magnetic signal. This study aims to:

1. Understand the implications for the remagnetization process on the boundary between rocks preserving primary magnetizations and rocks that have been remagnetised.
2. Determine the scale and characteristics of early rotations in the upper plate of an intraoceanic subduction zone.
3. Collate and compare data from surface sampling with data obtained from the International Continental Scientific Drilling Program “Oman Drilling Project” to obtain a more complete record of vertical variations in magnetization through the Oman crust.

Specific objectives are:

1. To study near complete ophiolitic sequences in the Oman ophiolite to characterise the behaviour of (re)magnetization in the Neotethyan lithosphere.

2. To identify the boundaries and extent of the remagnetization signature in the ophiolite, making use of palaeomagnetic analyses.

3. To determine the characteristics of crustal rotations and the original orientation of the spreading ridge in which the ophiolite formed using net tectonic rotation analysis (where applicable).

4. To investigate whether rock magnetic methods may be used to characterize the remagnetization signature in the ophiolite.

Chapter 2 – Geological Background and Previous Palaeomagnetic Studies

2.1 – Introduction to the Oman ophiolite

The Semail ophiolite of Oman is the best preserved, most well-known, and largest thrust sheet of oceanic crust and upper mantle in the world, with an along-strike length of 550 km and a total area of 10,000 km^2. For this reason it is also the most extensively studied ophiolite in the world (e.g. Lippard et al., 1986; Thomas et al., 1988; Nicolas et al., 1988). The massif covers the eastern border of the Arabian Peninsula (Figure 2.1) and was formed during the Late Cretaceous at a spreading ridge orthogonal to the Arabian passive continental margin (van Hinsbergen et al., 2019). The Semail ophiolite is part of a 8000 km long chain consisting of about 50 ophiolitic rock sequences, spanning from the Jurassic complexes in the western and central Mediterranean region (Alps, Apennines, Carpathians, Dinarides, Hellenides) to Cretaceous complexes in the eastern Mediterranean (Cyprus, Turkey, Syria) to complexes in the far east (Oman, Iran, Tibet) (Figure 2.1), all classified as 'Tethyan ophiolites'. A shift from mid-ocean ridge (MOR) type ophiolites in the western Mediterranean (Italian, Balkan ophiolites) to supra-subduction zone (SSZ) type ophiolites in the eastern Mediterranean and further east can be observed from a changing geochemical signal (Lippard et al., 1986) (Figure 2.1).

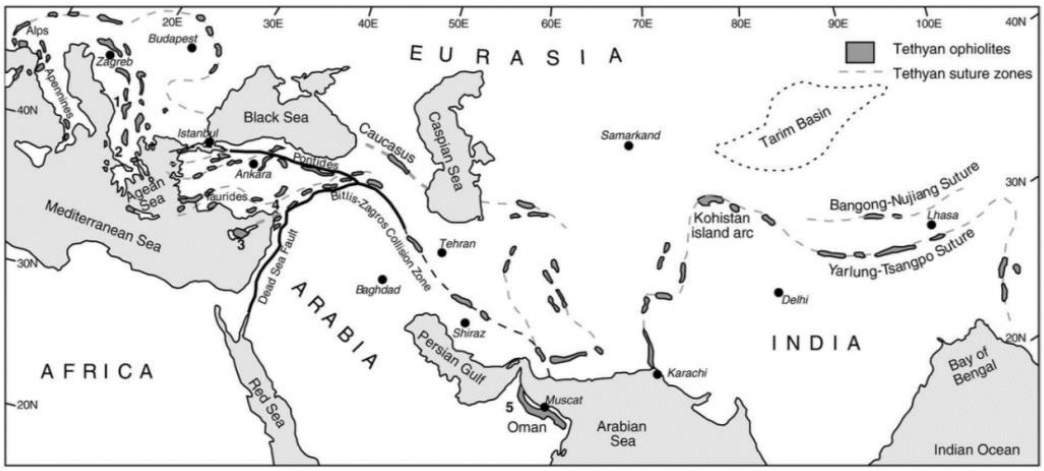

Figure 2.1 – Distribution of major Tethyan ophiolites and suture zones of the closed Neotethys Ocean, which can be found spanning from the Alpine to the Himalayan orogenic system. A shift from MOR type ophiolites to SSZ type ophiolites is observed from the western Jurassic ophiolites to eastern Cretaceous ophiolites (from Dilek and Furnes, 2009).

The Tethyan ophiolite chain formed in the Neotethys Ocean, an E-W oriented seaway that opened at the northern edge of Gondwanaland during the Permian-Triassic (~250 Ma) (Lippard et al., 1986; Stampfli, 2000; Stampfli and Borel, 2002; Dilek et al., 2007) (Figure 2.2a). Opening of Neotethys resulted in rifting of several microplates from Gondwanaland and slowly replaced the older Paleotethys Ocean (Figure 2.2b). The E-W oriented Neotethyan mid-oceanic ridge started to subduct underneath the Laurasian continent in the west during the Late Jurassic, which progressed eastwards until the eastern Neotethys Ocean subducted underneath the Eurasian continent during the Early Cretaceous (Figure 2.2c), related to the northwards movement of Gondwanaland (Stampfli, 2000; Stampfli and Borel, 2002; Dilek et al., 2009). Subduction rollback cycles followed during the closing stages of the Neotethys and caused the formation of supra-subduction zone crust (Stampfli and Borel, 2002; Dilek et al., 2009). All remaining Neotethyan ophiolites are associated with back-arc basins caused by this north-directed subduction.

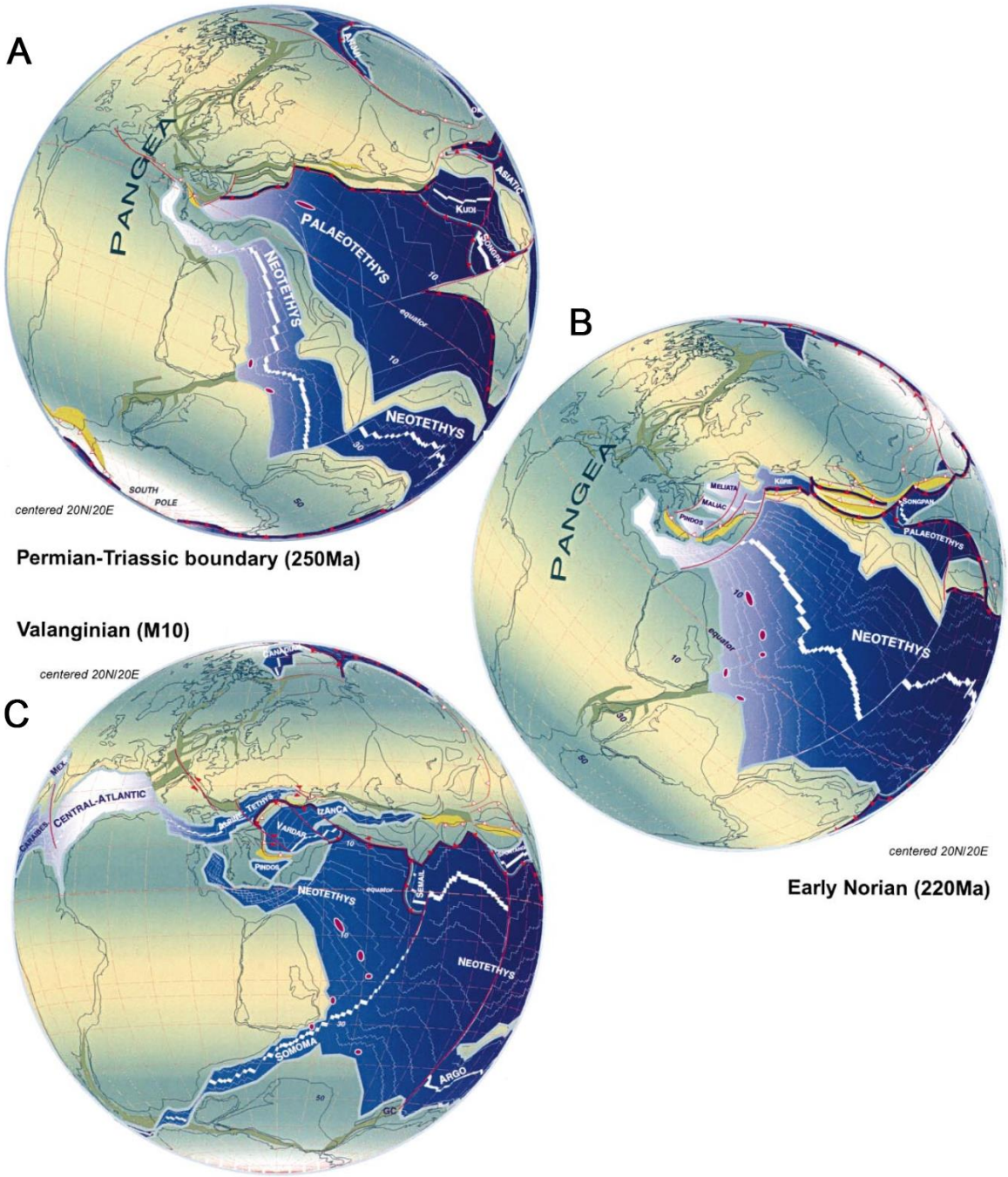

Figure 2.2 – Orthographic projections with Europe fixed in its present-day position showing the evolution of the Paleotethys and Neotethys Oceans: (a) Opening of the E-W oriented Neotethys Ocean to the north of Gondwanaland, separating northern microplates from the continent; (b) Neotethys replacing Paleotethys during N-S oriented spreading; (c) Subduction of the Neotethys slab underneath Eurasia. From Stampfli and Borel (2002).

2.1.1 – Formation and emplacement of the Oman ophiolite

The Semail ophiolite formed in the Cretaceous normal polarity superchron (121-83 Ma) during the Cenomanian age (100-90 Ma), based on U/Pb dating of zircons from plagiogranites that gave results of 97.3 to 93.5 Ma (Tilton et al., 1981; Rioux et al., 2013). The most recent geochemical data (MacLeod et al., 2013) indicate that the entire ophiolite formed in a supra-subduction zone setting immediately following subduction initiation, in contrast to previous interpretations that invoked a true mid-ocean ridge spreading system (e.g. Nicolas and Boudier, 2003).

Searle and Cox (1999) present emplacement models for both the northern and southern halves of the Oman ophiolite (Figure 2.3). In these models, the ophiolite formed during the Cenomanian between 97.3 and 93.5 Ma above a northeast dipping subduction zone in a SSZ setting (Figure 2.3a). They rule out obduction initiation at a mid-oceanic ridge setting as the protoliths in the ophiolite's metamorphic sole are not similar to the ophiolite's volcanic rocks; the metamorphic sole turns out to be much older (Triassic/Jurassic ocean floor basalts) than the Cenomanian ophiolite. Therefore obduction initiation in a subduction setting was proposed, starting around 93 Ma (Figure 2.3a-b). Obduction was completed around 74 Ma (Figure 2.3c) after which exhumation and extensional collapse broke the ophiolite into a dozen tectonic blocks (Figure 2.3d) (Searle and Cox, 1999).

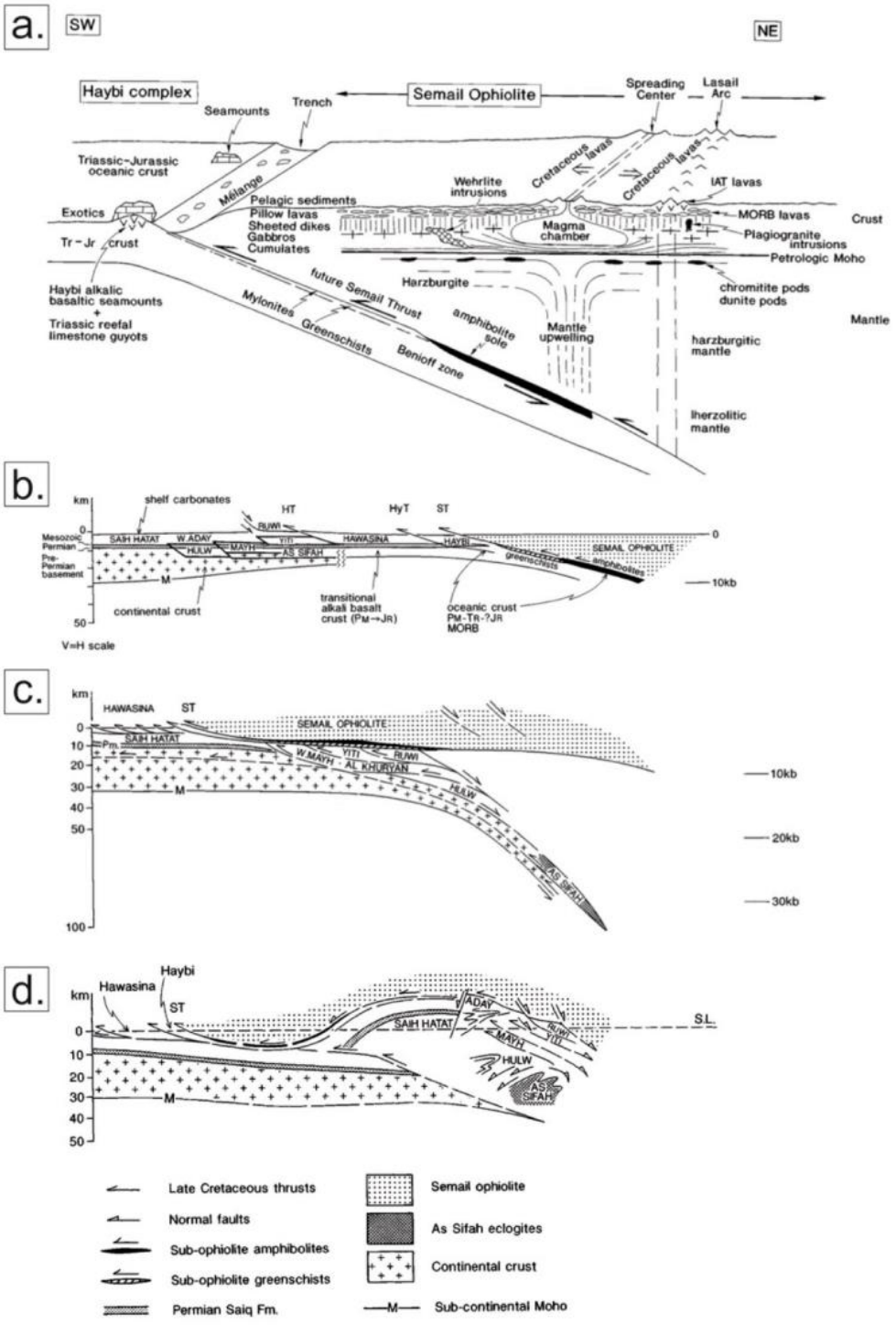

Figure 2.3 – Formation and emplacement of the Oman ophiolite (from Searle and Cox, 1999): (a) Accretion of SSZ type crust above an intraoceanic subduction zone led to formation of the ophiolite in the upper plate (~95 Ma), (b) Emplacement begins at 93 Ma, (c) Emplacement of the ophiolite completes at 74 Ma, (d) Exhumation and extensional collapse related to isostatic rebound of the underlying continental plate break the ophiolite up into multiple tectonic blocks.

2.2 – Stratigraphy of the Oman ophiolite

The Oman ophiolite in the Neotethyan suture zone represents the largest intact thrust slice in which all members of an ophiolitic sequence can be found. From top to bottom the ophiolite consists of (Figure 2.4): oceanic sediments (radiolarian cherts and umber), extrusive rocks (pillow lavas and lava flows), a sheeted dyke complex, gabbros, peridotites, and the metamorphic sole. Sampling for this study was focused on continuous crustal sequences where possible, from the lowest layered gabbros to the lava flows at the top.

Upper mantle peridotites and lower crustal gabbros are the most extensively exposed units of the Oman ophiolite, consisting of 8-12 km of tectonised peridotites overlain by 4-7 km of oceanic crust (Hopson et al., 1981; Lippard et al., 1986; Nicholas, 1989). The oceanic crustal sequence is divided into lower crustal rocks (layered gabbros, foliated gabbros, varitextured gabbros and the dyke rooting zone) and upper crustal rocks (sheeted dyke complex, extrusive lavas, and the sedimentary cover).

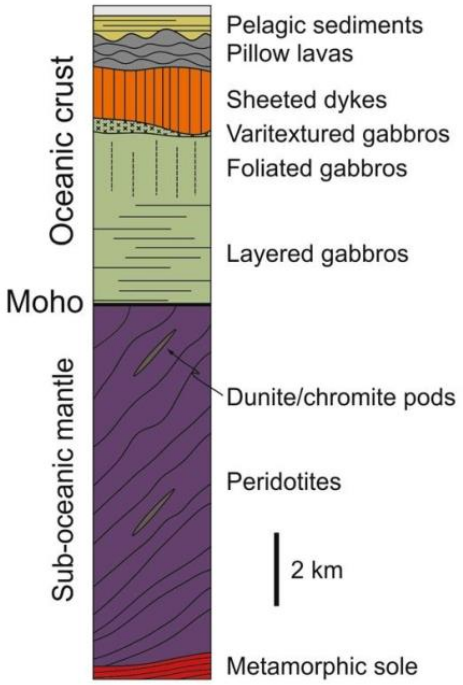

Figure 2.4 – Stratigraphic column of the Oman ophiolite. From Meyer (2015).

The following sections briefly describe the subdivisions of the ophiolite sampled for this study.

2.2.1 – The layered gabbros

The lowest two-thirds of the lower crustal sequence (~2 km thick) is made of layered gabbros with modal layering generally subparallel to the Moho. Modal layering occurs on scales of 0.5 cm to 2 m, mostly defined by variations in the mineral proportions of olivine, clinopyroxene, and plagioclase (Lippard et al., 1982; MacLeod et al., 2000) (Figure 2.5). Other primary minerals in the layered gabbros throughout the ophiolite are chrome spinel, orthopyroxene, hornblende, and titanomagnetite, in variable proportions (Lippard et al., 1986). Primary titanomagnetite grains with ilmenite exsolution lamellae mostly occur at the top of the layered gabbro sequence, while fine-grained secondary magnetite is found through the whole sequence as a common product of olivine and pyroxene alteration (Lippard et al., 1986).

In some localities individual layers in the gabbro can be followed for hundreds of metres along strike before they pinch out. Traveling upwards through the layered gabbro section the layering becomes more irregular and gradually dies out closer to the foliated gabbro sequence (Pallister and Hopson, 1981; Lippard et al., 1986). Magmatic foliations and lineations are commonly found superimposed parallel to the layering and are defined by the shape-preferred orientations of elongate crystals, mostly by the long axes of plagioclase, clinopyroxene, and olivine aggregates (MacLeod and Yaouancq, 2000; Yaouancq and MacLeod, 2000). These lineations and foliations define the magmatic flow in

the layered gabbros as crystals aligned themselves with the flow direction during crystallization.

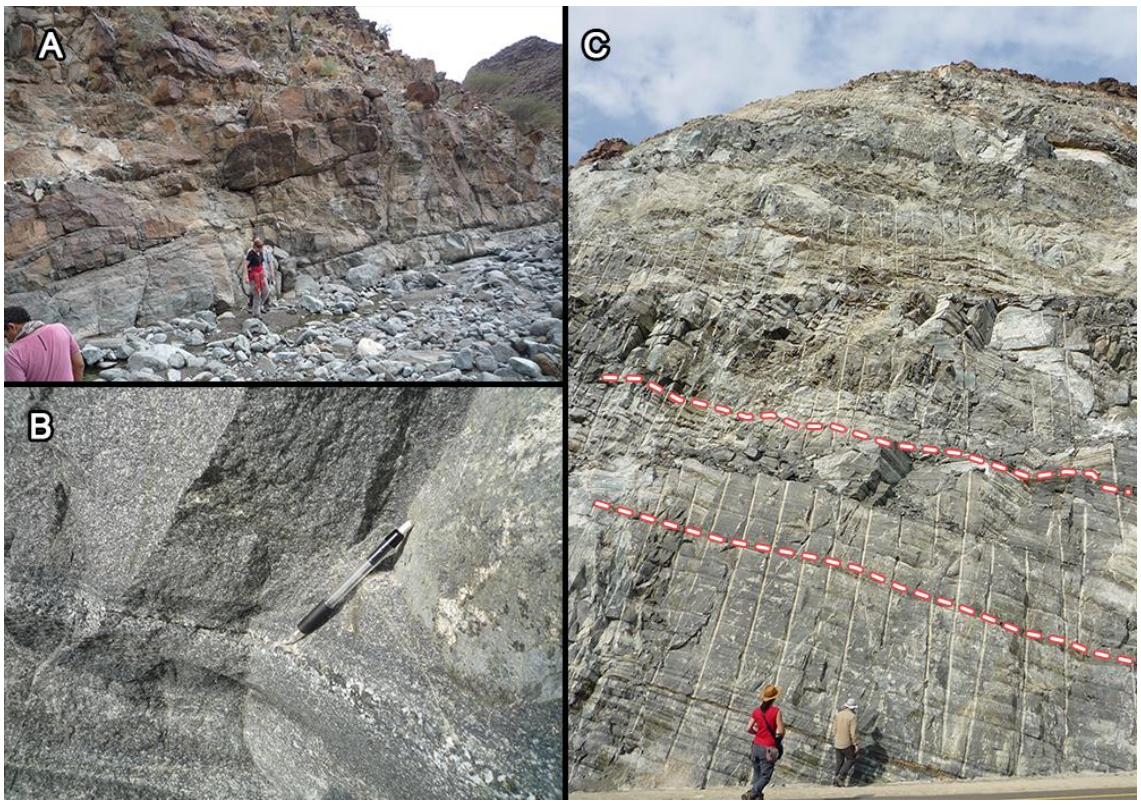

Figure 2.5 – Layered gabbros: (a) from Wadi Gideah (photo credit: M. Harris); (b) close-up from Salahi massif (photo credit: M. Harris); (c) from Salahi massif (photo credit: M. Harris). Dashed lines indicate layering.

2.2.2 – The foliated gabbros

Approximately the upper-third (1 km) of the lower crustal sequence is composed of medium-to-fine grained gabbros in which modal layering is absent and a sub-vertical magmatic foliation is present (Figure 2.6). The foliation is caused by preferred alignments of elongate crystals, in particular plagioclase and to a lesser extent clinopyroxene and olivine aggregates (Figure 2.6a). Other minerals commonly occurring in the foliated gabbros are fine-grained magnetites, coarse-grained titanomagnetites with ilmenite exsolution lamellae and secondary titanomaghemite from the alteration of plagioclase together with clinopyroxene (Lippard et al., 1986).

Figure 2.6 – Foliated gabbros; (a) close-up from Wadi Gideah, showing the preferred orientation of elongated minerals (photo credit: M. Harris) Dashed lines highlight the preferred direction of elongated pyroxene crystals; (b) from Wadi Abdah.

Fabric orientations generally vary over the whole foliated gabbro sequence, from foliations oriented parallel to the Moho and layered gabbros in the lower ~200 m of the sequence to Moho-perpendicular, subvertical foliations at the top, related to magmatic flow directions that transition from flowing horizontally in the layered gabbros to flowing steeply upwards towards a higher level melt lens (MacLeod and Yaouancq, 2000).

2.2.3 – The varitextured gabbros and the dyke rooting zone

At the top of the lower crustal sequence a ~200 m zone of varitextured gabbros can be found, representing a fossil axial melt lens system (MacLeod and Yaouancq, 2000) (Figure 2.7). It is believed that cumulate crystal residues

accumulate in these zones before magma passes upwards to form the upper crust through sheeted dykes. Grain sizes vary from 1 mm to 4 cm, and commonly present minerals are plagioclase, clinopyroxene, olivine, and hornblende, as well as both primary titanomagnetite minerals and primary interstitial magnetites.

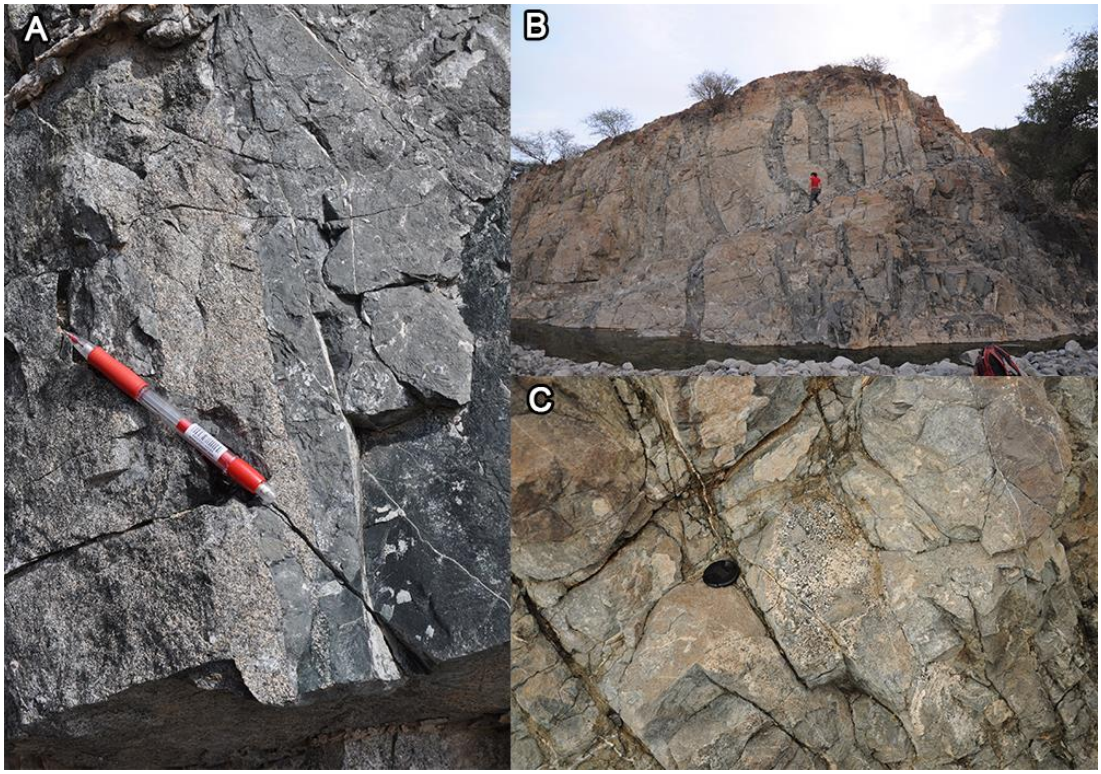

Figure 2.7 – Varitextured gabbros (VTG) and dyke rooting zone: (a) from Wadi Abyad, showing the contact between VTG and a dyke (photo credit: A. di Chiara); (b) from Wadi Gideah; (c) from Wadi Gideah, showing a patch of very coarse gabbro (photo credit: A. di Chiara).

In the top 50-100 m of the varitextured gabbros, the abundance of dykes gradually increases from 10% to 100%, rooting within the varitextured gabbros at various levels (Lippard et al., 1986; MacLeod and Yaouancq, 2000). This transitional sequence is referred to as the dyke rooting zone (DRZ) (Figure 2.7b), and whereas the transition from varitextured gabbros to dykes can clearly be seen in some places in the Oman ophiolites, this was not observed in all localities in this study. The dyke rooting zone is mostly recognised by fine-grained and thin

doleritic dykes cutting through the coarser-grained varitextured gabbros, with a trend that is similar to the sheeted dykes above.

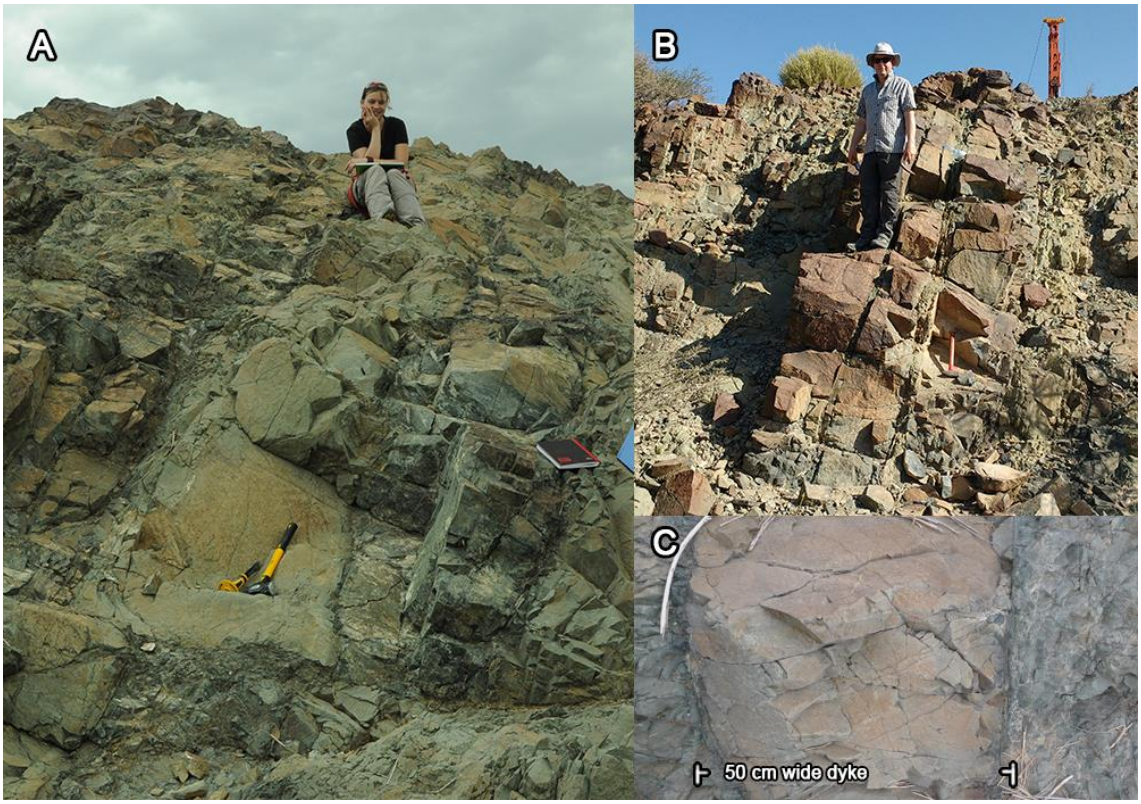

Figure 2.8 – (a) Sheeted dyke complex; (b) from Wadi Abdah, the drill of Oman Drilling Project hole GT3 in the background; (c) sheeted dyke chilled margin contact (photo credit: M. Harris).

2.2.4 – The sheeted dyke complex

Once the abundance of dykes in the dyke rooting zone becomes 100%, we call the sequence a sheeted dyke complex (Figure 2.8). This sheeted dyke complex is part of the upper crustal sequence and is generally 1.5 km thick. Is it composed of near vertical doleritic and basaltic dykes with sharp contacts between neighbouring dykes marked by chilled margins (Pallister and Hopson, 1981; Lippard et al., 1986) (Figure 2.8c). Individual dykes can be as thin as 0.1 m and as thick as 4 m. Zones of quartz and epidote veining can be found locally within the

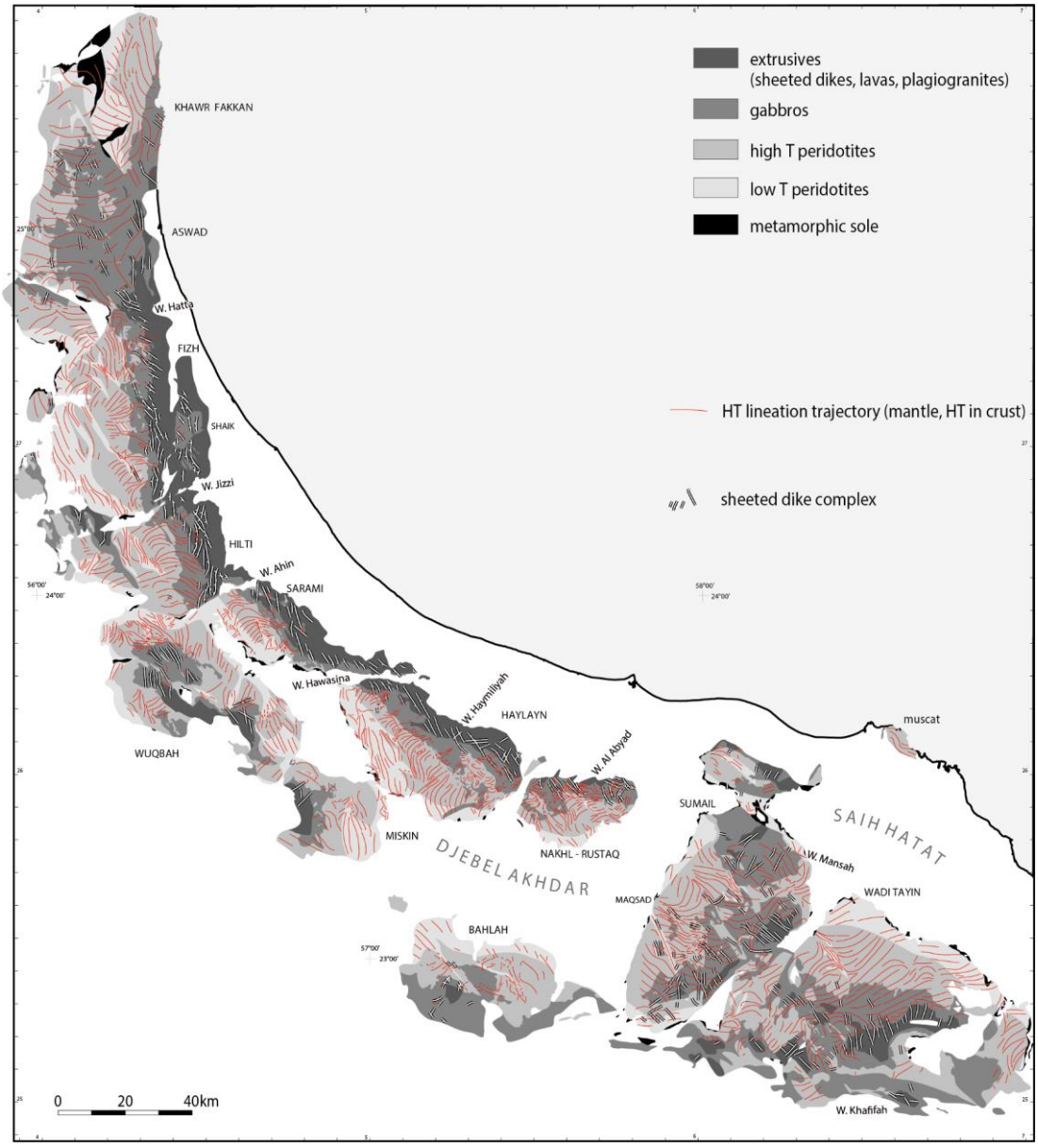

Figure 2.9 – Geological map of the Oman ophiolite modified from Nicholas et al. (2000). Note how the sheeted dyke orientations stay rather constant throughout the whole ophiolite.

sheeted dyke complex of Oman, usually trending parallel to the strike of the dykes; these are interpreted as the pathways of hydrothermal fluids (Lippard et al., 1986).

The orientation of the sheeted dyke complex represents the present day trend of the ridge at which the ophiolite formed. The sheeted dyke strikes tend to be very consistent through the whole ophiolite (Figure 2.9); generally trending

NNW-SSE in the northern massifs and more NW-SE in the central and southern massifs.

Commonly occurring minerals in the sheeted dykes are plagioclase, clinopyroxene, titanomagnetite, and ilmenite, and minor occurrences of olivine. Secondary skeletal grains of Ti-poor titanomaghemite sometimes make up 5% of the modal opaque minerals, and alteration to hematite is not uncommon (Shelton, 1984; Lippard et al., 1986).

2.2.5 – The extrusive sequence

The boundary between the sheeted dyke complex and the extrusive sequence can be gradual (~100 m) for pillow lavas and abrupt (~10 m) for lava flows (Figure 2.10). The extrusive sequence can be up to 2 km thick and has been divided into three separate magmatic events based on petrologic and geochemical grounds (Ernewein et al., 1988; Lippard et al., 1986; Perrin et al., 1994; 2000):

(i) V1 (Geotimes) ridge-axis basalts, consisting of large pillow lavas and lava flows that directly overly the sheeted dyke complex. The V1 units make up 60% of the total extrusive sequence. Often altered, common minerals in the V1 lavas are plagioclase, clinopyroxene, chlorite, quartz, hematite, and other iron oxides.

(ii) V2 (Lasail) lavas make up 35% of the extrusive sequence, and consist of small pillow lavas or lava flows, postdating the V1 lavas and associated with the beginning of intraoceanic thrusting. A sedimentary layer

between the V1 and V2 lavas is absent, indicating there was no interruption in volcanic activity between these magmatic events. Highly altered, common minerals in these lavas are olivine (altered to epidote and chlorite), clinopyroxene, and plagioclase. Compared to V1 lavas, the V2 lavas have a low titanium content.

(iii) V3 (Salahi) lavas only make up the top 5% of the extrusive sequence, and consist of thick lava flows that show columnar jointing and a doleritic texture, which formed between the beginning of oceanic thrusting, but before the obduction of the ophiolite onto the continent (Ernewein et al., 1988).

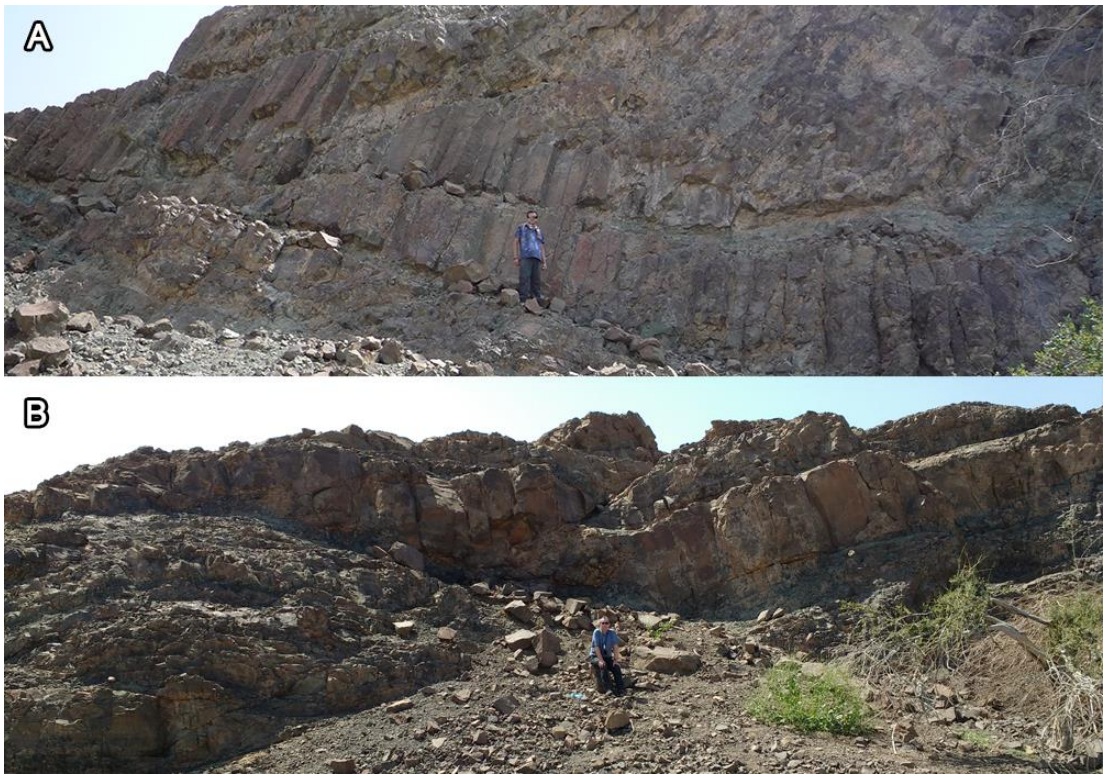

Figure 2.10 – Lava flows (V3); (a) from the Salahi massif (photo credit: A. di Chiara); (b) from Wadi Abdah.

2.3 – Previous magnetic studies of the ophiolite

Previous palaeomagnetic studies identified distinctly different magnetic declinations in the northern and southern massifs of the ophiolite, as shown in Figure 2.11. The northern massifs show an ESE/SE-oriented magnetization with

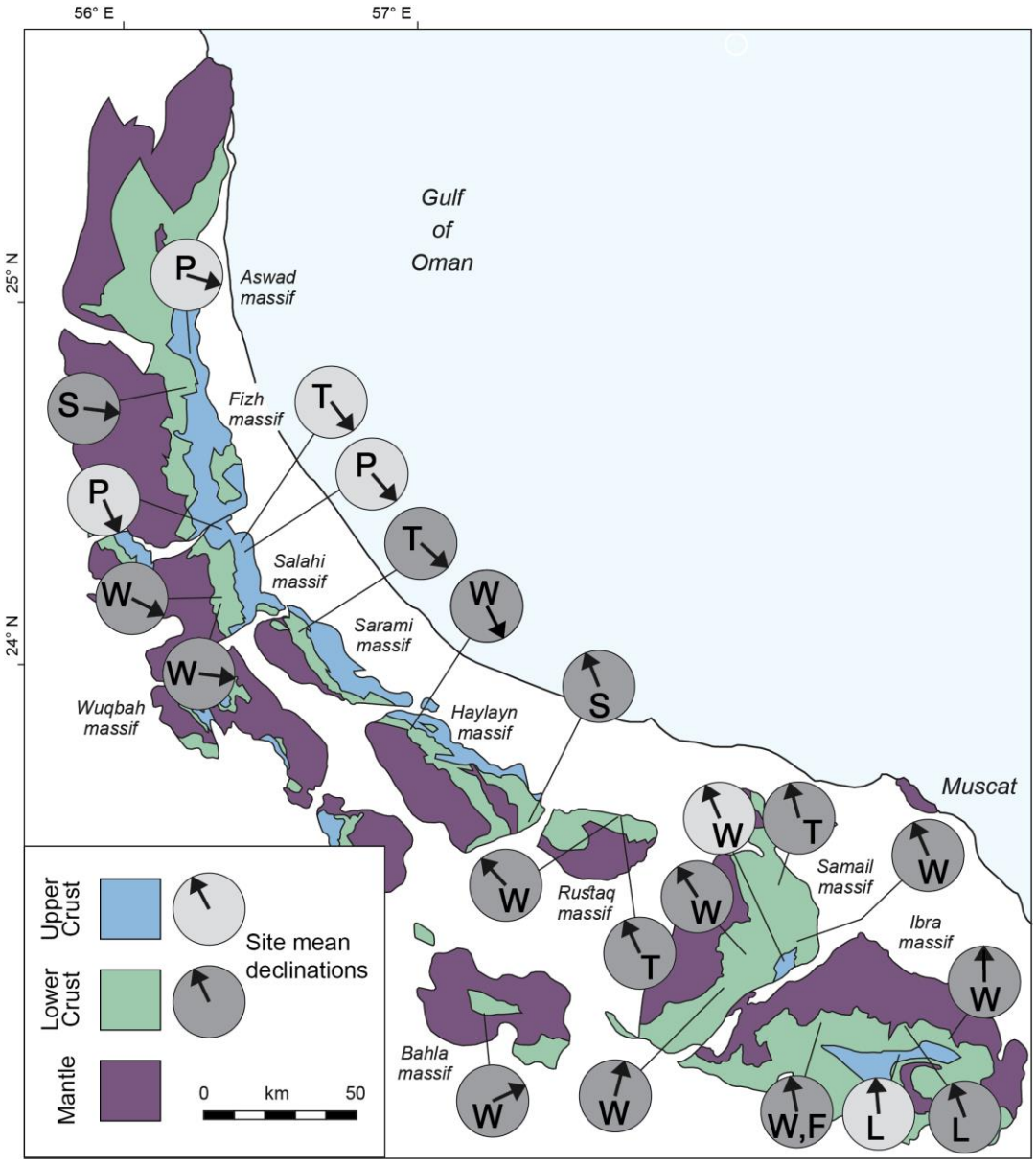

Figure 2.11 – Summary of previously published palaeomagnetic data showing the anomaly between declinations from the northern and southern massifs (modified from Weiler, 2000). Arrow = calculated mean remanence directions (tilt corrected). Sources: L = Luyendyk and Day (1982), S = Shelton (1984), T = Thomas et al. (1988), P = Perrin et al. (1994, 2000), Feinberg et al. (1999), W = Weiler (2000).

low inclinations, while in contrast the southern massifs show a consistent ~NNW-oriented magnetization with low inclinations (Luyendyk et al., 1982; Shelton et al., 1984; Thomas et al., 1988; Perrin et al., 1994, 2000; Feinberg et al., 1999; Weiler et al., 2000).

The earliest palaeomagnetic studies on the Oman ophiolite were carried out by Luyendyk et al. (1982) and Luyendyk and Day (1982) who sampled sheeted dykes, gabbros, and the upper peridotites of the Wadi Tayin massif within the southern half of the ophiolite (Figure 2.11, marked "L"). Their main aim was to test if ophiolite palaeomagnetism could be used as a proxy for oceanic crust magnetization by determining the magnetic properties in these rocks and assessing when magnetization was acquired. Luyendyk et al. (1982) found that pseudo single-domain (PSD) magnetite exsolved from titanomagnetite is the main carrier of the remanent magnetization in the sheeted dykes. Remanences were found to be ~N-directed with low inclinations. Reversed, antipodal remanence directions were also found in limited samples, inferred to be a chemical remanent magnetization (CRM) carried by secondary hematite. Luyendyk et al. (1982) suggested that a subseafloor high-temperature CRM is the most likely origin for this reversed remanence signal, related to hydrothermal metamorphism. Similar results were found for the underlying gabbros and mantle sequence sampled by Luyendyk and Day (1982), showing N-NW-directed declinations with shallow, positive inclinations. They observed variations in the magnetic mineralogy of the gabbros with depth, with primary exsolved PSD magnetite inferred to be the main carrier of the remanence in the upper gabbros

and PSD secondary magnetite the carrier in the lower gabbros and mantle sequence. The secondary magnetite was possibly formed by serpentinization of olivine in peridotite during hydrothermal circulation near the spreading centre. As the ophiolite formed in the Cretaceous Normal Superchron (114-83 Ma), Luyendyk et al. (1982) attributed these reversed polarity directions to a lesser known small mixed polarity interval. Based on the majority of normal polarity samples from the sheeted dykes and gabbros with a northern declination, Luyendyk et al. (1982) and Luyendyk and Day (1982) concluded that the spreading ridge at which the Oman ophiolite formed was oriented roughly N-S and located at an equatorial latitude of 9° in the Tethyan Ocean, after which it was obducted onto the Arabian continent without any significant rotation.

The pioneering studies of Luyendyk et al. (1982) and Luyendyk and Day (1982) in the southern massifs of the ophiolite were followed up in the northern massifs by Shelton (1984). His palaeomagnetic study (Figure 2.11, marked “S”) focused mainly on gabbros and a few dykes in the northern massifs and found inferred primary remanences directed to the SE that were strongly overprinted by the present day field. Thomas et al. (1988) later confirmed this SE remanence direction in other northern massifs by sampling gabbros and metalliferous sediments (umbers and iron-rich radiolarites) interbedded within the V1 and V2 volcanic units (Figure 2.11, marked “T”). They found several groups of low inclination magnetizations that show antipodal orientations; a NNE-SSW-directed magnetization found in the umbers and radiolarites of the northernmost Fizh massif and in the Birquat massif (south of the Semail massif), and a NW-SE-

directed magnetization in the Salahi and Sarami massifs (northern massifs). NW-SE-directed magnetizations were also found in a few samples from the Birquat massif carried by a single metamorphosed radiolarite exposure. Thomas et al. (1988) also analysed gabbros to compare their magnetization with that of the overlying umbers and radiolarites, and concluded that the gabbros carry a SE-directed magnetization that is similar to the direction found in the umbers.

The data of Luyendyk et al. (1982), Luyendyk and Day (1982), Shelton (1984), and newly acquired results from their own study allowed Thomas et al. (1988) to produce a diagram summarising the palaeomagnetic results acquired so far in Oman (Figure 17 in Thomas et al., 1988; Figure 2.11), that combines the results from umbers, radiolarites, dykes, and gabbros. From these data the difference between declinations in the northern and southern massifs of the Oman ophiolite had already become clear. Thomas et al. (1988) suggested that the NW-SE antipodal magnetizations recorded in sediments and dykes/gabbros were obtained during short, unconfirmed reversed polarity intervals within the Cretaceous Normal Superchron and were acquired roughly around the same age, whereas the NNE-SSW-directed (re)magnetizations recorded by sediments from the Fizh and Birquat massifs were acquired at a later date. At face value, the different magnetic directions could be the result of large differential tectonic rotations between different parts of the ophiolite, however Thomas et al. (1988) rejected this option because: (i) the sheeted dyke complex shows an along-strike continuity throughout the whole ophiolite (Figure 2.9); and (ii) both NNE-SSW and NW-SE palaeomagnetic directions were recorded within sediments and gabbros

of the same massif. Thomas et al. (1988) therefore suggested that different magnetic directions were obtained at different times during coherent rotation of the entire nappe. They proposed two models to explain the different remanence directions recorded through the Oman ophiolite. The first model involved a large continuous 145° clockwise rotation (CW), followed by a smaller counterclockwise (CCW) rotation related to the emplacement of the ophiolite onto the Arabian continent (Figure 2.12 – Model 1). In the second model, primary magnetizations were acquired before rotation, and were then followed by: (i) a 75° CCW rotation; (ii) remagnetization of the sediments; (iii) a 40° CW rotation and a 15° CCW rotation together with the African continent (Figure 2.12 – Model 2). This second model was favoured by Thomas et al. (1988) who proposed that the primary NW-SE magnetization was acquired in all samples first, and was later overprinted by the NNE-SSW magnetization only in the sediments. The model places the original orientation of the spreading ridge at 025-050°, bringing the sheeted dykes to their current orientation of 335° via a CCW rotation of 50°.

Later palaeomagnetic studies by Perrin et al. (1994) focused on the volcanic sequence of the Oman ophiolite in order to better constrain the large rotation of the nappe during emplacement. They sampled the three volcanic sequences (V1, V2, V3) in the Salahi massif (their Hilti block) hoping to obtain successive, discrete records of the rotational nappe movements on the seafloor. They found SE-ESE directions with shallow inclinations for the V1 and V2 lavas respectively and found a consistent northern direction with a shallow inclination

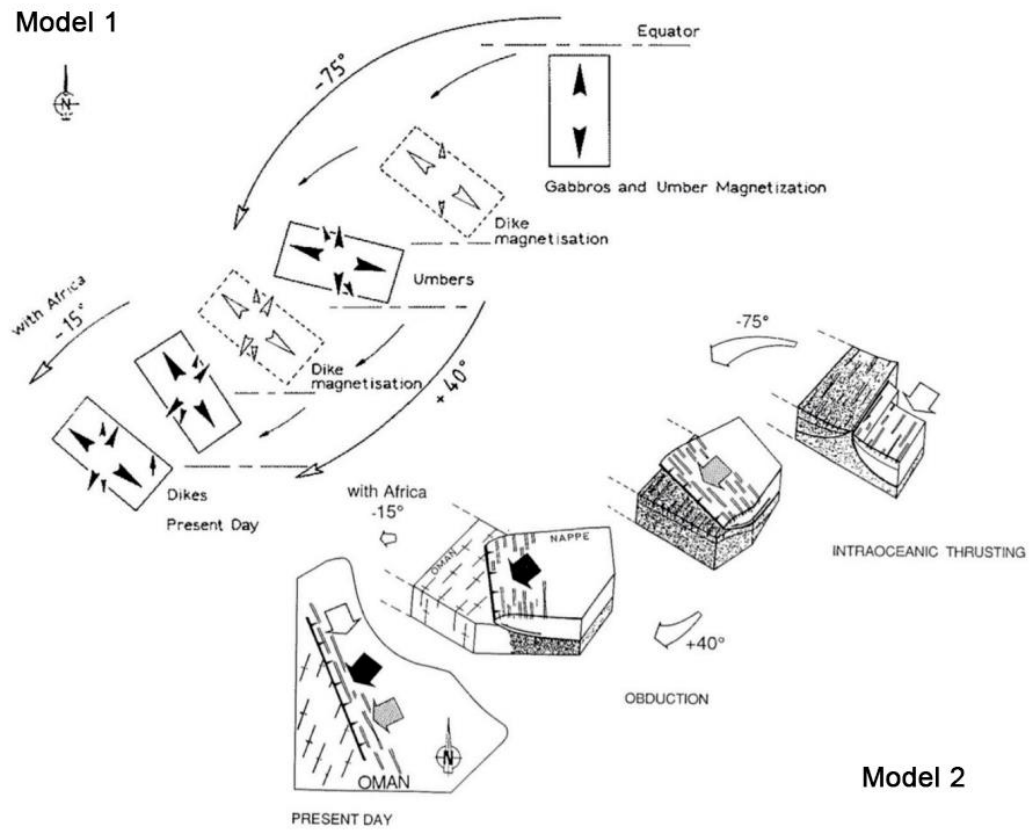

Figure 2.12 – Two models proposed by Thomas et al. (1988) for how (re)magnetization events during nappe rotations could lead to the declination anomalies found between the northern and southern massifs of the Oman ophiolite. See text for discussion.

in the V3 lavas (Figure 2.11, marked "P"). Perrin et al. (1994) then based their model for the entire Oman ophiolite on the results from the lavas from the Salahi massif and concluded that a large CW rotation (145-150°) of the Oman ophiolite occurred during its movement on the seafloor, between the detachment of the nappe and the end of the obduction (100-70 Ma). They suggested that the rotation can be described by a single Euler Pole located close to the nappe (~200 km away). Their model restores the spreading ridge orientation to NNW-SSE to N-S and places this at a palaeolatitude of 10°N (Figure 2.13).

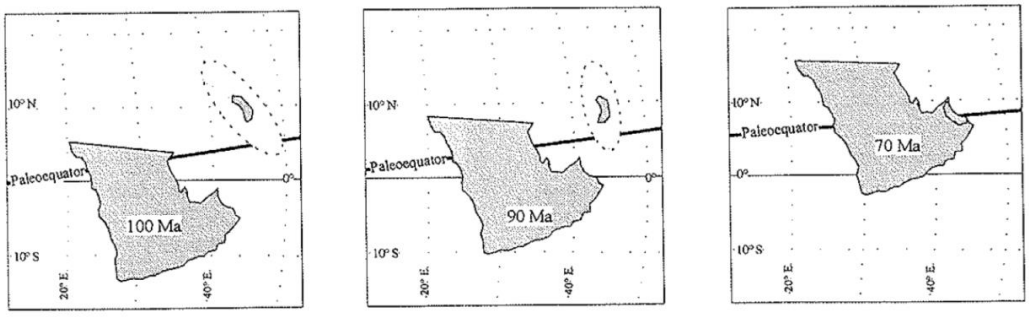

Figure 2.13 – Model of Perrin et al. (1994, 2000) showing a proposed 150° CW rotation of the entire Oman ophiolite in a single movement (see text for discussion). The model is in agreement with Model 1 from Thomas et al. (1988) (Figure 2.12).

Perrin et al. (2000) later returned to sample additional V1 and V2 volcanic sequences in other northern massifs (Aswad, Fizh, Hilti, Sarami, Wuqbah massifs) and at a single V1 lava site in the south (Wadi Tayin) (Figure 2.11, marked “P”). The later V2 lavas provided consistent E to ESE palaeomagnetic directions, however, the earlier V1 lavas from the northern massifs show scattered directions. Perrin et al. (2000) suggested that this was caused by differential rotations between the massifs prior to the eruption of the V2 lavas, and suggested that the entire ophiolite then behaved as a single tectonic unit after eruption of the V2 lavas.

The single V1 lava site from the southern massif reported by Perrin et al. (2000) had a shallow inclination and northern declination, giving a 90° difference between the magnetic directions in V1 lavas between the southern and northern massifs. Perrin et al. (2000) suggested that this indicated a 90°relative rotation between the northern and southern massifs which would have occurred before emplacement of the V2 lava sequences and during crustal accretion.

Feinberg et al. (1999) conducted an extensive palaeomagnetic study that focused on peridotites and gabbros from the southern massifs (Samail, Wadi Tayin, Muscat massifs), but importantly also sampled Permian basement rocks (metabasites) from the subophiolitic Saih Hatat tectonic window for the first time. Palaeomagnetic analysis of all their sampled units showed comparable results (Figure 2.11, marked "F") to previous palaeomagnetic studies in the southern massifs, with magnetization directions ranging between NW-NNE. These remanences in the lowest gabbro sequences and mantle peridotites were interpreted by Luyendyk and Day (1982) to be carried by secondary magnetite formed during serpentinization of olivine during hydrothermal circulation at the spreading ridge, early in the history of the ophiolite. Feinberg et al. (1999) instead proposed that these remanences are held by secondary magnetite produced during an obduction-related hydrothermal event that took place long *after* the formation of the ophiolite. They noted that hydrothermal activity driven by magmatism is limited to the upper oceanic crust, and is not likely to affect the lower crust (layered gabbros) or even deeper (into the peridotites). Feinberg et al. (1999) attempted to constrain the timing of acquisition of the NW magnetizations through comparison with the direction found in the basement rocks. Palaeomagnetic directions from the Permian-aged metabasites of the tectonic window show similar directions to those seen in the overlying mantle peridotites and crustal gabbros (Figure 2.14), suggesting that the ophiolitic rocks and older basement rocks acquired their stable NRM magnetization simultaneously during a late remagnetization event. Based on these results

Feinberg et al. (1999) proposed a model for the southern massifs of the Oman ophiolite that involved remagnetization of the basement rocks and the overlying ophiolite from the base upwards during obduction-related, high-temperature fluid flow (Figure 2.15). In this model, a decreasing metamorphic grade between the southern and northern massifs resulted in lower temperature metamorphism in the northern massifs, leading to less intense remagnetization that possibly only reached into the mantle peridotites. This model explains why a remagnetised remanence direction (N-NW) is only found in ophiolitic rocks in the southern massifs, whereas the crust in the northern massifs retains earlier primary SE-directed magnetizations. This model also suggests that magnetic directions from the southern massifs of the Oman ophiolite cannot be used to determine early intraoceanic rotations or initial ridge orientations.

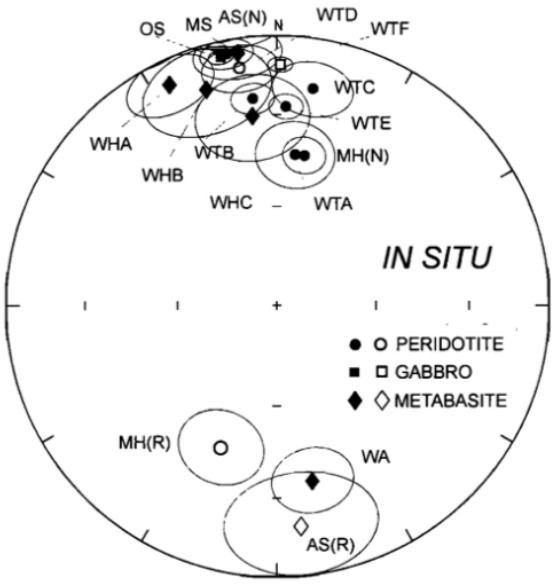

Figure 2.14 – Stereographic projection summarising the results of Feinberg et al. (1999).

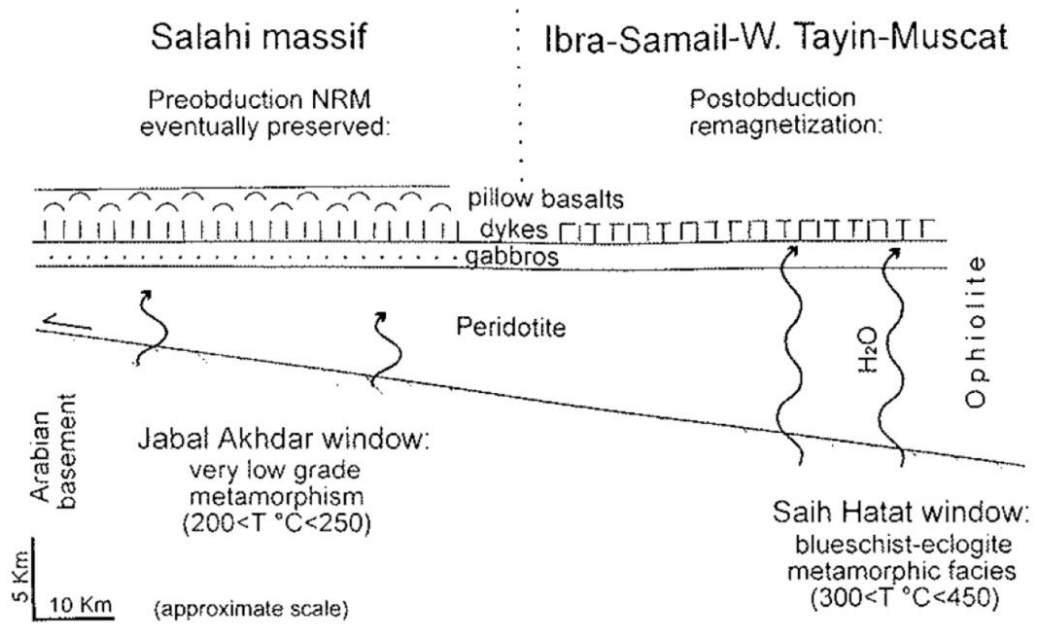

Figure 2.15 – Model of Feinberg et al. (1999) for obduction-related remagnetization of the southern massifs, caused by an upwards hydrothermal wave of high-temperature fluids expelled from beneath the ophiolite. Due to more intensive metamorphism beneath the thicker southern massifs the remagnetization was able to affect higher stratigraphic levels than in the northern massifs.

Shortly after the study by Feinberg et al. (1999), Weiler (2000) extensively sampled lower crustal layered gabbros throughout the entire ophiolite. Results (Figure 2.11, marked “W”) from layered gabbros in the northern massifs showed comparable SE-directed magnetizations to the V1 and V2 lavas sampled by Perrin et al. (1994, 2000). Layered gabbros in the southern massifs gave N-NW directions comparable to those published by Luyendyk and Day (1982) and Feinberg et al. (1999). However, Weiler’s (2000) analysis of the palaeomagnetic database raised a number of issued relating to the remagnetization model of Feinberg et al. (1999):

1. A positive fold test was inferred to exclude a post-emplacement magnetization, as it suggested magnetization was acquired before tilting related to emplacement. Instead, Weiler (2000) inferred that the

hydrothermal circulation that caused the formation of secondary magnetite occurred before emplacement of the ophiolite.

2. Secondary magnetite, thought by Feinberg et al. (1999) to carry the remagnetised signal, is not unique to the southern massifs and is frequently found as a magnetic carrier in ophiolitic rocks in the northern massifs. Nonetheless, the primary (magmatic) and secondary (hydrothermal) magnetite grains in the northern massifs carry similar magnetization directions, suggesting that secondary magnetite was formed early after primary magnetite and most likely related to early hydrothermal circulation near the spreading ridge.
3. Weiler (2000) questioned the relationship between the metabasites sampled by Feinberg et al. (1999) and the ophiolitic mantle and crustal rocks, and whether it can be proven that the ophiolite was emplaced onto these metabasites.

Instead, Weiler (2000) proposed that the remagnetization of gabbros in the southern massifs was the result of early, high-temperature hydrothermal circulation shortly after detachment at the spreading ridge, consistent with the results of Perrin et al. (1994, 2000) from the V2 lavas. Weiler (2000) therefore presented a new East Pacific Rise (EPR)-type microplate model to explain the 130° difference between the magnetization directions of the northern and southern massifs, similar to a model proposed earlier by Boudier et al. (1997). In this model, the palaeomagnetic declinations of each massif are restored back to the north (Figure 2.16). The rotations proposed by the model are inferred to be equivalent

to that of the Juan Fernandez microplate studied by Larson et al. (1992) and are implied to happen at the rapid rate of 20° per million years. This model breaks the ophiolite up into parts formed at two separate spreading ridge segments (see Figure 2.16):

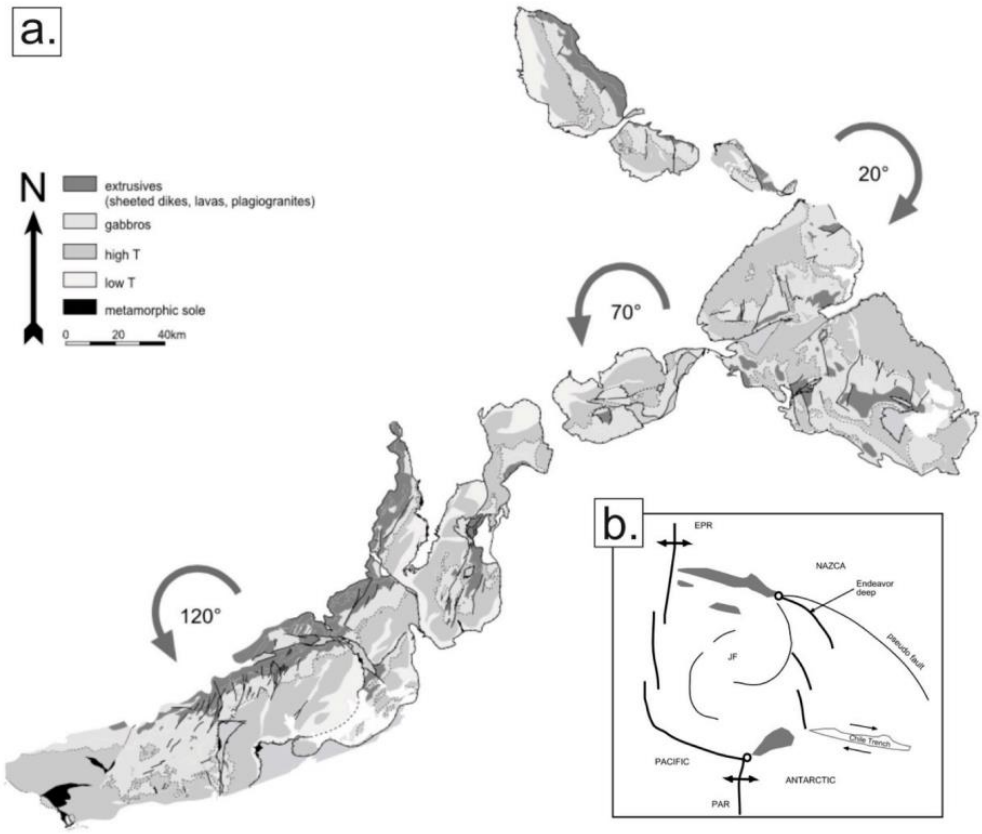

Figure 2.16 – Model of Weiler (2000) in which the Oman ophiolite shows similar behaviour to the Juan Fernandez microplate on the East Pacific Rise (EPR). (a) After back-rotating the mean magnetization orientations in individual massifs to north, the ophiolite is inferred to have a similar geometry to EPR microplate systems (see discussion in text). (b) Simplified model of the Juan Fernandez microplate system (Larson et al. (1992).

1. a NE-SW oriented spreading ridge formed the northern massifs, trapped on a rapidly accreting microplate, that would have to make a 120° CCW rotation to get to its current position. Such large rotations were earlier found by Perrin et al. (2000), and are therefore consistent with this model.
2. a younger NW-trending ridge formed the central and southern massifs

that would only need to experience a 20° CW rotation to get to its current position.

A later geochemical study by Macleod et al. (2013), however, provided compelling evidence that the whole Oman ophiolite formed directly above a subduction zone in an arc spreading setting, immediately following subduction initiation. Therefore, the models of Boudier et al. (1997) and Weiler (2000) that propose rotation of the ophiolite in a mid-oceanic ridge microplate or overlapping spreading centre setting cannot explain the rotations seen in the ophiolite and a different model must be proposed based on the geodynamics of subduction zones.

More recently, by extensively sampling a near complete and continuous crustal sequence in Wadi Abyad in the Rustaq massif (southern massifs), Meyer (2015) and Morris et al. (2016) provided more evidence that the Oman ophiolite experienced a late-stage remagnetization event. Lower crustal gabbros in this crustal section were found to carry a NNW-directed remanence magnetization that is comparable to those found elsewhere in the southern massifs (Luyendyk et al., 1982; Luyendyk and Day, 1982; Thomas et al., 1988; Feinberg et al., 1999; Weiler, 2000). Sampling upwards in the sequence revealed remanence directions that gradually become more N, NE, and eventually ENE-directed in the dyke rooting zone, a direction that is close to that of primary magnetizations in the northern massifs. Meyer (2015) and Morris et al. (2016) proposed that remagnetization occurred from the base upwards, with the original

magnetization being completely replaced in the lowermost gabbros and with primary magnetizations preserved at the top of sampled section. Importantly, low stability components in the upper parts of the section were found to have the same direction as the section below that is inferred to be completely remagnetised, suggesting that the extent of remagnetization decreased up section. Earlier interpretations of Feinberg et al. (1999) are consistent with these results and suggest that upward advection of metamorphic fluids related to the obduction and emplacement of the ophiolite was the cause for remagnetization in the ophiolite.

Based on these results, Morris et al. (2016) proposed a new rotation model in a supra-subduction zone setting that involves: (i) formation of the ophiolite along a NE-SW-oriented spreading ridge above an intraoceanic subduction zone;

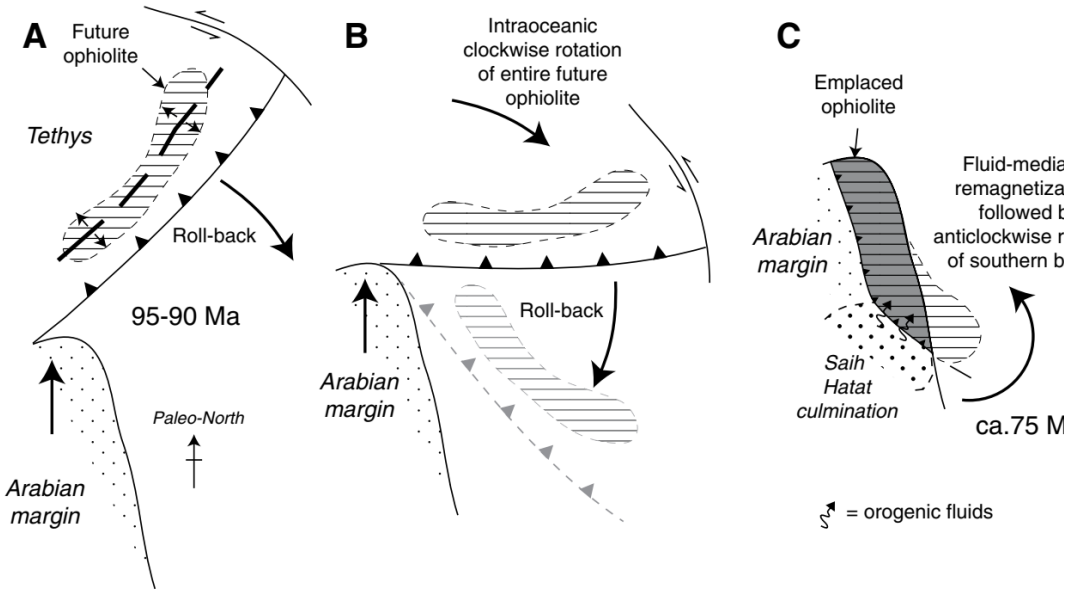

Figure 2.17 – Schematic model proposed by Morris et al. (2016) that explains rotation of the Oman ophiolite in a simple way in a suprasubduction zone setting: (a) Formation of the ophiolite along a NE-SW-oriented spreading ridge above a subduction zone; (b) clockwise rotation of the entire ophiolite caused by the northwards movement of Arabia and subduction roll-back; (c) emplacement onto the Arabian continent resulting in remagnetization and then back-rotation of the southern massifs in response to the development of the Saih Hatat structural culmination.

(ii) CW rotation of the entire ophiolite related to roll-back of the subduction system; (iii) eventual emplacement of the ophiolite onto the Arabian continent, resulting in a fluid-mediated remagnetization event; and (iv) final CCW back-rotation of the southern massifs driven by development of the Saih Hatat structural culmination (Figure 2.17). This model therefore removes the need for differential rotation between massifs in the ophiolite proposed by Weiler (2000).

Finally, the latest palaeomagnetic research in Oman was recently published by van Hinsbergen et al. (2019) (of which I am a co-author), who focused on sampling the sheeted dykes in nearly every massif of the ophiolite to restore the orientation of the supra-subduction zone ridge during spreading and ophiolite formation. Net tectonic rotation analysis was used to restore the sheeted dykes back to their original, vertical orientation, providing evidence for a consistently NNE-SSW trending spreading centre located in the upper plate above a young subduction zone, consistent with the geochemical signature of the ophiolitic sequence (MacLeod et al., 2013; Rioux et al., 2016; van Hinsbergen et al., 2019). Sheeted dykes from the southern massifs were not included in this analysis as they had previously been identified as remagnetised (Feinberg et al., 1999; Morris et al., 2016). Van Hinsbergen et al. (2019) propose a new model consistent with a supra-subduction zone ridge setting that places the trench orthogonal to the Arabian passive margin along a fracture zone (Figure 2.18):

(i) a new subduction zone initiates at 104 Ma along an ancient Arabian continent-parallel fracture zone, oriented NNE-SSW,

(ii) the Oman ophiolite forms at 95 Ma during forearc extension, followed

by large (100°) CW rotation, and finally obduction at 70 Ma.

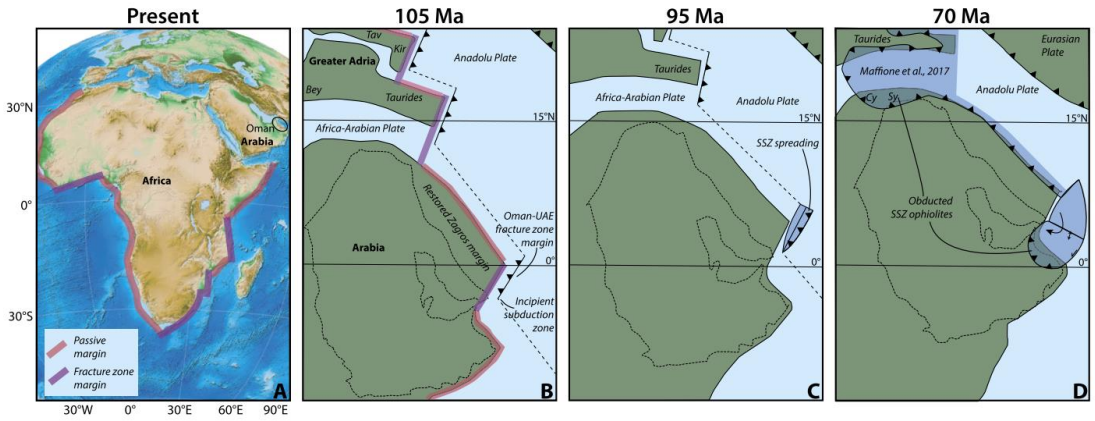

Figure 2.18 – Tectonic model of subduction initiation along the Arabian margin of Oman, proposed by van Hinsbergen et al. (2019). See text for discussion.

In summary, extensive palaeomagnetic studies in the Oman ophiolite have led to contradictory tectonic models that critically depend on understanding the nature of remagnetization of the southern massifs. The analysis of Meyer (2015) and Morris et al. (2016) suggests that the key to understanding the remagnetization event may lie within the transition zone from lower to upper crustal rocks. Hence, the present study has focused on systematically sampling additional complete sections in order to determine the vertical and spatial extent of remagnetization. The rest of this chapter therefore provides background geological information about the localities selected for sampling that may help to better understand the remagnetization event.

2.4 – Geology of sampling localities

Samples for this study were collected at five localities (Figure 2.19), selected with the aim of studying the extent and reach of the remagnetization

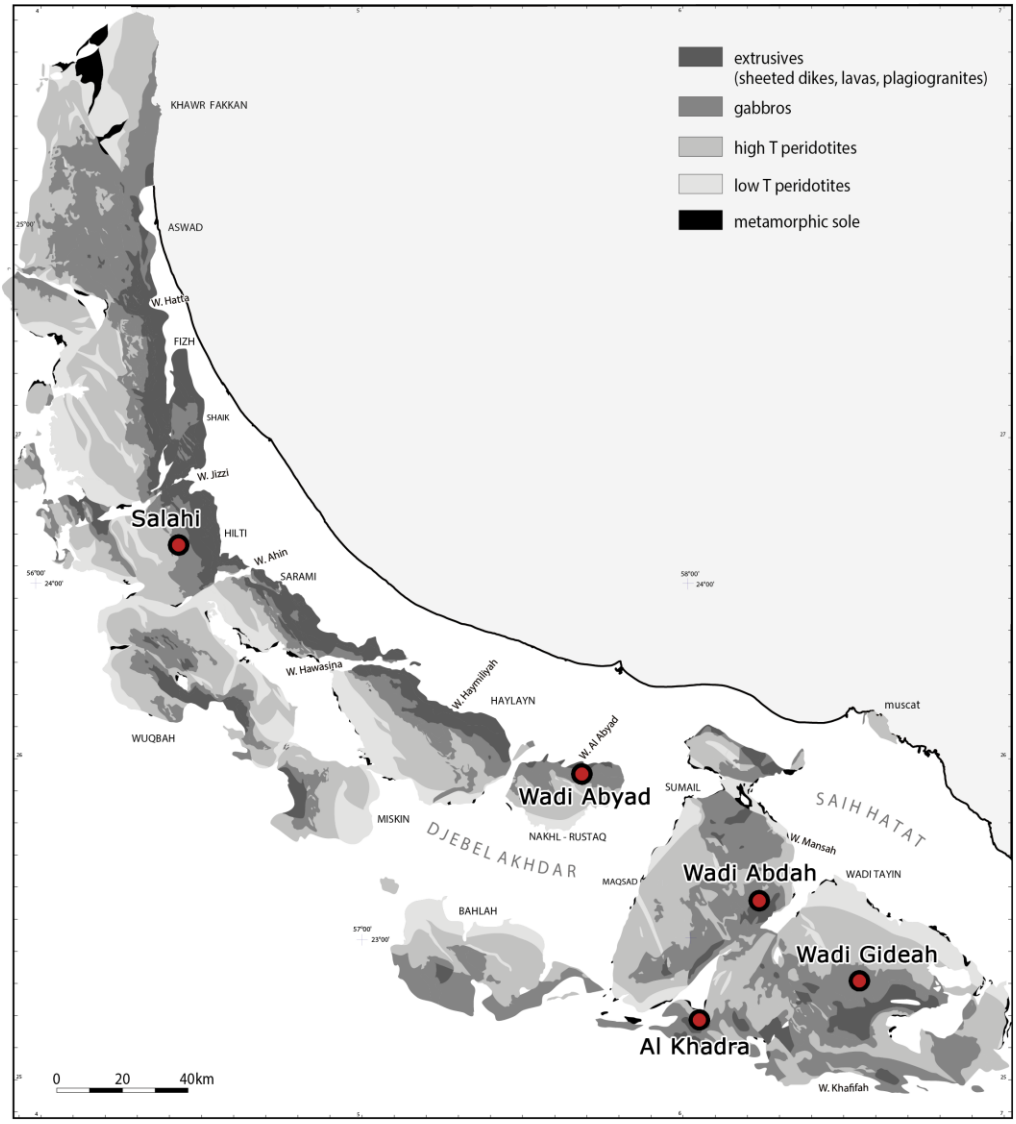

Figure 2.19 – Overview of sampling localities.

event that took place in the southern massifs of the Oman ophiolite (Feinberg et al., 1999; Morris et al. 2016). As described above, Meyer (2015) and Morris (2016) proved that remagnetization progressed from the bottom upwards in Wadi Abyad, resulting in complete overprinting of original magnetizations and preservation of a potentially primary ENE-oriented magnetization in the dyke rooting zone. For this study, therefore, the Wadi Abyad location was revisited to extend palaeomagnetic analysis into the sheeted dykes overlying the dyke

rooting zone and provide a complete section, as the original analysis at this locality was focused solely on the lower crust (note that lavas are not exposed in Wadi Abyad).

Two more complete crustal sections were sampled in the southern massifs to determine if further evidence for remagnetization progressing from the bottom upward could be found in locations other than Wadi Abyad. Wadi Abdah and Wadi Gideah were selected as these provide two complete sections starting in the lower oceanic crust (layered/foliated gabbros) and extending upwards to the dyke rooting zone and into the sheeted dyke complex. In Wadi Abdah, sampling could also be continued up into the lava flows overlying the sheeted dykes. These localities are also of particular importance as three of the drill sites (Holes GT1, GT2, and GT3) of the recent International Continental Scientific Drilling Program “Oman Drilling Project” were located at the same places, providing opportunities to compare results from surface and sub-surface and to provide context for the Oman Drilling Project results. This is important as the drill cores were (initially) azimuthally unoriented, and hence declinations in drill core samples are unknown.

A small outcrop called Al Khadra in Wadi Indam, consisting of a dyke and (pillow) lava flows, was sampled at the far south-western edge of the southern Ibra massif. It acts as a control site to see if remagnetization affected the upper crust this far west in the southern massifs.

Finally, a control locality in sub-horizontally layered gabbros of the Salahi block in the northern half of the ophiolite was sampled, outside the region

believed to be affected by the remagnetization event. As well as a direct palaeomagnetic comparison with the other localities, this control locality also facilitated a test of whether rock magnetic properties (via end-member modelling of isothermal remanence acquisition curves) may be used to distinguish sections carrying primary and remagnetised remanences in ophiolitic rocks.

The sections below provide more information on the exact locations of sampling in each of the five localities, as well as the surrounding geology.

2.4.1 – Wadi Abyad

Wadi Abyad, the "White Valley", is located around the oasis village of Al Abyad in the Rustaq massif, also known as the Nakhl block (Figures 2.20 to 2.22). The lower crustal rocks of Wadi Abyad progress from mantle peridotites in the south, through a moderately NE-dipping Moho into a 2.6 km thick sequence of layered, foliated, and varitextured gabbros, a dyke-rooting zone, and its overlying sheeted dykes (Figure 2.20).

In the previous study of Meyer (2015) and Morris et al. (2016), nearly all lithostratigraphic units were sampled from the lower crustal gabbros to the dyke rooting zone (DRZ) (Figure 2.20). In this study, sampling focused on the sheeted dykes above the DRZ to complete this pseudostratigraphical section. Samples collected by Meyer (2015) were also used in the IRM analysis. The stratigraphic units in Wadi Abyad can be described as follows, from the base upwards (MacLeod and Yaouancq, 2000; Morris et al., 2016):

1. Layered gabbros, with layering defined by variations in olivine, pyroxene,

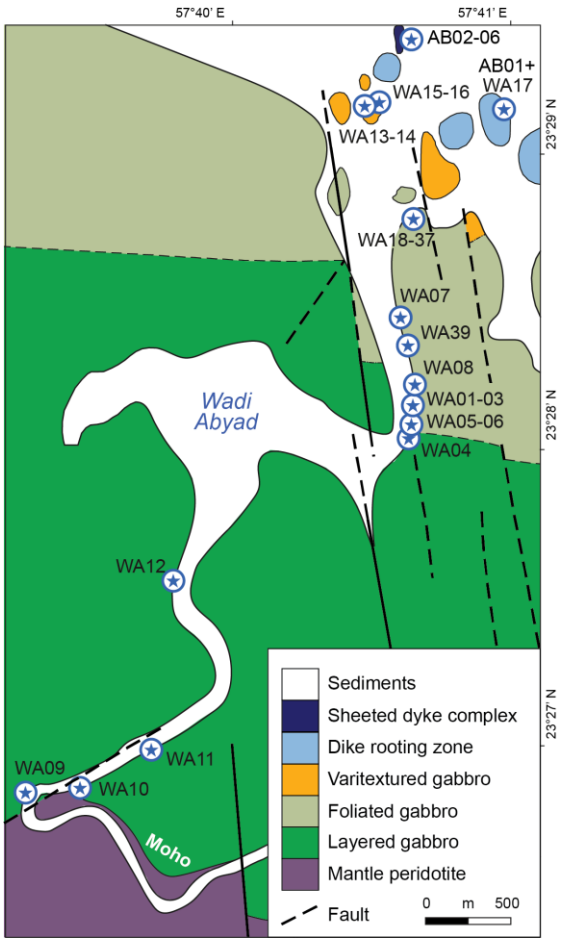

Figure 2.20 – A simplified geological map of the Wadi Abyad section, showing locations sampled by Meyer (2015) and this study (AB sites) as blue stars. (Modified from Meyer (2015))

and plagioclase and varying from centimetre to metre-scaled layers. The layering is consistently subparallel to the NNE-dipping Moho at the base of the gabbro section, and thus this orientation can be used as a palaeohorizontal surface for tilt correction of the palaeomagnetic data (Morris et al., 2016). Lineations measured in the gabbros define a WNW-ESE trend perpendicular to a NE-SW striking ridge. Samples from Meyer (2015) used in this study come from layered gabbro sites WA09-11 and WA04.

2. Foliated gabbros, in which preferred mineral orientations define a foliation

that is nearly perpendicular to the Moho, as well as a subvertical lineation. Samples from sites WA05-06, WA01-03, WA07-08, WA39, and WA19-37 from Meyer (2015) were used in this study.

3. Varitextured gabbros cut by discrete dykes, marked by high variability in grain size, texture, and composition over short distances. They represent the fossil axial melt lens (MacLeod and Yaouancq, 2000). Only samples from the individual cross-cutting dykes were used in this study (WA14 and WA16) (Meyer, 2015).
4. Dyke rooting zone, consisting of microgabbro and basaltic dykes separated by gabbro screens. It shows a gradational contact with the underlying varitextured gabbros. Samples from Meyer's (2015) study were used (WA17) and in addition more dykes (striking NE-SW) were sampled for this study during fieldwork in 2016 (Site AB01).
5. Sheeted dykes, directly overlying the dyke rooting zone, sampled as sites AB02-06 in this study. These dykes generally strike WNW-ESE, nearly perpendicular to the dykes from the dyke rooting zone, implying that the sheeted dykes may have formed at a later stage during the formation of Wadi Abyad than the dyke rooting zone and interacted with a younger NW-SE propagating ridge.

Figure 2.21 – Dyke rooting zone of Wadi Abyad (photo credit: M. Harris). Dashed lines indicate the dyke orientations.

Figure 2.22 – Sheeted dyke complex of Wadi Abyad.

2.4.2 – Wadi Abdah and Oman Drilling Project Hole GT3

Wadi Abdah is located in the Semail massif, with most sites located around a small village named Aswad, the “Black Village” (Figures 2.23 to 2.25). This locality was chosen for its proximity to Hole GT3 of the Oman Drilling Project. It provides a complete ophiolitic pseudostratigraphic sequence (Figure 2.23), from layered/foliated/varitextured gabbros into a dyke rooting zone/sheeted dykes and up into lava flows, and has not been significantly affected by ridge segmentation (Nicholas et al., 2008). The section provides excellent exposures of the dyke/gabbro transition zone of interest to both this study and the Oman Drilling Project.

For this study, nearly all lithostratigraphic units were sampled. Units can be described as follows, from the lowest sampled unit to the highest (Weiler, 2000; Nicholas et al., 2008):

1. Foliated, granular gabbros, exposed in the north of the area near the village of Aswad, with a magmatic foliation parallel to the general trend of the overlying sheeted dyke complex. The foliation is defined by oriented tabular plagioclase laths, elongated olivine aggregates, and clinopyroxene grains. Sites BD13-14 were sampled for this study in these foliated gabbros.
2. A sharp discordance is found between the foliated gabbros and the varitextured gabbros, with the base of the dyke rooting zone difficult to identify. The varitextured gabbros are characterised by an ophitic texture, with the clinopyroxene largely replaced by hornblende and altered olivine

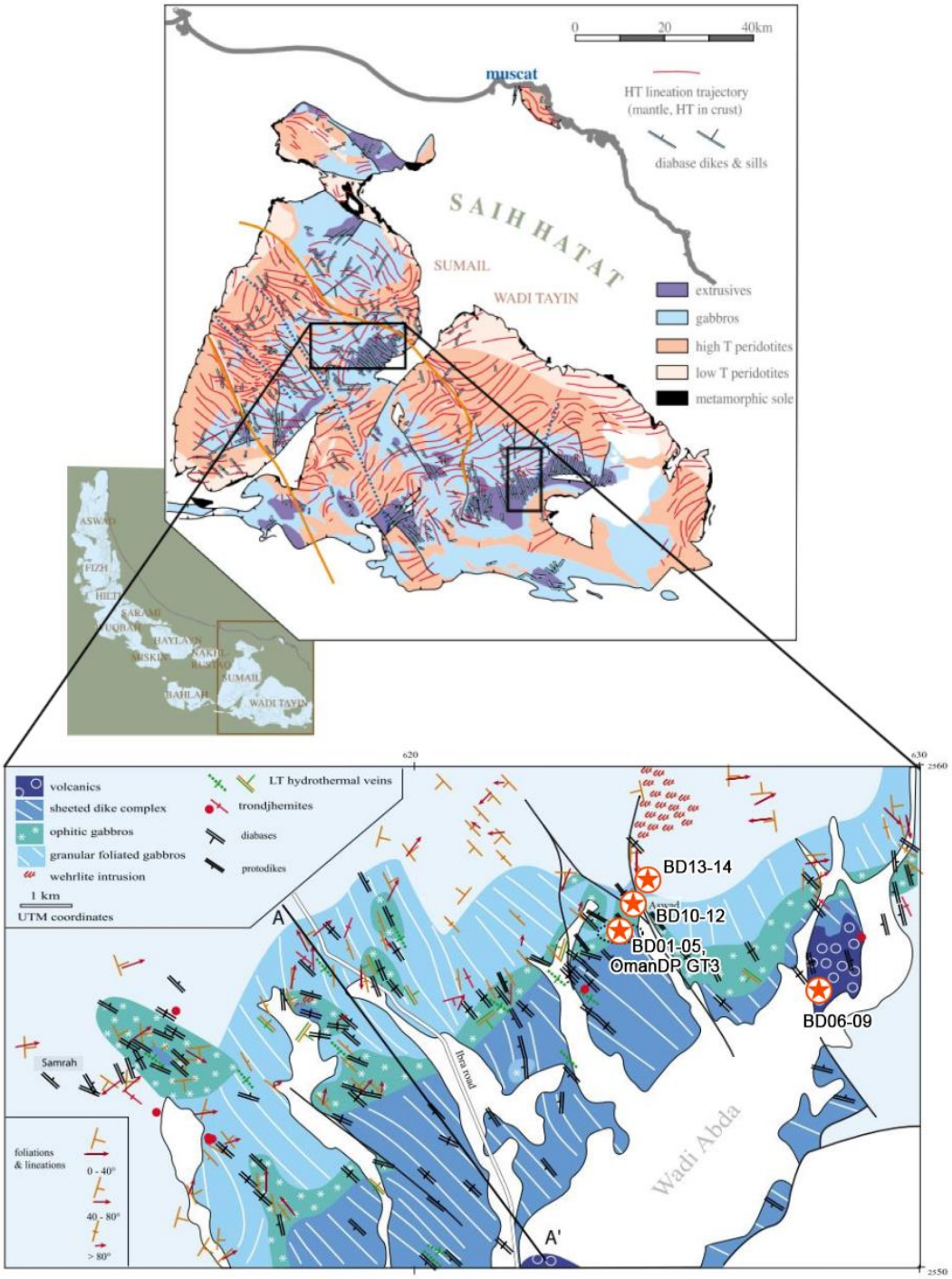

Figure 2.23 – An overview map of the southern massifs of the Oman ophiolite, with a zoomed-in geological map of the Wadi Abdah section, showing sample locations as red stars. Maps modified from Nicolas et al. (2000, 2008).

grains filling the mesh between the plagioclase laths. The gabbros are intruded by DRZ diabase dykes. Sites BD10-11 were sampled in the varitextured gabbros, and site BD12 in an intruding dyke.

Figure 2.24 – The Hole GT3 drill site of the Oman Drilling Project

Figure 2.25 – Core from Hole GT3 showing the contact between a dyke from the dyke rooting zone with varitextured gabbro.

3. The sheeted dyke complex that directly overlies the DRZ is composed of thick ~1 m diabase dykes with very fine-grained chilled margins. Older dykes are generally thicker and more altered, grading into epidosites, and are cut by thinner, darker, less altered younger dykes. Sites BD01-05 were

sampled from five individual dykes. A general NW-SE strike found in the dykes is consistent with a central, NW-SE-trending ridge system found from lineations measured and compiled from past studies (Nicolas et al., 2000) (Figure 2.23).

4. The columnar jointed lava flows in this study were sampled further away from the other sites, at one of the few locations in Wadi Abdah where lavas are exposed (sites BD06-09; Figure 2.23). Their orientations, striking WNW-ESE with a shallow dip of 26°S, are orthogonal to the orientations of dykes sampled around drill Hole GT3. An earlier study reveals that these lavas have a high titanium content (>1.1 wt.%) (Godard et al., 2003).

In addition to samples collected from sites BD01-14 at the surface, this study also uses drill core samples taken from Oman Drilling Project Hole GT3. Approximately 400 m of core was recovered in February 2017 using wireline diamond coring in the vertically oriented borehole, providing samples of sheeted dykes, the dyke rooting zone, and the varitextured gabbros.

2.4.3 – Al Khadra

Site Al Khadra, “The Green”, is located in Wadi Indam close to the village Al Khadra. It is a small outcrop consisting of a single thick dyke that cross-cuts pillow lavas overlain by lava flows (Figures 2.26 to 2.28). As a whole the outcrop and surrounding area has a shallow dip to the south (12°). Sampled units include:

1. A ~2 m thick NNE-SSW oriented dyke (site KD01) cross-cutting both the pillow lavas and lava flows.

2. Pillow lavas (site KD03) and lava flows (site KD02) that appear altered and contain chlorite and celadonite veins.

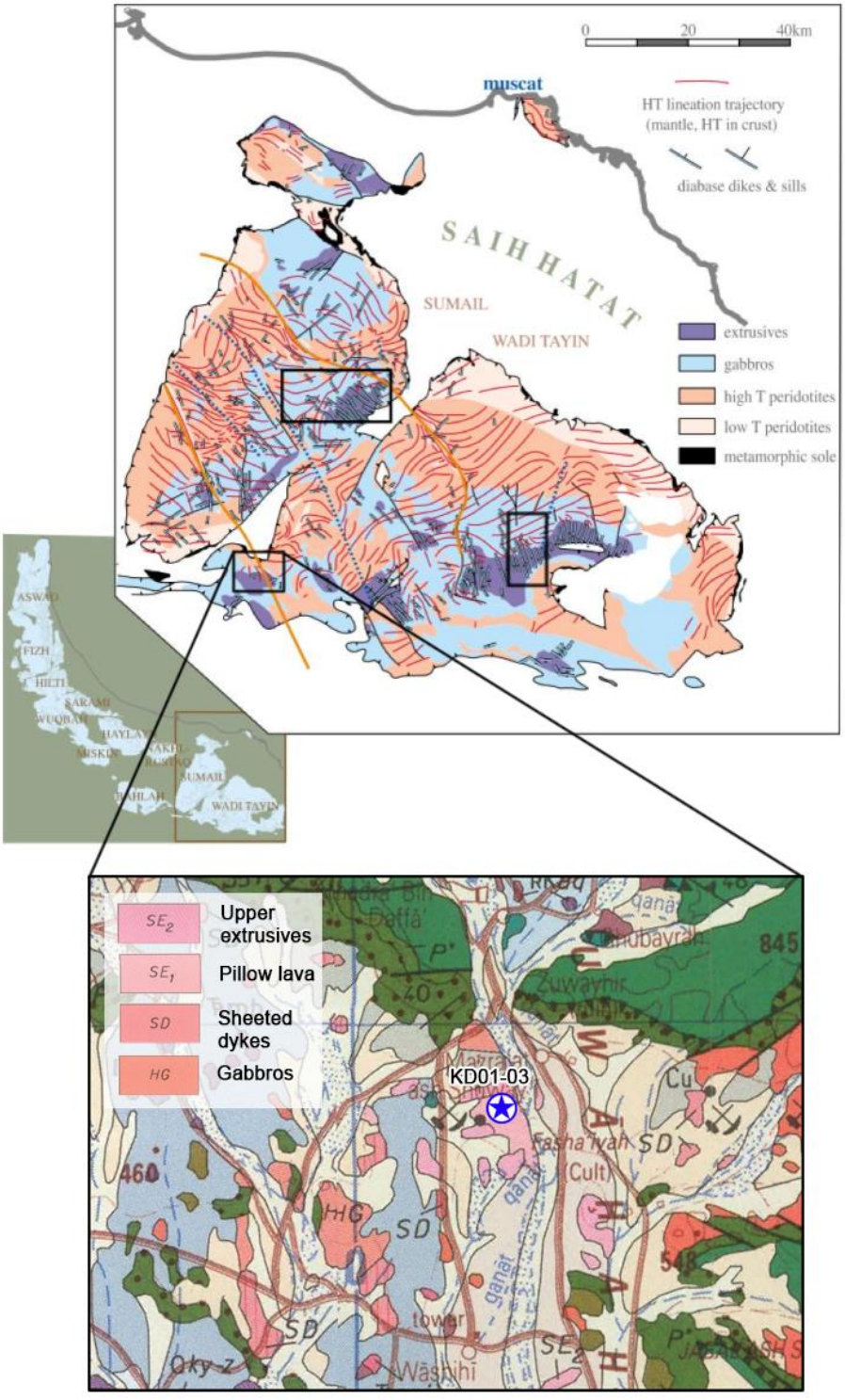

Figure 2.26 - An overview map of the southern massifs of the Oman ophiolite, with a zoomed-in geological map of the Al Khadra section, showing the sample location as a blue star. Maps modified from Nicolas et al. (2000) and the geological map from the Sultanate of Oman.

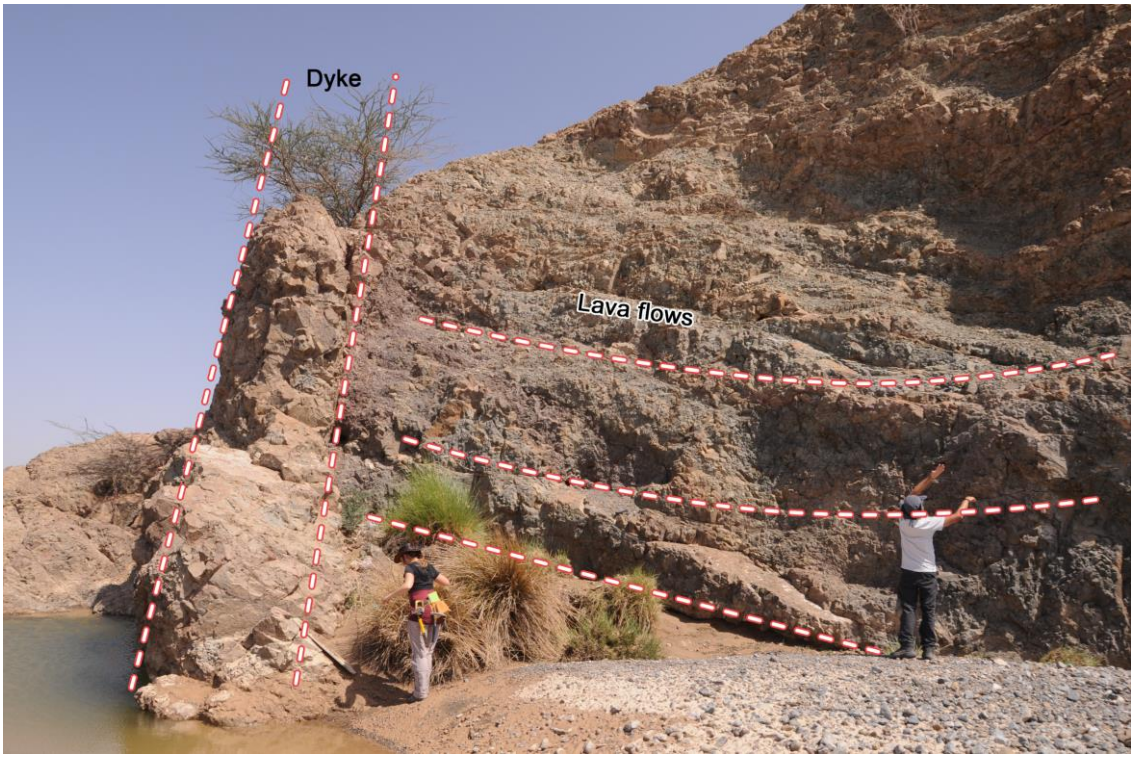

Figure 2.27 – The exposure at Al Khadra, showing a near vertical dyke on the left and lava flows on the right (photo credit: A. di Chiara). Dashed lines indicate a dyke and the orientation of lava flows.

2.4.4 – Wadi Gideah and Oman Drilling Project Holes GT1 and GT2

The study area of Wadi Gideah (Figures 2.28 to 2.30) is located in the Ibra massif, also known as the Wadi Tayin block, and was selected as it provides an extensive crustal section and because Holes GT1 and GT2 of the Oman Drilling Project are located here. Most sites are located in its N-S incised river valley, exposing mantle rocks in the north, through an E-W striking Moho into layered and foliated gabbros that generally dip 15° to the south. Further south outside the river valley, the varitextured gabbros, dyke rooting zone and sheeted dykes are exposed as shallow hills on an open plain, forming an east-west trending syncline with a nearly vertical south limb (Luyendyk et al., 1982).

Sampled units can be described as follows, from the lowest to the highest

sampled unit (Pallister et al., 1981; Luyendyk et al., 1982):

1. a 2.6 km thick sequence of cumulate layered gabbros with layering subparallel to the Moho (E-W striking, dipping 15° south). This orientation is therefore used as a palaeohorizontal surface for tilt correction of the palaeomagnetic data later in this study. Sites WG01-06 were sampled through the sequence at consistent intervals, with sites WG01-02 corresponding with the location of Hole GT1 of the Oman Drilling Project.
2. a 1 km thick sequence of granular foliated gabbros with a subvertical N-S trending foliation. Sites WG07-09 were sampled in this unit, and Hole GT2 of the Oman Drilling Project is located here.
3. a 1 km thick unit consisting of coarse-grained varitextured gabbros of isotropic composition in contact with dykes belonging to the dyke rooting zone. The dykes continue the N-S trending subvertical orientation that was also found in the foliated gabbros. Varitextured gabbros and dyke rooting zone dykes were sampled at two locations, represented by sites WG10-11 and WG12-13.
4. a 1.2-1.6 km thick sequence of subvertical N-S striking diabase sheeted dykes. Orientations of the sheeted dykes and dykes of the dyke rooting zone are the same, and correspond with the orientation of the foliated gabbros. Sites WG16, 19, 20, and 23 are located in the sheeted dykes.

In addition to rocks from sites WG01-23 collected from surface exposures, this study also used drill core samples taken from Oman Drilling Project Holes GT1

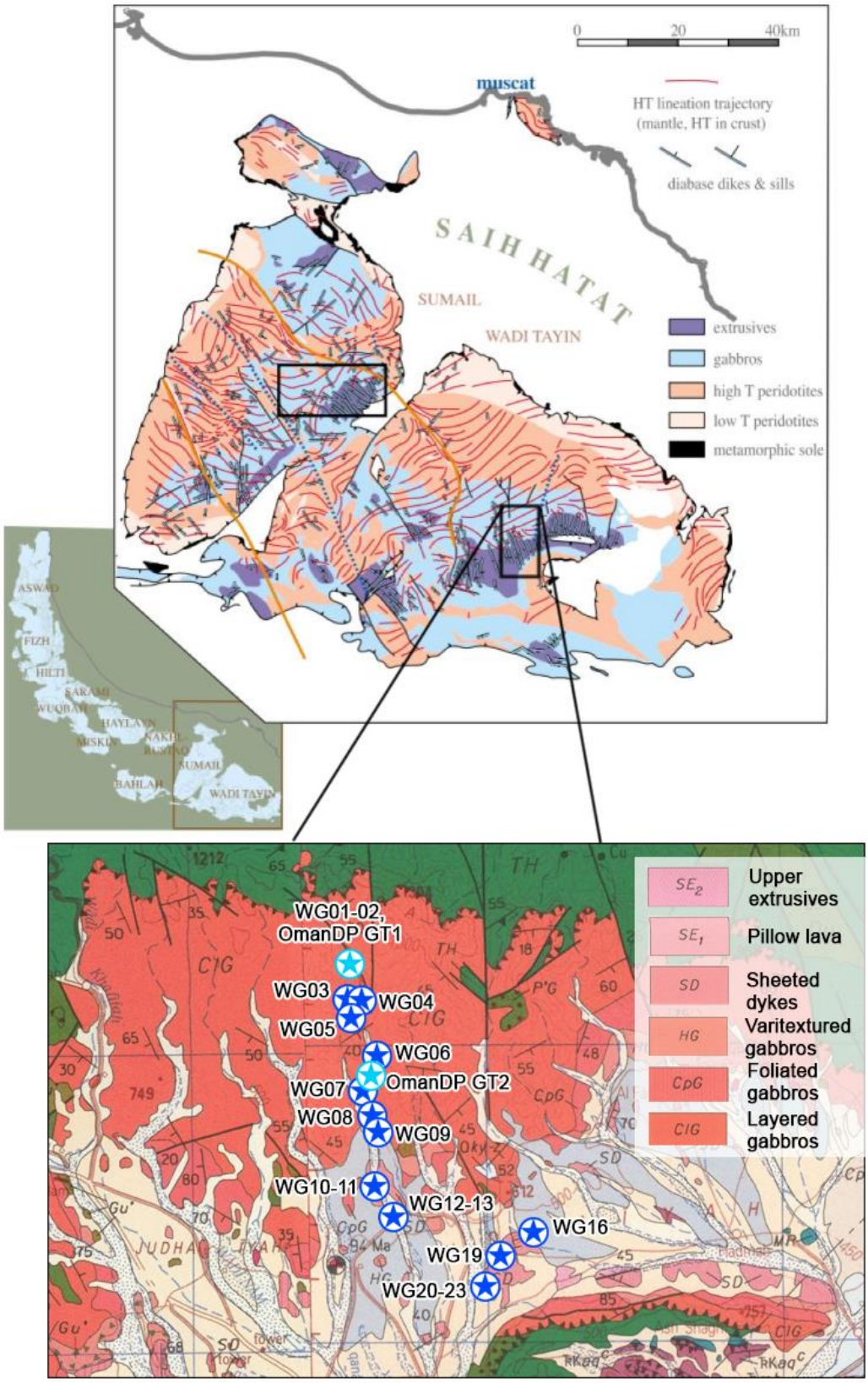

Figure 2.28 - An overview map of the southern massifs of the Oman ophiolite, with a zoomed-in geological map of the Wadi Gideah section, showing the sample locations as a blue stars. Maps modified from Nicolas et al. (2000) and the geological map from the Sultanate of Oman.

Figure 2.29 – Layered gabbros in Wadi Gideah (photo credit: M. Harris).

Figure 2.30 – The dyke rooting of Wadi Gideah (photo credit: A. di Chiara). Dashed lines indicate two dykes cutting through varitextured gabbro.

and GT2. Approximately 810 m of core was recovered between December 2016 and January 2017 using wireline diamond coring between the two boreholes. Hole GT1 was drilled vertically, whereas Hole GT2 was drilled at a 30° angle from the vertical in order to drill perpendicular to the layering in the gabbros. The aim of Hole GT1 was to collect core from Wadi Gideah's lowest crustal section, recovering layered gabbros, whereas Hole GT2 recovered cores starting in the mid-crustal section (foliated gabbros) down into the layered gabbros.

2.4.5 – Salahi massif

The Salahi massif, also known as the Hilti block, is the only locality in this study sampled in the northern half of the Oman ophiolite (Figures 2.31, 2.32, and 2.5c). Sampling was focused on the layered gabbros, to provide a comparison between remagnetised and non-remagnetised lower crustal rocks of the northern and southern ophiolite massifs.

The layered gabbros show layering defined by variations in the modal abundances of olivine, pyroxene, and plagioclase and vary from centimetre to metre-scaled layers. The layering was found to consistently strike NE-SW with a 23° dip to the NW. This orientation is used as a palaeohorizontal surface for tilt correction of the palaeomagnetic data.

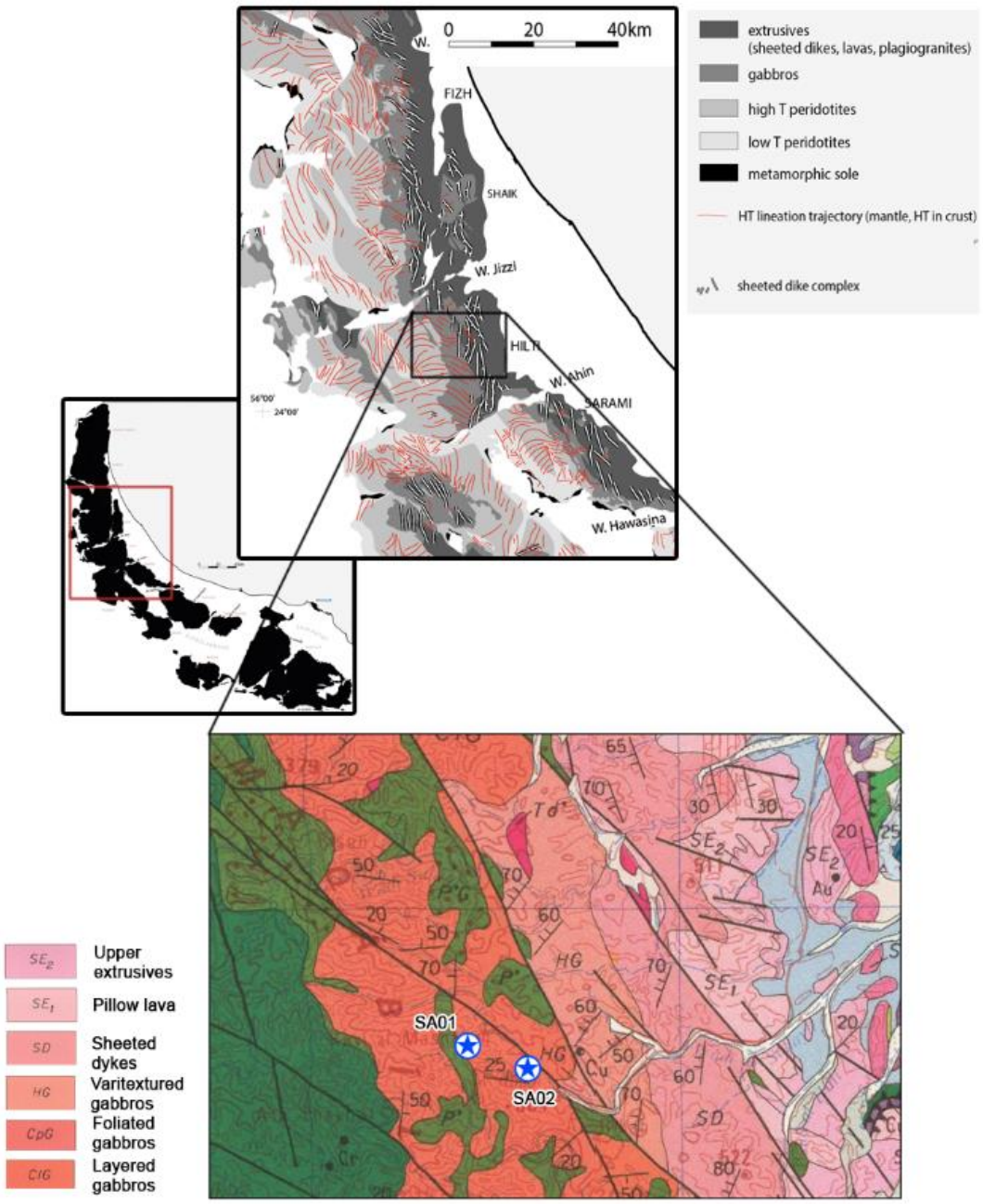

Figure 2.31 - An overview map of the northern massifs of the Oman ophiolite, with a zoomed-in geological map of the Salahi section, showing the sample locations as blue stars. Maps modified from Nicolas et al. (2000) and the geological map from the Sultanate of Oman.

Figure 2.32 – Pillow lavas of the Salahi massif

Chapter 3 – Theoretical background and Methodologies

3.1 – Introduction

Not only does the Earth's magnetic field protect us from the solar wind and cosmic radiation from outside our solar system, it also gives us the opportunity to look into the past of our planet. Magnetic minerals in the Earth's crust and mantle are capable of recording the ancient geomagnetic field and preserve that record for millions of years (Butler, 1992; Tauxe, 2010). The main objective of palaeomagnetic research is to explore that record and use it to study the changing geomagnetic field over time, to study movements of continental and oceanic plates, and to study the processes involved in the formation and evolution of rock units.

A rock that acquires a remanent magnetization records the direction of the geomagnetic field at the time of its formation. This direction can be described in terms of declination and inclination, where the declination is the angle from the geographic North Pole to the horizontal component (0-360°) in a clockwise manner, and the inclination is the angle from the horizontal (-90° to +90°) where downward is positive. Remanence directions can help us to reconstruct plate movements and create tectonic models.

Magnetism in atoms is caused by the orbital and spin motions of electrons around the nucleus, creating electrical currents that have a magnetic moment. Each atom is therefore capable of responding to external magnetic fields,

however depending on the magnetic behaviour of different materials only some rocks are capable of recording a remanent magnetization when exposed to an external magnetic field. This chapter describes the magnetic behaviour of different substances, types of remanent magnetization that can be acquired by rocks, laboratory methods that we use to retrieve information on the ancient geomagnetic field, and techniques that we apply to the resulting data to reconstruct tectonic histories.

3.2 – Properties of magnetic minerals

Rocks are generally made up of assemblages of ferromagnetic minerals (such as magnetite and hematite) within a matrix of diamagnetic minerals. Characteristics of the saturation magnetization, Curie temperature, grain size, and mineralogy strongly affect the magnetic properties of minerals. It is therefore important to understand how minerals acquire a magnetization and how their characteristics affect their magnetic properties and the behaviour of different types of magnetization. Magnetic behaviour (diamagnetic, paramagnetic, and ferromagnetic (sensu lato)) is dependent on the magnetic moments generated in atoms due to the orbital and spinning motions of the electrons, causing the atoms themselves to act like magnets.

Different materials have different magnetisability or "magnetic susceptibility" that describes how the intensity of their magnetization (***M***) relates to the applied external magnetic field (**H**). The relationship between ***M*** and ***H*** is:

$$\boldsymbol{M} = k\,\boldsymbol{H}$$

where *k* is the magnetic susceptibility. Variations in grain size, mineralogy and concentration control the susceptibility.

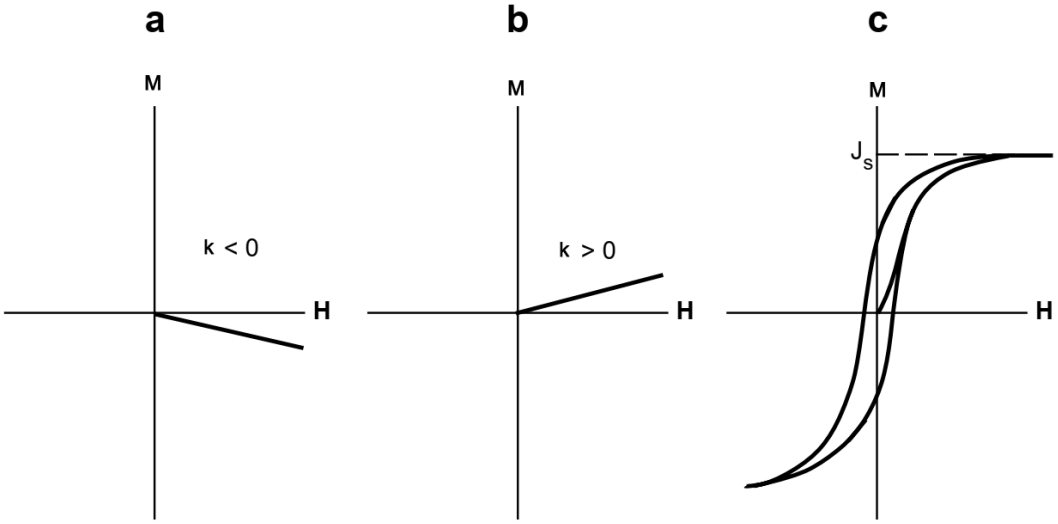

Figure 3.1 – Magnetization (M) versus magnetising field (H) for (a) diamagnetic materials, with a constant negative susceptibility (k), (b) paramagnetic materials, with a constant positive susceptibility (k), (c) ferromagnetic (sensu lato) materials, with the magnetization path exhibiting hysteresis and the susceptibility not exhibiting a simple constant. From Butler (1992).

3.2.1 – Diamagnetic behaviour

Diamagnetic materials act like non-permanent magnets; when an external magnetic field is applied to the material, an induced magnetization is acquired in the opposite direction (Lenz's law; Lenz, 1834) to the applied external magnetic field. On an atomic level the spins of the electrons are in equilibrium (all electrons are paired) and acquire a magnetic moment only for as long as an external magnetic field is applied. As soon as the external magnetic field is removed, the magnetization reduces back to a net magnetic moment of zero. The behaviour of the susceptibility in diamagnetic materials can be seen in Figure 3.1a. Susceptibilities of diamagnetic materials are a negative constant. Some examples

of diamagnetic materials are quartz, calcite, and plagioclase (Piper, 1987; Butler, 1992; Tauxe, 2010).

3.2.2 – Paramagnetic behaviour

Just like diamagnetic materials, paramagnetic materials also behave like magnets, only in this case when an external magnetic field is applied; the induced magnetization in the material is in the direction of the external magnetic field. On an atomic level, the spins of electrons are not in equilibrium because one or more electrons are unpaired, causing the atoms to have magnetic moments that do not initially interact with each other and that are randomly distributed in all directions with a resulting net magnetization of zero. Only when an external magnetic field is applied will the atoms line up with the magnetic field, producing a magnetization with a positive magnetic susceptibility (Figure 3.1b). Examples of paramagnetic materials are olivine, biotite, fayalite, and many iron-bearing silicate minerals (Butler, 1992; Tarling and Hrouda, 1993; Tauxe, 2010).

3.2.3 – Ferromagnetic behaviour

Unlike diamagnetic and paramagnetic materials, ferromagnetic materials act like permanent magnets that can be magnetised by external fields and stay magnetised. Just like paramagnetic materials, electrons in ferromagnetic materials are unpaired causing them to have magnetic moments, but unlike paramagnetic materials these electrons strongly interact (via electron coupling),

resulting in magnetizations with intensities that are orders of magnitude larger than for paramagnetic materials. The acquired magnetization is parallel to the external magnetic field with a positive susceptibility (Figure 3.1c) that exhibits hysteresis, which means that it is not constant and is irreversible.

The saturation magnetization is the maximum magnetization a material is able to obtain and is dependent on temperature. It decreases with an increasing temperature until it becomes zero at a peak temperature called the Curie temperature. Above the Curie temperature (580°C for magnetite and 675°C for hematite; Dunlop and Özdemir, 1997), the material becomes paramagnetic. This effect is reversible, so that once the material cools down again below the Curie temperature, it will once again display ferromagnetic behaviour.

Ferromagnetic materials are fundamental in palaeomagnetic research for their ability to record the direction of an applied external magnetic field. Even if the external magnetic field changes or is removed, the material has the ability to preserve that information for billions of years (Butler, 1992; Tauxe, 2010).

Electron coupling can be either parallel or antiparallel, depending on the crystal structure of the mineral involved in the coupling process. It results in different types of ferromagnetism:

(i) Parallel electron coupling is referred to as ferromagnetism (sensu stricto), even though the term ferromagnetism is also broadly used as a general term for materials that experience strong electron coupling. Some materials that experience pure parallel electron coupling are nickel and cobalt.

(ii) When materials experience antiparallel coupling between layers, they are referred to as antiferromagnetic. Ilmenite is an example of an antiferromagnetic mineral. When the spins of electrons in antiferromagnetic minerals are not parallel but slightly canted, this can lead to canted antiferromagnetism. The magnetizations produced by canted antiferromagnetism are slightly weaker than in antiferromagnetism. An example of a canted antiferromagnetic mineral is hematite at a temperature of -10°. Above this temperature it behaves as ferrimagnetic material.

(iii) Just like in antiferromagnetic materials, layers in ferrimagnetic materials experience antiparallel coupling, with the difference that now the magnetic moments between layers are not equal. The resulting net magnetic moment points in the direction of the dominant layer. Most magnetic materials that are of importance to palaeomagnetic research are ferrimagnetic, such as hematite (above -10°), magnetite, maghemite, pyrrhotite, and greigite.

3.2.4 – Magnetic domains of ferromagnetic minerals and hysteresis

A magnetic domain is a region within a magnetic material in which the magnetization is aligned in a uniform direction. The magnetization in ferromagnetic materials is controlled by various energies (magnetostatic,

interaction, and uniaxial magnetocrystalline energy) that can be present in very simple or complex combinations. Magnetostatic energy in a particle is energy stored due to the distribution of positive and negative charges at the particle surface caused by the magnetic moment. Magnetic domains therefore have an effect on the magnetostatic energy; the more domain walls are present in a magnetic particle, the smaller the magnetostatic energy will be since the surface area containing magnetic charges will be smaller. Large magnetic grains, such as magnetite with a diameter > 10 μm, contain more domain walls and therefore have less magnetostatic energy. These are referred to as multidomain (MD) grains. When the grain size decreases, the number of magnetic domains decreases as well. A grain becomes single domain (SD) when it is not energetically favourable to subdivide a grain further because the energy needed to create a domain wall will become larger than the magnetostatic energy saved due to a subdivision of the grain (Piper, 1987; Butler, 1992; Dunlop and Özdemir, 1997).

The size at which a magnetic particle is considered to be MD or SD varies between minerals. Magnetite > 10 μm is MD and only becomes SD at grain sizes < 1 μm (it is referred to as pseudo-single domain (PSD) in between), whereas hematite is SD < 15 μm (Butler, 1992; Dunlop and Özdemir, 1997). This difference is dependent on the saturation magnetization and magnetocrystalline anisotropy of minerals. Because magnetite has a much larger saturation magnetization than hematite (and therefore more magnetostatic energy), only very fine grained magnetite can be SD. Ferromagnetic minerals with a lower saturation

magnetization and high anisotropy do not form as many domain walls due to a lower magnetostatic energy, and therefore can be SD up to a larger grain size.

The interaction energy in ferromagnetic single domain minerals is the energy between the magnetization of individual particles and an externally applied magnetic field. The magnetic field required to force that magnetization to rotate is called the microscopic coercive force (*hc*).

Single domain ferromagnetic minerals follow an irreversible hysteresis loop in a changing external magnetic field that explains why these minerals retain their magnetization, even if the field changes. Figure 3.2 shows several stages in a hysteresis loop and the effect on the magnetic directions within SD grains. Between stages 0 and 2 an external magnetic field is applied and grain magnetizations begin to rotate because of the interaction energy until they are parallel to the field. The specimen will reach saturation magnetization (Ms) when all SD grains are aligned with the field (Figure 3.2c). This saturation magnetization is therefore dependent on the concentration of ferromagnetic minerals within a specimen.

If the external field is then removed, the magnetization in the whole specimen decreases until we reach stage 3 (Figure 3.2d) and the magnetization rotates to the nearest long axis of a SD grain as this minimises magnetostatic energy. The remaining magnetization is the remanent magnetization (*Mr*).

In the laboratory the magnetization of the specimen can be forced back to zero by applying an external magnetic field that points in the opposite direction as the initial applied field (Figure 3.2e). The magnetization decreases further until it is

zero (stage 4). The magnetic field required to achieve this is called the bulk coercive force or coercivity (*Hc*), and at this point the magnetizations of the SD ferromagnetic minerals are randomised and result in a zero net magnetization.

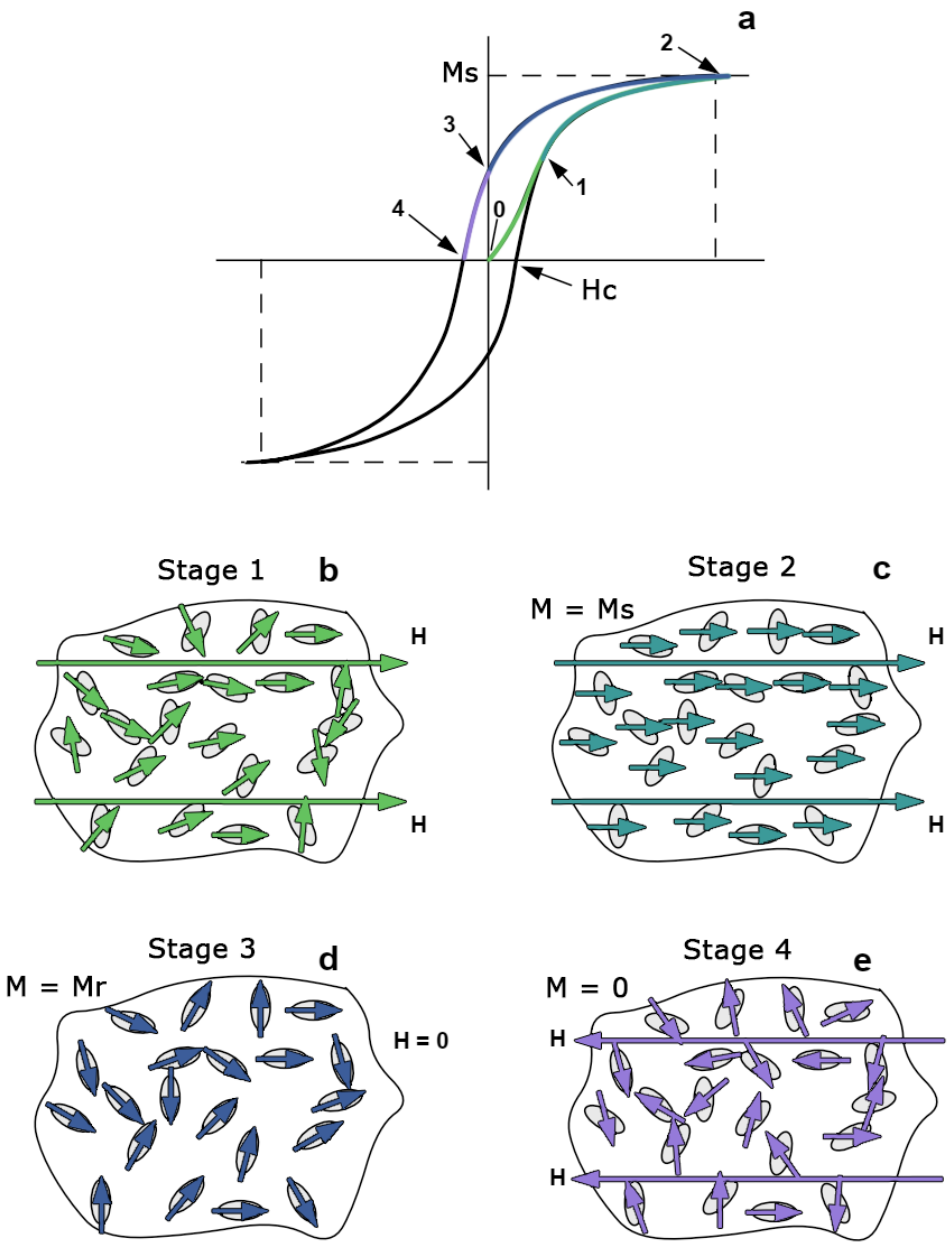

Figure 3.2 – (a) Hysteresis loop showing the magnetization behaviour of ferromagnetic materials for a synthetic sample containing 5% elongated SD magnetite particles. M is the magnetization, H is the applied field, Ms is the saturation magnetization, Mr is the remanent magnetization, Hc is the coercive force (coercivity of remanence). See text for details. (b-e) Magnetization directions within SD magnetite grains at various stages on the hysteresis loop. See text for details. (Modified from Butler, 1992).

The hysteresis continues by increasing the external field further in a negative direction until saturation is achieved, and is then completed by flipping the field back to its initial direction. The hysteresis loop shows that once SD ferromagnetic grains are magnetised, they are resistant to demagnetization and efficient in acquiring a remanent magnetization.

In a rock specimen, SD ferromagnetic minerals only make up a small proportion of the assemblage, and it is common to find a large percentage of MD and/or PSD grains that have a lower (microscopic) coercive force and lower remanent magnetization acquisition efficiency. Hysteresis in multidomain grains is very different from SD grains. An applied field that is strong will destroy domain walls until the saturation magnetization is achieved. The domains nucleate when the external field is removed. However they will acquire different positions based on a minimum requirement in energy. Because of this, the remaining remanent magnetization at a zero field is rather small. Additionally MD grain magnetizations are susceptible to decay over time and are therefore less effective in recording a stable, ancient direction.

In between SD and MD grains lies the area of pseudo-single domain (PSD) grains. They have an intermediate (microscopic) coercive force and remanent magnetization acquisition efficiency. Somewhere between large SD grains and small MD grains, these grains can have a few domain walls but have a large magnetic moment. They appear to be stable in retaining their remanent magnetization over time (Butler, 1992) and just like SD grains are important in palaeomagnetic analysis.

3.2.5 – Blocking temperature

In the hysteresis experiment described above the saturation magnetization of a SD grain can change its direction due to applied magnetic fields. Thermal activation can cause the same effects on SD grains by decaying the remanent magnetization of a grain over time to zero; this is known as magnetic relaxation and is described by the relaxation time. Grains with short relaxation times are not capable of holding on to their remanent magnetization for long before it decays. SD grains with a very short relaxation time are known as superparamagnetic (SP) grains; they have a strong magnetization like a SD grain, but their remanent magnetization decays to zero as soon as an external magnetic field is removed (like in a paramagnetic mineral). The temperature at which a material has a relaxation time equal to 100 seconds is known as the blocking temperature; at this temperature, a material will behave as superparamagnetic. Therefore any ferromagnetic material can become superparamagnetic if the temperature becomes higher than the blocking temperature (e.g. 550°C for a 0.1 nm x 0.02 nm SD magnetite; Butler, 1992). Other than dependent on thermal energy, this behaviour is also dependent on the energy barrier required to rotate the magnetization of a ferromagnetic mineral, dependent on the microscopic coercive force [*hc*], the volume of the grain, and the saturation magnetization. Once a material gets cooled below the blocking temperature, its magnetization becomes blocked again and the material behaves ferromagnetically (Butler, 1992; Tauxe, 2010).

3.3 – Types of remanent magnetization

The basic physical principles of the types of remanent magnetization that are relevant to ophiolitic rocks are described below.

3.3.1 – Natural remanent magnetization (NRM)

The natural remanent magnetization (NRM) is the sum of all remanent magnetizations a rock has acquired since its formation and prior to any laboratory treatment. Because the NRM depends on the geomagnetic field and geological processes that took place since the rock's formation, a NRM can consist of multiple components (Stacey, 1963; Butler, 1992; Tauxe, 2010). The magnetization that was acquired during rock formation is referred to as its primary magnetization, whereas anything that was acquired afterwards is referred to as a secondary magnetization, which is capable of altering or overprinting the primary component. Primary magnetizations in ophiolitic rocks are thermoremanent magnetizations and common secondary magnetizations are chemical remanent magnetizations, (thermo)viscous remanent magnetizations and natural isothermal remanent magnetizations, all of which are examined below. Since secondary magnetizations are capable of completely overprinting a primary magnetization, it may be difficult to acquire a meaningful timing of remanence acquisition. The most stable remanence component, which has the highest coercivity and/or unblocking temperature is therefore referred to as the

characteristic remanent magnetization (ChRM). Determining whether a ChRM represents a primary or secondary magnetization requires consideration of the broader context of the data, e.g. comparing with magnetizations from other localities/lithologies, and the application of palaeomagnetic field tests (see below).

3.3.2 – Thermoremanent magnetization (TRM)

A thermoremanent magnetization (TRM) is the most common form of magnetization in igneous rocks, acquired during cooling of the rock from above the Curie temperature in the presence of a magnetic field (Néel, 1955; Butler, 1992). Once a single domain ferromagnetic grain cools down to its blocking temperature, the grain will experience an increase in its relaxation time, and as a result its magnetization will become fixed. These grains obtain their most stable state once the rock cools to ambient surface temperatures and will then be resistant to effects of changes to the geomagnetic field. Pseudo-single domain grains are also capable of acquiring a TRM that is stable against time decay and demagnetization by magnetic fields after cooling. Larger multi-domain grains are less efficient in carrying a TRM, will decay more quickly over time, and are more likely to pick up a secondary viscous remanent magnetization at a later time after cooling.

In oceanic crust, lithologies can have different cooling times; in the case of extrusive rocks, like pillow lavas, cooling can take place instantaneously, causing

the ferromagnetic grains to lock in their magnetization soon after formation of the rock. Intrusive rocks can cool down over thousands of years, and can also be reheated by later intrusions (e.g. sheeted dykes). It is therefore possible that TRMs record a mixture of magnetization directions acquired over time; the measured TRM is always the sum of these magnetizations (Butler, 1992; Tauxe, 2010).

3.2.3 – Chemical remanent magnetization (CRM)

Chemical reactions due to a change in chemical environment can form or alter (ferromagnetic) minerals that may then acquire a chemical remanent magnetization (CRM) in the presence of a magnetic field. Either existing minerals can be altered to form ferromagnetic minerals, or new ferromagnetic minerals can be created from precipitation from a solution (Butler, 1992; Dunlop and Özdemir, 1997). The temperature during the formation of a CRM is usually constant, unlike the decreasing temperature during TRM acquisition. When ferromagnetic minerals are created through alteration or precipitation, new grains grow from an initial volume of zero, will have short relaxation times, and will initially be superparamagnetic. When the grains keep growing, their relaxation times will increase until they become stable single domain. The moment at which this happens is the blocking volume, and just like the blocking temperature for TRMs, this is the point where the CRM is acquired (Butler, 1992).

Hydrothermal alteration and serpentinization are metamorphic processes that are quite common in oceanic crust, which may produce CRMs in newly formed/altered ferromagnetic grains (Alt, 1995).

3.2.4 – Thermoviscous remanent magnetization (TVRM)

After the formation of a rock, it may experience periods of reheating, which may or may not come paired with metamorphism. If the reheating temperature stays below the Curie temperature, ferromagnetic minerals with a peak unblocking temperature at or below the reheating temperature will acquire a thermoviscous remanent magnetization (TVRM) and become remagnetised (Pullaiah, 1975; Butler, 1992). Any ferromagnetic minerals with peak unblocking temperatures higher than the reheating temperature will not be affected and keep their original magnetization.

If only heat is involved in a reheating process, and no chemical alteration, we can predict the effect of long-term heating on ferromagnetic minerals acquiring a TVRM. Figure 3.3 shows the relationship between the relaxation time and temperature, in which the lines connect conditions that can unblock the magnetization in ferromagnetic single domain grains. It shows two regions, A and B, with different behaviour. Ferromagnetic grains in the B region can acquire TVRMs when exposed to modest temperatures like 300°C or lower if they are exposed to that temperature for (geologically) long periods of time. These grains are considered to be unstable primary magnetization carriers. Grains distributed

in the B region can have widely variable blocking temperature distributions. Ferromagnetic grains in the A region have laboratory unblocking temperatures much closer to the Curie temperature (e.g. within 100° of the Curie temperature of magnetite, 580°C). In order to reset these grains, the reheating temperature would have to approach the Curie temperature closely. Therefore, these grains are more resistant to remagnetization and more stable during reheating, unless reheating approaches temperatures that close to the Curie temperature.

If temperatures during reheating fall within the greenschist facies metamorphic range (300-500°C), it is likely that rocks will (partially) retain their primary NRM. Once temperatures fall into the amphibolite facies range (550-750°C) it is much less likely that any primary NRM will survive (Figure 3.3). However, this is a prediction that only takes heating into account; as soon as heating becomes paired with metamorphism and/or fluid flow, chemical changes

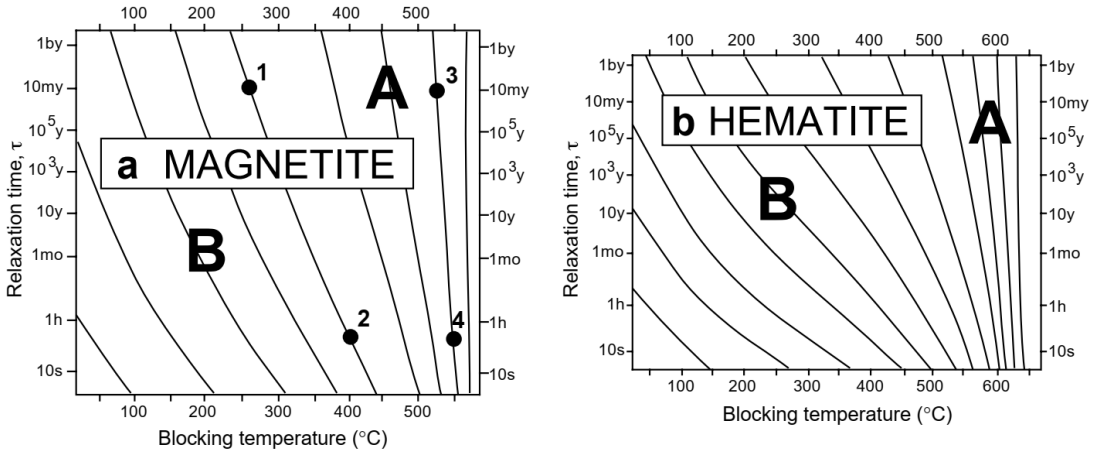

Figure 3.3 – Blocking temperature diagrams for (a) magnetite and (b) hematite. Combined temperature and relaxation time conditions that can unblock (reset) the magnetization in SD magnetite/hematite grain populations are connected by lines. From Butler (1992), redrawn from Pullaiah et al. (1975).

can alter the ferromagnetic minerals which can chemically remagnetise the rock and form a chemical TVRM (Butler, 1992).

3.3.5 – Viscous remanent magnetization (VRM)

A viscous remanent magnetization (VRM) can be acquired when a rock is exposed to a magnetic field for a (geologically) long time. Unstable ferromagnetic minerals with low relaxation times, like pseudo-single domain and multidomain ferromagnetic grains, are prone to acquire a VRM through thermal activation of domain walls (Dunlop, 1983; Butler, 1992). The interaction energy within these grains between the internal magnetization and the external magnetic field will cause their magnetization to align with the magnetic field, even long after the rock's formation. In a palaeomagnetic analysis, VRMs are usually regarded as noise, but are luckily easily removed by demagnetization, revealing the primary magnetization that is carried by more stable grains.

3.3.6 – Isothermal remanent magnetization (IRM)

An isothermal remanent magnetization (IRM) is a secondary magnetization that can be acquired when a rock is exposed to strong magnetic fields in a short time, as is the case when a rock gets struck by lightning. IRM is acquired in ferromagnetic grains when the applied field is higher than the coercive force of that grain (Cox, 1961). A lightning strike can create a magnetic

field of 10-100 mT (Butler, 1992), which is likely to reset the magnetization in ferromagnetic grains, and can affect any rocks within two metres of the impact.

IRM can also be imparted to specimens in the laboratory as well, by exposing them to a magnetic field generated by an electromagnet. The techniques involving laboratory induced IRM and its related analyses are described in section 3.9 of this chapter.

3.4 – Palaeomagnetic fold test

As explained before, an NRM can consist of multiple components, the most stable of which is referred to as the ChRM. Because we cannot prove that a ChRM is primary using only laboratory tests, palaeomagnetic field tests can be used to provide information about the timing of acquisition of a ChRM. These include fold/tilt, reversal, baked contact and conglomerate tests (Butler, 1992; Figure 3.4). In this study, however, only a fold test is employed (McElhinny, 1964; McFadden and Jones, 1981; Tauxe, 2010). This compares remanence directions between two or more sites before and after applying a tilt correction (Figure 3.4, compare c and f) that restores sampled units to either a palaeohorizontal or palaeovertical orientation. Remanence directions pass a fold test if they are dispersed when plotted in geographic coordinates on a stereographic projection but converge after a tilt correction is applied. This implies that the remanence directions were acquired before folding or tilting occurred. When a fold test fails, the remanence directions become more scattered, meaning the remanence

directions were acquired post-folding or post-tilting in age. To determine the significance of a fold test, statistical approaches to evaluating the distributions before and after untilting are used. Here the fold test formulation of Tauxe & Watson (1994) is used, which combines eigen analysis and parameter estimation (bootstrap) techniques and gives confidence limits on the degree of unfolding required to produce the tightest grouping of data.

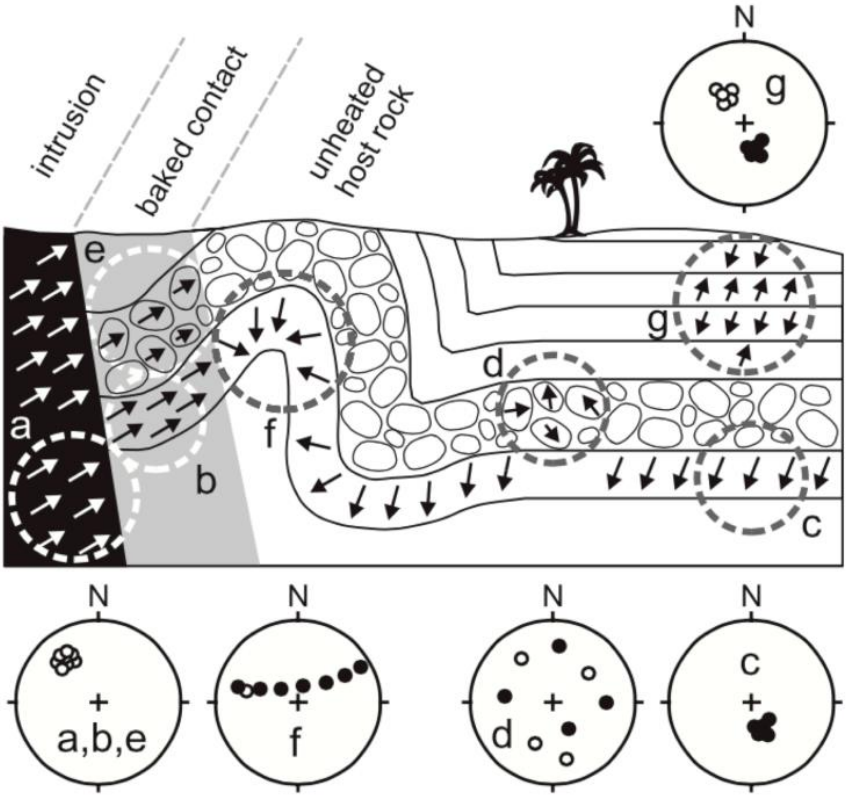

Figure 3.4 – Schematic illustration showing the four palaeomagnetic field tests that we can apply to test the stability of our palaeomagnetic data: (a, b, c) baked contact test, (d, e) conglomerate test, (c, f) fold test, (g) reversal test. Black arrows represent magnetization directions, black circles on the stereonets represent downward remanence directions, open circles represent upward directions. See text for discussion (from Morris, 2003).

Samples from the International Continental Scientific Drilling Program Oman Drilling Project were collected using drilling techniques during which relative vertical axis rotations of individual core pieces occurred, resulting in palaeomagnetic data without azimuthal control (i.e. lacking declination data). In

the case of these samples, an inclination-only fold test was applied that compares inclinations before and after a tilt correction (Arason and Levi, 2010).

3.5 – Sample collection and preparation

Sampling in the Oman ophiolite focused on collecting oriented samples for palaeomagnetic analysis. As discussed in Chapter 2, the southern half of the Oman ophiolite has been subjected to a remagnetization event, whereas the northern half of the ophiolite has retained its original, primary magnetization. For the purpose of understanding remagnetization of the southern massifs of the Oman ophiolite, sampling was focused on four localities from the Ibra, Samail, and Rustaq massifs, and one control locality from the Salahi massif in the northern half of the ophiolite. Samples were collected from a total of 48 sites at these five localities over two field seasons: (i) along a full transect from layered gabbros upwards into sheeted dykes in Wadi Gideah (north of the city Ibra in the middle of the Wadi Tayin block/Ibra massif), to tie in with sampling conducted by the Oman Drilling Project (see below);

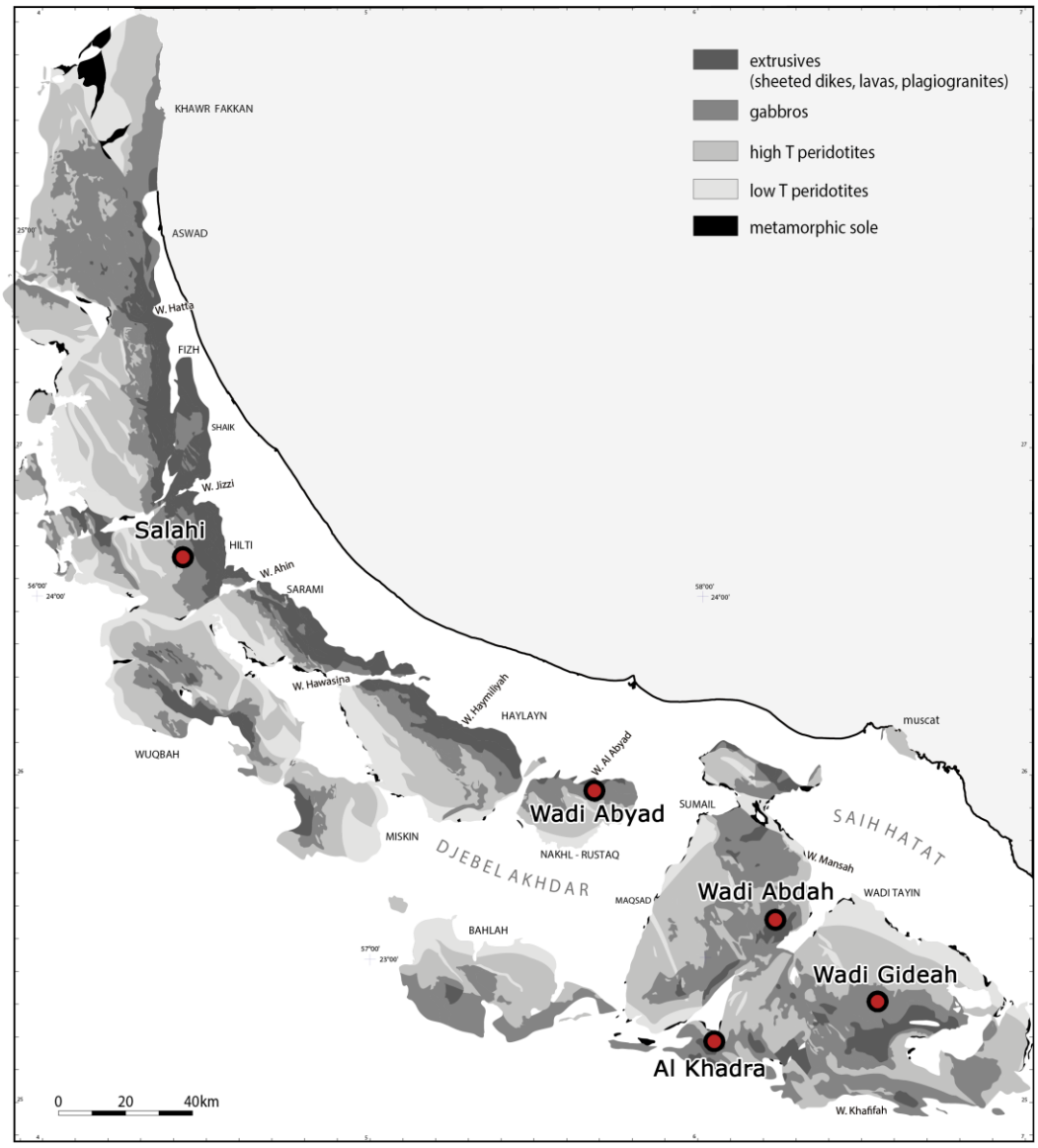

Figure 3.5 – Sampled localities on a simplified geological map (modified from Nicholas et al. (2000)).

(ii) in the dyke rooting zone and upwards into the sheeted dyke complex in Wadi Abyad in the Rustaq massif, to complete a crustal transect started by Meyer (2015); (iii) in layered gabbros, foliated gabbros, sheeted dykes, and lavas in the area of Wadi Abdah in the Semail block/Samail massif, again to tie in with sampling conducted by the Oman Drilling Project (see below); (iv) in lava flows and a crosscutting dyke at Al Khadra on the south-western edge of the Ibra

massif/Wadi Tayin block; and (v) in gabbro samples from the Salahi (Hilti) massif, outside the inferred zone of remagnetization in order to allow comparison between remagnetised rocks and those carrying a presumed primary remanence. Locations and lithologies of the sampled sites can be found in Table 3.1 and Figure 3.5.

Table 3.1 - Lithologies and locations of sampled sites.

Site	Lithology	Locality	Massif	UTM Zone	Easting	Northing	Latitude	Longitude
AB01	Dyke rooting zone	Wadi Abyad	Rustaq massif	40Q	569636	2597099	23°28'57.77"N	57°40'55.46"E
AB02-03	Sheeted dykes	Wadi Abyad	Rustaq massif	40Q	569056	2597796	23°29'19.72"N	57°40'34.60"E
AB04	Sheeted dykes	Wadi Abyad	Rustaq massif	40Q	569091	2597969	23°29'25.34"N	57°40'35.86"E
AB05	Sheeted dykes	Wadi Abyad	Rustaq massif	40Q	569098	2597990	23°29'26.02"N	57°40'36.15"E
AB06	Sheeted dykes	Wadi Abyad	Rustaq massif	40Q	569118	2598070	23°29'28.62"N	57°40'36.83"E
BD01	Sheeted dykes	Wadi Abdah	Samail massif	40Q	624022	2556662	23° 6'50.65"N	58°12'40.13"E
BD02	Sheeted dykes	Wadi Abdah	Samail massif	40Q	624066	2556692	23° 6'51.62"N	58°12'41.68"E
BD03	Sheeted dykes	Wadi Abdah	Samail massif	40Q	624046	2556662	23° 6'50.65"N	58°12'40.97"E
BD04	Sheeted dykes	Wadi Abdah	Samail massif	40Q	623989	2556647	23° 6'50.17"N	58°12'38.96"E
BD05	Sheeted dykes	Wadi Abdah	Samail massif	40Q	624026	2556670	23° 6'50.91"N	58°12'40.27"E
BD06	Lava flow	Wadi Abdah	Samail massif	40Q	628006	2555427	23° 6'9.41"N	58°14'59.79"E
BD07	Lava flow	Wadi Abdah	Samail massif	40Q	628011	2555415	23° 6'9.02"N	58°14'59.96"E
BD08	Lava flow	Wadi Abdah	Samail massif	40Q	628019	2555400	23° 6'8.53"N	58°15'0.24"E
BD09	Lava flow	Wadi Abdah	Samail massif	40Q	628015	2555390	23° 6'8.20"N	58°15'0.10"E
BD10	Varitextured gabbro	Wadi Abdah	Samail massif	40Q	624226	2557055	23° 7'3.37"N	58°12'47.41"E
BD11	Varitextured gabbro	Wadi Abdah	Samail massif	40Q	624228	2557058	23° 7'3.47"N	58°12'47.48"E
BD12	Dyke rooting zone	Wadi Abdah	Samail massif	40Q	624229	2557082	23° 7'4.25"N	58°12'47.52"E
BD13	Foliated gabbro	Wadi Abdah	Samail massif	40Q	624538	2557554	23° 7'19.51"N	58°12'58.52"E
BD14	Foliated gabbro	Wadi Abdah	Samail massif	40Q	624517	2557617	23° 7'21.57"N	58°12'57.81"E
KD01	Dyke	Al Khadra	Ibra massif	40R	603771	2517707	22°45'48.96"N	58° 0'38.86"E
KD02-03	Lava flow	Al Khadra	Ibra massif	40R	603771	2517707	22°45'48.96"N	58° 0'38.86"E
SA01	Layered gabbro	Salahi Massif	Salahi massif	40R	444100	2665784	24° 6'12.27"N	56°26'59.92"E
SA02	Layered gabbro	Salahi Massif	Salahi massif	40R	445760	2665324	24° 5'58.04"N	56°27'58.89"E
WG01	Layered gabbro	Wadi Gideah	Ibra massif	40Q	655697	2532322	22°53'29.72"N	58°31'4.53"E
WG02	Layered gabbro	Wadi Gideah	Ibra massif	40Q	655626	2532342	22°53'30.39"N	58°31'2.08"E
WG03	Layered gabbro	Wadi Gideah	Ibra massif	40Q	655590	2531349	22°52'58.63"N	58°31'1.10"E
WG04	Layered gabbro	Wadi Gideah	Ibra massif	40Q	656061	2531233	22°52'54.19"N	58°31'16.94"E
WG05	Layered gabbro	Wadi Gideah	Ibra massif	40Q	655805	2530755	22°52'38.74"N	58°31'7.75"E
WG06	Layered gabbro	Wadi Gideah	Ibra massif	40Q	656114	2529811	22°52'7.91"N	58°31'18.29"E
WG07	Foliated gabbro	Wadi Gideah	Ibra massif	40Q	655975	2528586	22°51'28.17"N	58°31'12.97"E
WG08	Foliated gabbro	Wadi Gideah	Ibra massif	40Q	656154	2527688	22°50'58.88"N	58°31'18.89"E
WG09	Foliated gabbro	Wadi Gideah	Ibra massif	40Q	656309	2527105	22°50'39.84"N	58°31'24.15"E
WG10	Varitextured gabbro	Wadi Gideah	Ibra massif	40Q	656229	2525217	22°49'38.56"N	58°31'20.62"E
WG11	Dyke rooting zone	Wadi Gideah	Ibra massif	40Q	656229	2525217	22°49'38.56"N	58°31'20.62"E
WG12-13	Dyke rooting zone	Wadi Gideah	Ibra massif	40Q	656758	2524249	22°49'6.91"N	58°31'38.82"E
WG14	Varitextured gabbro	Wadi Gideah	Ibra massif	40Q	656758	2524249	22°49'6.91"N	58°31'38.82"E
WG16	Sheeted dykes	Wadi Gideah	Ibra massif	40Q	660870	2523389	22°48'37.55"N	58°34'2.71"E
WG19	Sheeted dykes	Wadi Gideah	Ibra massif	40Q	660692	2522839	22°48'19.73"N	58°33'56.26"E
WG20	Sheeted dykes	Wadi Gideah	Ibra massif	40Q	660042	2522265	22°48'1.26"N	58°33'33.26"E
WG23	Sheeted dykes	Wadi Gideah	Ibra massif	40Q	659924	2522000	22°47'52.72"N	58°33'29.06"E

All sites were sampled by collecting oriented hand samples. The only exception is site BD01 that was drilled in the field using a petrol-driven rock drill. Hand samples were chosen carefully in fresh-looking rocks, avoiding fractured areas that are more prone to weathering. The dip and dip direction of a flat planar surface of each hand sample were measured in situ before removing it from the host rock, and orientation data recorded and marked onto the sample and notebook. It was then removed from the exposure, labelled, and bagged. At each site, the orientation of structures such as the modal layering of layered gabbros, lava flows, the magmatic foliation in foliated gabbros, and the margins of sheeted dykes were recorded. These orientations were later used in the interpretation of the results.

Oriented cores (25 mm in diameter) were drilled perpendicular to the oriented surface of each hand sample in the laboratory at the University of Plymouth using a palaeomagnetic, water-cooled pillar core drill with a diamond drill bit. These cores were cut to standard size specimens (22 mm in height) using a water-cooled, circular dual-bladed diamond saw, often providing multiple specimens per core. Most field sites consist of 3-4 hand samples, providing about 12 specimens per site on average.

During the second field season, we attempted to collect cores with a water-cooled, diamond drill bit using a standard petrol-powered field rock drill at the Wadi Abdah locality. However due to technical difficulties with the drill we were only able to collect five samples this way. The remaining sites in Wadi Abdah

were therefore hand sampled, and drilled in the laboratory in Plymouth as described above.

During this study various magnetic techniques have been applied to the specimens, mostly in the Palaeomagnetic Laboratory at the University of Plymouth. These included measurements of anisotropy of magnetic susceptibility (AMS), variation of magnetic susceptibility with temperature, alternating field (AF) and thermal demagnetization, and bulk susceptibility measured after each thermal demagnetization step. In addition, isothermal remanent magnetization (IRM) acquisition curves were acquired at the Palaeomagnetic Laboratory "Fort Hoofddijk" at the University of Utrecht (the Netherlands). In both laboratories, Helmholtz cages shield both the instruments and specimens from the Earth's magnetic field. This field is on average approximately 46,000 nT, which is reduced to <1,000 nT inside the cages. Each technique applied to the specimens and the related data analysis is described in detail below.

3.6 – Anisotropy of magnetic susceptibility

Anisotropy of magnetic susceptibility (AMS) is a petrofabric tool used to determine the crystallographic- or shape-preferred orientation of minerals in rocks (e.g., Tarling and Hrouda, 1993). However, shape-preferred anisotropy dominates in rocks containing magnetite, such as those sampled here. AMS is geometrically described by an ellipsoid with principal axes corresponding to the minimum (k_{min}), intermediate (k_{int}), and maximum (k_{max}) susceptibilities (Tarling

and Hrouda, 1993; Figure 3.6). The relative magnitude of the susceptibility axes defines the shape of the AMS ellipsoid, which can be: (1) isotropic ($k_{min} = k_{int} = k_{max}$) when grains are not aligned preferentially; (2) oblate ($k_{min} < k_{int} \approx k_{max}$) when grain alignment defines a foliation plane; (3) triaxial ($k_{min} < k_{int} < k_{max}$) when grain alignment results in a well-defined foliation and a lineation; or (4) prolate ($k_{min} \approx k_{int} < k_{max}$) when grain alignment defines a lineation. In the case of many igneous rocks, prolate fabrics are linked to magmatic flow as k_{max} is most often coincident with the long axes of grains, which orient themselves parallel to the flow (e.g. during the emplacement of an intrusion). Oblate fabrics are linked to the development of foliations in the rock (Tarling & Hrouda, 1993). If a material is dominantly SD however, the magnetic fabric and rock fabric may not correspond due to an inverse magnetic fabric or due to interactions between ferrimagnetic grains (Ferré, 2002).

The strength of anisotropy in a specimen is described using the corrected anisotropy degree (P_J; Jelínek, 1978), where $P_J = 1.0$ indicates an isotropic fabric

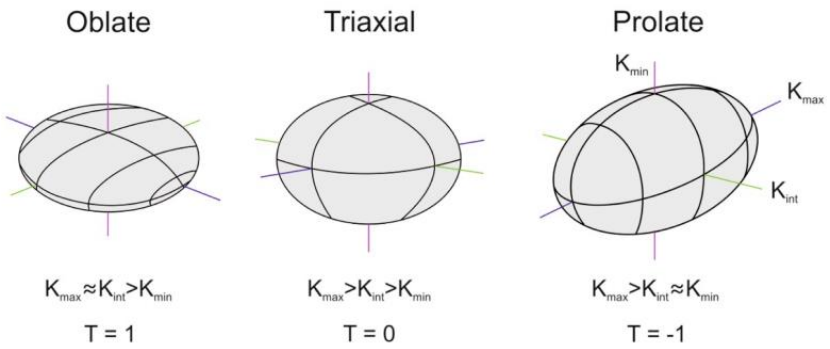

Figure 3.6 – Shapes of AMS ellipsoids for oblate (planar fabrics), tri-axial, and prolate (linear fabric) shapes. The ellipsoids are defined by three orthogonal axes, Kmax (maximum), Kint (intermediate), and Kmin (minimum). The shape parameter T is oblate for T = 0 to 1, tri-axial for T = 0, and prolate for T = -1 to 0. From Meyer (2015).

and, e.g., P_J = 1.05 indicates 5% anisotropy. The shape of the ellipsoid is described by the shape parameter (*T*; Jelínek, 1978), where -1.0 < *T* < 1.0 indicate prolate/oblate fabrics respectively (Jelínek, 1978). A *T* value close to zero indicates a triaxial anisotropy in a specimen where neither foliation nor lineation dominates the shape. However, fabrics at site-level are best defined by the relative distributions of specimen principal axes. Hence, a triaxial fabric at a site is characterized by three distinct, orthogonal clusters of k_{min}, k_{int}, and k_{max} axes, oblate fabrics are marked by a cluster of k_{min} axes and a girdle distribution of k_{int} and k_{max} axes, and prolate fabrics by a cluster of k_{max} axes and a girdle distribution of k_{int} and k_{min} axes. AMS measurements were performed on all specimens using an AGICO KLY-3 Kappabridge running the AGICO SUSAR software. Specimens are inserted into a holder in three positions to measure around three axes while spinning. A fourth (static) measurement provides the bulk susceptibility, up to a sensitivity of 2 x 10^{-8} (SI units). The data can then be read and visualised on stereographic projections using the AGICO software Anisoft42, which projects the K_{max}, K_{int}, and K_{min} axes separately using blue squares, green triangles, and pink dots (Figure 3.7).

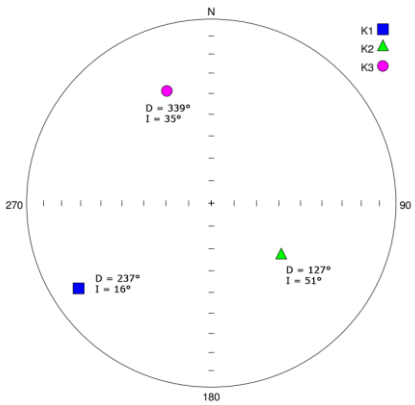

Figure 3.7 – Example of a stereographic projection showing the three principal anisotropy axes. K_{max} = blue squares, K_{int} = green triangles, K_{min} = pink circles.

AMS represents the sum of the contributions from all the minerals in a rock. In the case of ophiolitic mafic lithologies, this can include contributions from diamagnetic plagioclase, paramagnetic olivine and clinopyroxene crystals and ferromagnetic oxides (such as magnetite). Such oxides may be either primary interstitial magmatic phases, occur as exsolution products in silicate crystals, e.g. in plagioclase or clinopyroxene, or be produced by alteration, e.g. by serpentinization of olivine. Because of its high magnetic susceptibility, magnetite will dominate the AMS signal if present in concentrations of > 0.1 wt.% (Figure 3.8; Tarling & Hrouda, 1993).

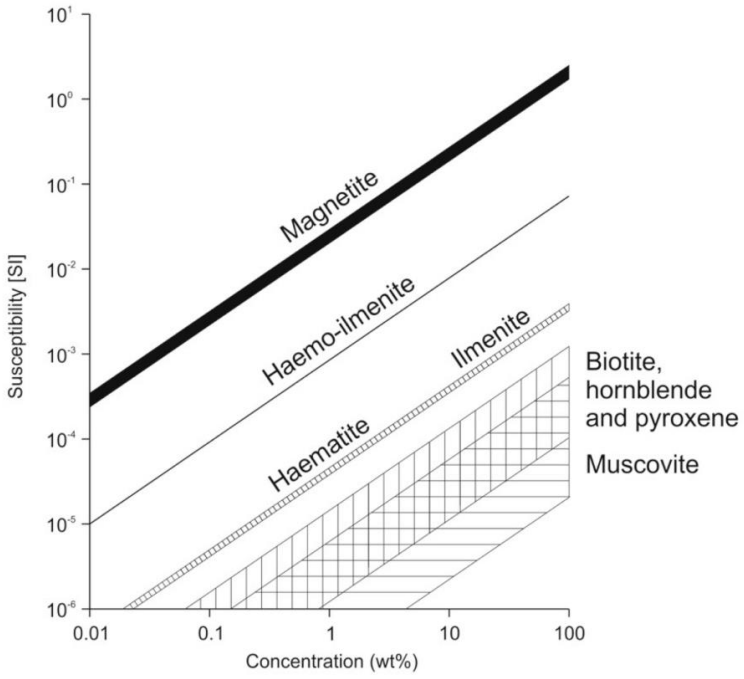

Figure 3.8 – The concentration (wt%) of common ferromagnetic and paramagnetic minerals to the bulk susceptibility of a rock. Both ferromagnetic and paramagnetic minerals can contribute to the bulk susceptibility of a rock, however ferromagnetic minerals will dominate the signal even if present in small concentrations (modified from Tarling and Hrouda, 1993).

3.7 – Measurement of remanent magnetizations and demagnetization techniques

The NRM of a rock may consist of multiple components obtained over time (Collinson, 1983; Butler, 1992; Tauxe, 2010). To recover the most geologically significant ChRM component, therefore, it is necessary to remove lower stability overprints by laboratory treatment. This can be achieved by stepwise demagnetization of a specimen, which will gradually remove any secondary components that may be present. As the ChRM is usually the most stable magnetic component in a specimen, we expect the secondary components to be removed first during demagnetization at a lower temperatures or applied fields, leaving the ChRM intact until higher temperatures/applied fields are reached (Collinson, 1983; Butler, 1992; Tauxe, 2010). Specimens can either be subjected to a progressively increasing alternating field or to increased temperature steps in order to be demagnetised. These techniques exploit variations in coercivity or unblocking temperature, respectively, as magnetic grains of a low coercivity and/or low unblocking temperature are more likely to carry secondary magnetizations (Tauxe et al., 2010) and hence become removed during the early stages of the demagnetization treatment. Both techniques were used on specimens in this study to allow comparison of results between the techniques.

3.7.1 – Alternating field demagnetization

In the case of AF treatment, samples were demagnetised using an AGICO LDA-3

AF Demagnetiser and magnetizations were then measured with a Molspin fluxgate spinner magnetometer and an AGICO JR-6 spinner magnetometer. The AF demagnetiser subjects specimens to an alternating field while tumbling them around two orthogonal axes in a zero field environment. This randomizes the magnetizations of grains with coercivities less than the peak applied field, effectively removing their contribution to the NRM. Magnetic grains with a higher coercivity than the peak field will be unaffected by the alternating external field. When the alternating field is increased stepwise, higher coercivity grains will be gradually demagnetised, until eventually the remanence decreases to the noise level of the magnetometer. Peak alternating field were typically increased in steps of 5 mT until 35 mT, then steps of 10 mT until a maximum of 100 mT was reached.

3.7.2 – Thermal demagnetization

Thermal demagnetization uses thermal energy to stepwise destroy the magnetization in a specimen. Specimens were thermally demagnetised in a magnetically shielded furnace (Magnetic Measurements Ltd Thermal Demagnetizer models MMTD1 and MMTD80) in steps of 10-50°C until a maximum of 600°C was reached. In some extreme cases specimens had to be heated up to even higher temperatures, up to a maximum of 740° C. During each heating and cooling cycle, specimens were held at the specified temperature for a minimum of 40 minutes, then cooled down to room temperature by the in-built fan.

As the temperature for the specimens stepwise increases, (ferro)magnetic grains will unblock, and as they do completely lose any geologically meaningful remanent magnetization. Once a specimen is cooled down to room temperature (and therefore below the blocking temperature of many grains), they will regain their ability to acquire a remanent magnetization, but in the zero-field of the oven this magnetization will be random in direction and therefore not contribute to the net magnetization of the specimen (Collinson, 1983; Butler, 1992; Tauxe, 2010). Therefore, by stepwise increasing the temperature, more grains will lose their remanent magnetization between treatments and cease to contribute to the net magnetization of the specimen, until only the remanence carried by the most stable grains with the highest unblocking temperatures remains.

Between each heating step, the magnetization of the samples was measured using an AGICO JR-6A spinner magnetometer and a Molspin fluxgate spinner magnetometer, and the susceptibility was measured using a Bartington magnetic susceptibility meter or by using the AGICO KLY3 Kappabridge to monitor oven-induced alteration. Specimens were demagnetised until the magnetic signal was close to zero. In order to minimise the effect of any magnetism that could be acquired in any residual magnetic field while cooling in the oven, specimens were arranged in antipodal positions between each heating step.

3.8 – Statistical analysis of demagnetization data

During a demagnetization experiment, the remanent magnetization vector of a specimen will change as secondary components are removed until a stable component is obtained and isolated, after which the magnetization vector will decay in a straight line to the origin. The resulting demagnetization plots from either AF or thermal demagnetization can be plotted as orthogonal vector diagrams, or Zijderveld diagrams (Zijderveld, 1967). These diagrams show changes in declination, inclination, and intensity as the remanence components change through demagnetization (Figure 3.9).

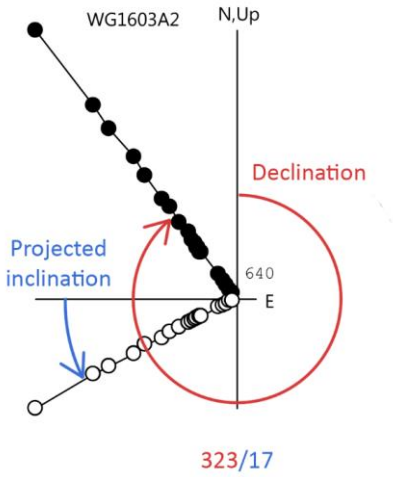

Figure 3.9 – Example of a Zijderveld diagram showing the declination through solid black circles, inclination through white circles.

Declinations of magnetization components are plotted on N-E-S-W axes, where the declination is the angle a point makes with the north axis in a clockwise manner, and the (apparent) inclinations are plotted on Up-Down axes oriented in

either a N-S or an E-W plane. The true inclination is related to the apparent inclination in the following way:

$$tan_{inclination} = tan_{inc-apparent} \mid cos_{declination} \mid$$

for a N-S vertical plane.

The intensity of a point is proportional to the distance of that point from the origin of the Zijderveld diagram. When multiple points in the demagnetization path form a linear segment, these can be interpreted as a magnetization component, and the declination and inclination of this can be calculated by fitting a least-squares line through the points. A rock specimen can contain multiple components of magnetization of which the coercivities or unblocking temperatures may (partially) overlap; this results in Zijderveld plots composed of multiple linear segments that can be connected by a kink (no overlap between components) or a bend in the path (components overlap) (Figure 3.10). The ChRM, the component of most interest, typically has the highest coercivity or unblocking temperature, usually resulting in a path that leads towards the origin.

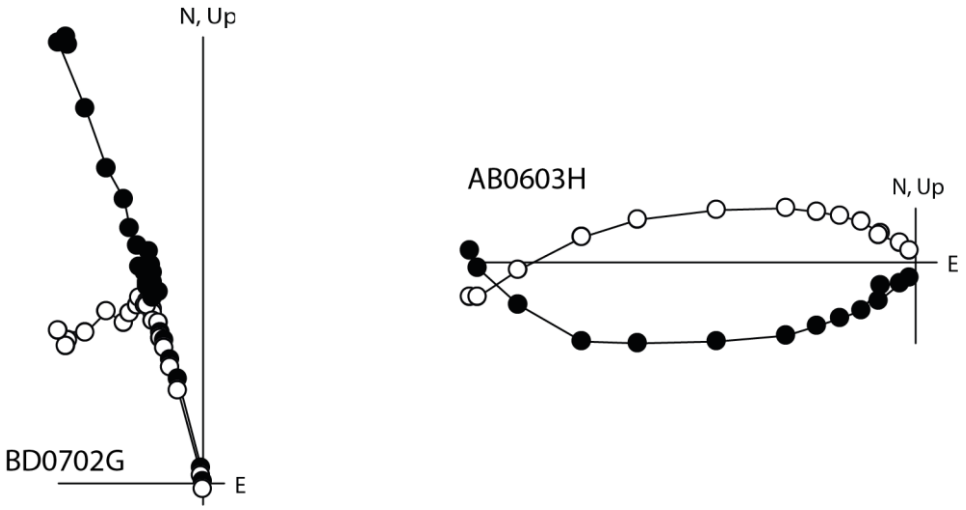

Figure 3.10 – Example of a Zijderveld diagram displaying multiple components of which the coercivities/unblocking temperatures do not overlap (left) and (partially) overlap (right).

Least square best-fit lines are fitted to the various magnetization components using principal component analysis (PCA) (Kirschvink, 1980), defining the declination, inclination, and maximum angular deviation (MAD) of components. In this study, components with MAD angles ≤ 10° were considered statistically acceptable, and those with MAD angles > 10° were rejected from further analysis (Butler, 1992; Tauxe, 2010). All components were picked using a modified version of the "MacPaleomag" software written by Jeffrey Gee (Scripps Institution of Oceanography).

For each sampled site, site means directions of the ChRM components were calculated using Fisher statistics (Fisher, 1953) in Excel. The Fisher (1953) precision parameter *k* and the α_{95} cone of confidence were used to determine the statistical significance of site mean directions, based on the dispersion of the data around the calculated mean directions. The precision parameter *k* is given by:

$$k = \frac{(N-1)}{(N-R)}$$

where *N* is the number of vectors and *R* is the length of their resultant. This describes the dispersion of ChRM directions around the calculated mean, where high values for *k* represent a minimal dispersion. The α_{95} cone of confidence is given by:

$$cos\alpha_{95} = 1 - \frac{N-R}{R}\left\{\left(\frac{1}{0.05}\right)^{\frac{1}{N-1}} - 1\right\}$$

which indicates the level of confidence on the calculated mean direction, i.e.

there is a 95% probability that the true mean direction of the population of grains carrying the magnetization lies within the α_{95} cone of confidence. As α_{95} is very dependent on the number of vectors, it is preferable to have mean directions calculated from six or more samples (Tauxe, 2010). A site mean direction in this study is considered to be reliable when $\alpha_{95} < 15°$ and $k > 15$.

3.9 – Rock magnetic experiments

The techniques described below provide further information about the magnetic properties of specimens, in particular their magnetic mineralogy and their magnetic grain size.

3.9.1 – Temperature dependence of magnetic susceptibility

Constraints on the magnetic mineralogy of a specimen may be provided by determining Curie temperatures via the variation of low field magnetic susceptibility with temperature. An AGICO KLY-3 Kappabridge coupled with a CS-3 furnace apparatus was used to perform thermomagnetic susceptibility measurements on specimens to provide information on ferromagnetic mineral(s) that are carrying the specimen magnetizations. Crushed powders from core leftovers were placed into a glass test tube to a depth of 1.5 cm into which a thermocouple was inserted. The software SUSTE from AGICO then allows for automated measurements of the susceptibility as the temperature was gradually increased to 700° and cooled back to room temperature. During each

experiment, susceptibility was measured roughly every 3°C during warming and cooling. The AGICO software Cureval was then used to process the data to subtract the signal due to the empty furnace and thermocouple, and Curie temperatures determined using the inverse susceptibility method of Petrovský and Kapička (2006).

3.9.2 – Acquisition of isothermal remanent magnetization and end-member modelling

Palaeomagnetic directional information can distinguish between remagnetised and primary remanences if the direction of the remagnetised remanence is significantly different from the primary remanence. By using end-member modelling of the acquisition curves of isothermal remanent magnetization (IRM), we try to use rock magnetic characterization to recognise remagnetised (or partly remagnetised) specimens from the localities in Wadi Gideah, Wadi Abyad, and Salahi Massif, which are completely remagnetised, partly remagnetised from bottom to top, and not remagnetised respectively. For this study, the Matlab script used was written by David Heslop and can be found on his website (http://people.rses.anu.edu.au/Heslop_d). This technique has previously been successfully applied to sedimentary and volcanic rocks (Gong, 2009; Hinsbergen, 2010; Meijers, 2010; Dekkers, 2012, 2014; Aben, 2014; Huang, 2015a,b,c; Pastor-Galán, 2016), but has never before been applied to ophiolitic rocks.

Whereas palaeomagnetic studies focus on remanence directions to recognise remagnetization, end member modelling of IRM curves instead focuses on the magnetic properties of a rock, in particular their magnetic grain size range. Grain growth assisted by fluids can take place at low temperatures and result in remagnetization (Elmore et al., 2006), and rocks remagnetised by a chemical remanent magnetization (CRM) may contain an abundance of very small magnetic particles of magnetite or greigite (Rowan & Roberts, 2006, 2008). Grain growth by chemical remagnetization therefore adds magnetic particles to the already existing magnetic signal in a rock without the need to replace the original grain assemblages carrying a primary magnetization. As the original and newly grown magnetic particles were formed by different processes, these are characterised by different magnetic particle distributions and properties, and the IRM acquisition curves of these can be mathematically unmixed into various 'end-members' (Weltje, 1997; Heslop & Dillon, 2007). In the case of a pure thermoviscous remagnetization setting, the grain size distribution of magnetic particles should not change, and therefore this technique would not be able to distinguish between original and remagnetised particles.

After acquiring IRM curves, end-member modelling allows us to interpret them in groups using the algorithm of Weltje (1997). This algorithm assumes that the measured data (**X**) are a linear mixture of a number of invariant constituent components, which are called end-members. The algorithm requires all data curves to be normalised to their maximum value, thus representing the data as proportions and eliminating the need for prior knowledge of magnetic minerals

properties. The data matrix **X** can be described as a linear model **X = AS + ε**, where the matrix **S** represents the form, or remanence curve, of each end-member, **A** represents the abundancies of each end-member, and **ε** is the error marge. Two requirements are that the abundancies of the end-members **A** are never negative and that the shape of the end-member curves **S** must be monotonic until saturation of the curve is achieved (Heslop & Dillon, 2007). As the model is linearly dependent, this also means that **S** must be linearly dependent, such that one end-member can never be a linear combination of other end-members. This requires some pre-processing of the input IRM curves where the curves are forced to be monotonic and any negative values are removed. In order to achieve meaningful end-members, at least 30-50 IRM input curves should be used (Dekkers, 2012) as the method makes use of inherent variability within the presented dataset. As the shape and abundance of the end-members are dependent on the input curves, a large variation in one of the IRM curves could result in a very different end-member if less than 30 input curves were used to calculate them.

Two things must be noted about this technique: (i) both the end-member properties and the end-member mixing proportions in each specimen are calculated from the same dataset, and therefore the same end-member can be calculated from different mixtures of invariant points. Mathematically speaking an end-member therefore is not a unique solution; (ii) the shape and abundances of the calculated end-members are dependent on the IRM data set, which is a closed data set because all curves have to be normalised to their maximum value.

Therefore, changing the abundance of one end-member will directly change the abundance of the other(s). These two points make it clear that in order to achieve a clear end-member analysis, the end-member signatures must make sense in a geological context and their significance must be clearly understood.

One of the crucial steps in decomposing the IRM dataset is determining the number of meaningful end-members that are present. By comparing the measured data **X** and the resulting model **AS** the coefficient of determination r^2 can be determined for end-member models with an increasing number of end-members (starting with 2) (Heslop & Dillon, 2007). When an insufficient number of end-members are used in the model, the calculated r^2 will be low (<0.5), whereas models considered to be good will have a higher r^2 (>0.8). Increasing the number of end-members from this point on will provide only little improvement in the quality of the model. This can be illustrated by plotting r^2 against the number of end-members used; the resulting slope will provide a visual guideline for the optimum number of end-members in the calculated model. A steeply increasing slope at a low number of end-members means that the quality of the model is still being increased as more end-members are added, and the slope flattening out at a higher number of end-members means that the additional end-members do not add any more information to the model. Choosing a number of end-members in that range will likely result in overinterpretation of the data, and therefore the number of end-members to use is preferably chosen at the point where the slope starts to lessen in angle. The other way of determining the number of end-members is by comparing the shape of the end-member models;

when two or more end-members are (nearly) identical in shape, they are better merged together into a single end-member with basically the same meaning. In that case, the model with the lesser number of end-members is chosen as the optimum model.

In total, 155 specimens were processed from three localities; 38 specimens from the completely remagnetised section in Wadi Gideah, 71 specimens from Wadi Abyad, variably remagnetised from the bottom to the top, and 46 specimens from the control section in the Salahi Massif, outside the region of remagnetization. The IRM acquisition curves for all specimens were measured with a robotised 2G DC-SQUID (Direct Current Superconducting Quantum Interference Device) magnetometer (instrumental noise level = 3 x 10^{-12} Am^2) with an in-line setup for IRM acquisition curves up to 700 mT at Palaeomagnetic Laboratory 'Fort Hoofddijk' at Utrecht University (Netherlands). The acquisition curves were then processed as follows: (1) IRM acquisition curves had to be smoothed to remove small deviations, so small negative IRM data points at low field steps were set to zero, and the curves were monotonically smoothed in Excel by giving each deviating data 'spike' a new value in between the values of the preceding and succeeding data points; (2) The coefficient of determination r^2 for multiple numbers of end-members (ranging from 2 to 9) was calculated by running the model in MATLAB 2007a (The Mathworks, Natick, MA, USA). The optimum number of end-members was chosen using the criteria described earlier (more detailed criteria will be presented in the Results section). (3) For each end-member model the end-member parameters were calculated.

3.9.3 – End-member component analysis

It is also important to know that an end-member may contain a magnetic signature that is made up of two coercivity distributions, e.g. magnetite and hematite that co-exist in the same rock. End-member modelling does not provide solutions based on the magnetic mineralogy, but rather on the processes involved in forming these minerals. One technique that shows more insight into the coercivity distributions that an end-member is made of is the component analysis by Kruiver et al. (2001), based on cumulative log Gaussian (CLG) analysis.

In the case where a rock is made up of a mixed magnetic mineralogy, the contributions of the individual magnetic minerals add linearly, resulting in a cumulative curve. A measured IRM curve can be decomposed into several CLG curves by distinguishing between their difference in saturation IRM (SIRM), their mean coercivity ($B_{1/2}$), and their dispersion parameter (DP). The same decomposition can be applied to the previously calculated end-members, thus decomposing the end-members even further into end-member components. CLG analysis is a combination of the analyses of the linear acquisition plot of the acquisition curve (LAP), the gradient of said acquisition plot (GAP) and the standardised acquisition plot (SAP) (Figure 3.11). All three representations are acquired from Kruiver's Excel workbook (Kruiver et al., 2001) by forward fitting a curve to match the end-member acquisition curve. This is done by changing the initial values for the SIRM, $\log(B_{1/2})$, and DP until an optimised goodness of fit is achieved by minimising the squared residuals for each plot. Up to six components

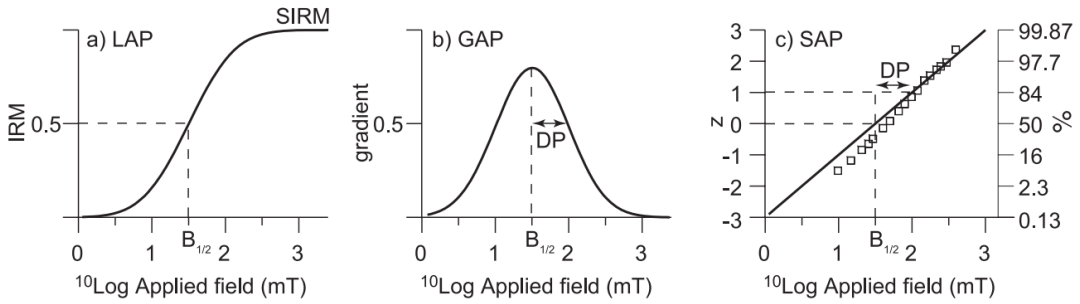

Figure 3.11 – Examples of IRM acquisition curves used in CLG analysis; (a) a linear acquisition plot (LAP). SIRM = saturation IRM, (b) the gradient of the acquisition plot (GAP). DP = dispersion parameter that represents one standard deviation, (c) standardised acquisition plot (SAP). On all plots $B_{1/2}$ is the field at which half of the SIRM is reached. Squares in the SAP are measured data from a titanomagnetite. From Kruiver et al. (2001).

can be added per plot. Kruiver et al. (2001) also established that smaller IRM values in the low-coercivity portion of the acquisition curves are more susceptible to random noise. Therefore any components with a very low coercivity (1-5 mT) picked in the acquisition curves over only a few datapoints were disregarded from further analysis and regarded as random noise.

Kruiver's CLG analysis aims to separate components with different coercivities from a single IRM or end-member curve, therefore adding valuable data on the magnetic mineralogy to the end-member modelling analysis. Even with (partly) overlapping coercivities the method is able to distinguish between different components (Figures 3.12). However it should be noted that with an increasing coercivity overlap, more data points are required for a meaningful separation of coercivity components, and eventually with (almost) entirely overlapping coercivity spectra it may become harder to distinguish between different components. In this case it will be necessary to use additional

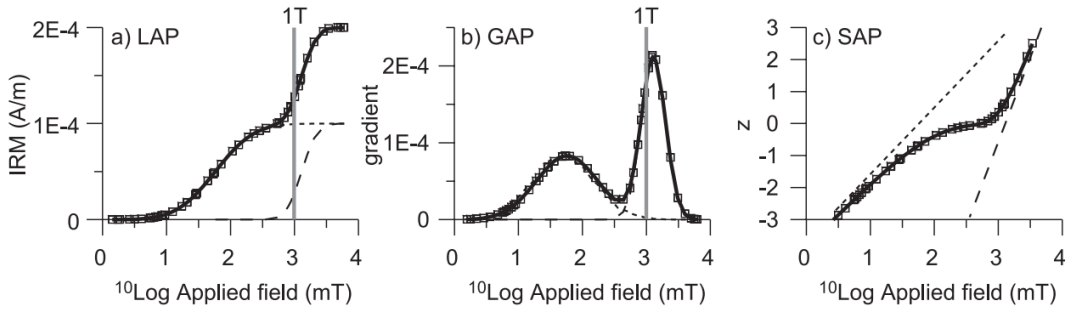

Figure 3.12 – Example of linear, gradient, and standardised acquisition plots for a modelled mixture of magnetite (SIRM = 0.1 mA/m, $\log(B_{1/2})$ = 1.76, DP = 0.48) and goethite (SIRM = 0.1 mA/m, $\log(B_{1/2})$ = 3.11, DP = 0.19). Squares represent data points, the short-dashed line represents component 1, the long-dashed line component 2. From Kruiver et al. (2001).

information, such as thermal demagnetization paths, to distinguish between minerals with similar coercivities.

3.10 – Structural analysis of palaeomagnetic data

3.10.1 – Standard tilt corrections

Structural corrections need to be applied to palaeomagnetic data to restore sampled geological units to their orientation at the time of remanence acquisition. Standard tilt corrections achieve this by assuming that tilt took place about a strike-parallel, horizontal rotation axis, e.g. by untilting layered gabbros and lava flows back to a palaeohorizontal and dykes back to a palaeovertical. The resulting declinations can then be used to determine vertical axis rotations by comparing them to an appropriate reference direction. This method divides the total deformation of an area into two steps around two orthogonal axes (horizontal, then vertical), where most of the tectonic interpretation relies on the second, vertical axis rotation alone.

For sites with a shallow dip that are not overturned, this method may provide correct rotation estimates. However when the dip of a site becomes steeper this method may result in erroneous declinations (Tarling, 1983), leading to incorrect interpretations. The method assumes a horizontal rotation axis, whereas in nature this is rarely the case and the rotation axis is more likely to be inclined. More importantly, in the case of palaeovertical dykes, any component of rotation around a dyke-normal axis cannot be quantified using standard tilt corrections as such components do not change the observable orientation of the dyke. We therefore need to apply a different method that uses a single, inclined rotation axis to untilt our sites.

3.10.2 – Net tectonic rotation analysis

In contrast to standard tilt corrections, net tectonic rotation analysis defines a single rotation about an inclined axis that simultaneously restores the site mean magnetization vector (SMV) to the reference magnetization direction (RMV) and the structure back to its initial orientation (horizontal for layered gabbros and lava flows, and vertical for dykes). To achieve this, the net tectonic rotation analysis of Allerton and Vine (1987) is used, which has been successfully employed in many previous studies in ophiolites (e.g. Allerton and Vine, 1987; Morris et al., 1990; Morris et al., 2002; Inwood et al., 2009; Maffione et al., 2015; Morris et al., 2017; van Hinsbergen et al., 2019). This method assumes that no internal deformation is present in a sampled site so that the angle β between the SMV and the present day pole (PDP) to the structure remains constant through

the deformation (Allerton and Vine, 1987). Therefore the possible initial positions of the PDP can be described as a small circle of radius β that is centred on the RMV on a stereographic projection.

In the palaeohorizontal (layered gabbro or lava flow) case of NTR analysis, only one solution for the net rotation is produced, with the steepest point on the small circle with radius β surrounding the RMV chosen as the initial orientation of the PDP, as this represents the minimum dip (Figure 3.13).

The palaeovertical (dyke) case of NTR analysis often provides two solutions for the initially vertical dyke orientation, corresponding to the two points where the small circle (radius β) surrounding the RMV intersects the horizontal plane (primitive of the stereonet) (Figure 3.13). In the case where the small circle does not intersect with the horizontal, the shallowest point on the circle is chosen, which allows the PDP to be rotated to its steepest possible initial orientation. In this case, the dyke can never be restored to a vertical.

In both cases, NTR analysis restores the SMV to the RMV, and the PDP to its initial orientation at the same time, by rotating around an inclined axis at the intersection point of the great circle bisectrix of the pair of structural poles (present day and initial) and the bisectrix of the SMV and RMV (Allerton and Vine, 1987) (Figure 3.13). The rotation is then described by the azimuth and plunge of the rotation pole, and the angle and sense (clockwise or counterclockwise) of rotation. Uncertainties in the input vectors can also be incorporated into the analysis to give the most robust estimate of rotation parameters (Morris et al., 1998).

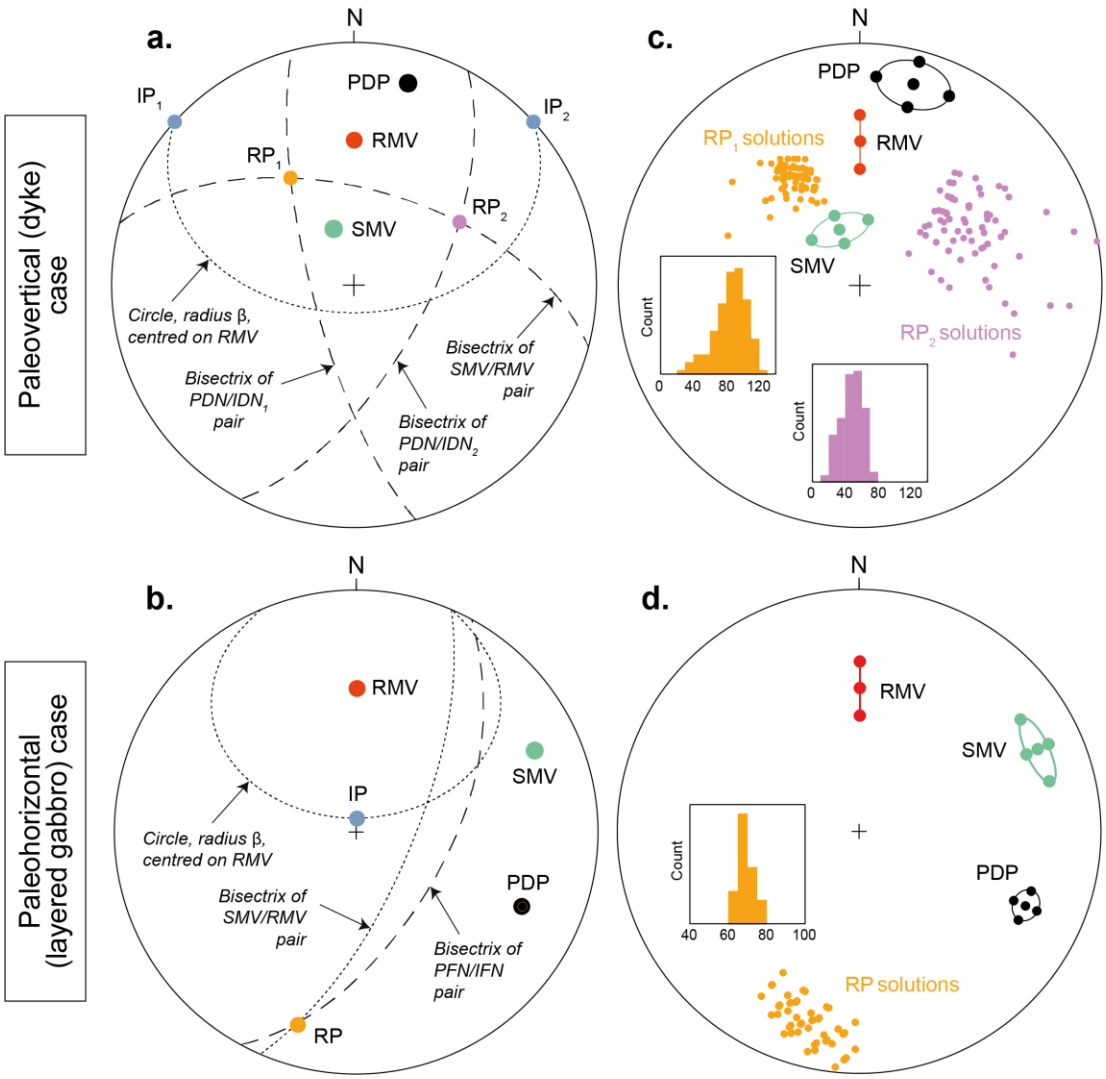

Figure 3.13 – Net tectonic rotation for a palaeovertical case (e.g. a dyke) and a palaeohorizontal case (e.g. a layered gabbro or lava). (a-b) Stereographic projections showing the site mean magnetization vector (SMV), reference magnetization direction (RMV), present day pole (PDP), initial orientation solutions (IP) (two for palaeovertical case, one for palaeohorizontal case), and rotation poles (RP), (c-d) Histograms of the rotation angles and stereographic projections of 75 calculated solutions for each RP. From Morris et al. (2017).

3.11 – Optical petrography

Thin sections from the Oman Drilling Project of holes GT1, GT2, and GT3 were observed in plane polarised, cross polarised, and reflected light to determine the relative grain size of ferromagnetic, opaque minerals through the section, and to observe their relationship with surrounding minerals.

3.12 – Shipboard methods for the Oman Drilling Project

The Oman Drilling Project (OmanDP) is an International Continental Scientific Drilling Program (ICDP) collaboration to investigate the ancient seafloor that is now the ophiolite of Oman. The main goals of the project are to fully understand the processes creating oceanic crust and the overall relationship between oceanic crust, shallow mantle, the hydrosphere, atmosphere, and biosphere. Many scientific objectives of the project are directly linked to the objectives of this PhD project, mainly investigating processes in the critical dyke-gabbro transition zone via study of cross-cutting igneous relationships, metamorphic mineral assemblages, and geochemical alteration.

Between December 2016 and March 2017, three 400-m long cores were drilled in the lower to upper crustal sequences of the southern massifs of the Oman ophiolite; Hole GT1 (layered gabbros) and Hole GT2 (foliated/layered gabbros) in Wadi Gideah in the Ibra/Tayin massif, and Hole GT3 (dyke/gabbro transition zone) in Wadi Abdah in the Semail massif. These cores were measured and analysed on board the Japanese scientific drilling ship *Chikyū* where I worked

on palaeomagnetic measurements and analysis as part of the Scientific Party for two months during Phase I of the project. The results give us the opportunity to compare specimens obtained from the surface in Wadi Abdah and Wadi Gideah to specimens obtained at depth in the ophiolite at the same locations.

The following sections describe the shipboard palaeomagnetic methods, statistical analysis, field tests and corrections (where different from the methods in the laboratory at the University of Plymouth).

3.12.1 – Measurement of remanent magnetization and demagnetization techniques

Discrete samples (square, 8 cm^3) were taken from the working halves of cores of Holes GT1, GT2, and GT3 at a spacing of roughly one sample per metre. Because cores recovered by rotary drilling can rotate relative to each other, their azimuthal orientations are not constrained and all magnetic data are reported relative to the core reference frame; X points positive into the working half of the cores, Z points positive down the core, and Y is positive orthogonal to X and Z in a right-hand sense.

All measurements took place in a permalloy shielded room blocking out 99% of the Earth's magnetic field. Remanent magnetizations of all discrete samples were measured with a Natsuhara Giken SMD-88 fluxgate spinner magnetometer and associated software. Stepwise AF demagnetization of samples was performed using a Natsuhara Giken DEM-95C system with a sample tumbling mechanism capable of producing fields up to 180 mT. Stepwise thermal

demagnetization was performed using a Natsuhara Giken TDS-1 thermal demagnetiser, capable of heating samples up to 700°C. Both the AF and thermal demagnetisers had an ambient field of less than 5 nT. Königsberger values (Q) were calculated for all holes, defining the ratio of the induced magnetization to the remanent magnetization of a sample, which can be useful when interpreting the origin of magnetic anomalies.

We obtained magnetization directions using principal component analysis (Kirschvink, 1980) in the software "MacPaleomag" by Jeffrey Gee (Scripps Institution of Oceanography) and analysed the data using inclination-only statistics (Arason and Levi, 2010). Components were picked using the same approach as in section 3.8. The depth of samples is presented as a function of the *Chikyū* adjusted depth (CAD) and is used as the sample value in most figures.

3.12.2 – Anisotropy of magnetic susceptibility measurements

In addition to alternating field and thermal demagnetization, the bulk susceptibility and anisotropy of magnetic susceptibility (AMS) were measured prior to demagnetization using an AGICO KLY-3 Kappabridge susceptibility meter and the AGICO software "Susar". In addition for cores of Hole GT3, the temperature dependence of susceptibility was measured by coupling the Kappabridge with a CS-3 furnace apparatus using AGICO software "Suste7".

Chapter 4 – Rock magnetic experiments and magnetic fabric analyses

4.1 – Introduction

The magnetic mineralogy in a rock defines its ability to retain a stable remanent magnetization over geological time, and therefore knowing which (ferro)magnetic minerals are present is crucial information in understanding a rock's magnetic signal. This chapter focuses on techniques that help us determine not only the type of magnetic minerals present in our specimens, but also the strength and shape of the magnetic fabrics defined by their preferred orientations.

Unblocking temperature and coercivity characteristics obtained from thermal and alternating field demagnetization provide broad information on the magnetic minerals present in individual specimens, but this can be supplemented by additional rock magnetic experiments to provide more detail. The variation of magnetic susceptibility with temperature gives estimates of the Curie temperature(s) of ferromagnetic minerals in specimens; combined with the unblocking temperatures obtained from thermal demagnetization these allow us to determine which ferromagnetic mineral dominates the magnetic signal and if any secondary ferromagnetic mineral is present. Isothermal remanent magnetization (IRM) acquisition experiments aid determination of the coercivity spectra of specimens, providing indirect evidence of the grain sizes of the

ferromagnetic minerals. Finally, anisotropy of magnetic susceptibility (AMS) analysis helps to determine the shape and strength of the magnetic fabrics, potentially providing information on the magmatic fabrics present in the sampled lithologies.

4.2 – Unblocking temperature and coercivity data from demagnetization experiments

4.2.1 – AF demagnetization and median destructive fields

Alternating field (AF) demagnetization can be used to help determine which magnetic minerals dominate the remanence signal in specimens. The coercivity of a magnetic mineral largely depends on its domain state. Single domain (SD) magnetite has a strong resistance to AF demagnetization and high coercivity, whereas multi domain (MD) magnetite has a low resistance with a low coercivity. Pseudo-single domain (PSD) magnetite falls in between SD and MD magnetite. Magnetite grains usually demagnetize in fields lower than 100 mT. If hematite and goethite are present within a specimen, the remanence will not fully demagnetize as these minerals have coercivities > 100 mT (the maximum peak field produced by the AF demagnetizer used in this study).

The median destructive field (MDF) is the field strength that reduces NRM intensity by 50%. Determining the MDF from remanence decay paths, as well as observing the shape of the intensity curve, helps to determine the magnetic minerals present in specimens and even allow estimation of the grain sizes of

magnetite (if present) by comparing with standard magnetite AF demagnetization curves (Figure 4.1). However, if the NRM is characterised by a negative inclination with an antiparallel overprint, the decay curve of remanence won't be monotonic during AF demagnetization; in these circumstances the MDF may not be useful to determine magnetic minerals and grain sizes present in a specimen.

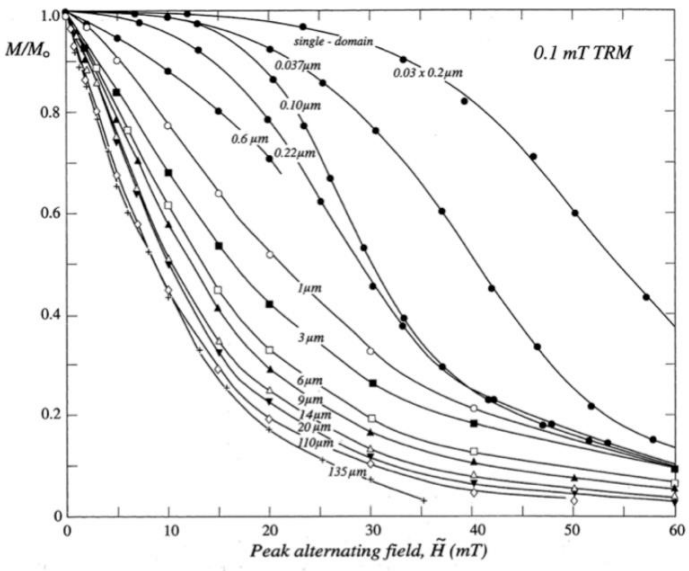

Figure 4.1 – Alternating field demagnetization curves for a range of magnetite grains. The shape of the curves reflects an increase in magnetite grain size from SD (sigmoidal) to MD (exponential). From Dunlop and Özdemir (1997).

A complete dataset from specimens of Wadi Abyad was studied (Figure 4.2). Specimens from the dyke rooting zone of Wadi Abyad (site AB01) produce remanence decay paths that generally reach a MDF value at 30-40 mT with 90% of their initial remanent magnetization lost at 70 mT, whereas specimens from the overlying sheeted dyke complex (AB02-05) of Wadi Abyad and Wadi Gideah tend to be much "softer" with MDF values of only 5-10 mT (Figure 4.2).

Comparing these results with the standard demagnetization curves of magnetite (Figure 4.11, Argyle et al. 1994) suggests that specimens from the dyke

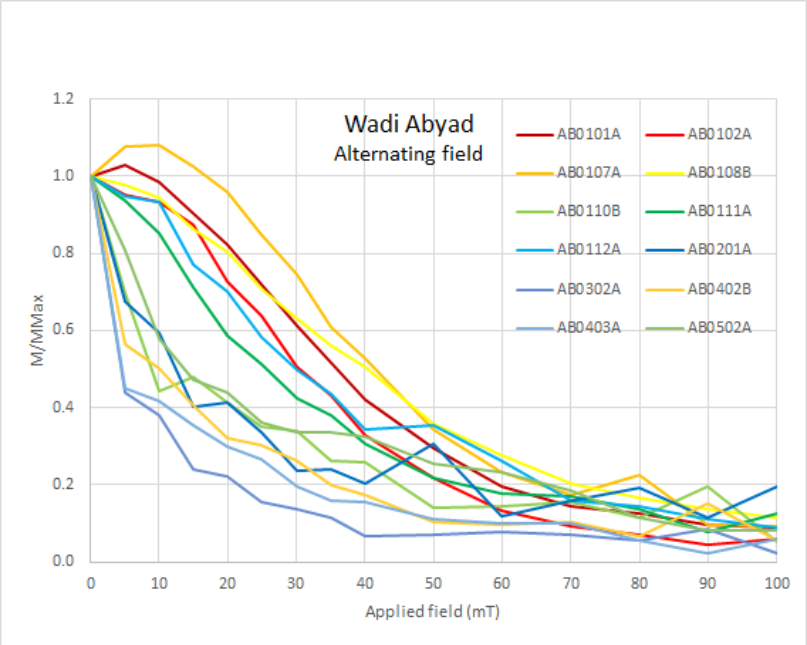

Figure 4.2 – Examples of normalised magnetization intensity curves against field strength for AF demagnetised specimens.

rooting zone contain fine-grained SD magnetite (0.1 µm). The sheeted dyke specimens with MDFs of only 5-10 mT are consistent with presence of large PSD magnetite grains (20 µm) or even large MD magnetite grains (>135 µm). Similar results are found in a study of van Hinsbergen et al. (2019) that found MD magnetite grains in sheeted dyke samples in the Wadi Gideah locality.

Section 4.3 expands further on coercivity spectra inferred from isothermal remanent magnetization (IRM) acquisition curves from the Wadi Abyad, Wadi Gideah, and Salahi massif localities.

4.2.2 – Thermal demagnetization and unblocking temperatures

The unblocking temperature is the temperature at which a ferromagnetic grain starts behaving superparamagnetic (see section 3.1.6) and is mainly dependent on the mineralogy and grain size (Butler, 1992; Tauxe, 2010).

Depending on the magnetic mineralogy in a natural sample, unblocking can occur over very narrow temperature ranges (e.g. close to the Curie temperature of pure magnetite; 580°C, or pure hematite; 680°C), or over a wider, lower distribution of temperatures when e.g. titanium (Ti) impurities are present in magnetite grains (Tarling & Hrouda, 1993; Butler, 1992; Tauxe, 2010). Low unblocking temperatures may also be associated with the presence of pyrrhotite (Curie temperature of 320°C). Intensity decay paths from thermal demagnetization may therefore give information on the magnetic mineralogy of a specimen.

We can divide the intensity decay curves from thermal demagnetization into unblocking temperature windows based on step-like decreases in remanence intensity:

(i) A high-temperature window that is common in the majority of specimens, which unblocks between 500-590°C.

(ii) An intermediate-temperature window in a large number of specimens, which unblocks generally between 250-450°C, focused around 300°C.

(iii) A low-temperature window that is found at some sites, which unblocks between 100-200°C.

Figure 4.3 shows representative remanence intensity curves derived from thermal demagnetization, ordered by locality.

In Wadi Abyad, all samples have maximum unblocking temperatures of ~580°C. In some dyke rooting zone specimens a 20% decrease in the remanence intensity can also be seen in an intermediate-temperature window of 300-400°C (AB0111B, Figure 4.3). This could be due to presence of minor pyrrhotite in these

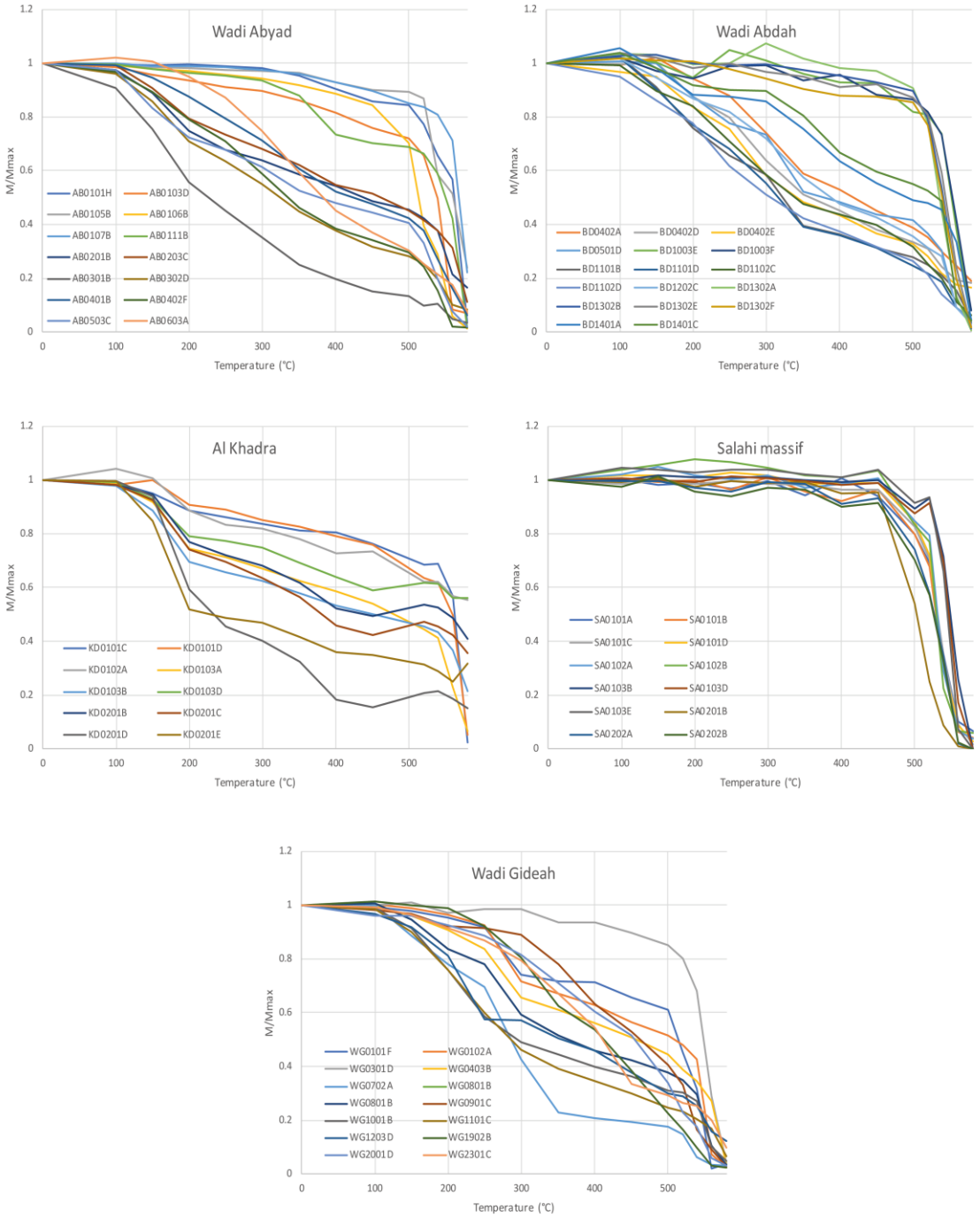

Figure 4.3 – Examples of normalised magnetization intensity curves against temperature for thermally demagnetised specimens.

samples. Sheeted dyke specimens, in contrast, show more distributed unblocking across a wide temperature range, suggesting presence of (titano)magnetite with a range of grain sizes.

Maximum unblocking temperatures of ~580°C are also seen throughout Wadi Abdah and Gideah, again indicating magnetite as the dominant remanence carrier. Specimens from sites BD10 and 13 (varitextured and foliated gabbros) and WG03 (layered gabbros) have discrete unblocking where more than 80% of the remanence is lost in the high-temperature window. Remaining specimens from this locality exhibit more distributed unblocking, with many specimens showing a step-like decay in intensity in the intermediate-temperature window, again consistent with presence of minor pyrrhotite.

Specimens from the dyke and lava flows of Al Khadra show variable behaviour; some of the specimens show one high-temperature window of 500-580°C (e.g. KD0101C, Figure 4.3), whereas remaining specimens lose 40-50% of their initial remanence in a low-temperature window of 100-200°C (KD0201D, Figure 4.3). These data are consistent with presence of magnetite and titanomagnetite in these rocks.

Layered gabbro specimens from the Salahi massif show very consistent and discrete unblocking; they lose 90-95% of their initial remanence in a high-temperature window of 500-580°C (Figure 4.3).

Overall, these experiments show that the majority of specimens have maximum unblocking temperatures of ~580°C, which indicates that magnetite is likely the dominant carrier of the remanence signal in these rocks. Specimens exhibiting distributed unblocking over a wide temperature range may also contain titanomagnetite (with a range of compositions) or this may reflect variations in ferromagnetic grain sizes within these rocks. Intermediate

unblocking temperatures of 300-400°C may indicate the presence of pyrrhotite in some specimens. However there is only limited evidence for this in the results of high temperature susceptibility experiments (section 4.3).

4.3 – High temperature susceptibility experiments

Thermomagnetic susceptibility measurements can provide information about the magnetic minerals present in a specimen as well as their contributions to the net susceptibility. Curie temperatures may be inferred from changes in susceptibility that occur as a specimen is heated and cooled. In this study, the inverse susceptibility method of Petrovský and Kapička (2006) is used to determine unblocking temperatures.

Figure 4.4 shows examples of thermomagnetic curves from all five localities and all lithologies. Solid lines represent the heating curves whereas dashed lines represent their respective cooling curves. In many specimens (including examples from all lithologies and localities), a bump in susceptibility on the heating curves can be seen at around 250-300°C (e.g. AB0501B, Figure 4.4) followed by a slight decrease in susceptibility. This suggests the presence of titanomagnetite/titanomaghemite in addition to magnetite. One specimen from the dyke rooting zone in Wadi Abdah (BD1202E in Figure 4.4 shows two discrete temperatures where susceptibility is lost on heating (300-350°C and ~580°C), suggesting presence of pyrrhotite and magnetite in this specimen.

The temperature variation of susceptibility is irreversible in the majority of specimens, with susceptibility values commonly being higher after heating,

suggesting that new, stronger magnetic phases of (titano-)magnetite have formed during the heating cycle (up to ~700°C). In all specimens from the Al Khadra locality, however, susceptibility values become lower after heating, suggesting mineralogical transformations were induced by the experiments. In the heating curves, steep drops in susceptibility occur around 450°C, in some cases followed by a further drop at 515°C (e.g. KD0101D, Figure 4.4). This behaviour could imply the occurrence of both Ti-rich and Ti-poor titanomagnetite respectively.

More than half of the specimens from the Wadi Abyad, Wadi Abdah, and Wadi Gideah localities display clear Hopkinson peaks (Hopkinson, 1889) associated with the Tc, ranging between 540-580°C (e.g. WG2303C, Figure 4.4), indicating that nearly-pure, fine-grained magnetite is the dominant carrier of the magnetic signal in the gabbros and dykes (Dunlop and Özdemir, 1997). The remaining specimens from these localities show a steep decrease in susceptibility at 560°C which is associated with the Tc of magnetite (e.g. AB0101P, Figure 4.4).

The sheeted dykes of locality Wadi Abdah show a temperature variation of magnetic susceptibility that seems to continue past 700°C. As there is no evidence for hematite being a primary magnetic carrier in these specimens based on maximum unblocking temperatures around 580°C, this behaviour may be due to partial oxidation during heating of magnetite, or maghemitised magnetite, which is common in mafic magmatic rocks (Dunlop and Özdemir, 1997).

Step-wise susceptibility decreases are seen in the layered gabbro specimens of the Salahi block (e.g. SA0203D, Figure 4.4), with the first drop in

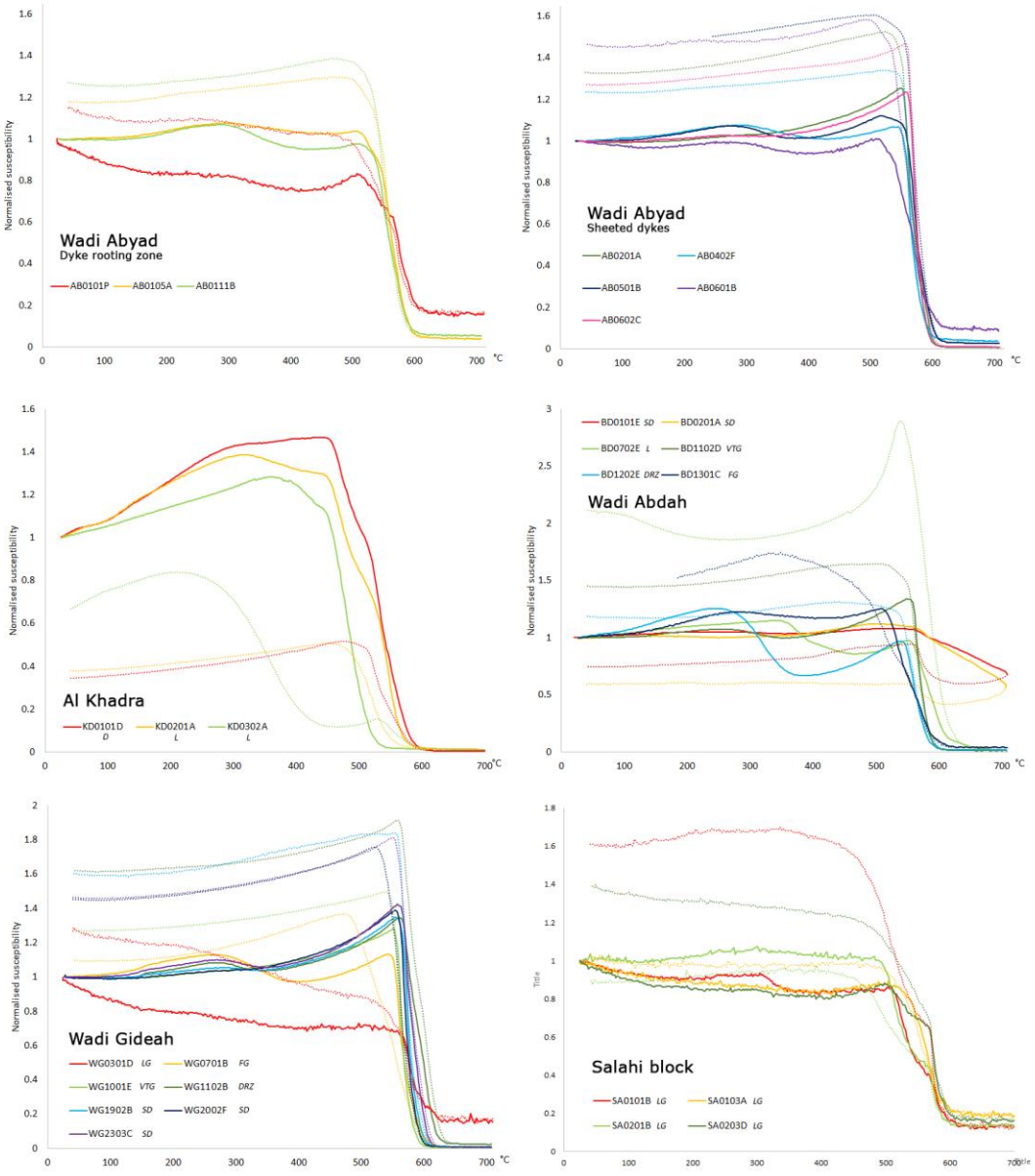

Figure 4.4 – Examples of normalised thermomagnetic curves per locality. Solid lines represent heating curves up to 700°C, dashed lines represent the cooling curves back to ambient temperature.

susceptibility happening around 490-510°C and a further decrease happening at 560-570°C as the Tc is reached. This is possibly related to the presence of titanomagnetite in these specimens.

In summary, Curie temperatures close to 580°C suggest that magnetite is the main carrier of the magnetic signal in the Wadi Abyad, Wadi Abdah and the

Salahi massif localities, combined with presence of titanomagnetite in some specimens (evidenced by bumps in heating curves and step-wise decreases of susceptibility). Results from Wadi Gideah suggest that fine-grained magnetite dominates the magnetic signal here, although a susceptibility hump at 300°C suggests that some titanomagnetite might be present. Lower Tc's recorded in specimens from Al Khadra imply that more Ti-rich titanomagnetite is the dominant carrier of the magnetic signal. These results are comparable with results found in the studies of Meyer (2015) and van Hinsbergen et al. (2019).

4.4 – Isothermal remanent magnetization (IRM) experiments

As explained in Chapter 3, isothermal remanent magnetization (IRM) can be imparted in specimens by exposing them to a direct magnetic field generated by an electromagnet. Increasing the peak applied field in a step-wise fashion results in progressively higher IRM intensities, and once the coercivities of all grains have been exceeded the magnetization reaches saturation (i.e. a saturation IRM (or SIRM) is reached). The shape of the IRM acquisition curve is dependent on the type and domain state of all combined ferromagnetic minerals present within a specimen. Single domain (SD) fine-grained magnetite reaches a maximum SIRM by an applied field of 300 mT, whereas multi domain (MD) magnetite only needs a few 10's mT to saturate. Hematite generally requires stronger fields of 1.5-5.0 T to become fully saturated (Lowrie, 1980).

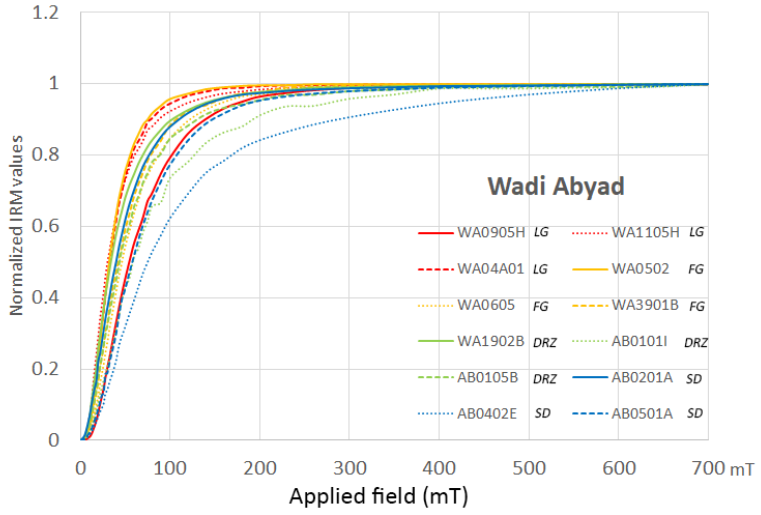

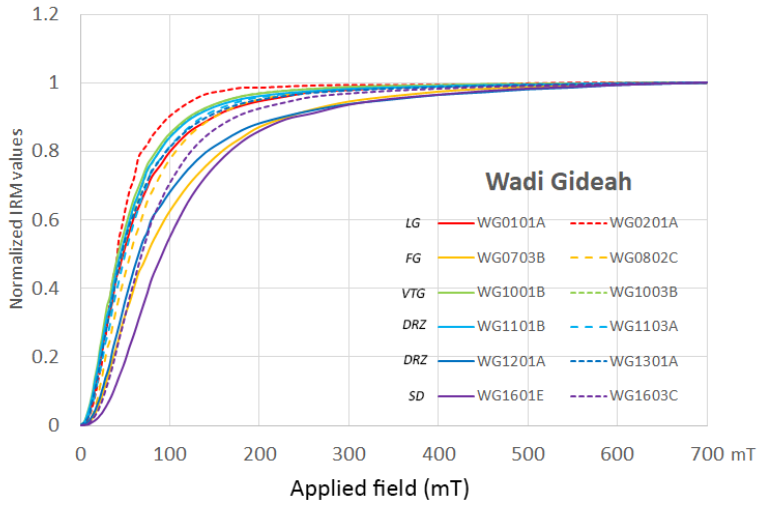

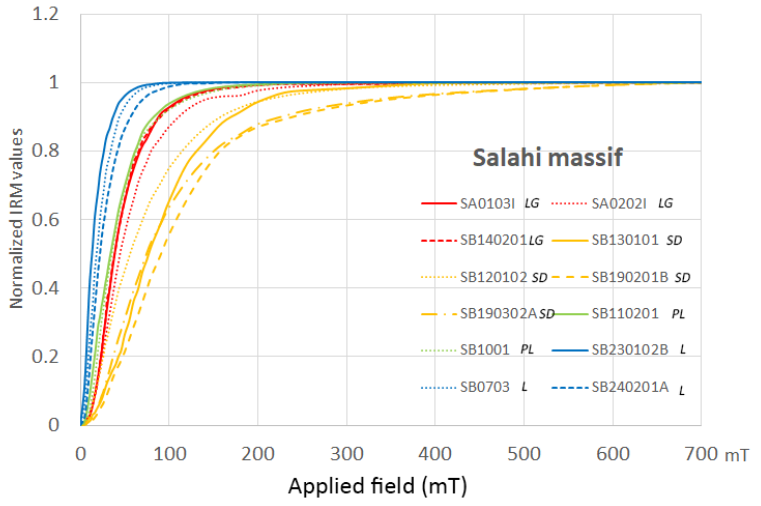

Figure 4.5 – Examples of normalised IRM acquisition curves for Wadi Abyad, Wadi Gideah, and the Salahi massif.

IRM acquisition experiments were conducted on 155 specimens in a stepwise increasing field up to a peak maximum field of 700 mT. Figure 4.5 shows results for representative specimens from the Wadi Abyad, Wadi Gideah, and Salahi massif localities. The various sampled lithologies are colour-coded and plotted within the same diagram, to compare acquisition curves between lithologies.

Layered and foliated gabbros of Wadi Abyad all reach saturation by 300 mT (e.g. WA04A01, Figure 4.5). Specimens from the dyke rooting zone and the sheeted dyke complex saturate between 300-500 mT (e.g. AB0101I, Figure 4.5), with specimens from site AB04 requiring peak fields of 700 mT to fully saturate (AB0402E, Figure 4.5). With the saturation of the gabbros consistently being achieved by 300 mT and the saturation of the dykes generally ranging between 300-500 mT, the data suggests that low-to-medium coercivity fine-grained magnetic carriers are present, with no indication of high coercivity minerals (except at the one sheeted dyke site that reached saturation at 700 mT). These IRM results are consistent with the evidence for dominance of (titano)magnetite in these rocks based on Curie temperatures (Section 4.3).

As in Wadi Abyad, layered gabbros in Wadi Gideah reach saturation by 300 mT (e.g. WG0201A, Figure 4.5), and similar results are found for the varitextured gabbros. The foliated gabbros saturate at higher fields, ranging between 500-600 mT (e.g. WG0703B, Figure 4.5). Specimens from the dyke rooting zone generally saturate by 300 mT (e.g. WG1103A, Figure 4.5), with the exception of specimens from a single dyke that saturate by 700 mT (WG1201A, Figure 4.5). The sheeted dykes saturate between 500-700 mT (e.g. WG1601E, Figure 4.5). These data

suggest that a range of magnetic carriers are present in these specimens, with low coercivity fine-grained magnetic carriers found in the layered gabbros, varitextured gabbros, and dyke rooting zone, and medium coercivity magnetic carriers present in foliated gabbros and sheeted dykes. The Curie temperatures suggested that magnetite is the dominant magnetic carrier in Wadi Gideah (section 4.3), suggesting that SD to PSD magnetite is the dominant magnetic carrier in these specimens.

Layered gabbros and pillow lavas from the Salahi massif saturate by 200-300 mT (e.g. SA0103I, Figure 4.5). The lavas reach saturate at even lower fields of 100 mT (e.g. SB230102B, Figure 4.5), suggesting very low coercivity magnetic carriers. As in Wadi Gideah, the sheeted dykes only saturate at 500-700 mT (e.g. SB190201B, Figure 4.5), suggesting the presence of medium coercivity magnetic carriers. Based on the Curie temperatures obtained in Section 4.3, this suggests that SD to PSD (titano)magnetite is the dominant carrier of the magnetic signal in the specimens from the Salahi massif. Some MD (titano)magnetite may also be present in the lavas based on their saturation in very low applied field, and these results are comparable with the results from van Hinsbergen et al. (2019) who found evidence for MD magnetite in samples all over the Oman ophiolite.

4.5 – Magnetic fabrics

Magnetic fabric analyses allow determination of the preferred orientations of magnetic minerals in rocks (Tarling and Hrouda, 1993). The

orientations of the principal axes of the anisotropy of low field magnetic susceptibility in igneous rocks may be related to the orientations of magmatic lineations and foliations observed in the field, providing additional insights into the magmatic processes involved in the formation of the oceanic crust preserved in the Oman ophiolite.

The anisotropy of magnetic susceptibility (AMS) was measured on 629 specimens and is described in the following sections by pseudostratigraphic level in geographic coordinates. Data are presented on equal area stereographic projections and additional diagrams of anisotropy parameters. The shape parameter T describes the shape of specimen AMS ellipsoids (oblate for $0 < T \leq 1$ and prolate for $-1 \leq T < 0$), whereas the corrected anisotropy degree P_J describes the strength or intensity of the anisotropy (Jelínek, 1981). These can be plotted against each other, or against the bulk susceptibility of specimens. Site mean AMS parameters and bulk susceptibilities are reported in Table 4.1.

4.5.1 – Magnetic fabrics in the layered gabbros

Layered gabbros were sampled in two localities; Wadi Gideah in the southern Ibra/Wadi Tayin massif and the Salahi massif in the north. Figure 4.6 shows AMS parameters for the layered gabbro specimens in dark green. Layered gabbro specimens from Salahi have predominantly prolate AMS ellipsoids, whereas in Wadi Gideah ~50% of the specimens display prolate ellipsoids with relatively weak anisotropies and the other 50% exhibit triaxial ellipsoids with a range of anisotropies up to 1.27 (Figure 4.6). There is a positive correlation

Table 4.1 - Summary of site mean AMS parameters in geographic coordinates. n = number of specimens, Km = bulk susceptibility, Dec = declination, Inc = inclination, conf. angle = semi-angle of 95% cone of confidence, Pj = anisotropy strength parameter, T = AMS shape parameter.

Site	Lithology	Layering/foliation/dyke orientation (dip dir / dip)	n	Km	K maximum Dec / Inc / conf. angle			K intermediate Dec / Inc / conf. angle			K minimum Dec / Inc / conf. angle			Pj	T
Wadi Abyad (Rustaq massif / Nakhl block):															
AB01	Dyke rooting zone	141/59	66	9.23E-03	200.8	50.7	18.9	131.8	65.3	9.5	319.7	35.1	8.5	1.028	0.199
AB02	Sheeted dykes	305/82	14	3.90E-02	210.6	38.4	7.7	47.2	48.7	15.7	327.7	49.2	62.3	1.036	-0.097
AB03	Sheeted dykes	305/82	12	4.38E-02	278.1	53.5	23.8	359.1	43.3	36.9	126.7	34.1	5.1	1.062	0.475
AB04	Sheeted dykes	189/34	30	5.63E-03	202.6	30.0	12.9	120.1	26.0	18.6	352.4	57.9	3.8	1.009	0.344
AB05	Sheeted dykes	195/44	11	1.82E-02	176.2	37.3	25.9	84.5	37.6	35.1	345.6	75.3	31.8	1.011	0.085
AB06	Sheeted dykes	200/71	16	5.72E-02	313.5	64.8	58.3	130.5	32.2	25.4	285.1	66.2	13.2	1.018	0.276
Wadi Abdah (Samail massif / Semail block):															
BD02	Sheeted dykes	046/81	14	6.32E-04	192.5	20.9	43.0	130.1	78.4	27.8	47.3	77.1	35.4	1.003	0.062
BD03	Sheeted dykes	046/85	11	9.55E-03	134.8	43.1	12.6	6.9	63.7	46.3	284.2	34.1	27.9	1.017	-0.457
BD04	Sheeted dykes	045/87	10	3.44E-03	129.1	26.3	24.4	304.6	72.0	14.1	244.5	24.8	53.3	1.011	0.051
BD05	Sheeted dykes	048/76	5	4.89E-03	250.5	57.9		129.5	74.4	37.3	355.1	38.1	64.5	1.009	0.195
BD07	Lavas	160/26	16	1.19E-02	200.7	79.3	24.4	210.2	41.1	27.2	48.0	28.6	17.0	1.004	0.121
BD08	Lavas	160/26	14	1.53E-02	197.3	52.6	23.9	141.2	29.3	22.9	7.1	44.6	6.7	1.017	0.290
BD09	Lavas	160/26	18	1.98E-03	148.4	81.8	12.1	53.8	47.9	47.9	334.8	45.6	41.0	1.007	-0.404
BD10	Varitextured gabbros	048/86	14	8.45E-04	151.3	72.0	12.1	324.0	45.2	45.8	305.7	40.8	66.5	1.014	0.351
BD11	Varitextured gabbros	048/86	14	1.41E-02	350.7	61.7	2.8	129.0	21.9	3.4	226.1	17.0	2.4	1.044	0.287
BD12	Dyke rooting zone	048/86	11	1.56E-02	327.8	76.0	11.6	144.8	40.8	47.0	161.6	19.5	69.7	1.097	0.342
BD13	Foliated gabbros	330/60	15	3.57E-03	295.6	24.4	26.3	2.3	77.4	24.8	90.8	42.2	21.9	1.094	-0.234
BD14	Foliated gabbros	330/60	13	5.46E-02	271.0	55.9	5.1	141.6	23.0	5.5	40.2	23.9	3.5	1.161	-0.081
Al Khadra (Ibra massif / Wadi Tayin block):															
KD01	Dyke	345/85	11	3.47E-02	34.8	80.6	55.0	187.1	83.3	32.0	238.7	17.7	30.7	1.006	0.220
KD02/03	Lavas	180/12	19	2.66E-02	280.5	83.3	16.5	60.4	41.3	28.2	214.0	39.8	50.1	1.016	0.087
Salahi Massif (Salahi massif / Hilti block):															
SA01	Layered gabbros	051/23	16	4.95E-04	119.2	13.5	38.8	25.4	37.7	18.1	218.6	59.4	15.4	1.113	-0.720
SA02	Layered gabbros	285/41	8	4.41E-04	276.5	50.0	10.8	67.9	50.0	70.7	133.2	35.9	22.2	1.027	0.091
Wadi Gideah (Ibra massif / Wadi Tayin block):															
WG01	Layered gabbros	155/33	24	2.43E-03	222.7	20.6	4.3	323.5	27.7	5.3	100.6	53.3	4.3	1.163	-0.240
WG02	Layered gabbros	155/33	8	1.81E-03	236.0	39.3	7.1	334.9	19.1	34.9	83.3	47.7	5.5	1.091	-0.363
WG03	Layered gabbros	155/33	13	2.47E-03	20.8	49.7	135.8	323.5	53.7	19.7	136.3	68.9	31.8	1.080	-0.156
WG04	Layered gabbros	155/33	17	2.31E-03	241.2	9.2	3.3	343.8	68.8	20.4	2.9	66.0	33.4	1.111	-0.347
WG05	Layered gabbros	155/33	14	1.82E-03	232.7	22.7	8.7	241.9	58.9		57.8	67.7	7.2	1.107	-0.084
WG06	Layered gabbros	155/33	11	5.77E-03	275.1	52.3	12.4	161.1	26.8	24.4	58.8	29.6	7.1	1.151	0.308
WG07	Foliated gabbros	073/80	8	3.75E-02	168.3	21.9	33.8	270.1	49.9	13.3	60.0	36.6	7.8	1.110	0.049
WG08	Foliated gabbros	198/87	15	2.17E-02	262.2	54.4	5.1	146.6	22.5	24.2	49.9	30.0	5.7	1.174	0.185
WG09	Foliated gabbros	198/87	13	1.54E-02	239.7	39.9	10.6	339.0	55.3		54.6	55.3	9.2	1.126	0.239
WG10	Varitextured gabbros	062/84	17	5.50E-02	329.3	54.6	31.0	340.5	62.2	36.9	174.2	44.8	17.4	1.022	0.184
WG11	Dyke rooting zone	062/84	17	2.64E-02	20.1	56.9	13.4	251.8	35.0	20.8	162.1	50.0	33.3	1.037	0.267
WG12	Dyke rooting zone	062/84	11	2.25E-02	20.8	66.6	11.7	159.6	62.4	80.2	204.1	19.2	10.5	1.028	0.439
WG14	Varitextured gabbros	062/84	16	5.25E-02	269.1	32.1	14.0	148.3	58.4	21.2	23.7	38.1	22.1	1.022	0.056
WG16	Sheeted dykes	076/73	14	1.51E-02	269.1	23.7	25.4	153.5	72.7	19.0	339.3	36.7	44.2	1.008	0.127
WG19	Sheeted dykes	069/57	11	1.57E-02	38.4	47.4	46.2	177.1	59.2	23.1	317.7	36.8	23.5	1.004	-0.163
WG20	Sheeted dykes	059/79	16	3.28E-02	280.0	69.5	21.1	24.2	67.1	33.3	79.5	19.8	43.1	1.008	0.155
WG23	Sheeted dykes	086/88	8	4.30E-02	269.3	68.9	6.9	100.5	21.5	11.8	7.7	5.0	37.3	1.008	-0.124

between P_J and the bulk susceptibility, suggesting that the intensity of anisotropy is dependent on the concentration of ferromagnetic particles in these specimens.

Figure 4.7 shows the orientations of the principal axes of the anisotropy, K_1 (K_{max}), K_2 (K_{int}) and K_3 (K_{min}) on equal area stereographic projections, with great circles representing the orientation of the layering shown in red. Two main fabric types are seen:

(i) Sites that exhibit prolate AMS ellipsoids, where the K_{max} axes lie in or close to the plane of modal layering and where K_{int} and K_{min} axes form a great circle girdle distribution (sites SA01-02, WG03-04). K_{max} axes

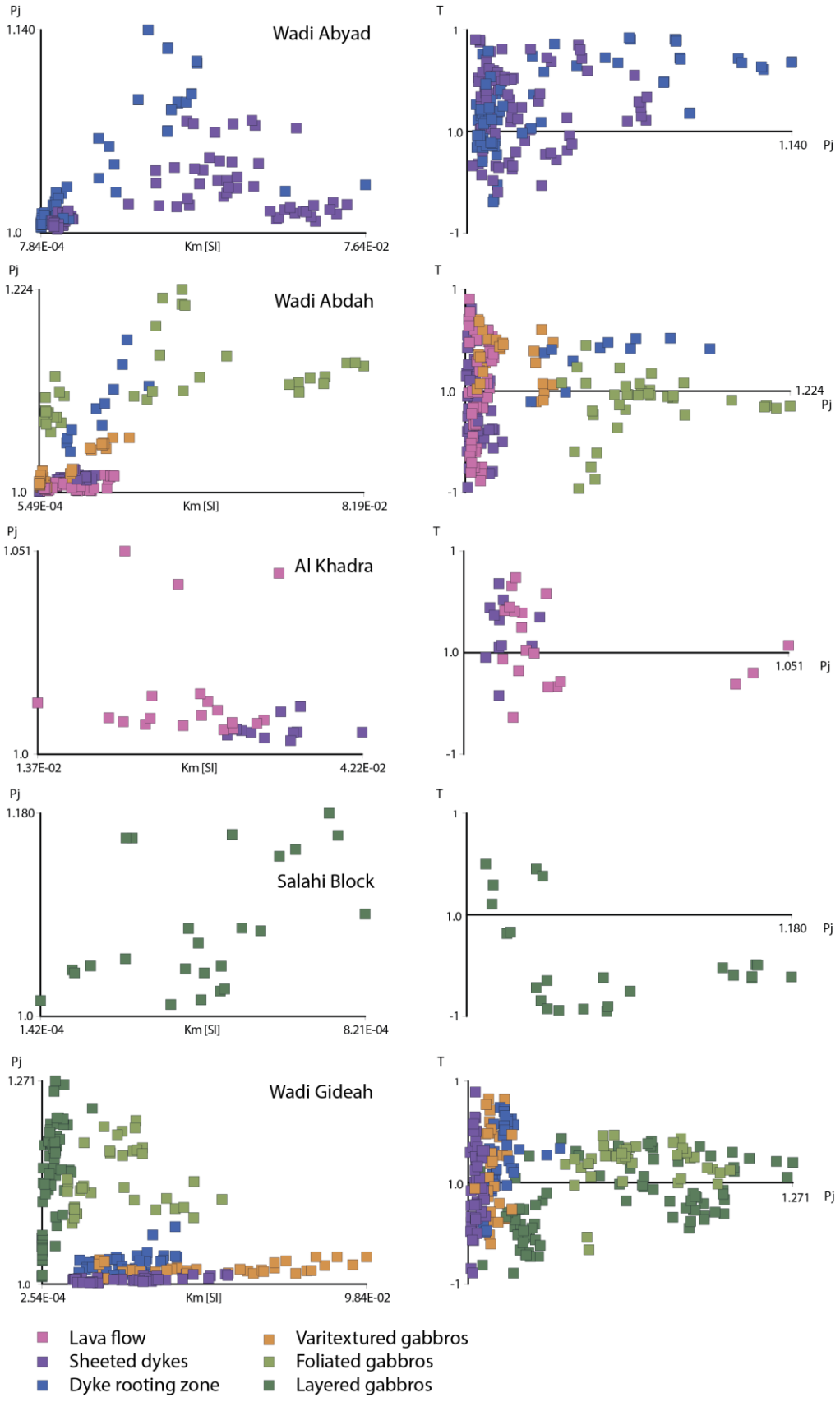

Figure 4.6 – Summary of AMS parameters for each locality and lithology sampled in this study. (Left) Corrected anisotropy degree against mean susceptibility. Mind the different scales on the Y-axes for each plot. (Right) Corrected anisotropy degree against shape parameter.

represent the magnetic lineation in these sites, interpreted to result from magmatic flow during emplacement of the layered gabbros in the lower crust.

(ii) Sites that exhibit triaxial AMS ellipsoids where the K_{max}, K_{int}, and K_{min} form individual clusters (WG01-02, WG05-06, Figure 4.7). In these cases the K_{max} principal axes lie within or close to the plane of layering of the gabbros.

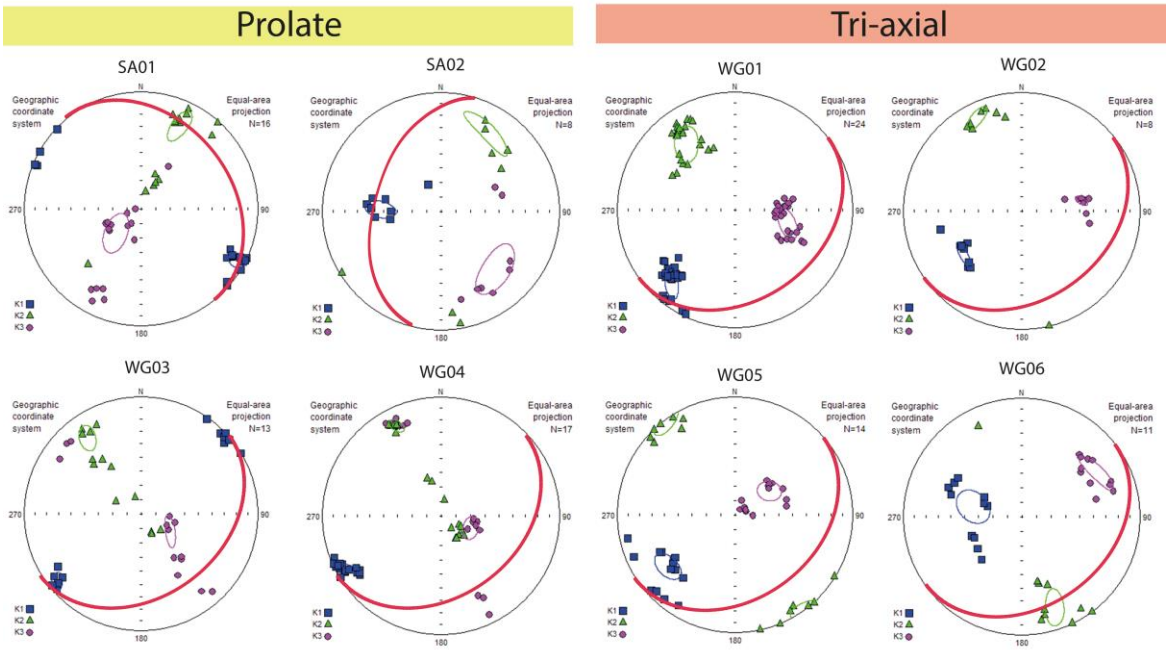

Figure 4.7 – AMS data from layered gabbro sites sampled in the Oman ophiolite. The AMS principal axes are shown as blue squares (K_{max}), green triangles (K_{int}), and pink circles (K_{min}), Jelínek (1978) confidence ellipses are plotted for each principal axis, red great circles show the orientation of the gabbro layering.

4.5.2 – Magnetic fabrics in foliated gabbros

AMS in foliated gabbros was measured at two localities in the southern massifs; Wadi Abdah in the Samail massif and Wadi Gideah in the Ibra massif. Foliated gabbro specimens are displayed as light green squares in Figure 4.6. The

majority of foliated gabbro specimens in Wadi Gideah exhibit triaxial to slightly oblate AMS ellipsoids, whereas the majority of foliated gabbro specimens in Wadi Abdah show triaxial fabrics with a minority group of prolate specimens. Little correlation can be seen between the corrected anisotropy degree P_J and the bulk susceptibility, however P_J does slightly increase with bulk susceptibility.

AMS fabrics in the five foliated gabbro sites may be divided into two groups:

(i) Sites that exhibit triaxial AMS ellipsoids, where the K_{max}, K_{int}, and K_{min} form individual clusters (BD14, WG07-08, Figure 4.8). In all three sites K_{max} lies within or close to the plane of magmatic foliation (red great circles). In the case of site BD14, K_{min} axes also lie in this plane.

(ii) Sites that display complex results (BD13, WG09, Figure 4.8) with no clear relationship to the measured magmatic foliation.

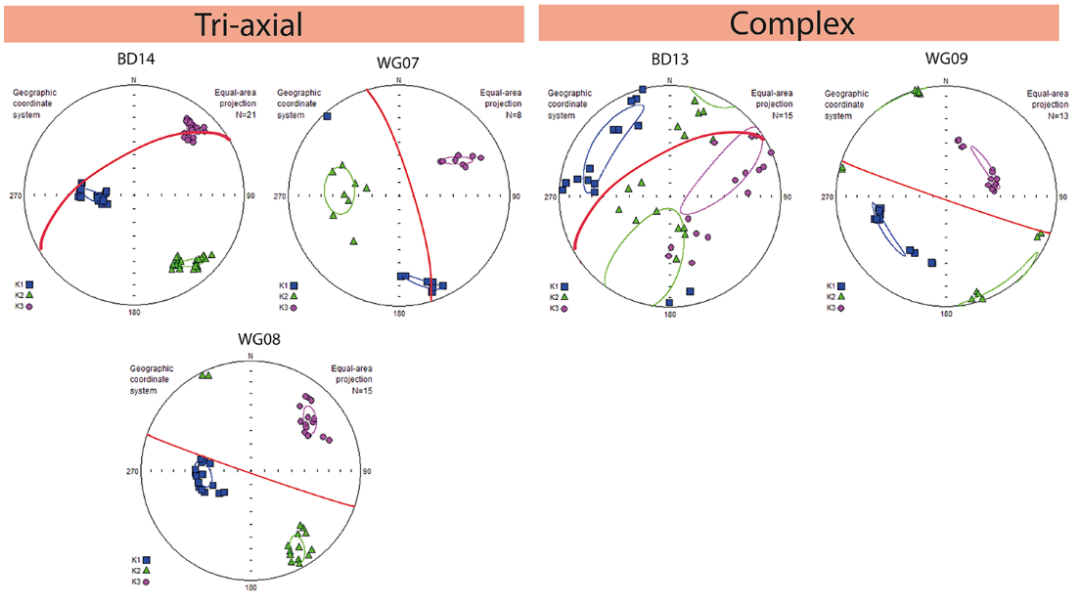

Figure 4.8 – AMS data from foliated gabbro sites sampled in the Oman ophiolite. The AMS principal axes are shown as blue squares (K_{max}), green triangles (K_{int}), and pink circles (K_{min}), Jelínek (1978) confidence ellipses are plotted for each principal axis, red great circles show the orientation of the gabbro foliation.

4.5.3 – Magnetic fabrics in varitextured gabbros

Varitextured gabbros were only sampled in the Wadi Abdah and Wadi Gideah localities. AMS parameters for these rocks are plotted as orange squares in Figure 4.6. Varitextured gabbro specimens from Wadi Abdah generally show oblate to triaxial behaviour with a weak P_J that slightly increases with susceptibility (Figure 4.6). Similar behaviour can be seen for the varitextured gabbros of Wadi Gideah, although here half of the specimens show triaxial behaviour.

At a site-level, the AMS results can be subdivided into three groups (Figure 4.9):

(i) site WG10 that shows a poorly-defined oblate fabric,

(ii) a weakly-defined prolate fabric in site BD10,

(iii) triaxial fabrics in sites BD11 and WG14.

This reflects the complex textures in these gabbros, marked by high variability in grain size, texture and composition over short distances (often on length scales < 1m), that results from the influence of volatiles (mainly water vapour) during the crystallization of these rocks within an axial melt lens (MacLeod and Yaouancq, 2000).

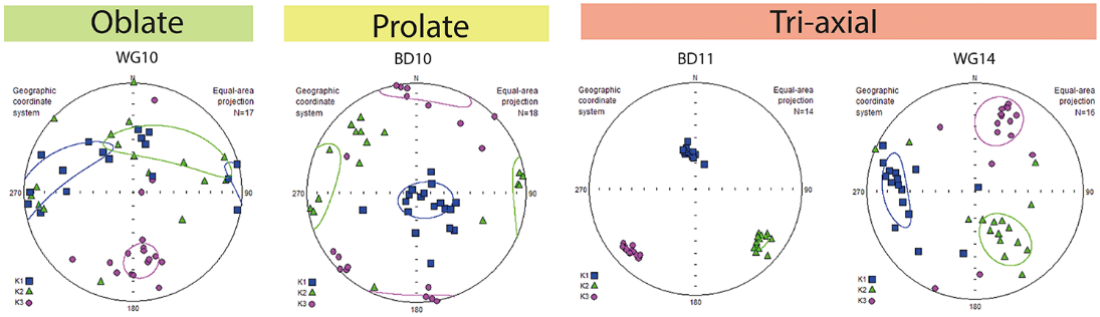

Figure 4.9 – AMS data from varitextured gabbro sites sampled in the Oman ophiolite. The AMS principal axes are shown as blue squares (K_{max}), green triangles (K_{int}), and pink circles (K_{min}), Jelínek (1978) confidence ellipses are plotted for each principal axis.

4.5.4 – Magnetic fabrics in the dyke rooting zone and sheeted dykes

The dyke rooting zone was thoroughly sampled and studied in Wadi Abyad, given its importance to analysis of the remagnetization of the ophiolite, and was also sampled in Wadi Abdah and Wadi Gideah. In addition, sheeted dykes were sampled at these localities and a single dyke was sampled at Al Khadra. The majority of specimens from the sheeted dyke and dyke rooting zone sites display oblate AMS ellipsoids with a maximum T = 0.90 (Table 4.1; Figure 4.6). A limited number of specimens in these sites display prolate and triaxial behaviour.

In Wadi Abyad and Wadi Abdah, a clear correlation can be seen between the corrected anisotropy degree P_J and the bulk susceptibility; the value of P_J increases as the bulk susceptibility increases, indicating that the anisotropy strength is dependent on the concentration of ferromagnetic particles in these rocks (Figure 4.6).

The AMS fabrics are compared to dyke orientations measured in the field in Figure 4.45, and may be subdivided into four groups:

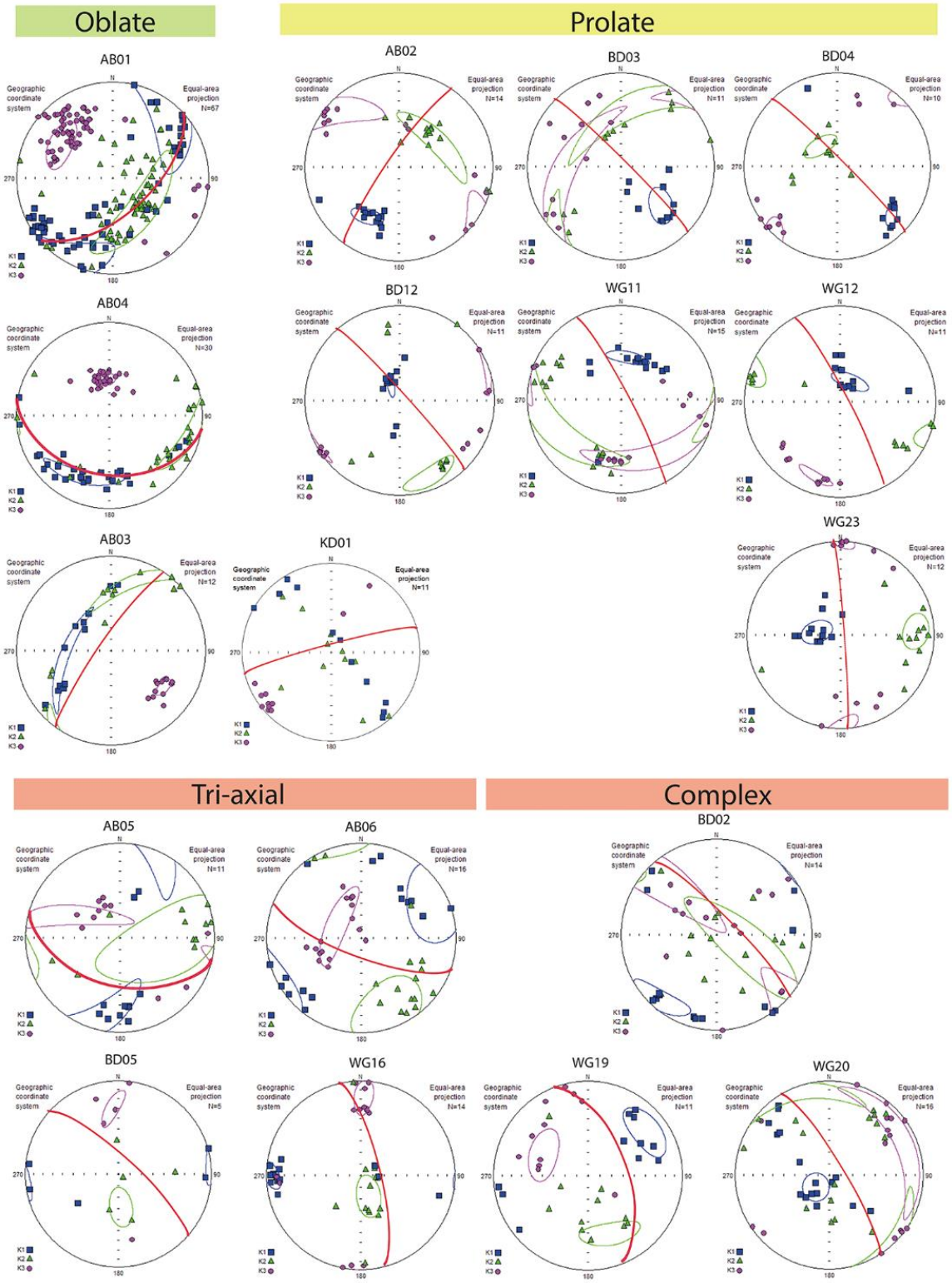

Figure 4.10 – AMS data from dyke sites sampled in the Oman ophiolite. The AMS principal axes are shown as blue squares (K_{max}), green triangles (K_{int}), and pink circles (K_{min}), Jelinek (1978) confidence ellipses are plotted for each principal axis, red great circles show the orientation of the dykes.

(i) Sites that show oblate AMS ellipsoids where K_{max} and K_{int} define a great circle girdle (AB01, AB03-04, KD01, Figure 4.10). In the case of the three sites from Wadi Abyad, K_{max} and K_{int} axes almost perfectly lie within the dyke plane, with K_{min} axes close to the pole to the dyke. The magnetic fabrics are aligned with the foliation of the dykes. In contrast, the oblate fabric at site KD01 does not show any correlation with the dyke orientation.

(ii) Sites that show prolate AMS ellipsoids where K_{int} and K_{min} form a great circle girdle and K_{max} is found as a cluster within or close to the dyke plane (AB02, BD03-04, BD12, WG11-12, WG23, Figure 4.10).

(iii) Sites with triaxial AMS ellipsoids (AB05-06, BD05, WG16, Figure 4.10) showing variable or no correlation with dyke orientations.

(iv) Sites that neither show individual clusters nor clear girdle distributions (BD02, WG19-20, Figure 4.10) that are described as complex sites.

4.5.5 – Magnetic fabrics in lavas

Lava flows were extensively sampled at the Wadi Abdah and Al Khadra localities, but were not exposed elsewhere. Lava specimens are plotted as pink squares in Figure 4.6. Specimens from the lava flows of Wadi Abdah show both prolate and oblate behaviour with no correlation found between the P_J and bulk susceptibility (Figure 4.6). No correlation is found between P_J and bulk susceptibility for sites from Al Khadra either, and the T versus P_J diagram shows that specimens with a higher P_J tend to have prolate fabrics.

The AMS results were plotted against the lava flow orientations (Figure 4.11) and divided into two groups:

(i) Sites that show oblate fabrics. At site BD08, the lava flow orientation roughly correlates with the girdle distribution of K_{max} and K_{int} principal axes, and K_{min} axes lying close to the pole to the lava flow. In the case of site BD07, there is a mismatch between the orientation of the lava flow and a girdle distribution of K_{max} and K_{int} principal axes; this could be due to local variability in internal fabrics within the lava flows.

(ii) Sites BD09 and KD02-03 that show prolate fabrics. In these cases, there is a weak correspondence between the lava flow orientations and girdle distributions of K_{int} and K_{min} axes, with K_{max} axes near the pole to the lava flow.

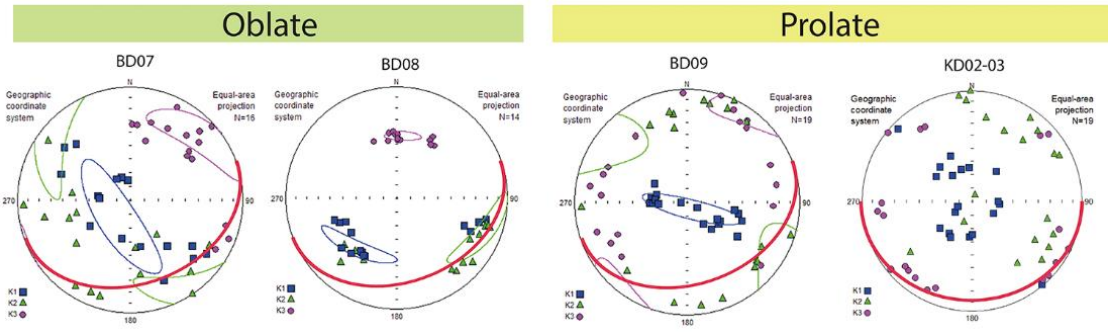

Figure 4.11 – AMS data from lava sites sampled in the Oman ophiolite. The AMS principal axes are shown as blue squares (K_{max}), green triangles (K_{int}), and pink circles (K_{min}), Jelínek (1978) confidence ellipses are plotted for each principal axis, red great circles show the orientation of the lava layering.

4.5.6 – Insights into geological processes from magnetic fabrics

The most informative AMS results in this study come from the layered gabbros (Wadi Gideah and Salahi massif) and the dyke rooting zone/sheeted dyke

complex (Wadi Abyad, Abdah and Gideah). Figure 4.12 shows the distributions of K_{max} principal axes from these pseudostratigraphic levels in relation to corresponding structural orientations (plotted as black lines).

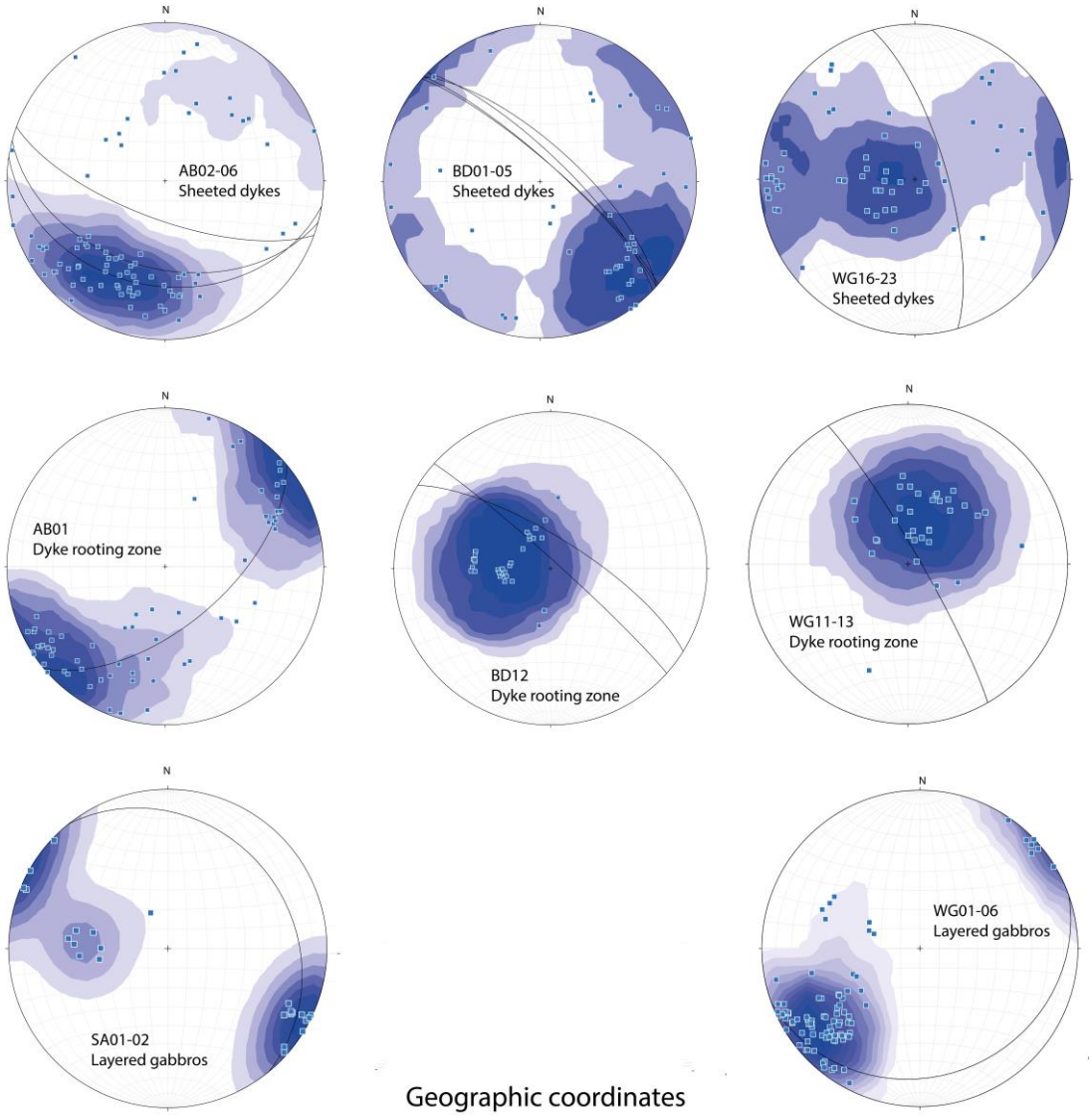

Figure 4.12 – Equal area stereographic projections of the AMS K_{max} principal axis for the sheeted dykes, dyke rooting zone, and layered gabbro sites of this study. Great circles show the orientation of the dykes and the Moho orientation measured close to the layered gabbros respectively.

The layered gabbros sampled in this study show magnetic fabrics that are parallel to the measured magmatic layering, with maximum AMS principal axes aligned sub-horizontally within the plane of layering in the gabbros (Figure 4.12).

The data form a SW-oriented cluster in Wadi Gideah and a SE-NW-trending cluster in the Salahi massif. Similar fabrics from layered gabbros in Wadi Abyad and Wadi Khafifah have been recently reported by Meyer (2015) and Morris et al. (2019). These data can be compared to regional-scale magmatic lineations mapped across the ophiolite by Nicolas et al. (2000). For example, Figure 4.13 shows a structural map of the southern half of the Oman ophiolite that shows lineation trajectories as red lines based on a compilation of thousands of field measurements of lineations (Nicolas et al., 2000). A NW-SE oriented ridge axis (dotted line) was inferred from these lineations (Figure 4.13).

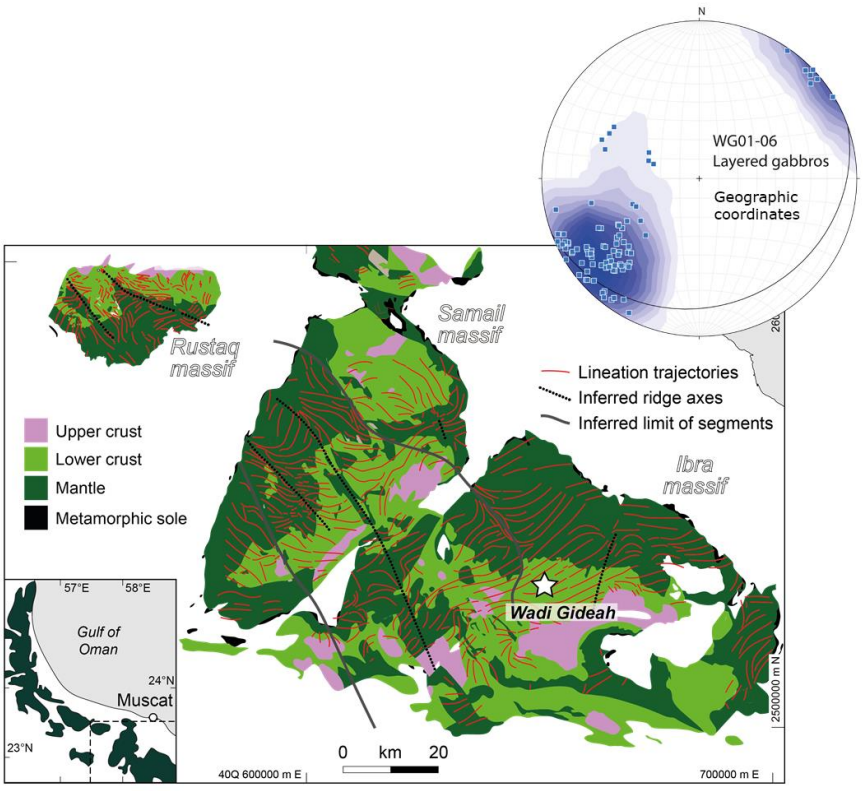

Figure 4.13 – Equal area stereographic projection of the AMS K_{max} principal axis of the layered gabbros of Wadi Gideah against a structural map of the southern massifs of the Oman ophiolite (from Nicholas et al., 2000). Red lines represent the lineation trajectories, black lines the inferred ridge axis. Note how the NE-SW lineation trajectories correlate with the measured K_{max} orientation.

A stereographic projection of the combined K_{max} axes from the layered gabbro sites in Wadi Gideah in geographic coordinates (location shown by a star symbol on the map) demonstrates an excellent correlation with the lineation trajectories measured in the field, which trend NE-SW orthogonal to the inferred orientation of the ridge axis. A similar correlation is seen with mapped lineation trajectories in the Salahi massif (not shown). This suggests that the magnetic lineation in these sites results from regional-scale magmatic flow away from the spreading ridge. An alternative explanation is that the coaxial K_{max} axes and structural lineations result from drag-induced shearing of a crystal mush during overturning of the mantle beneath the spreading ridge.

The K_{max} axes of the dyke rooting zones and sheeted dyke complexes measured at Wadi Abyad, Wadi Abdah and Wadi Gideah all show clear relationships with the measured dyke orientations (Figure 4.12). K_{max} axes at these sites lie within or close to the dyke plane, suggesting alignment of magnetic minerals during dyke emplacement. However, K_{max} axes vary in their plunge between localities, suggesting that magmatic flow in the dykes could have happened either horizontally or vertically during emplacement. Similar variability in inferred emplacement directions of sheeted dykes has been documented in the slow-spreading rate Troodos ophiolite (Staudigel et al., 1992), where imbrication of AMS fabrics along opposing dyke margins allowed determination of initial emplacement kinematics.

Finally, palaeomagnetic analysis of the southern massifs of the ophiolite (this study – Chapters 5 and 6; Feinberg, 1999; Meyer, 2015; Morris et al., 2016)

indicates that all of the rocks sampled in this study (excluding the Salahi massif) have been remagnetised during emplacement of the ophiolite onto the Arabian continental margin in the Late Cretaceous. The correspondence between magnetic fabrics (that are dominated by (titano)magnetite in these rocks due to its high susceptibility) and macroscopic magmatic structures (layering and dyke orientations) (Figure 4.14), therefore, suggests that the distribution and shape preferred orientation of any new ferromagnetic grain assemblages produced during remagnetization were largely controlled by pre-existing silicate petrofabrics.

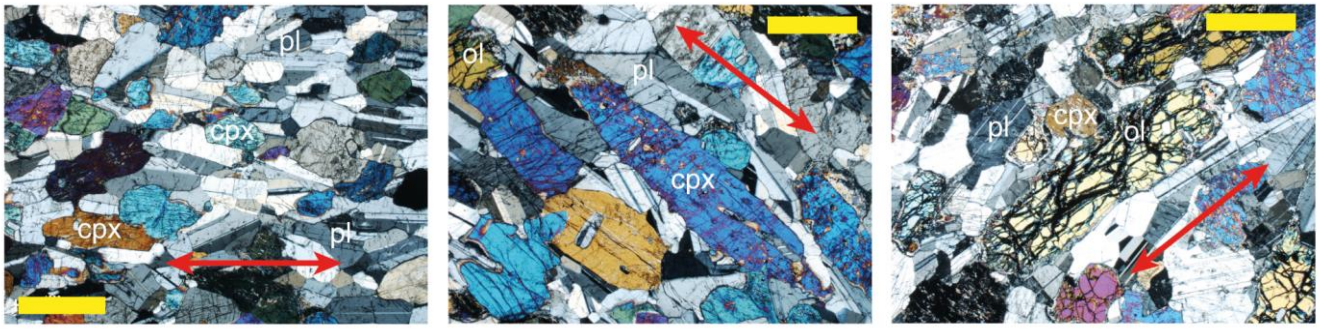

Figure 4.14 - Photomicrographs of thin sections of layered gabbros from Wadi Abyad, showing correlation of K_{max} axes (red arrows) with preferred orientations of silicate crystals and of secondary magnetite in olivine crystals (bottom). Yellow scale bars = 1.0 mm. From Morris et al. (2019).

4.6 – Summary

Rock magnetic experiments and magnetic fabric analysis provide information about the mineralogy of the magnetic minerals that carry the remanence magnetization, about their grain sizes, and about their shape and orientation. Both unblocking temperatures and Curie temperatures suggest that (titano-)magnetite is the main carrier of the magnetic signal in the sampled rocks.

Anisotropy of magnetic susceptibility suggests that the magnetic fabrics in these rocks reflect magmatic fabrics formed during accretion of the Oman ophiolite by seafloor spreading, with lower crustal layered gabbro fabrics controlled either by magmatic flow during emplacement or by deformation of crystal mushes during plate divergence, and dyke fabrics controlled by variable emplacement directions during formation of the upper crust.

Chapter 5 - Palaeomagnetic results

5.1 – Introduction

The main aims of this research are to determine the extent and nature of remagnetization of the southern massifs of the Oman ophiolite and whether any primary magnetizations survive in this region. Earlier palaeomagnetic studies in Oman have highlighted a dichotomy of remanence directions across the ophiolite (as discussed in Chapter 2). SE-directed magnetizations in the northern massifs are accepted to represent primary (seafloor) magnetizations that have been highly rotated in a clockwise sense during the evolution of the ophiolite (e.g. Perrin et al, 1994, 2000). This contrasts with predominantly NW/NNW-directed magnetizations in the southern massifs that have been interpreted either as primary magnetizations that reflect a different rotation history between the northern and southern massifs (e.g. Thomas et al., 1988; Weiler, 2000), or secondary magnetizations acquired during emplacement of the ophiolite (Feinberg et al., 1999). More recently, Meyer (2015) and Morris et al. (2016) identified a transition in directions upwards through the crust in Wadi Abyad that supported the remagnetization hypothesis and suggested that higher crustal levels (across the dyke-gabbro transition) in the southern massifs might preserve clockwise rotated primary magnetizations.

This chapter presents the results of the palaeomagnetic analyses conducted on samples from four localities in the Ibra, Semail and Rustaq massifs

in the region inferred to have experienced remagnetization based these on previous studies. These are compared to a control locality in the northern Salahi massif, outside the zone of inferred remagnetization. The remanence characteristics of specimens subject to detailed demagnetization experiments are presented first, followed by the distributions of site mean directions of magnetization based on principal component analysis of the demagnetization data. These new results are then interpreted and placed in the context of the published palaeomagnetic database from Oman and the timing, extent and nature of remagnetization are discussed. Finally, a net tectonic rotation analysis of data from sites believed to carry primary magnetizations is presented to aid tectonic interpretation of the ophiolite.

5.2 – NRM Intensities

The specimens collected for this study show a wide range of remanence intensities, from ~10^{-3} A/m for many of the sheeted dykes and layered gabbros to very high intensities >10 A/m for some dykes and lava flows. The intensities of all specimens, arranged by lithology, are shown in the histograms of Figure 5.1. The range of intensities found in this study is comparable to that of previous studies of the Oman ophiolite (e.g. Luyendyk et al., 1982a, 1982b; Thomas et al., 1998; Perrin et al., 1994, 2000; Weiler, 2000; Feinberg (1999); Meyer (2015); van Hinsbergen et al.,2019). They are also comparable to the range of NRM intensities reported from studies of samples from the crust in the modern oceans (e.g. Gee

and Kent, 2007). The only exceptions come from two sheeted dyke sites (W16 and W20) from the Wadi Gideah locality, which contain specimens with intensities between 10 and 372 A/m. These two sites are believed to have been struck by lightning, as explained later in this chapter, and these intensities should therefore not be regarded as ancient NRM intensities. All specimens inferred to be affected by lightning are coloured black in the intensity histograms in Figure 5.1.

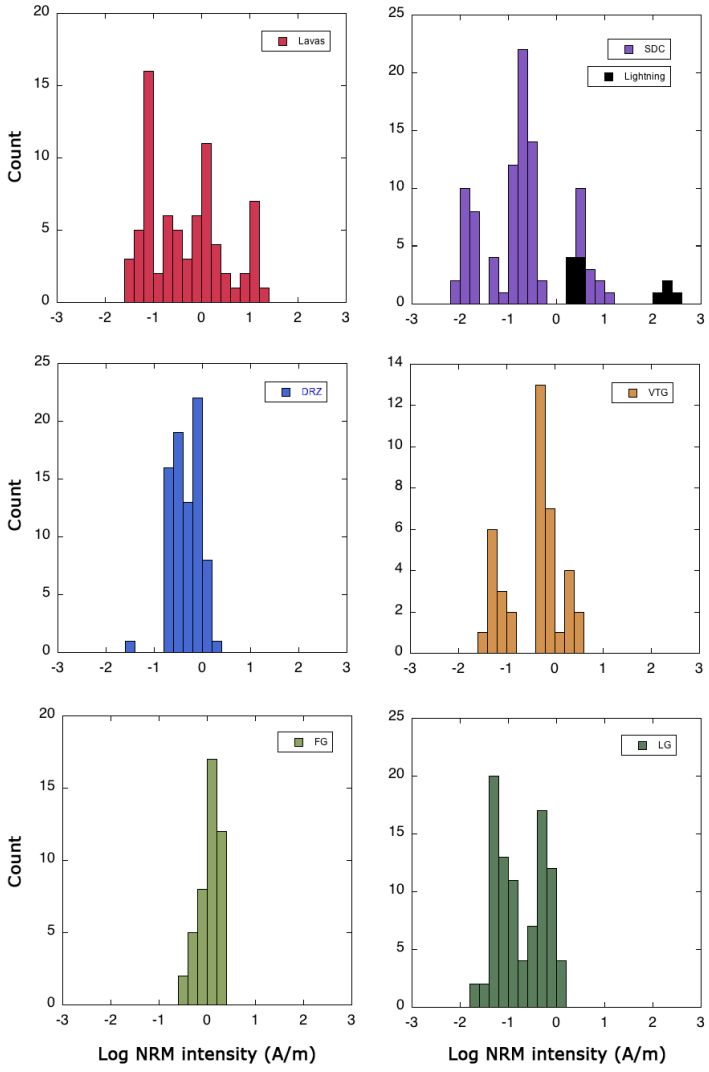

Figure 5.1 – Histograms of the NRM intensities for each pseudostratigraphic level sampled in the Oman ophiolite. SDC = sheeted dyke complex; DRZ = dyke rooting zone; VTG = varitextured gabbros; FG = foliated gabbros; LG = layered gabbros.

5.3 - Demagnetization results

Alternating field or thermal demagnetization can reveal characteristic remanent magnetization (ChRM) components in specimens that can then be used in subsequent analyses. Rocks, however, can contain multiple components where the ChRM may be partly overprinted or hidden by a secondary, younger component. These components are typically carried by grains with lower relaxation times than the ChRM (Tauxe et al., 2010), resulting in lower coercivities during AF treatment and lower unblocking temperatures during thermal demagnetization.

The majority of specimens in this study were subjected to thermal demagnetization (which proved more effective in previous studies), but at least one specimen per hand sample was treated using AF demagnetization for comparison. Representative orthogonal vector plots (Zijderveld, 1967) are presented for all five localities of this study in Figures 5.2 to 5.6. Zijderveld plots are grouped by location (Wadi Abyad, Wadi Abdah, Wadi Gideah, Al Khadra, and the Salahi Massif) and include examples of both thermally and AF demagnetised specimens in geographic coordinates. Remanence components were isolated via principal component analysis (Kirschvink, 1980) using the software "MacPaleomag" written by Jeff Gee (see Section 3.8). Components were picked where points in the Zijderveld plots formed straight lines, with MAD angles ≤ 10°. ChRM components were chosen as components with the highest coercivity or unblocking temperature where these lines pointed towards the origin.

5.3.1 – Characteristic remanent magnetizations of Wadi Abyad

AF demagnetization of specimens from the dyke rooting zone of Wadi Abyad resulted in clear and straightforward demagnetization paths (e.g. AB0105A; Figure 5.2). Most specimens lost more than 90% of their NRM by the maximum applied field of 100 mT, with only a few specimens retaining up to 50% of their NRM. In the sheeted dykes, AF treatment resulted in similar behaviour but with less linear demagnetization paths (e.g. AB0401A; Figure 5.2). All specimens subjected to thermal demagnetization generally showed more complex and often curved demagnetization paths in both the dyke rooting zone and the sheeted dykes (e.g. AB0111B and AB0503C; Figure 5.2), but still yielded clear ChRMs to the origin at higher temperature steps. Magnetizations are in all cases destroyed by 580°C, which suggests that magnetite is likely to be the main carrier of the NRM (Tarling, 1983). The majority of specimens also display a north-directed secondary component removed by 10 mT or 250°C that is close to the present day field (PDF) direction in Oman (International Geomagnetic Reference Field = 001.4/35.6°). ChRM directions show significantly different declinations and inclinations from these more recent overprints and are considered to be ancient remanences. The same logic is applied to the four other localities.

ChRMs picked for the six Wadi Abyad sites give varied results in terms of their direction. Specimens from the dyke rooting zone (site AB01) predominantly give easterly-directed ChRMs with moderate inclinations, with similar results from AF and thermal treatment. The sheeted dykes that overlie the dyke rooting zone show ChRM directions that are more ESE, in particular sites AB02, 04, and

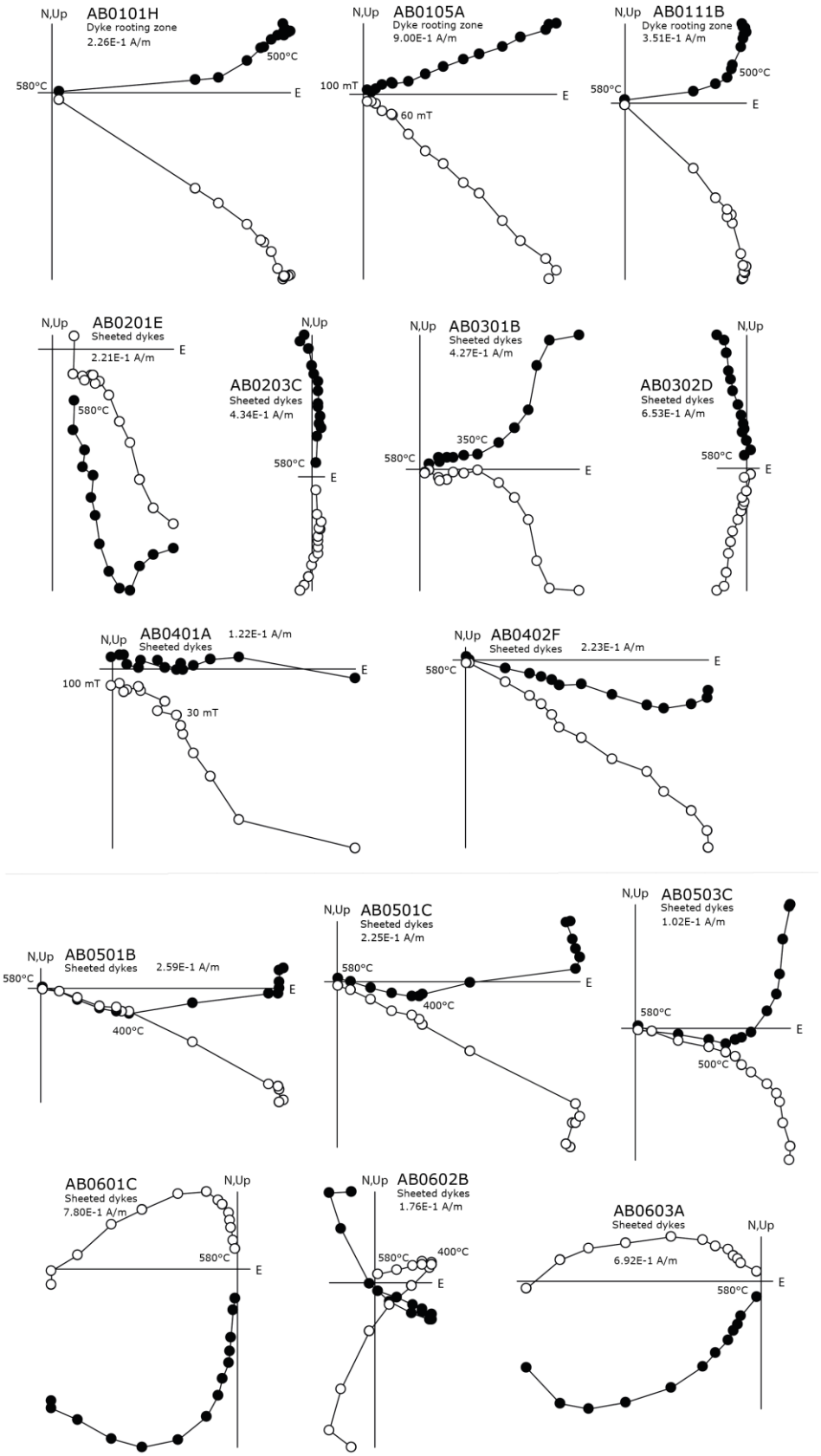

Figure 5.2 - Representative Zijderveld diagrams of both alternating field and thermal demagnetization for specimens from Wadi Abyad (geographic coordinates). Steps are shown in °C for thermal demagnetization or mT for alternating field demagnetization.

05. An exception is site AB03, which shows ChRM directions similar to the dyke rooting zone. In the case of sites AB02 and AB03, 80% of specimens are completely overprinted in the PDF direction. These specimens were rejected from further analysis, but were retained in a dataset of PDF magnetizations. The remaining specimens show ChRMs similar to sites AB04 and 05. Specimens from site AB06 display curvilinear demagnetization paths that do not reach stable endpoints but instead define great circle demagnetization paths on stereographic projections (e.g. AB0601C; Figure 5.2). Specimens from site AB05 also define great circle demagnetization paths, however these do have a clear endpoint. Both sites are used in a great circle analysis and described later in this chapter.

5.3.2 – Characteristic remanent magnetizations of Wadi Abdah

Determination of ChRMs for Wadi Abdah is very straightforward as the majority of specimens have a shallowly inclined NW-NNW-directed magnetization (Figure 5.3). This includes all specimens from the lowest foliated gabbros (sites BD13-14), varitextured gabbros and dyke rooting zone (sites BD10-12) to the sheeted dykes at the top of the section (sites BD01-05). The only sites behaving differently are the lava flows from sites BD06 to BD08, which display NW-directed ChRMs, but with a more moderate, negative inclination. It is notable that some sites in Wadi Abdah have considerably higher unblocking temperatures compared to sites from Wadi Abyad, with specimens from site BD04 (sheeted dykes) retaining around 80% of their magnetization until 640°C. Magnetization in

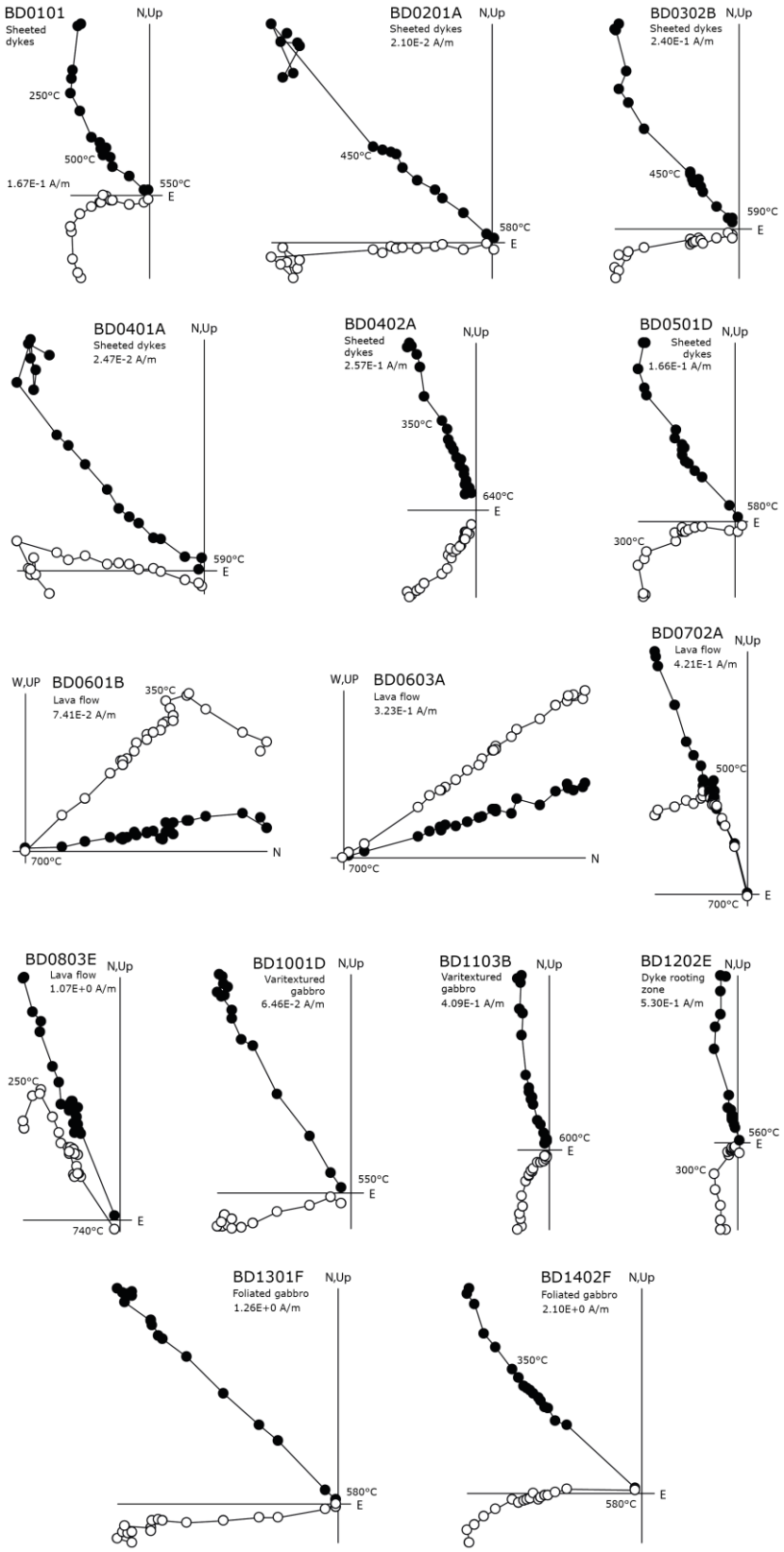

Figure 5.3 - Representative Zijderveld diagrams of both alternating field and thermal demagnetization for specimens from Wadi Abdah (geographic coordinates). Steps are shown in °C.

the lava flows of sites BD06-08 decays rapidly at even higher temperatures, in many cases reaching 700-740°C. This suggests that a mineral with a high unblocking temperature might be one of the carriers of the NRM in these specimens. The remaining sites and specimens show a more gradual decay and lose the majority of their magnetization by 580°C. Just like in Wadi Abyad, many specimens display a small, northerly-directed secondary overprint that is removed by 250°C and is interpreted as a PDF overprint.

5.3.3 – Characteristic remanent magnetizations of Al Khadra

ChRM directions in the section sampled at Al Khadra display a moderately inclined, NE-directed magnetization (sites KD01 and KD03, Figure 5.4). The majority of specimens from the lava flow sampled at site KD02 were completely overprinted by a north-directed PDF component (e.g. KD0201A and KD0201D in Figure 5.4), but remaining specimens from this site show the same NE direction as the dyke and lava flow from sites KD01 and KD03 (e.g. KD0202B; Figure 5.4). All AF specimens showed single-component decay of the magnetization to the origin with very low coercivities (< 40 mT). Unblocking temperatures vary between the dyke (site KD01) and lava flows (sites KD02 and KD03), being 580°C for the dyke and between 580-640°C for the lava flows. This suggests that different magnetic carriers might be present in these samples. A small PDF overprint is found in half of the thermally demagnetised specimens from KD01/03 and is removed by 250°C, yet is absent in any of the AF demagnetised specimens.

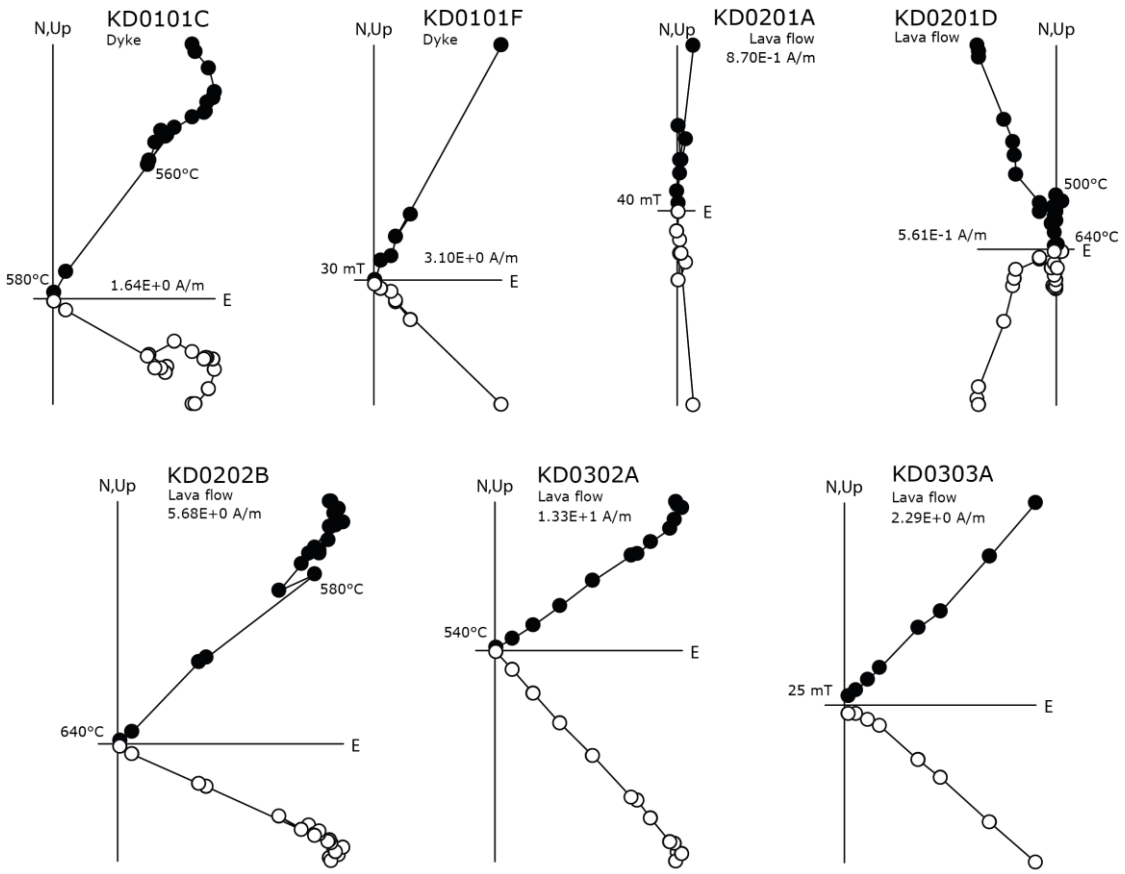

Figure 5.4 - Representative Zijderveld diagrams of both alternating field and thermal demagnetization for specimens from Al Khadra (geographic coordinates). Steps are shown in °C for thermal demagnetization or mT for alternating field demagnetization.

5.3.4 – Characteristic remanent magnetizations of Wadi Gideah

Demagnetization characteristics of specimens from Wadi Gideah are very similar to those seen in Wadi Abdah, with a dominant NW-directed ChRM and shallow inclinations for all lithologies from layered gabbros to sheeted dykes (Figure 5.5). Specimens generally show a clear component going to the origin that can be slightly curved or noisy in thermally treated specimens; AF specimens are always straight. Both AF and thermal specimens show a small secondary, north-directed PDF overprint that in most cases is removed by 10 mT or 250°C.

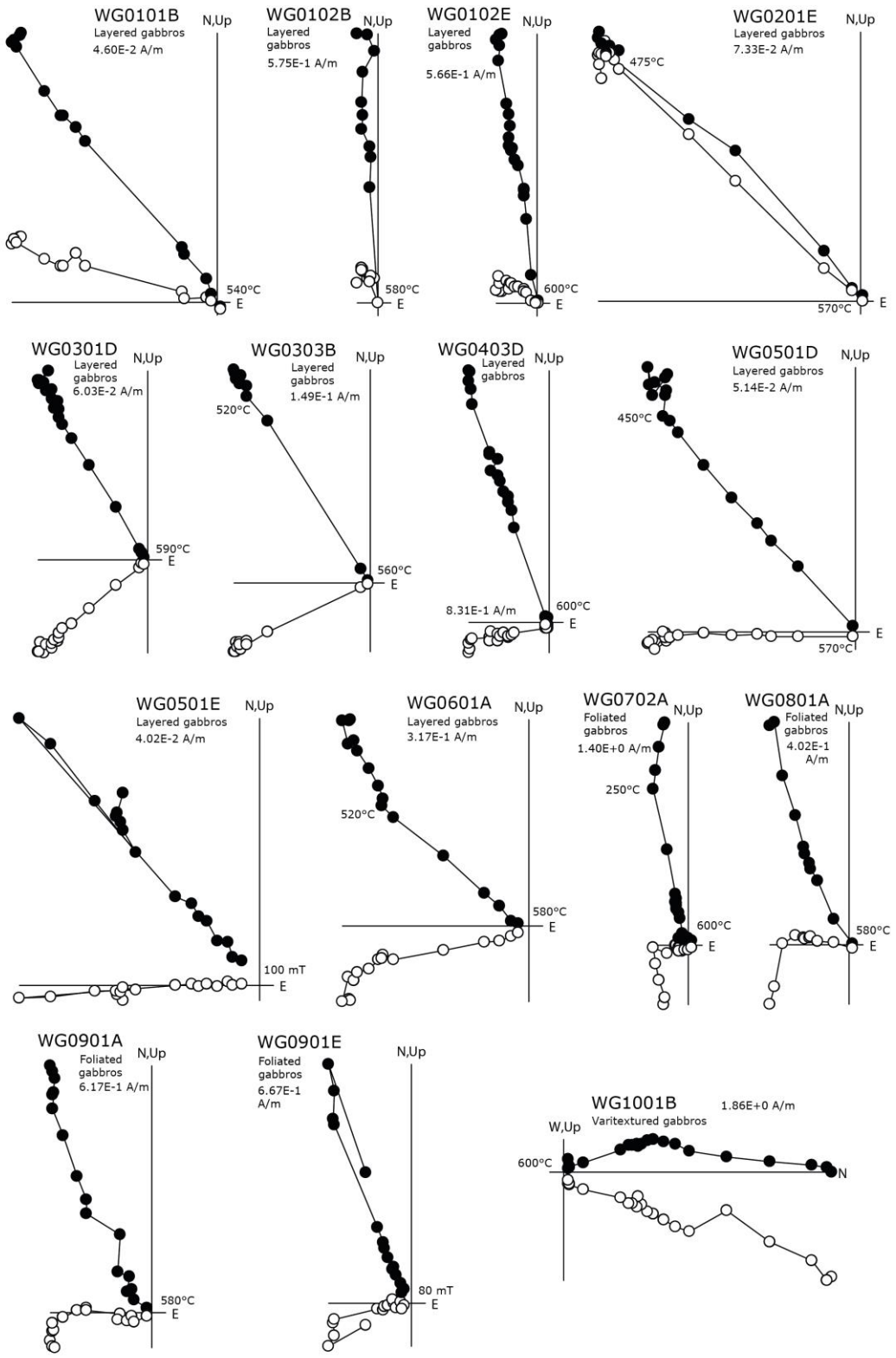

Figure 5.5 - Representative Zijderveld diagrams of both alternating field and thermal demagnetization for specimens from Wadi Gideah (geographic coordinates). Steps are shown in °C for thermal demagnetization or mT for alternating field demagnetization.

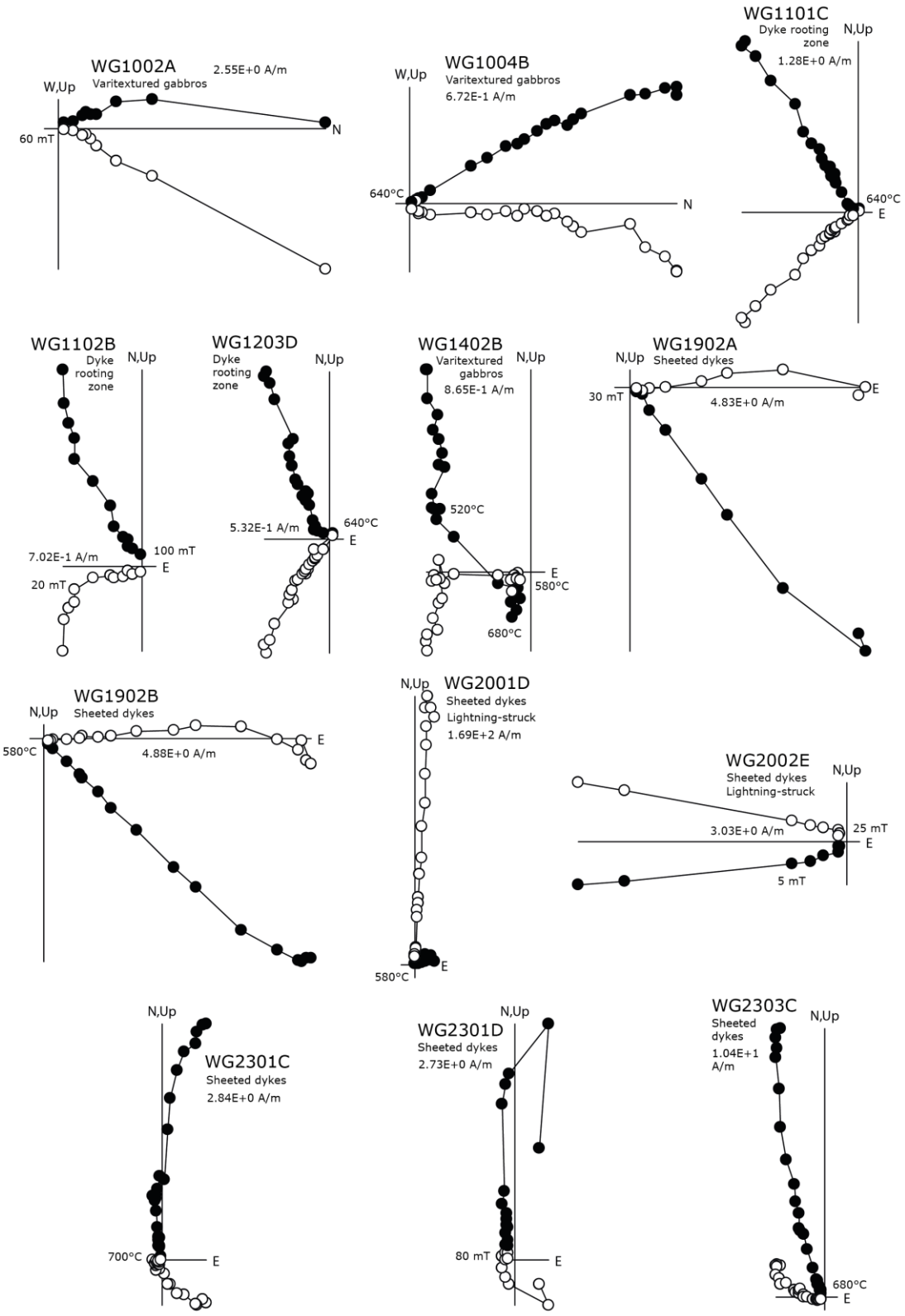

Figure 5.5 (cont.) - Representative Zijderveld diagrams of both alternating field and thermal demagnetization for specimens from Wadi Gideah (geographic coordinates). Steps are shown in °C for thermal demagnetization or mT for alternating field demagnetization.

Two sheeted dyke sites, WG16 and WG20 had to be disregarded from further analysis as they are believed to have been affected by lightning. Evidence for this is: (i) exceptionally high intensities, reaching magnitudes of more than 150 A/m; (ii) geologically implausible vertical ChRM directions (e.g. WG2001D, Figure 5.5); and (iii) very rapid AF decay of the magnetization, losing most of magnetization by 15 mT (e.g. WG2002E, Figure 5.5). Another sheeted dyke site, WG19, proved to have very scattered and noisy demagnetization behaviour, with only specimen WG1902 displaying a coherent demagnetization path, directed towards the southeast.

5.3.5 – Characteristic remanent magnetizations of the Salahi Massif

Layered gabbros from the Salahi Massif, i.e., in at the control locality in the northern massifs of the Oman ophiolite outside the zone of inferred remagnetization, show SE-directed, moderately inclined ChRMs (Figure 5.6). The decay of magnetization begins at ~475°C in thermally treated specimens, with maximum unblocking temperatures of 580°C. AF treated specimens lose their magnetization gradually and all magnetization is gone by 80 mT. No secondary components are observed in any specimens, instead all specimens show a single component to the origin.

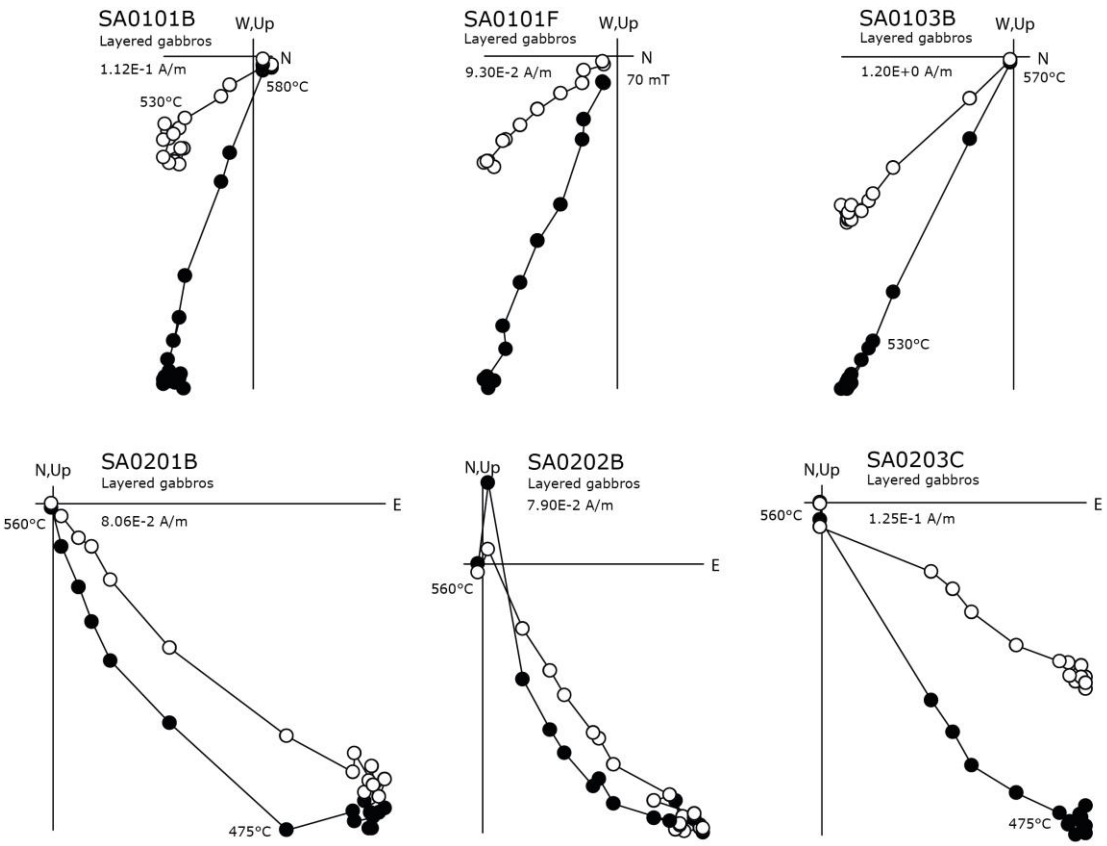

Figure 5.6 - Representative Zijderveld diagrams of both alternating field and thermal demagnetization for specimens from Salahi massif (geographic coordinates). Steps are shown in °C for thermal demagnetization or mT for alternating field demagnetization.

5.3.6 – Present day field components

All secondary components that were picked from the five localities were combined in one stereographic projection in order to compare the results with the calculated IGRF for Oman (declination/inclination = 001.4/35.6°). The results are shown in Figure 5.7a and display a cluster surrounding the IGRF direction. The scatter in these directions is comparable to that generated by the TK03 statistical model of the geomagnetic field (Tauxe and Kent, 2004; dark blue in Figure 5.7b), and may therefore be attributed to palaeosecular variation.

Specimens from Wadi Abyad sites AB05 and 06 (sheeted dykes) contain great circle paths that provide further evidence for a secondary PDF overprint.

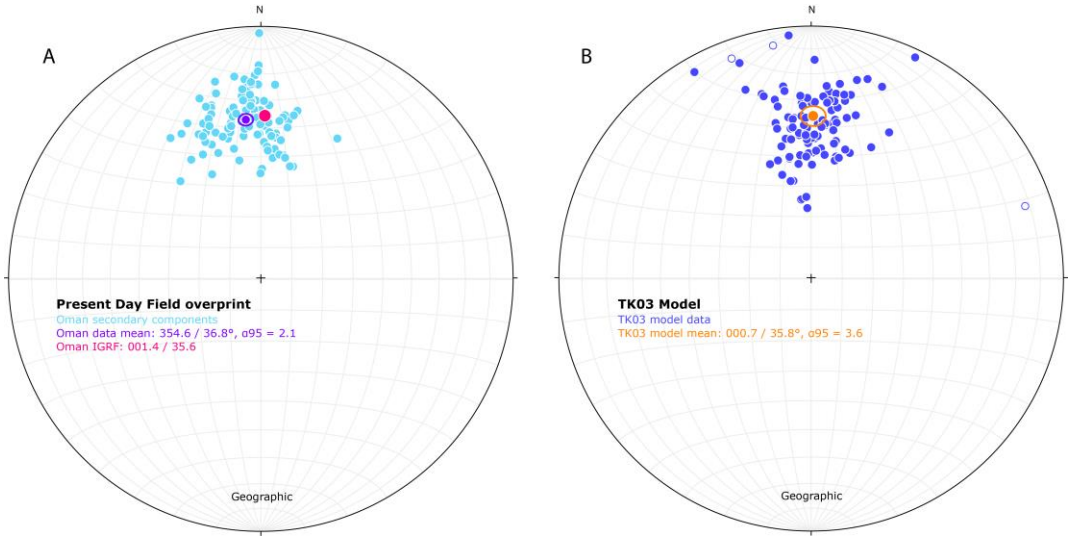

Figure 5.7 – Equal area stereographic projection in geographic coordinates showing (a) the distribution of secondary components of all combined sites with a NNW declination and mean inclination of 36.5°, close to the Oman IGRF (red dot), (b) TK03 model distribution with a northern mean direction and inclination of 35.8°. Notice how similar the model results are to the measured secondary components.

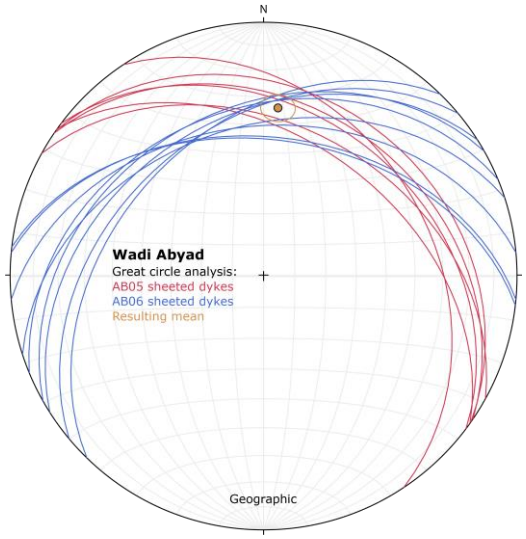

Figure 5.8 – Equal area stereographic projection in geographic coordinates showing the results of great circle analysis on the sheeted dykes of Wadi Abyad. Notice how the resulting mean direction compares to the calculated means of the measured secondary components and TK03 model results in Figure 5.7, suggesting that these dykes are overprinted by the present day field.

Using the method of McFadden and McElhinny (1988), these great circle paths in geographic coordinates suggest a mean overprint direction of 004.9/33.9° (n = 15) that is close to the IGRF direction of 001.4/35.6° (Figure 5.8).

5.4 - Site-level characteristic remanent magnetizations

Prior to calculating site mean directions, ChRM components with maximum angular deviation (MAD) angles >10° were considered unreliable and rejected from further analysis. Four sites had too few acceptable ChRM picks to allow calculation of mean directions. Across all remaining sites, 393 specimen ChRM directions were then used to calculate site mean directions of magnetization and associated Fisher (1953) statistics, all of which have α_{95} cones of confidence < 15° and Fisher precision parameters (k) > 15.

Table 5.1 lists the site mean magnetization directions from the five main localities in both geographic and tilt corrected coordinates in pseudostratigraphic order down the section. Figures 5.9 and 5.12 show these mean directions on stereographic equal area projections. The Wadi Abdah and Wadi Gideah crustal sections are seen to be dominated by consistently NNW-NW-directed magnetizations, in contrast to the sheeted dykes and dyke rooting zone sampled near the top of the Wadi Abyad section and the layered gabbros in the Salahi massif (control section) that display ENE/ESE-directed and ESE/SSE-directed magnetizations, respectively. The more limited data from the Al Khadra lavas and dyke have NE-directed remanences. These data are discussed and interpreted by locality below.

Table 5.1 - Site-level mean magnetization directions from the five localities studied in this research, in geographic and tilt coordinates. n = number of specimens; N = total number of specimens; Dec = declination; Inc = inclination; a95 = 95% cone of confidence; k = Fisher precision parameter; R = resultant vector.

Site	Lithology	n/N	Geographic coordinates Dec / Inc		Tilt corrected Dec / Inc		α_{95}	k	R	UTM	Easting	Northing
Wadi Abyad (Rustaq massif / Nakhl block):												
AB02	Sheeted dykes	2/11	159.2	0.1	154.7	18.7			2.0	40Q	569056	2597796
AB03	Sheeted dykes	2/11	77.1	3.2	80.4	-19.0			2.0	40Q	569056	2597796
AB04	Sheeted dykes	26/29	102.4	24.7	92.8	11.1	4.1	48.8	25.5	40Q	569091	2597969
AB05	Sheeted dykes	7/9	105.7	15.3	100.2	4.6	4.5	185.0	7.0	40Q	569098	2597990
AB06	Sheeted dykes	2+9 GCA/12	151.2	-38.4	144.8	-9.5	12.1	15.3	10.3	40Q	569118	2598070
AB01	Dyke Rooting Zone	57/60	80.1	39.8	68.5	15.7	1.7	121.8	56.5	40Q	569636	2597099
Tilt correction (dip direction/dip): 032/32 - Moho												
Wadi Abdah (Samail massif / Semail block):												
BD06	Lava flow	15/16	345.2	-35.0	346.2	-6.1	3.9	99.2	14.9	40Q	628006	2555427
BD07	Lava flow	11/11	338.0	-35.1	340.3	-6.7	6.3	53.0	10.8	40Q	628011	2555415
BD08	Lava flow	8/12	334.5	-34.4	337.4	-6.4	4.0	195.0	8.0	40Q	628019	2555400
BD01	Sheeted dykes	5/5	304.2	0.3	300.2	19.7	8.0	93.4	5.0	40Q	624022	2556662
BD02	Sheeted dykes	13/13	307.7	0.8	303.6	21.4	1.9	470.4	13.0	40Q	624066	2556692
BD03	Sheeted dykes	9/9	326.5	4.9	322.2	31.0	6.6	61.1	8.9	40Q	624046	2556662
BD04	Sheeted dykes: main dyke	4/4	318.1	-6.6	316.5	17.7	8.3	123.1	4.0	40Q	623989	2556647
BD04	Sheeted dykes: minor dyke	3/3	345.2	29.0	341.5	57.7	8.0	236.4	3.0	40Q	623989	2556647
BD05	Sheeted dykes	2/2	320.1	3.7	315.5	28.1			2.0	40Q	624026	2556670
BD12	Dyke Rooting Zone	7/9	341.9	11.0	339.4	39.6	4.8	157.6	7.0	40Q	624229	2557082
BD10	Varitextured gabbro	12/12	327.6	10.4	321.9	36.6	3.5	151.4	11.9	40Q	624226	2557055
BD11	Varitextured gabbro	12/12	340.2	19.8	335.6	48.1	2.9	223.0	12.0	40Q	624228	2557058
BD13	Foliated gabbro	7/12	314.8	2.9	310.1	25.8	1.6	1451.6	7.0	40Q	624538	2557554
BD14	Foliated gabbro	17/17	313.8	6.0	307.9	28.4	1.6	474.2	17.0	40Q	624517	2557617
Tilt correction (dip direction/dip): 171/29 - Lava orientation												
Wadi Gideah (Ibra massif / Tayin block):												
WG19	Sheeted dykes	3/10	138.2	-2.9	134.6	-34.3	8.4	218.5	3.0	40Q	660692	2522839
WG23	Sheeted dykes	9/10	354.8	7.8	0.3	38.4	8.1	41.1	8.8	40Q	659924	2522000
WG11	Dyke Rooting Zone	9/10	328.8	10.0	326.7	42.8	6.8	57.6	8.9	40Q	656229	2525217
WG12	Dyke Rooting Zone	7/7	344.3	26.9	351.3	59.2	5.5	121.4	7.0	40Q	656758	2524249
WG10	Varitextured gabbro	10/14	342.6	14.4	345.8	47.1	8.7	31.7	9.7	40Q	656229	2525217
WG14	Varitextured gabbro	5/12	329.0	2.6	327.6	35.4	11.4	46.0	4.9	40Q	656758	2524249
WG07	Foliated gabbro	5/5	335.7	-1.4	335.8	31.6	11.0	49.3	4.9	40Q	655975	2528586
WG08	Foliated gabbro	10/12	330.7	-6.7	330.2	26.2	3.4	204.3	10.0	40Q	656154	2527688
WG09	Foliated gabbro	5/10	337.3	-0.1	337.7	32.9	3.0	667.9	5.0	40Q	656309	2527105
WG01	Layered gabbro	16/19	342.5	-7.8	343.2	24.9	7.1	27.9	15.5	40Q	655697	2532322
WG02	Layered gabbro	6/6	325.4	-27.6	326.5	5.0	12.8	28.4	5.8	40Q	655626	2532342
WG03	Layered gabbro	12/12	329.6	18.4	326.9	51.2	5.0	74.9	11.9	40Q	655590	2531349
WG04	Layered gabbro	14/14	329.5	5.1	328.0	37.9	5.2	59.9	13.8	40Q	656061	2531233
WG05	Layered gabbro	11/11	330.0	0.7	328.9	33.6	6.1	57.1	10.8	40Q	655805	2530755
WG06	Layered gabbro	10/10	328.2	-0.4	327.0	32.3	9.0	30.0	9.7	40Q	656114	2529811
Tilt correction (dip direction/dip): 155/33 - Layered gabbro orientation												
Al Khadra (Ibra massif / Tayin block):												
KD01	Dyke	10/11	33.9	23.0	37.6	32.7	3.4	199.0	10.0	40R	603771	2517707
KD02/03	Lavas	15/19	44.1	33.2	50.9	41.3	5.3	53.4	14.7	40R	603771	2517707
Tilt correction (dip direction/dip): 180/12 - Lava orientation												
Salahi (Salahi massif / Hilti block):												
SA01	Layered gabbro	16/16	114.0	18.4	109.4	7.0	2.9	162.1	15.9	40R	444100	2665784
SA02	Layered gabbro	7/7	155.8	23.0	145.0	26.8	5.7	113.5	6.9	40R	445760	2665324
Tilt correction (dip direction/dip): 051/23 - Layered gabbro orientation												
Present field components (all localities):		107/484	354.6	36.8			2.1	41.9	104.5			

5.5 – Discussion and interpretation of the remanence data

5.5.1 – Salahi massif layered gabbros (control section)

SE-directed site mean directions in the Salahi Massif in geographic coordinates become slightly shallower when a standard tilt correction is applied (based on layering of the gabbros, dip direction/dip = 051/23) (Figure 5.9). These results suggest large clockwise rotation of the ophiolite (see section 5.7 below) and are consistent with previously reported palaeomagnetic data from extrusive sequences (Thomas et al., 1998; Perrin et al., 1994, 2000) and gabbros (Weiler, 2000) in the same massif, and with data from other localities in the northern massifs of the ophiolite (Thomas et al., 1998; Perrin et al., 1994, 2000; Weiler, 2000; van Hinsbergen et al., 2019). These directions are interpreted to represent highly rotated pre-deformational "primary" magnetizations, preserved outside of the region of remagnetization to the south.

Interestingly, Perrin et al. (2000) reported data from both the older (V1) and younger (V2) extrusive sequences in the Salahi massif (referred to as Hilti massif in their paper), and used these to infer significant clockwise rotation of the ophiolite during the emplacement of the lavas. Sampling of these same sequences by Di Chiara and Morris (pers. comm) has, however, yielded new unpublished remanence data that when subject to net tectonic rotation analysis demonstrates that only extensional tilting was experienced between emplacement of the V1 and V2 lavas, with large clockwise rotation occurring after crustal construction.

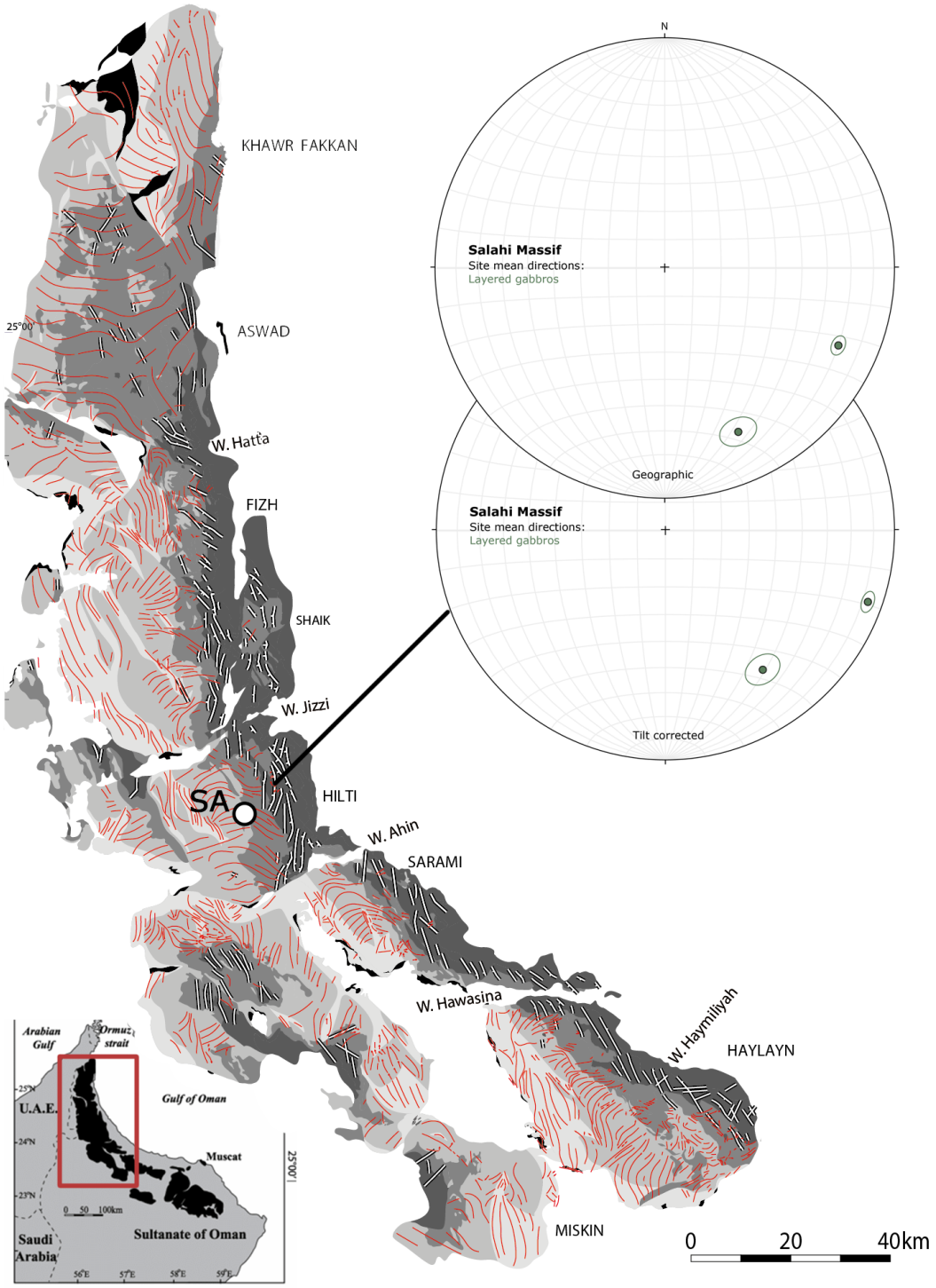

Figure 5.9 – Equal area stereographic projections in both geographic and tilt corrected coordinates showing the site mean magnetization directions of the Salahi massif. Map modified from Nicolas et al. (2000).

5.5.2 – Wadi Abyad dyke rooting zone and sheeted dyke complex

E/SE-directed magnetizations are found in the topmost stratigraphical levels (dyke rooting zone and sheeted dykes) exposed in Wadi Abyad. Only specimens from sites AB01 (dyke rooting zone), 04, and 05 (sheeted dykes) could be used to calculate site mean directions, as sites AB02 and 03 (sheeted dykes) had an insufficient number of specimens yielding interpretable ChRMs to allow calculation of a mean direction. The site-level results majorily show sites with an east to southeast-directed declination (AB01, 04, 05). Specimens from the sheeted dykes (AB04-05) and dyke rooting zone (AB01) of Wadi Abyad show a slightly different direction of magnetization, with the sheeted dykes being more ESE-directed and the dyke rooting zone more ENE-directed (Figure 5.11). An applied tilt correction to remove the dip of the local Moho (dip direction/dip = 032/32) brings the inclination to much shallower values.

Site AB06 shows no clear stable endpoints for the majority of specimens, instead defining great circle paths. In order to make sense of this site, great circle analysis was performed to calculate a site-level ChRM using nine established great circles and the only two interpretable endpoints. The results are shown in Figure 5.10 and become much shallower and SE-directed after the Moho tilt correction (Figure 5.10b).

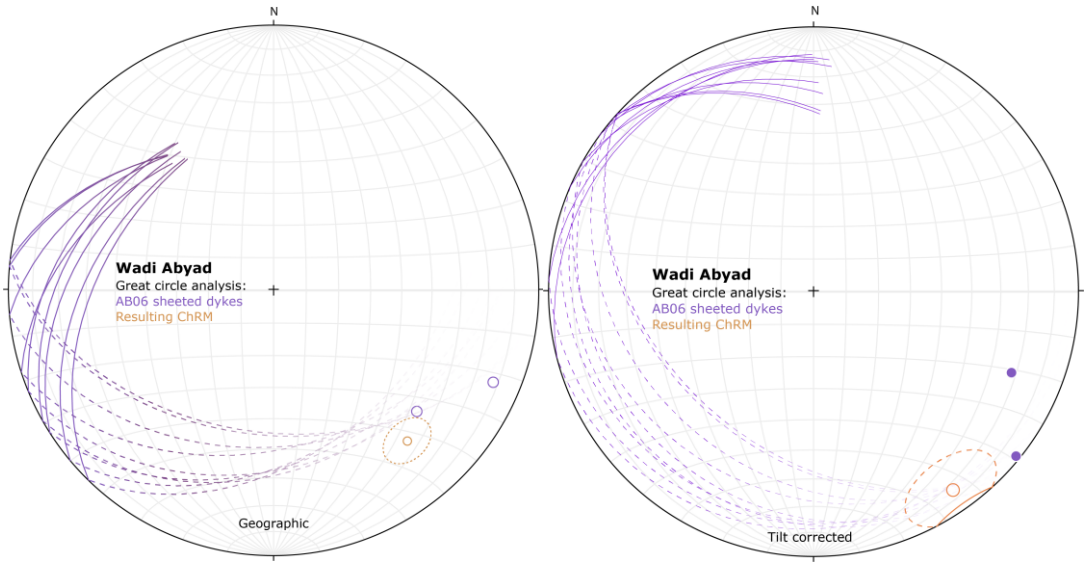

Figure 5.10 – Equal area stereographic projections in geographic coordinates showing the results of great circle analysis on the sheeted dyke site AB06 of Wadi Abyad. The majority of AB06 specimens do not provide stable endpoints, yet their great circle paths migrate towards the two interpretable endpoints. Tilt correction shows a shallow, SE-directed mean ChRM.

Results for the dyke rooting zone (with ENE-directed magnetizations) are comparable to those of the uppermost site sampled in Wadi Abyad by Meyer (2015), whereas the sheeted dykes in the section display an ESE-directed magnetization.

Interpretation of these data is best achieved by combining them with those acquired by Meyer (2015) from the layered gabbros at the base of the crust up to the dyke rooting zone at the boundary between the lower and upper crust. These data are presented (along with the new sites sampled in this study) in the equal area stereographic projection of Figure 5.11. This reveals a progression of site-level magnetization directions up through the crust that provides key evidence for the magnetization and tectonic history of the section and of the Oman ophiolite in general.

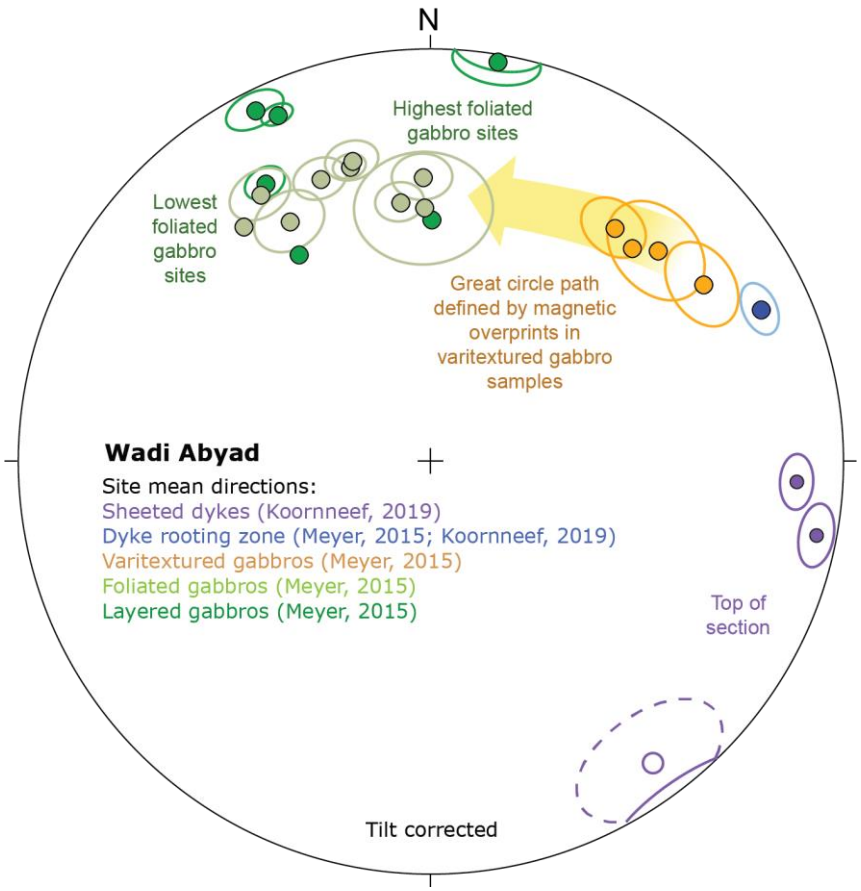

Figure 5.11 – Equal area stereographic projection in tilt corrected coordinates showing site mean magnetization directions of sites of Meyer (2015) and this study combined with their associated α_{95} cones of confidence. Note the progressive change in magnetization direction from the base to the top of the sequence.

The key observations are:

- The layered gabbros and lowermost foliated gabbros (Meyer, 2015) show a consistent NW direction (Figure 5.11)
- These NW directions are very similar to those reported by Feinberg et al. (1999) from gabbros and peridotites of the southern massifs, and importantly from Permian metabasites underlying the emplaced ophiolite (exposed in the Saih Hatat window into the continental basement; see Figure 2.14)

- Further up the section, the varitextured gabbros and dyke rooting zone (Meyer 2015 and this study) show a direction that is more intermediate between NW and SE
- The new data from the sheeted dykes shows the most southeasterly-directed magnetizations in the entire section
- Overprints found in specimens from the varitextured gabbros and dyke rooting zone show directions that are similar to the NW directions seen lower in the section (Meyer, 2015; Morris et al., 2016)
- The data overall form a girdle distribution between the NW directions at the base of the section to the SE ones at the top

These observations are best explained by remagnetization of the section from the base upwards, as proposed in the general model for remagnetization by Feinberg et al. (1999). In particular, the similarity of directions in the lower part of the ophiolite section (Late Cretaceous in age) with that of the basement metabasites (Permian in age) can only be explained by sharing a common magnetization direction acquired during the emplacement of the ophiolite onto the Arabian margin. This is further supported by presence of NW components overprinting the upper parts of the section. Meyer (2015) and Morris et al. (2016) suggested that the directions found in the dyke rooting zone represent the upper limit of the fluid-mediated remagnetization event proposed by Feinberg (1999). The data from this study show that moving even further up the section, into the sheeted

dykes, the directions become more SE, similar to directions seen in the northern massifs that are presumed to be outside the zone of remagnetization.

NE-directed magnetizations in the highest foliated gabbros and varitextured gabbros at this locality (Figure 5.11) were interpreted by Meyer (2015) to reflect (near-) complete overlap of the unblocking temperature spectra of a NW-directed overprint and a ESE/SE-directed primary component, giving rise to anomalous NE composite directions. This possibility is discussed further in section 5.6 below.

An alternative explanation for the girdle distribution of directions found in Wadi Abyad is that it might be caused by bulk rotation of the ophiolite when the massifs were still cooling from the top down. Slow cooling combined with rapid early rotation of the ophiolite might result in the lower crust acquiring its magnetization when rotation was nearly finished, whereas in the upper crust (dyke rooting zone and sheeted dykes) cooling happened more rapidly, causing the magnetization to be locked earlier in the rotation process. However, in the northern massifs of the Oman ophiolite all stratigraphic units (from layered gabbros to lavas) share a highly rotated SE direction. We therefore rule out this explanation, because it would be geologically unfeasible for the northern and southern massifs to have such different cooling histories.

5.5.3 – Wadi Abdah and Wadi Gideah crustal sections

In addition to characterising the lowermost foliated and layered gabbros of Wadi Abyad (Meyer, 2015; Morris et al., 2016), NW directions dominate all

stratigraphical levels in Wadi Abdah and Wadi Gideah (Figure 5.12). In geographical coordinates we find well-defined site mean directions that cluster in the NW with both positive and negative inclinations. These change to positive inclinations with a NW declination once structural correction is applied to the sites.

Only one site in Wadi Abdah could not be used to calculate a site-level mean direction due to having an insufficient amount of specimens. The remaining 13 sites provide consistent results. A tilt correction was applied to all sites to remove the dip of the local lava flow orientations (dip direction/dip = 171/29), which changes the inclinations of most sites to moderate positive values (except for the lavas, that retain shallow negative inclinations).

In Wadi Gideah, after disregarding two lightning-struck sites (WG16 and WG20), mean directions were calculated at the 15 remaining sites. In geographic coordinates most sites display shallowly-inclined, NW directions (both normal and reversed) and these move to steeper (30-50°) positive inclinations after applying a tilt correction based on the layering in the gabbros (dip direction/dip = 155/33°).

Given the compelling evidence outlined above that NW directions in the southern massifs of the ophiolite result from a regional-scale remagnetization event, these data suggest that the entire sampled sections in both Wadi Abdah and Wadi Gideah have been affected by this event. Unlike Wadi Abyad, they do not preserve any primary remanences towards the top of the exposed section,

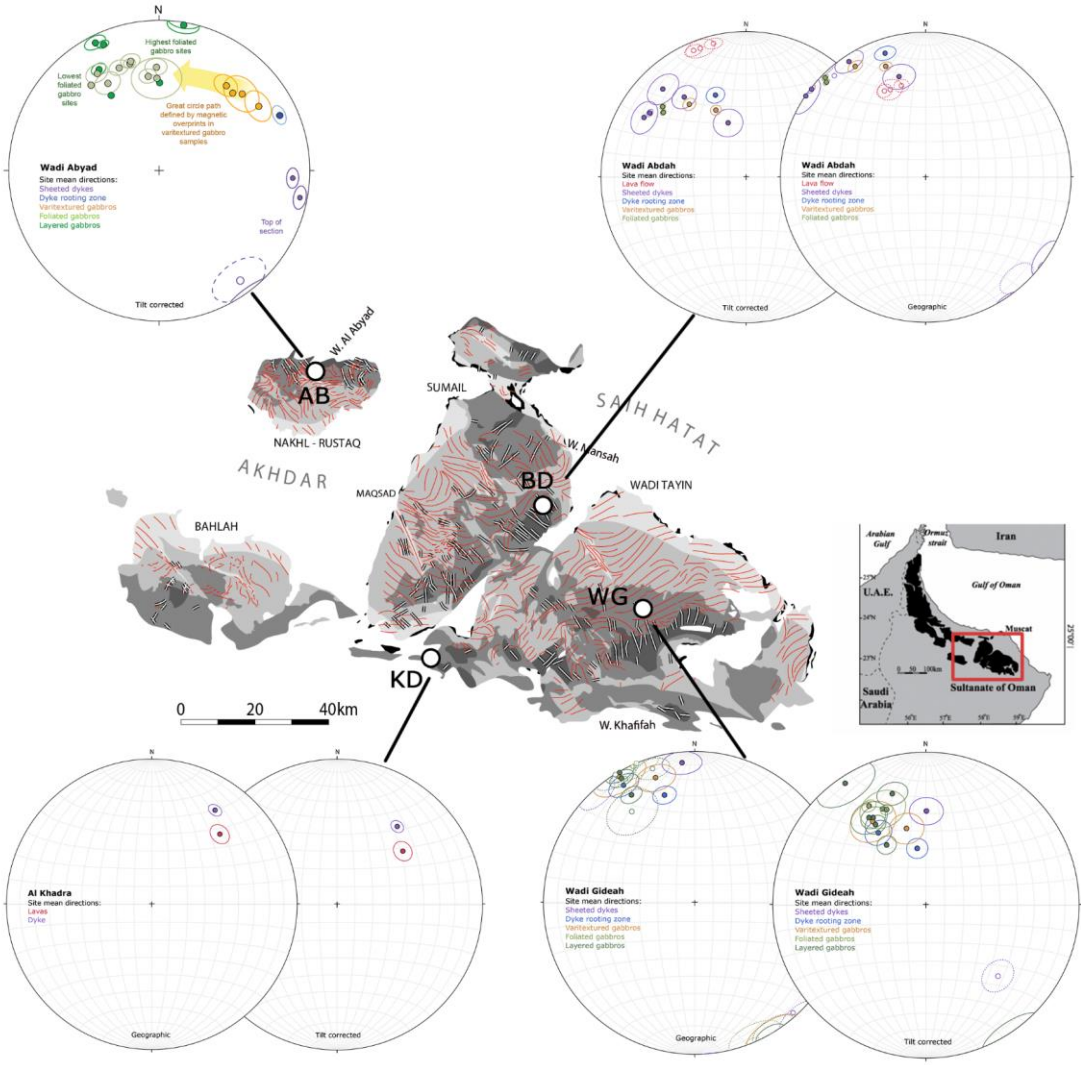

Figure 5.12 - Equal area stereographic projections in both geographic and tilt corrected coordinates showing the site mean magnetization directions of Wadi Abyad (AB), Wadi Abdah (BD), Al Khadra (KD), and Wadi Gideah (WG) for each sampled lithology (dark green = layered gabbros, light green = foliated gabbros, orange = varitextured gabbros, blue = dyke rooting zone, purple = sheeted dykes, pink = lavas). Map modified from Nicolas et al. (2000).

suggesting that the upper pseudostratigraphic limit of remagnetization varies spatially across the ophiolite.

One exceptional site in the Wadi Gideah sheeted dyke section (site WG19) does shows a SE direction, with a moderate, negative inclination after tilt correction. This may hint at patchy preservation of an original magnetization in the sheeted dykes, but since nearby sites (WG16 and WG20) in the sheeted dykes

in this area have been demonstrably struck by lightning (see sections 5.2 and 5.3.4) we exclude this anomalous site from further consideration.

5.5.4 – Al Khadra pillow lavas and cross-cutting dyke

Sampling at this locality was limited to a series of lava flows (sites KD02 and KD03) that are cut by a single, orthogonally-oriented dyke (site KD01), and all three units share a common NE direction (Figure 5.12). In order to calculate site mean statistics for the sites at Al Khadra, ChRMs of specimens from lava flows of sites KD02 and KD03 were combined to calculate a mean as the majority of specimens from site KD02 represented a PDF overprint. The remaining specimens of KD02 displayed the same magnetic direction as specimens from lava flow KD03 and were therefore considered as one site. A tilt correction based on the dip of the lava flows (dip direction/dip = 180/12°) steepens the inclination to ~45°.

As in Wadi Abyad, NE-directed ChRMs at these sites may be interpreted as magnetizations that represent a composite direction resulting from (nearly) overlapping demagnetization spectra of an original SE magnetization and a NW remagnetization. However, this would require an overlap of both the coercivities and the unblocking temperature spectra, as the same directions are isolated by both alternating field and thermal data (Figure 5.4). An alternative explanation is that the locality has not been remagnetised and has rotated less than other massifs. In the absence of more extensive data it is difficult to make a conclusive interpretation, therefore more sampling in this area is needed.

5.6 – Timing and origin of NNW/NW and NE magnetizations

A palaeomagnetic fold test (Tauxe and Watson, 1994) may be used to determine the timing of acquisition of NW remanences relative to the obduction and emplacement of the Oman ophiolite onto the Arabian continent. This fold test compares multiple site mean magnetization directions from various localities before and after applying tectonic tilt corrections to determine if magnetization directions become more dispersed or more concentrated upon correction.

In formulating the fold test, data from the Wadi Abdah and Wadi Gideah localities reported here are combined with that from the Khafifah and Wadi Abyad localities reported by Meyer (2015) to create a regional dataset. Only sites with NW-NNW-directed magnetizations were included. One site in Wadi Gideah (WG19) was excluded, as discussed above (Section 5.5.3).

The tectonic tilt corrections for Wadi Gideah and Wadi Abdah assume that the local orientation of the layered gabbros and lavas respectively represent a palaeohorizontal surface prior to tectonic deformation. In Meyer's (2015) study, the Moho was used to represent the palaeohorizontal for the Wadi Abyad and Khafifah localities. A statistical bootstrap fold test is applied to these data (Tauxe and Watson, 1994) that provides confidence limits on the degree of unfolding required to produce the tightest grouping of data. The results can be seen in Figure 5.13, the data input can be found in Table 5.2. The red, dashed lines in Figure 5.13 represent trends of the largest eigenvalues (τ_1's) of the orientation matrices as a function of untilting. The green line is the cumulative distribution of 500 maxima of τ_1, and the vertical dashed lines are the bounds that enclose 95%

Table 5.2 - Input data for fold test. Site mean magnetisation directions for four locations of the Oman ophiolite in geographic coordinates and their corresponding local structure for tilt correction in dip direction / dip. Dec = declination, Inc = inclination; LG = layered gabbros, FG = foliated gabbros, VTG = varitextured gabbros, DRZ = dyke rooting zone, SD = sheeted dykes, L = lavas.

Site	Litho	Geographic Dec / Inc		Dip direction / Dip		Site	Litho	Geographic Dec / Inc		Dip direction / Dip	
Wadi Abdah (this study)						**Wadi Abyad (Meyer, 2015)**					
BD01	SD	304.2	0.3	171	29	WA12	LG	296.7	46.1	32	32
BD02	SD	307.7	0.8	171	29	WA04	LG	312.6	33.4	32	32
BD03	SD	326.5	4.9	171	29	WA05	FG	302	33.6	32	32
BD04	SD	318.1	-6.6	171	29	WA01	FG	318.4	42.2	32	32
BD04	SD	345.2	29	171	29	WA02	FG	324.6	44.7	32	32
BD05	SD	320.1	3.7	171	29	WA03	FG	326.2	44	32	32
BD06	L	345.2	-35	171	29	WA08	FG	305.1	41.8	32	32
BD07	L	338	-35.1	171	29	WA39	FG	329.4	60.8	32	32
BD08	L	334.5	-34.4	171	29	WA07	FG	336.3	55.2	32	32
BD10	VTG	327.6	10.4	171	29	WA Transect	FG	324.8	57.1	32	32
BD11	VTG	340.2	19.8	171	29						
BD12	DRZ	341.9	11	171	29						
BD13	FG	314.8	2.9	171	29						
BD14	FG	313.8	6	171	29						
Wadi Gideah (this study)						**Khafifah (Meyer, 2015)**					
WG01	LG	342.5	-7.8	155	33	KF03	LG	340.9	-8.3	173	29
WG02	LG	325.4	-27.6	155	33	KF04	LG	358	1.4	173	29
WG03	LG	329.6	18.4	155	33	KF05	LG	0	-3	173	29
WG04	LG	329.5	5.1	155	33	KF06	LG	359.7	-3.6	173	29
WG05	LG	330	0.7	155	33	KF08	LG	355.2	7.8	173	29
WG06	LG	328.2	-0.4	155	33	KF02	FG	333.2	10.5	173	29
WG07	FG	335.7	-1.4	155	33	KF10	FG	334.7	-11.6	173	29
WG08	FG	330.7	-6.7	155	33	KF11	FG	330.2	-1.9	173	29
WG09	FG	337.3	-0.1	155	33	KF transect	FG	336.9	6.9	173	29
WG10	VTG	342.6	14.4	155	33	KFS01	FG	328.2	-10.2	173	29
WG11	DRZ	328.8	10	155	33	KFS02	FG	332	-3.9	173	29
WG12	DRZ	344.3	26.9	155	33	KFS03	D	350.3	13.1	173	29
WG14	VTG	329	2.6	155	33	KFS04	FG	324.7	1.9	173	29
WG23	SD	354.8	7.8	155	33						

of them. If these bounds were to include 0% untilting, this would indicate that the magnetization was acquired after tilting. If the bounds include 100%, as in this case, this indicates that the magnetization was acquired before tilting (Tauxe and Watson, 1994). This positive fold test therefore suggests that the NW/NNW-directed magnetizations found in Wadi Abdah, Wadi Gideah, Wadi Abyad and Khafifah were acquired before the tectonic event that tilted and structurally disrupted the Moho and overlying ophiolitic units, which occurred during late-stage formation of structural basement culminations and large-scale gravity sliding of the ophiolite in the Campanian (Lippard et al., 1986). In a different

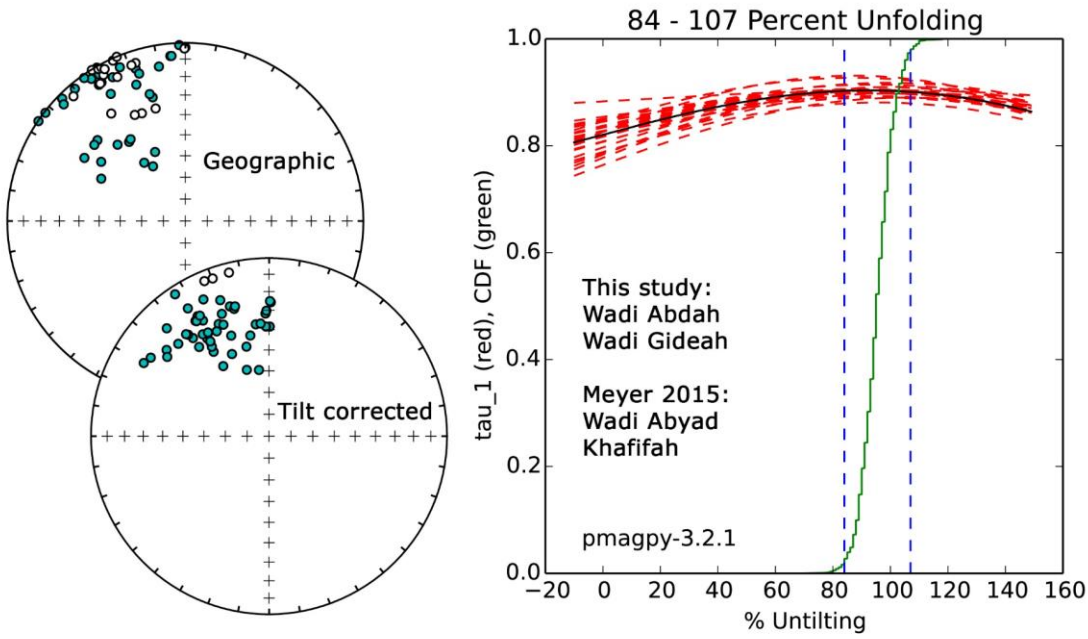

Figure 5.13 – Positive bootstrap fold-test (Tauxe and Watson, 1994) which demonstrates that remagnetization in Wadi Abyad, Wadi Abdah, Wadi Gideah, and Khafifah occurred prior to tilting of the Moho at these localities. The red dotted lines contain the trend of the eigenvalues of the eigenvalues of the orientation matrices during progressive untilting. The green line represents the cumulative distribution function of 1000 maxima of the eigenvalues, the dashed blue lines are the bounds that enclose 95% of them.

geological context, such pre- tilting orogenic remagnetization has also been demonstrated in the Canadian Cordillera (Enkin et al., 2000), where an early fluid-mediated remagnetization associated with a migrating diagenetic front passes a fold test (but was then overprinted by a second, thermal remagnetization event after deformation).

Normally these results would imply that the NW/NNW-directed magnetizations that dominate most southern massifs of the ophiolite (see Chapter 2.5.1) represent primary, pre-deformational remanences. However, as discussed in section 5.5.2 above, there is compelling evidence for these magnetizations to have been acquired by remagnetization during the emplacement of the ophiolite onto the Arabian continent. Feinberg et al. (1999)

attributed this to production of secondary magnetite during serpentinization produced by upwards circulation of orogenic fluids, resulting in complete remagnetization up to the layered gabbro unit, and in places even further up. Results from Wadi Abyad obtained in the present study, combined with the previous analyses by Meyer (2015) and Morris et al. (2016), support this interpretation and confirm that remagnetization occurred from the base of the ophiolite upwards. The NW/NNW direction found in Wadi Gideah and Wadi Abdah is therefore strongly suggested to be a secondary remagnetization acquired before Campanian structural disruption of the Moho, while the emplacing ophiolite retained a structural integrity.

The tilt corrected site mean directions in both Wadi Gideah and Wadi Abdah exhibit significant directional scatter that likely results from palaeosecular variation (PSV) during acquisition of remanences during remagnetization. Deenen et al. (2011) has shown that associated VGP distributions provide an effective way to assess whether palaeomagnetic data scatter reflects PSV, or whether PSV is under- or over-represented. Using their methodology, VGPs calculated for 14 sites in Wadi Abdah and 14 sites in Wadi Gideah (excluding the anomalous direction at site WG19) yield the following mean VGPs and associated Fisher (1953) statistics:

Wadi Abdah: mean VGP = 320.0/54.7, A_{95} = 9.7, N = 14

Wadi Gideah: mean VGP = 328.4/66.9, A_{95} = 6.6, N = 14

The upper and lower limits of A_{95} defined by Deenen et al. (2011) are:

$A95_{max} = 82 \times N^{-0.63}$ $A95_{min} = 17 \times N^{-0.40}$

which for N = 14 give limits for a distribution attributable to PSV of 5.9 < A_{95} < 15.6. This analysis demonstrates, therefore, that the scatter of site mean directions in these localities is consistent with PSV during a protracted period of remanence acquisition during remagnetization.

The nature of basement metamorphism and fluids expelled upwards through the ophiolite during its emplacement onto Arabia are believed to vary along the ophiolite. First, sub-ophiolite amphibolites with peak temperatures of 840-870 °C and 11.8-13.9 kbar (45-50 km depth) related to initiation of the Semail subduction event (cooling age of 95 Ma, Hacker et al., 1996) can be found in metamorphic sole localities along the whole length of the Oman ophiolite (Searle & Cox, 2002). Additionally, in the southern, remagnetised massifs, located above the most intensively recrystallised domain in the continental substratum (Feinberg et al., 1999), eclogite-facies rocks are found that reached temperatures of 540 °C and were expelled from 78 km depth (20 kbar) along the subduction zone at 79.1 Ma during late-emplacement of the ophiolite (Searle et al., 2004). Melting of protoliths in the southern parts of the ophiolite generated crustal melt that intruded the mantle peridotites and Moho as granitic dykes, offering fluid pathways into the ophiolitic crust (Searle & Cox, 2002). The metamorphic grade of the continental basement decreases to the north (Fig. 5.14), hence fluids advecting up into the ophiolite and responsible for its remagnetization in the south were likely to be more abundant and at higher temperatures than the less abundant/lower temperature fluids generated in the north (Feinberg et al., 1999).

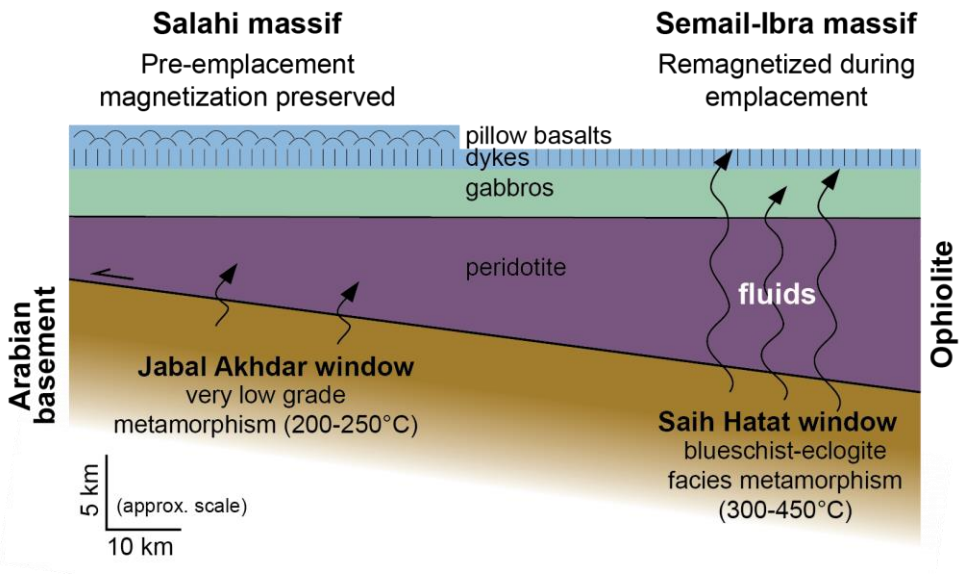

Figure 5.14 - Model for Late Cretaceous remagnetization of the Oman ophiolite proposed by Feinberg et al. (1999), modified to show variable upper limits of remagnetization in the southern massifs.

Under these circumstances, several alternate scenarios may be envisaged for the magnetic processes involved in the remagnetization event (Figure 5.15), the predictions of which may be compared to the changes in remanence characteristics seen through the Wadi Abyad section (Figure 5.16), that provides a profile from completely remagnetised NNW to assumed primary ESE remanences up-section:

(i) Fluids may have been sufficiently hot to produce a partial thermoremanent remagnetization (pTRM) that overprints the primary TRM (Figure 5.15A). Peak metamorphic temperatures in the continental basement rocks beneath the ophiolite are estimated to be 300-450°C (Feinberg et al., 1999), providing an upper limit for the likely temperature

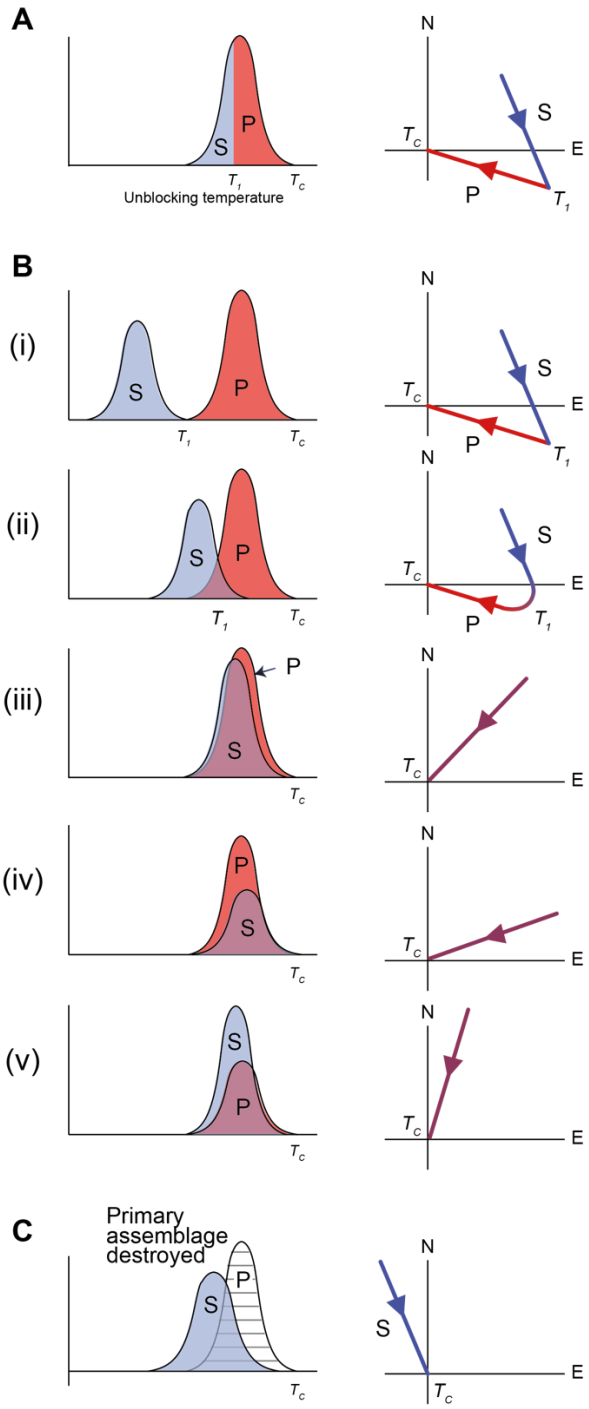

Figure 5.15 Schematic diagram illustrating various remagnetization scenarios and resulting demagnetization paths (only N-E horizontal plane shown) predicted for a NNW secondary component (S) and a ESE primary component (P): **A.** a purely thermal event affecting a single primary population of ferromagnetic grains, resulting in acquisition of a secondary partial thermoremanent (pTRM) overprint with maximum unblocking temperature T_1 (that may be higher than the actual temperature experienced, Pullaiah et al., 1975) and a sharp break point in the demagnetization path at temperature T_1; **B.** Growth of a new assemblage of ferromagnetic grains carrying a secondary chemical remanent magnetization (CRM), whose unblocking temperature spectra may be distinct from that of the primary assemblage (i), partially overlap with it (ii), resulting in a curved demagnetization path over the temperature interval of overlap, or (nearly) completely overlap with that of the primary assemblage (iii-v), resulting in a linear demagnetization path with a direction determined by the relative intensity of the components. Note that CRM due to migration of hot fluids may also be associated with a superimposed pTRM; **C.** Alteration resulting in simultaneous growth of a new ferromagnetic grain assemblage (carrying a CRM) and destruction of the primary grain assemblage, erasing all traces of the original TRM.

of orogenic fluids advecting upwards into the ophiolite. This would equate to maximum unblocking temperatures in the laboratory of ~450-500°C (for SD magnetite; Pullaiah et al., 1975). Partial thermal resetting on its own would be expected to produce sharp breakpoints between secondary and primary components in thermal demagnetization experiments, and with

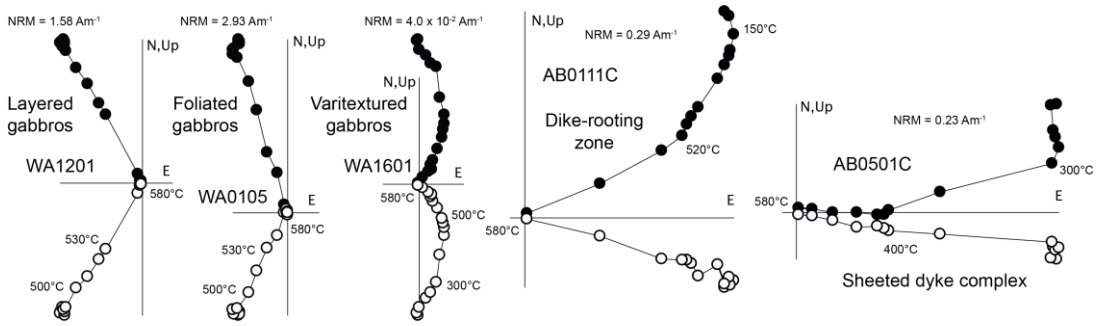

Figure 5.16 - Examples of Zijderveld plots through the Wadi Abyad crustal section, showing progressive changes in remanence direction and structure upwards from the base. Specimens from the layered, foliated and varitextured gabbros from Meyer (2015).

temperatures reducing as fluids advect upwards away from their source this might be expected to result in a progressive decrease in these breakpoint temperatures up-section. This is not seen, however, in the demagnetization results from Wadi Abyad (Figure 5.16), and it is unlikely therefore that remagnetization was a purely thermal event.

(ii) Fluids may have resulted in precipitation of a new population of magnetite grains, resulting in a grain-growth chemical remanence (CRM) that overprints the initial thermal remanence (Figure 5.15B). In this case, the unblocking temperature spectra of the secondary population would be controlled by its distribution of ferromagnetic grain sizes, rather than the temperature of formation (McClelland-Brown, 1982). Hence, a CRM acquired at low temperatures can be carried by grains with unblocking temperatures that might extend up to the Curie temperature. This produces a high likelihood that unblocking temperatures of the secondary and primary assemblages will overlap significantly (McClelland-Brown, 1982). This can result in curvilinear demagnetization paths in cases of

partial overlap (Figure 5.15B(ii)), or linear paths in an intermediate direction between the primary and CRM directions in cases of (near) complete overlap (Figure 5.15B (iii-v)). This is similar to the situation seen in demagnetization paths for the highest foliated gabbros, the varitextured gabbros and the dyke rooting zone in Wadi Abyad (Figure 5.16).

(iii) More commonly, fluids responsible for formation of a CRM are also at elevated temperatures, and the CRM will be accompanied by a pTRM (McClelland-Brown, 1982), resulting in a thermochemical remanence. This may be difficult to distinguish from a CRM overprint.

(iv) Finally, fluid migration (± associated elevated temperatures) may simultaneously result in production of a new ferromagnetic grain population carrying a CRM/thermochemical remanence and destruction/replacement of the initial assemblage that carried the primary remanence (Figure 5.15C). In this case, all traces of the original TRM may be eradicated. In Wadi Abyad this may explain the presence of single component remanences in the remagnetised NW/NNW direction in the layered gabbros and lowermost foliated gabbros (Figure 5.16), and the dominance of this remagnetised direction in the Wadi Gideah and Wadi Abdah sections.

As discussed above, the intermediate directions of the highest foliated gabbros, varitextured gabbros and the dyke rooting zone in Wadi Abyad that lie between a NW/NNW remagnetised and ESE/SE “primary” magnetization

direction can be explained as magnetic directions with a (near) complete overlap of the demagnetization spectra of two components. In order to test this idea further, an Excel spreadsheet was developed that may be used to perform simple forward modelling of demagnetization paths and Zijderveld plots of two populations of grains. This uses the beta distribution function embedded in Excel as a convenient way of representing stability spectra of two overlapping components. The beta distribution is a probability distribution defined on the interval [0, 1] and parametrized by two positive parameters, α and β, that control the shape of the distribution. This function was used to create two probability functions with adjustable magnitudes and symmetry/skewness over individually defined temperature intervals, for components with different directions. These probability distributions were then summed to determine the intensity and direction of magnetization of the resulting magnetization at each temperature step. These data were then used to create synthetic Zijderveld plots, and the spreadsheet used to explore the effects of varying overlaps in unblocking temperature spectra of two components of varying intensity on resulting demagnetization paths.

The results of using this approach to produce simple and non-unique forward models to replicate the varying demagnetization paths seen in specimens through the Wadi Abyad section are shown in Figure 5.17. For the secondary remagnetised component we used a NNW declination with a shallow inclination (340/29), representing the mean tilt corrected direction of the lowermost sections of Wadi Abyad reported by Meyer (2015). For the primary

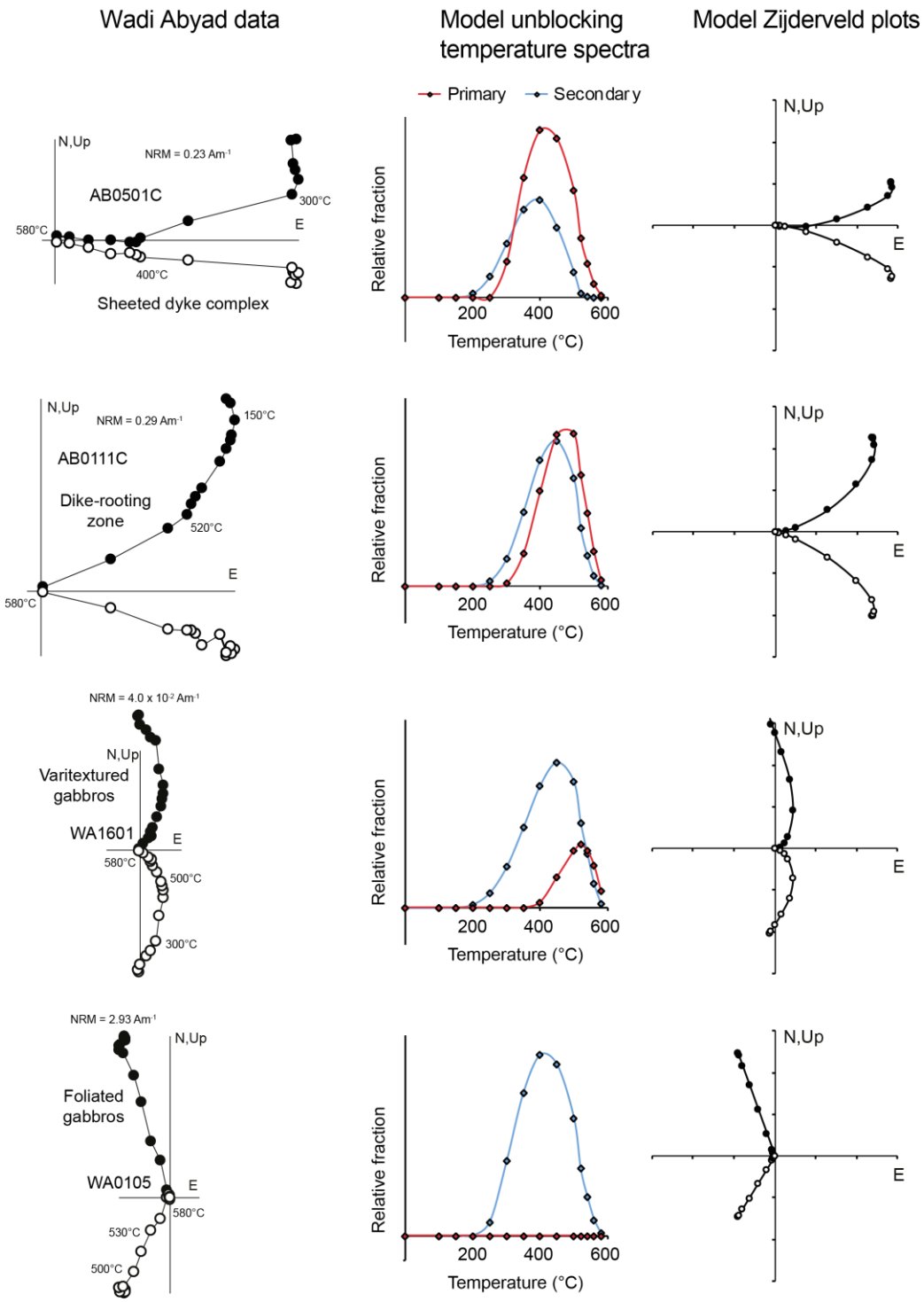

Figure 5.17 - Results of forward modelling of Zijderveld diagrams seen in Wadi Abyad.

component we used the southeastern direction found in the sheeted dykes of Wadi Abyad at site AB05 (100/05), which are assumed to be the least remagnetised, or even original, magnetization.

Results show that the variation in demagnetization paths up through the section may indeed be explained by varying degrees of overlap of the unblocking temperatures of the two components, with an upward increase in the relative intensity of the primary component accounting for changes in net remanence characteristics. These results strongly support the interpretation that the remagnetization event affecting the southern massifs of the Oman ophiolite involved the acquisition of a grain-growth CRM (or TCRM) that increases in intensity down-section. Note that NW/NNW remanences in the base of the Wadi Abyad section (and in Wadi Abdah and Gideah) require complete replacement of the primary magnetization, consistent with destruction of the primary magnetic phases during fluid-mediated alteration.

5.7 – Net tectonic rotation (NTR) analysis

Net tectonic rotation (NTR) analysis provides an alternative to standard palaeomagnetic tilt corrections that avoids arbitrarily dividing the total deformation at a site into a tilt plus a vertical axis rotation (Allerton and Vine, 1987; Morris et al., 1998). Instead, the deformation is described by rotation around a single inclined axis that simultaneously restores the observed magnetization back to an appropriate reference direction and the observed structure back to as close as possible to vertical (for dykes) or horizontal (for lavas and layered gabbros). The principal assumption is that internal deformation of the sampled unit has not affected the magnetization vector, and therefore that the angle (beta) between the remanence and the pole to the structure is

conserved (Allerton and Vine, 1987). This technique is particularly powerful in the case of sheeted dykes in ophiolites since components of rotation around dyke-normal axes cannot be resolved using standard tilt corrections to the vertical (Morris and Anderson, 2002) and can give rise to anomalous declinations and inferred rotations. This technique may only be applied to sites believed to hold a primary magnetization, and was therefore only applied to sites SA01 and SA02 from the Salahi massif, the uppermost sites in Wadi Abyad (sites AB01-06), and the Al Khadra dyke (site KD01), although doubt remains about the interpretation of the NE remanence at this latter site.

A reference direction needs to be used in NTR analysis to represent the direction of the magnetic field at the time the remanence was acquired. In this case, a reference declination of 000° was used, assuming a normal magnetic polarity (as the ophiolite formed during the Cretaceous Normal Superchron, 126–83 Ma; Gradstein et al., 2012). This implies that the net rotation calculated at each site arises from a combination of plate motion and deformation. The reference inclination was calculated using tilt corrected, unremagnetised palaeomagnetic data from lavas reported by previous studies in the north of the ophiolite. Data from Perrin et al. (2000), Shelton (1984), Weiler (2000), and van Hinsbergen et al. (2019) were combined, giving a reference inclination of 21.5° ± 6.6° (Figure 5.18).

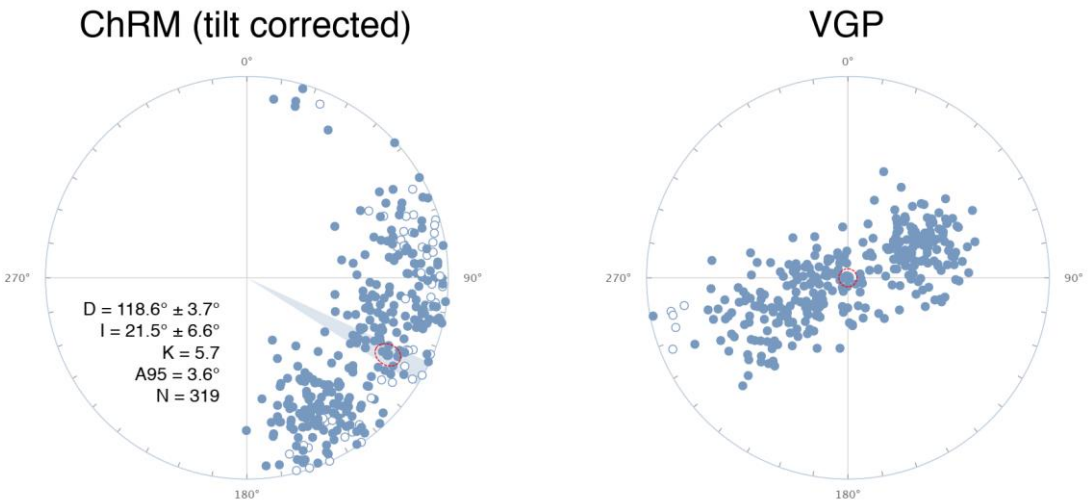

Figure 5.18 – Equal area projections in tilt corrected coordinates of combined ChRM data from Shelton (1984), Perrin et al. (2000), Weiler et al. (2000) and van Hinsbergen et al. (2019) showing a calculated mean ChRM with an inclination of 21.5° (from van Hinsbergen et al. (2019)).

At each site, uncertainties in the input vectors (observed magnetization, reference direction and pole to the geological structure) were propagated through the NTR analysis to give multiple estimates of the rotation parameters (following the method of Morris et al., 1998). An α_{95} of 5° was assumed for the poles to structures measured in the field. Dyke sites typically return two sets of solutions correponding to two alternate restored dyke strikes, whereas layered gabbros (assumed to have originally horizontal layering) return single solutions.

Site	Lithology	Preferred solution						Alternate solution					
		Rotation axis		Rotation		Initial structure		Rotation axis		Rotation		Initial dyke	
		Azimuth	Plunge	Magnitude	Sense	Strike	Dip	Azimuth	Plunge	Magnitude	Sense	Strike	Dip
Salahi massif													
SA01	Layered gabbros	227.9	77.9	108.0	CW	14.5	0						
SA02	Layered gabbros	261.5	77.9	147.0	CW	5.3	0						
Wadi Abyad													
AB04	Sheeted dykes	234.1	49.1	92.0	CW	19.9	90	50.5	32.2	176.1	CCW	160.1	90
AB05	Sheeted dykes	225.8	58.3	98.5	CW	11.2	90	54.1	27.2	177.1	CCW	168.8	90
Al Khadra													
KD01	Dyke	2.0	80.7	36.7	CW	132.9	90	16.7	26.4	157.2	CW	47.1	90

Table 5.3 - Results of the net tectonic rotation (NTR) analysis (Allerton and Vine, 1987) showing the results for the orientation of the rotation axis, the rotation magnitude and sense, and the restored initial orientation of the structure (layered gabbros or dykes). Reference direction used: D = 000°, I = 21.5° ± 6.6°. In situ structure orientations used in the analysis can be found in Table 5.1. In the case of dykes, two sets of solutions were obtained at each site. The preferred solution was used for tectonic interpretation, whereas the alternate solution was discarded.

Results of the NTR analysis can be found in Table 5.3. Figure 5.19 displays the distributions of the calculated rotation parameters using histograms and contoured equal area stereographic projections of the rotation axes. The layered gabbro sites from the Salahi massif suggest large 110-150° CW rotations around sub-vertical axes, suggesting not much tilting occurred at these sites. These rotations are consistent with regional-scale clockwise rotation of the ophiolite as proposed in recent tectonic models (Morris et al., 2016; van Hinsbergen et al.,

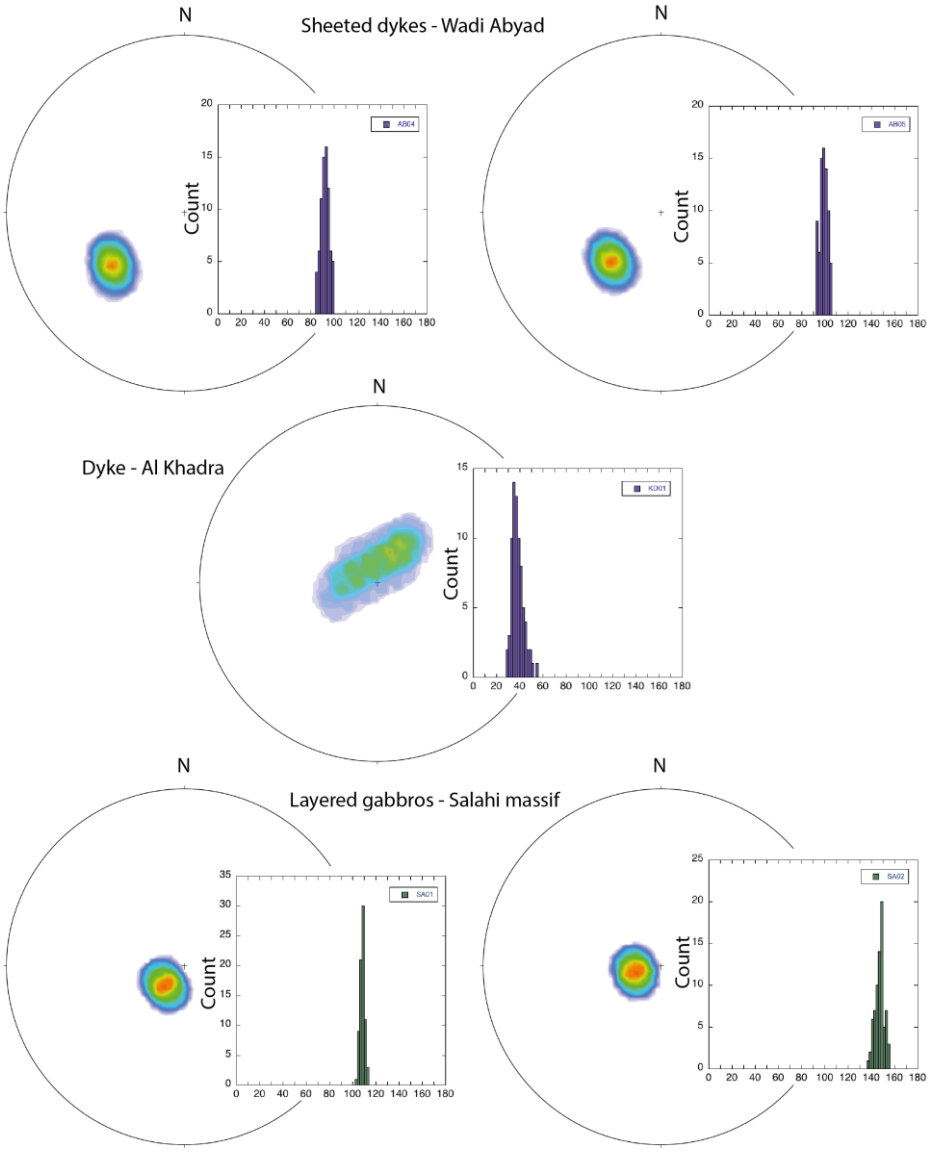

Figure 5.19 – Net tectonic rotation results from dykes in Wadi Abyad and Al Khadra, and layered gabbros from the Salahi massif. Histograms show rotation angles, contoured equal area stereographic projections show the rotation axes.

2019). The dykes from Wadi Abyad provide two sets of solutions of which the clockwise solutions were accepted, on the basis of the regional rotation history. The ~100° CW rotation around a moderately plunging axis at this locality may be decomposed into a large vertical axis component and a component of tilting during deformation that may have resulted from extensional faulting during spreading. Importantly, restored NNE-SSW initial dyke strikes (011-020°) in this section (Table 5.3) are consistent with a recent reconstruction of the ridge system reported by van Hinsbergen et al. (2019) that indicated NNE-SSW initial strikes in the sheeted dyke complex across the unremagnetised northern massifs (Figure 5.20). This provides additional support for the assumption that magnetizations in the sheeted dykes in Wadi Abyad represent primary TRMs.

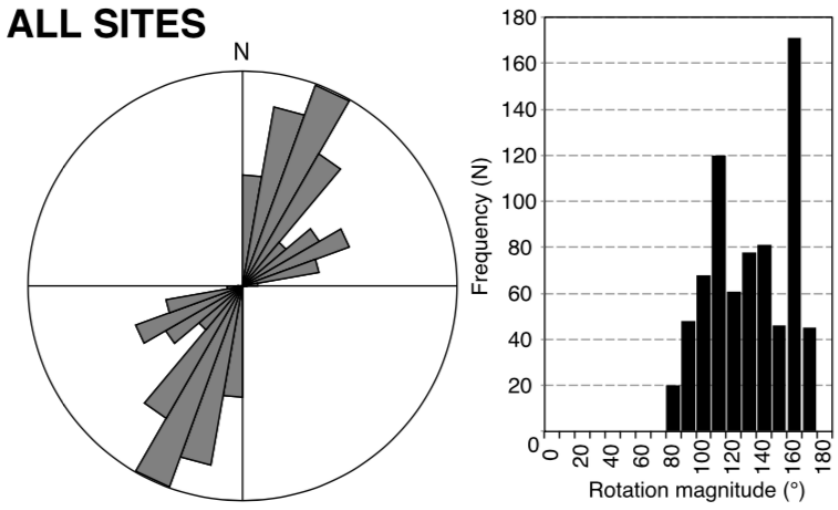

Figure 5.20 - Permissible initial dyke strikes and associated rotation angles for all sites in the sheeted dyke complex analysed by van Hinsbergen et al. (2019).

The dyke site from Al Khadra provides two solutions, one involving a ~40° CW rotation around a sub-vertical axis, and the other a ~160° CW rotation around a shallowly plunging axis. The solution involving rotation around a shallow axis

was rejected as this would result in overturned initial orientations for the pillow lavas that are cut by the dyke. The alternate ~40° CW rotation is substantially lower than that seen at the other localities and the magnitude of rotation of the ophiolite inferred by previous workers. This may reflect: (i) differential local rotation of the sampled units in the Ibra massif relative to the other localities; or (ii) the remanence in this dyke representing a composite magnetization due to overlapping unblocking temperatures of a SE-directed primary and NNW-directed secondary component, invalidating the NTR approach. The restored NW-SE initial dyke strike for the preferred solution (133°) is not consistent with the regional initial NNE-SSW trend of the ridge system revealed by the analysis of van Hinsbergen et al. (2019), supporting the inference that the magnetization at this site is not the original TRM direction.

5.8 – Summary

The palaeomagnetic data obtained in this study provides further insights into the nature and extent of remagnetization of the southern massifs of the Oman ophiolite. New data reported here from Wadi Abyad extends the record further up in the pseudostratigraphy. Data from the dyke rooting zone shows the same E/SE-oriented magnetization reported by Meyer (2015) but with a much larger dataset of specimens. Importantly, the sheeted dykes that overlie the dyke rooting zone have a magnetization direction with a SE orientation. This direction is much more compatible with data from the northern massifs, including the data reported here from the Salahi massif locality and that provided by previous

studies (Thomas et al., 1988; Perrin et al., 1994, 2000; Weiler et al., 2000; van Hinsbergen et al., 2019), where this SE oriented magnetization is thought to be the primary direction, unaffected by the remagnetization event that affected the southern massifs. The gradual changes in remanence structure and direction observed through the Wadi Abyad crustal section suggests that the effects of the remagnetization event become less significant upwards, consistent with an interpretation where the remagnetization is related to CRM overprinting of an original SE magnetization during upwards advection of fluids related to ophiolite emplacement (and prior to structural disruption of the palaeohorizontal). The compatibility of SE directions at the highest sites in the section with non-remagnetised SE directions in the northern massifs (together with consistency of initial dyke orientations determined using net tectonic rotation analysis) suggests that primary magnetizations are still preserved at the top.

Sites in Wadi Abdah and Wadi Gideah, that are located at the eastern edge of the Semail massif and the center of the Ibra massif respectively, show directions that remain consistently NW-directed from the bottom of the stratigraphy to the top (layered gabbros to lava flows). This suggests that these localities have been completely overprinted by the remagnetization event.

Al Khadra is located at the southwestern edge of the Ibra massif and shows NE magnetization directions that are likely to represent intermediate directions between a SE primary and a NW remagnetised direction. As in the case of the NE intermediate directions seen in Wadi Abyad, this suggests that the remagnetization event has affected this area.

The nature of this regional-scale remagnetization event will be explored further in the next chapter, where an attempt is made to use rock magnetic techniques to discriminate between remagnetised and non-remagnetised rocks using end member modelling of IRM curves.

Chapter 6 – Isothermal remanent magnetization analysis

6.1 – Introduction

Palaeomagnetic directional information, statistical fold tests and NTR analysis (Chapter 5) are capable of distinguishing between remagnetised and primary remanences in all our sampled sites. From the remanences alone, however, it is hard to distinguish between primary and remagnetised remanences, as the demagnetization spectra of both remanences (nearly completely) overlap. In this chapter therefore an attempt is made to use end-member modelling of the acquisition curves of isothermal remanent magnetization (IRM) to try to distinguish between remagnetised and non-remagnetised specimens. For this analysis, specimens were selected from Wadi Gideah, which is completely remagnetised, Wadi Abyad which is remagnetised at the bottom of the section and non-remagnetised at the top, and the Salahi massif which is thought to hold "primary" magnetizations. It was hoped that this method may also help to illustrate the mechanism of remanence acquisition of both remagnetised and non-remagnetised rocks.

IRM acquisition curves were measured for 155 specimens; 38 from Wadi Gideah, 71 from Wadi Abyad, and 46 from the Salahi massif, covering the sections from the bottom (layered gabbros) to the top (dykes/lavas). Data were acquired using an automated, robotic sample handling system attached to a 2G Superconducting Rock Magnetometer at the Paleomagnetic Laboratory Fort Hoofddijk, University of Utrecht, and the analyses were made possible by a

research grant from EPOS (European Plate Observing System). Analyses were conducted in collaboration with Professor Mark Dekkers (University of Utrecht). As IRM curves are very susceptible to changes in magnetic grain size (see Chapter 3), end-member modelling has proven to be very capable of picking out different lithologies (Dekkers et al., 2014), especially between gabbros, dykes, and lavas. Applying end-member modelling to a single locality, covering gabbros, dykes, and lavas, would therefore result in multiple end-members that interpret different lithologies, but not necessarily distinguish between remagnetised and non-remagnetised remanences. Therefore the end-member modelling study focused on comparing lithologies between the localities, reducing the variability in the shapes of the IRM curves so that end-member modelling can pick out the small differences that we may not be able to see at a glance. End-member modelling has been successfully applied to studies of sedimentary and volcanic rocks so far (Gong et al., 2009; van Hinsbergen et al., 2010; Meijers et al., 2010; Dekkers et al., 2012, 2014; Aben et al., 2014; Huang et al., 2015a, b, c; Pastor-Galán et al., 2016), and the present study is the first time that end-member modelling has been applied to an ophiolite.

In this chapter, end-member modelling is first applied to all 155 specimens, from all three localities and the complete range of lithologies (layered, foliated, and varitextured gabbros, dyke rooting zone, sheeted dykes, and lava flows), in order to test if this method is capable of distinguishing between differences in magnetic grain assemblages between the lithologies. We then focus on testing a dataset of IRM curves from only gabbros (remagnetised

gabbros from Wadi Gideah and Wadi Abyad, non-remagnetised gabbros from the Salahi massif) and another dataset containing only data from dykes (remagnetised dykes from Wadi Gideah, non-remagnetised dykes from the Salahi massif, and a mixture of partly remagnetised and non-remagnetised dykes from Wadi Abyad). After end-members have been calculated, they were divided into various coercivity distributions that can be linked to specific magnetic minerals. For this we use the component analysis method of Kruiver et al. (2001) (see Chapter 3).

6.2 – End-member modelling of all specimens

Figures 6.1 and 6.2 summarise the end-member modelling and component analysis results of a dataset that contains all specimens.

The calculated two end-member (EM) model has an r^2 value of 0.77797, whereas the three end-member model gives an r^2 of 0.90365 and convexity (measure of curvature) of -2.4722. The four end-member model reaches an even higher r^2 value of 0.92948 but a lower convexity of -2.0869. Any model that includes five or more end-members is characterised by a virtual duplication of end-members, which is why these models are rejected due to overinterpretation of the dataset (Figure 6.1a). We choose to compare a three and a four end-member model (Figure 6.1b-e) named Model 1 (with 3 end-members) and Model 2 (with 4 end-members): comparing both models we find a virtual duplication of two end-members. The remaining end-member of Model 1 gets split up into two end-

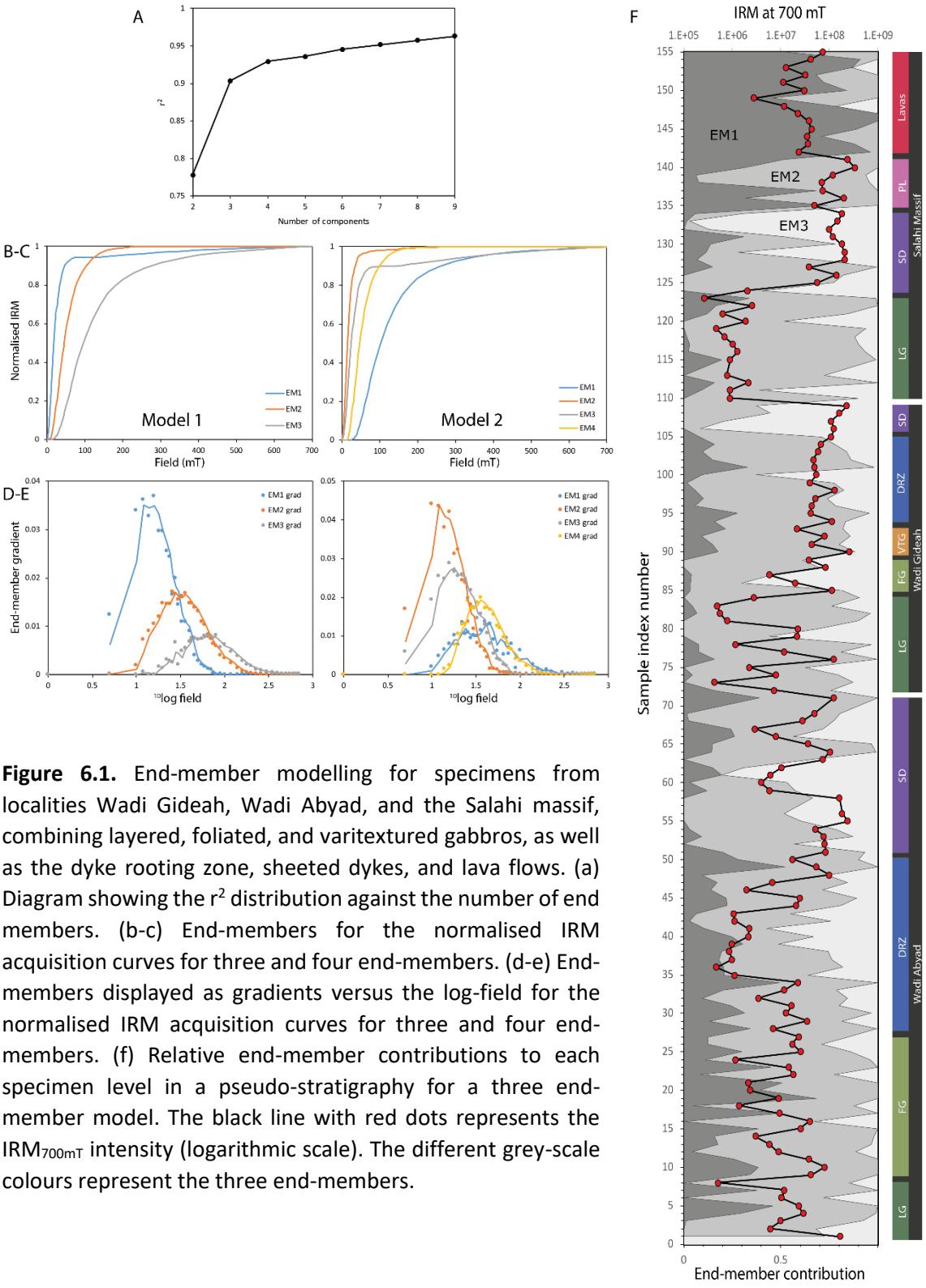

Figure 6.1. End-member modelling for specimens from localities Wadi Gideah, Wadi Abyad, and the Salahi massif, combining layered, foliated, and varitextured gabbros, as well as the dyke rooting zone, sheeted dykes, and lava flows. (a) Diagram showing the r^2 distribution against the number of end members. (b-c) End-members for the normalised IRM acquisition curves for three and four end-members. (d-e) End-members displayed as gradients versus the log-field for the normalised IRM acquisition curves for three and four end-members. (f) Relative end-member contributions to each specimen level in a pseudo-stratigraphy for a three end-member model. The black line with red dots represents the IRM_{700mT} intensity (logarithmic scale). The different grey-scale colours represent the three end-members.

members in Model 2 (Figure 6.1c+e). A four end-member model therefore does not provide more geologically interpretable end-members than a three end-member model. In addition, in the r^2 diagram in Figure 6.1a, the break of slope

occurs at three end-members. Therefore, we continue to use the three end-member model to interpret this dataset.

Figure 6.1f shows the relative end-member contributions in a pseudostratigraphic order. Note that the vertical scale is a sample index number and does not correspond linearly to height in the sections. The bar on the right provides information about the lithology and locality a specimen relates to. The greyscale colours visually represent the percentages of the end-members present in each specimen for our chosen three EM model. It appears that the three end-members can be related to the lithologies: (i) EM1, the softest end-member, is highly abundant in the lava flows of the Salahi massif; (ii) EM3, the hardest end-member, can be found as the most abundant end-member in most of the dykes at all three localities; and (iii) EM2 is mostly found as the abundant end-member in the gabbro sections.

We applied IRM component analysis (Kruiver et al., 2001) to the three end-members to see if they could be broken down into different coercivity components (Figure 6.2). This resulted in a total of six components (C1 to C6, from the softest to the hardest component) that are required to fit the normalised end-member IRM acquisition curves (Table 6.1). The first and softest end-member, EM1, consists of three components C1, C2, and C5 (Figure 6.2). Component C2 with a $B_{1/2}$ of 18.6 mT contributes to 86% of the saturated isothermal remanent magnetization (SIRM) and is interpreted to be Ti-poor titanomagnetite (Day et al., 1977; Lowrie et al., 1990). Component C5 represents only 5% of the SIRM with a $B_{1/2}$ of 316.2 mT and is interpreted to represent either segregation of magnetite

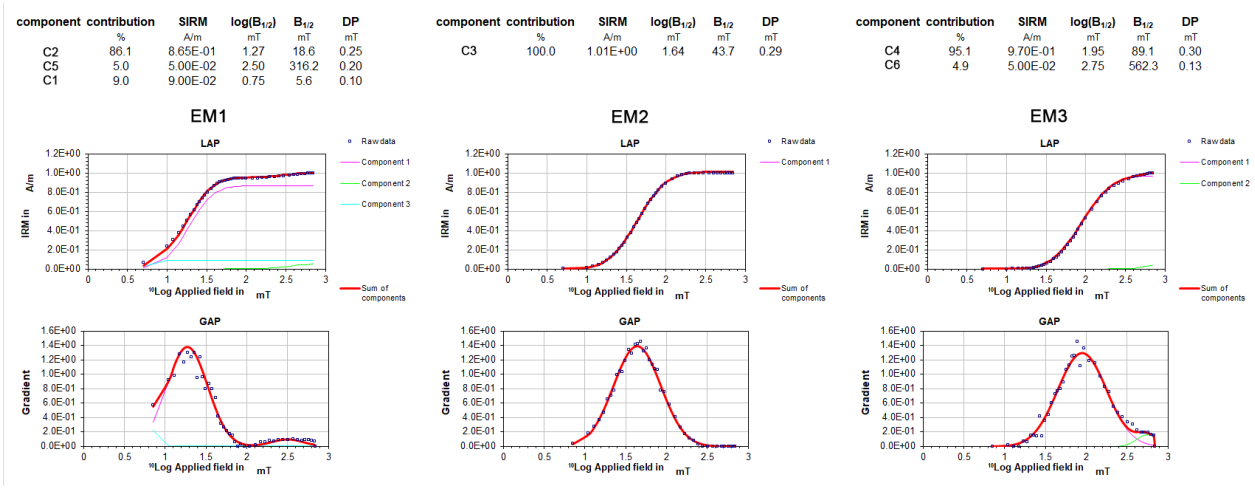

Figure 6.2 - IRM component analysis (Kruiver et al., 2001) of the preferred three end-member model. Squares represent the calculated data points from end-member modelling used to fit the IRM components.

or exsolved magnetite lamellae. The remaining component C1 applies to 9% of the SIRM but only has a $B_{1/2}$ of 5.6 mT. This component was required in the component analysis to provide a good fit to the model based on one measurement, which causes the distribution of the model to be skewed towards the left. This component is therefore not given any geological meaning and could simply be the result of particles being thermally activated (Egli, 2004; Heslop et al., 2004).

End-member EM2, mostly occurred in the gabbro sections, consists only of one component, C3 with a $B_{1/2}$ of 43.7 mT. This typically represents Ti-poor titanomagnetite (Day et al., 1977; Lowrie et al., 1990). Given that in EM1 we also found a Ti-poor titanomagnetite component (C2), these two components might represent titanomagnetite with variable titanium content (C3 containing more titanium than C2). Components with the lowest amount of titanium will from now on be referred to as near-stoichiometric magnetite.

End-member EM3, the magnetically hardest end-member and mostly found in the dykes, requires two components C4 and C6 for a good fit. Component C6 only contributes 5% of the total SIRM and is very hard with a B1/2 of 562.3 mT. We could interpret this component to represent hematite, traces of which could be present in the specimens (Kruiver and Passier, 2001). An alternative explanation is that this component represents a magnetically very hard intergrowth of magnetite, or segregation of magnetite. Component C4 makes up 95% of the total SIRM and has a high $B_{1/2}$ of 89.1 mT. We interpret this to be Ti-rich titanomagnetite (Day et al., 1977; Lowrie, 1990).

This analysis shows that six components are needed to fit the end-members. The lava flows that mainly consist of EM1 seem to mostly contain variations of Ti-poor titanomagnetite. Sheeted dykes seem to contain mostly EM3, consisting of Ti-rich titanomagnetite, but also contain EM2, consisting of Ti-poor titanomagnetite. The gabbros seem to contain EM2 (Ti-poor titanomagnetite) in all localities, but additionally contain EM3 (Ti-rich titanomagnetite) in Wadi Gideah, and EM1 (near-stoichiometric magnetite) in Wadi Abyad.

Whereas this analysis proved successful to distinguish between lithologies in a dataset containing all specimens, it is hard to distinguish between differences in remagnetised and non-remagnetised remanences. However, some trends can be seen in the abundancy of end-members between dykes and gabbros from different localities that seem to be linked to variations in titanium content in titanomagnetite, and possibly variations in magnetite growth. In order to study

these trends in more detail, the next sections will perform end-member modelling and component analysis using datasets derived only from gabbros and dykes.

6.3 – End-member modelling of gabbros

Figures 6.3 and 6.4 summarise the end-member modelling and component analysis results of a dataset that contains only the gabbros from localities Wadi Gideah, Wadi Abyad, and the Salahi massif.

Similar to the working method described in section 6.2, in this analysis a three EM model was preferred over a four EM model (Figure 6.3a-e). The relative contributions of the end-members (Figure 6.3f) shows that the gabbros of Wadi Abyad are mostly made up of an equal mixture of EM2 and EM3, the gabbros of Wadi Gideah mostly of EM1 and EM3 (where EM2 is almost non-existent), and the gabbros of the Salahi massif are mostly made up of EM3 with smaller amounts of EM1 and EM2. The three end-members require four IRM components (G1 to G4, soft to hard, Table 6.1) to provide a good fit to the end-member IRM acquisition curves (Figure 6.4). These components have the same meanings as components C1-C6 from the previous dataset.

End-member 1, mostly found in Wadi Gideah and in small amounts in Wadi Abyad and the Salahi massif, consists of three components, G1, G3, and G4. Component G1 makes up only 5% of the SIRM and represents Ti-poor titanomagnetite with a $B_{1/2}$ of ~20 mT. Component G3 makes up the majority of

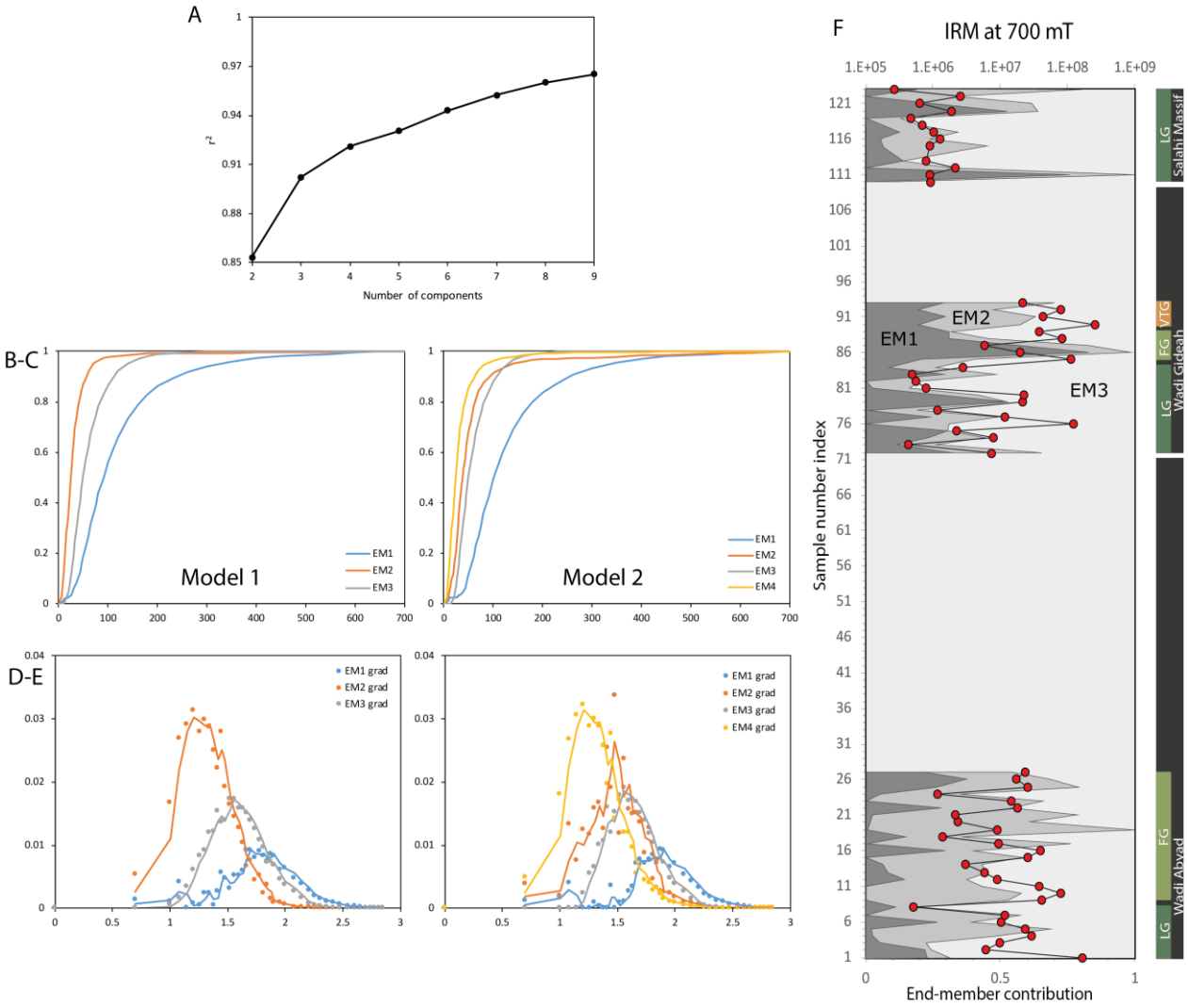

Figure 6.3 - End-member modelling for gabbro specimens from localities Wadi Gideah, Wadi Abyad, and the Salahi massif. (a) Diagram showing the r^2 distribution against the number of end members. (b-c) End-members for the normalised IRM acquisition curves for three and four end-members. (d-e) End-members displayed as gradients versus the log-field for the normalised IRM acquisition curves for three and four end-members. (f) Relative end-member contributions to each specimen level in a pseudo-stratigraphy for a three end-member model. The black line with red dots represents the IRM_{700mT} intensity (logarithmic scale). The different grey-scale colours represent the three end-members.

the SIRM with 90% and has a $B_{1/2}$ of 93 mT, representing Ti-rich titanomagnetite. Component G4 makes up only 5% of the SIRM and has a $B_{1/2}$ of 560 mT. As in the previous dataset (section 6.2), this could be interpreted either as traces of hematite, or as segregation/growth of magnetite.

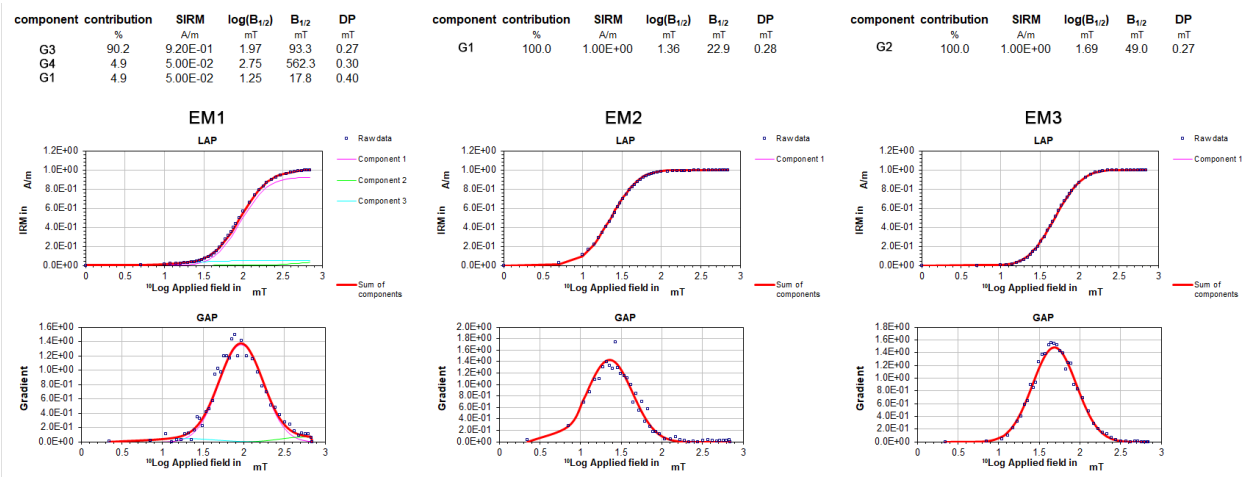

Figure 6.4 - IRM component analysis (Kruiver et al., 2001) of the end-members of the preferred three end-member model. Squares represent the calculated data points from end-member modelling used to fit the IRM components.

End-member 2 consists solely of component G1, representing Ti-poor titanomagnetite. End-member 3 consists only of component G2 with a $B_{1/2}$ of 49 mT, associated with titanomagnetite with a higher titanium content than component G1, hereafter referred to as Ti-moderate titanomagnetite.

The gabbros in the Salahi massif seem to be mostly controlled by Ti-moderate titanomagnetite, and in lower amounts by Ti-rich titanomagnetite and Ti-poor titanomagnetite. The gabbros in Wadi Gideah are controlled in nearly equal amounts (on average) by a mixture of Ti-rich titanomagnetite and Ti-moderate titanomagnetite. The gabbros of Wadi Abyad are controlled by an equal mixture of Ti-poor titanomagnetite and Ti-moderate titanomagnetite. Knowing that Wadi Gideah is remagnetised, the Salahi massif is non-remagnetised, and the gabbros of Wadi Abyad are mostly remagnetised but with remnants of a non-remagnetised direction, we could interpret that the remagnetised signal is characterised by higher amounts of titanium. The highest

contributions of titanium-rich minerals in this analysis are found in Wadi Gideah, in component G3. In Wadi Abyad, the remagnetised signal could be caused by Ti-moderate titanomagnetite in component G2 and a smaller amount of Ti-rich titanomagnetite. The main difference between Wadi Gideah and Wadi Abyad is that Wadi Abyad has a large proportion of EM2 (near-stoichiometric magnetite) that is non-existent in Wadi Gideah. It is this that might carry the non-remagnetised remanences, whilst remagnetised signals are controlled by titanomagnetite.

6.4 – End-member modelling of dykes

Figures 6.5 and 6.6 summarise the end-member modelling and component analysis results from a dataset that contains only the dykes (dyke rooting zone and sheeted dykes) from Wadi Gideah, Wadi Abyad, and the Salahi massif.

A similar working method to section 6.2 is applied to determine which end-member model is most significant. From a three EM model onwards, the convexity does not change significantly (Figure 6.5a) and all models become virtual duplicates of one another. In Model 2 (Figure 6.5c+e) two end-members seem to represent an end-member from Model 1 that has been split up, however these seem to be nearly identical. To avoid overinterpretation of the dataset, we chose a two end-member model for the following analysis.

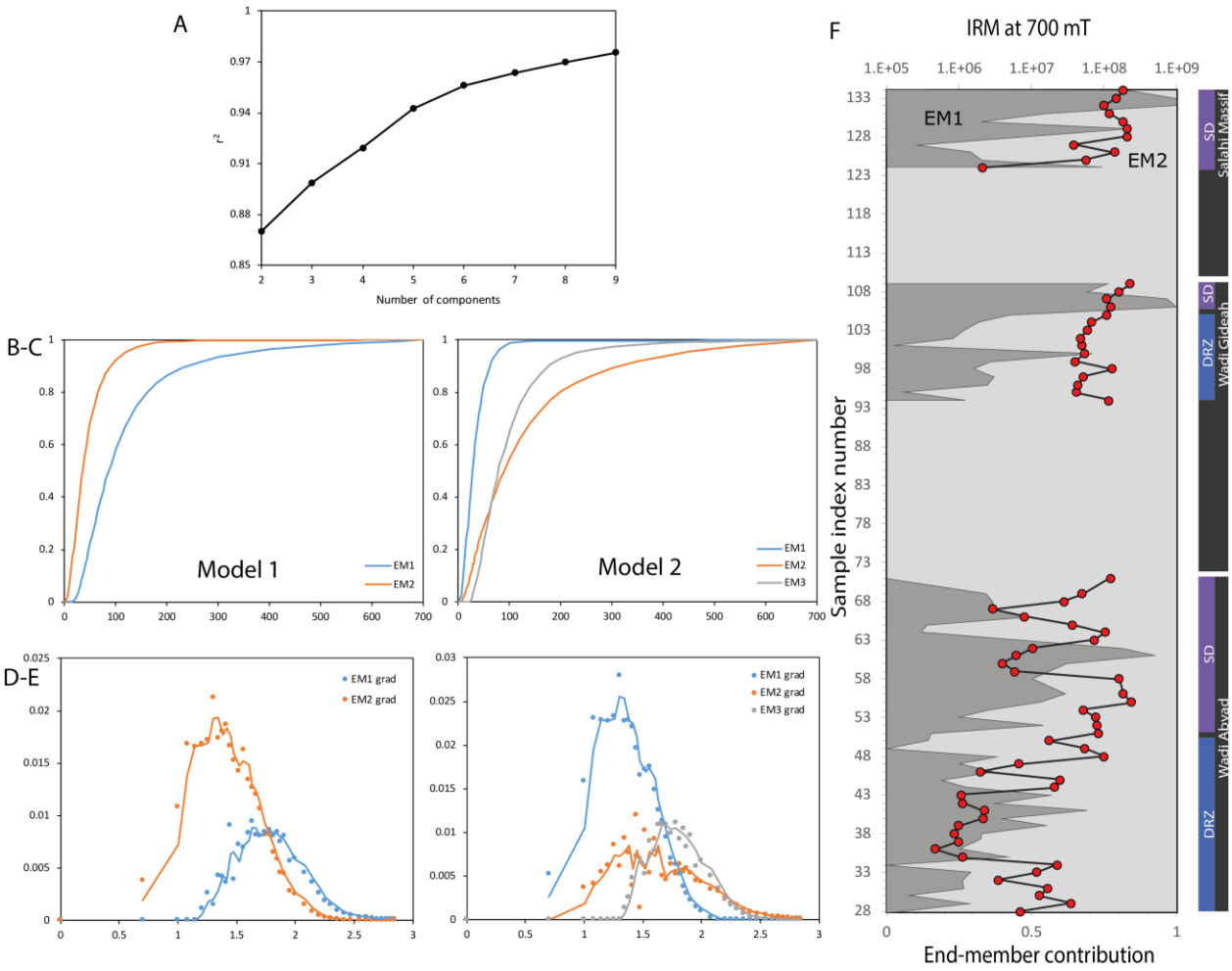

Figure 6.5 - End-member modelling for dyke specimens from localities Wadi Gideah, Wadi Abyad, and the Salahi massif. (a) Diagram showing the r^2 distribution against the number of end members. (b-c) End-members for the normalised IRM acquisition curves for two and three end-members. (d-e) End-members displayed as gradients versus the log-field for the normalised IRM acquisition curves for two and three end-members. (f) Relative end-member contributions to each specimen level in a pseudo-stratigraphy for a two end-member model. The black line with red dots represents the IRM_{700mT} intensity (logarithmic scale). The different grey-scale colours represent the three end-members.

It seems that EM2 is more dominant in the dykes of Wadi Gideah (Figure 6.5f) and moderately occurring in the dyke rooting zone of Wadi Abyad. In the sheeted dykes of Wadi Abyad, EM1 becomes slightly more dominant. EM1 is also found to be the more dominant end-member in the Salahi massif.

component	contribution	SIRM	log($B_{1/2}$)	$B_{1/2}$	DP
	%	A/m	mT	mT	mT
D2	93.2	9.60E-01	1.91	81.3	0.31
D3	6.8	7.00E-02	2.75	562.3	0.25

component	contribution	SIRM	log($B_{1/2}$)	$B_{1/2}$	DP
	%	A/m	mT	mT	mT
D1	100.0	1.01E+00	1.53	33.9	0.34

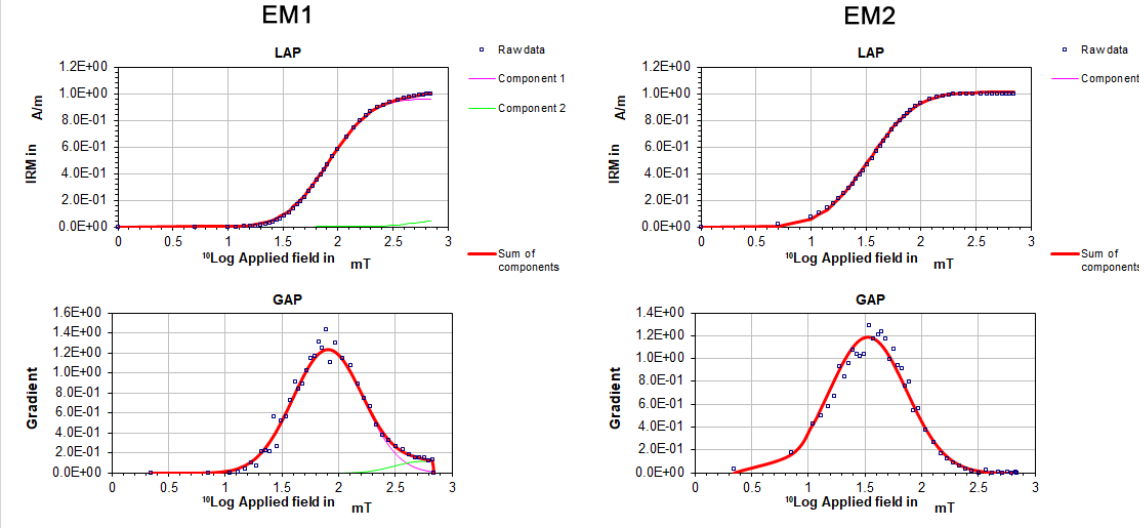

Figure 6.6 - IRM component analysis (Kruiver et al., 2001) of the end-members of the preferred two end-member model. Squares represent the calculated data points from end-member modelling used to fit the IRM components.

The two end-members are made of three components, D1 to D3 (soft to hard) (Figure 6.6, Table 6.1). The majority of end-member 1 is made up of component D2 with a 93% contribution to the SIRM and a $B_{1/2}$ of 81 mT. Similar to the previous datasets, this component is interpreted as Ti-moderate titanomagnetite. A smaller amount of the SIRM is made of component D3 with a $B_{1/2}$ of 560 mT, which like in previous datasets is interpreted as either hematite or magnetite segregation/intergrowth. End-member two solely consists of the softest component D1 with a $B_{1/2}$ of 34 mT. This is interpreted to be near-stoichiometric magnetite.

The analysis of this dataset seems to suggest that the highest titanium contents (EM1) are found in sites that are non-remagnetised, and that the lowest

(to non-existent) titanium contents (EM2) are found in sites that are remagnetised.

Table 6.1 - Summary of IRM component analysis. Columns show the end-members associated with an analysis, their fitted components, the contribution (Cont.) of these components in percentage, the field at which half of the saturated IRM is reached ($B_{1/2}$ in mT), the locality and/or lithology where the end-member mostly occurs, and the mineralogical interpretation of the components.

End-member	Component	Cont. (%)	$B_{1/2}$ (mT)	Mostly occurring in: Locality	Lithology	Interpretation
Component analysis on all specimens combined:						
EM1	C1	9.0	5.6	Salahi	Lavas	No geological meaning
	C2	86.1	18.6			Near-stoichiometric magnetite
	C5	5.0	316.2			Segregation of magnetite or exsolved magnetite lamellae
EM2	C3	100	43.7	All	Gabbros	Ti-poor titanomagnetite
EM3	C4	95.1	89.1	All	Dykes	Ti-rich titanomagnetite
	C6	4.9	562.3			Hematite / magnetite intergrowth / segregation of magnetite
Component analysis on all gabbro specimens:						
EM1	G1	4.9	17.8	Gideah	-	Ti-poor titanomagnetite
	G3	90.2	93.3			Ti-rich titanomagnetite
	G4	4.9	562.3			Hematite / magnetite intergrowth / segregation of magnetite
EM2	G1	100	22.9	Abyad	-	Ti-poor titanomagnetite
EM3	G2	100	49.0	Abyad + Gideah + Salahi	-	Ti-moderate titanomagnetite
Component analysis on all dyke specimens:						
EM1	D2	93.2	81.3	Abyad + Salahi	-	Ti-moderate titanomagnetite
	D3	6.8	562.3			Hematite / magnetite intergrowth / segregation of magnetite
EM2	D1	100	33.9	Gideah	-	Near-stoichiometric magnetite

6.5 – Summary and discussion

When applied to full ophiolitic sequences that range from gabbros to dykes and lavas, end-member modelling proves to be successful in distinguishing between these different lithologies. In this study, which also marks the first time that end-member modelling has been applied to ophiolitic rocks, the analysis picks out very different end-member compositions for each of the lithologies that we propose are linked to variations in magnetic grain sizes and compositions between gabbros, dykes, and lavas.

When we apply end-member modelling to only gabbros or only dykes from the Salahi massif, Wadi Gideah, and Wadi Abyad, results indicate two contradicting situations:

(i) In the gabbros, remagnetization seems to be linked to magnetic minerals with moderate to high titanium content.

(ii) In the dykes, remagnetization seems to be linked to magnetic minerals with a low titanium content or near-stoichiometric magnetite.

Earlier in Chapter 4 we already found evidence for the occurrence of titanomagnetite in all three localities from high-temperature susceptibility experiments, even though the majority of specimens display Curie temperatures close to 580°C. If the titanium content in the specimens is low enough, a Curie temperature of 580°C of magnetite can still be seen. However, IRM analysis and end-member modelling are not capable of determining precise compositions (e.g. Ti content) in magnetic minerals, and results are therefore speculative. Further analysis of the composition of the magnetic minerals is needed to give more quantitative answers to this question.

Perhaps one of the most peculiar results of this analysis comes from the end-member analysis of the gabbros; whereas we expected to see different end-member compositions between Wadi Gideah and Wadi Abyad (both remagnetised) and the Salahi massif (non-remagnetised), instead we find that Wadi Gideah and the Salahi massif have the same end-member composition, whilst Wadi Abyad is different from both of them (Figure 6.3f). This suggests that

gabbros in Wadi Abyad may have had a different history compared to those in Wadi Gideah and the Salahi massif during accretion prior to emplacement of the ophiolite.

Since an early study of Juteau et al. (1988) there has been an ongoing discussion about discontinuities in the spreading axis that formed the Oman ophiolite. Along-strike variations in the sheeted dykes suggest that propagating ridges (or "penetration zones" of MacLeod and Rothery, 1992) segmented the palaeo-spreading ridge on a scale of every 50-100 km, similar to what we see today along the East Pacific Rise. One of these propagators was discovered in the Haylayn massif, to the immediate NW of the Rustaq massif that contains Wadi Abyad. Intrusion of this NW-SE propagating ridge while the lower crust in Wadi Abyad was still hot resulted in large-scale magmatic deformation of the gabbros and intrusion of a swarm of NW-SE oriented sheeted dykes that cut the older dykes (Juteau et al., 1988; Reuber et al., 1991; MacLeod and Rothery, 1992; Nicolas and Boudier, 1995). This may indicate that the Wadi Abyad sequence experienced a different thermal history to Wadi Gideah, i.e. it may have remained at hotter temperatures for a prolonged time. This is supported by low cooling rates found for Wadi Abyad reported by Coogan et al. (2002) and van Tongeren et al. (2008). Evidence for NW-SE propagating structures was also found in this study in the topmost sheeted dykes, which are NE-SW oriented but cut by later NW-SE dykes (Figure 2.21). NE-SW orientations were also found in the uppermost foliated gabbro fabrics in Wadi Abyad (Meyer, 2015). Last but not least, unpublished geochemical data of MacLeod (pers. comm) shows that layered and

foliated gabbros on the west side of Wadi Abyad (the side of the propagator) have more evolved mineral compositions than those on the eastern side.

There is no evidence for such propagators being located near the other sampled localities in the Salahi massif and Wadi Gideah. Hence, a more prolonged cooling history in Wadi Abyad related to the effects of a nearby propagating ridge during crustal accretion might result in differences between the composition and/or grain-size of magnetic minerals between the Rustaq massif, and the Salahi and Ibra massifs, accounting for the different signal found for Wadi Abyad in the end-member modelling.

Chapter 7 – Oman Drilling Project results

7.1 – Introduction

The International Continental Scientific Drilling Program (ICDP) Oman Drilling Project (OmanDP) that operated between December 2016 and September 2018 aimed to investigate the Oman ophiolite to understand the relationships between the oceanic crust, shallow mantle, hydrosphere, atmosphere, and biosphere. It is a multidisciplinary project that sampled the ophiolitic sequence from the upper crust to the basal thrust in 15 holes (diamond-cored and rotary-drilled) that cover over 5000 metres of rock. Three diamond-core drilled holes were of particular interest for this PhD as they cover large parts of the ophiolitic upper to lower crustal sequence: Holes GT1 and GT2 drilled in Wadi Gideah, covering layered gabbros and the foliated-to-layered gabbros transition respectively, and Hole GT3 drilled in Wadi Abdah, covering the transition from sheeted dykes and the dyke rooting zone into varitextured gabbros (Figure 7.1).

In February/March 2017 I spent several weeks on the drill site of GT3 where I assisted the Phase I Scientific Party of OmanDP in core logging activities. Duties I was involved in included basic visual core description (core length, depth, lithology, prominent features) and sketching, restoring broken cores, and scanning the cores on a rotating core scanner that generates an “unrolled” photograph of the core (Figure 7.2). In the summer of 2017 I was part of the Phase

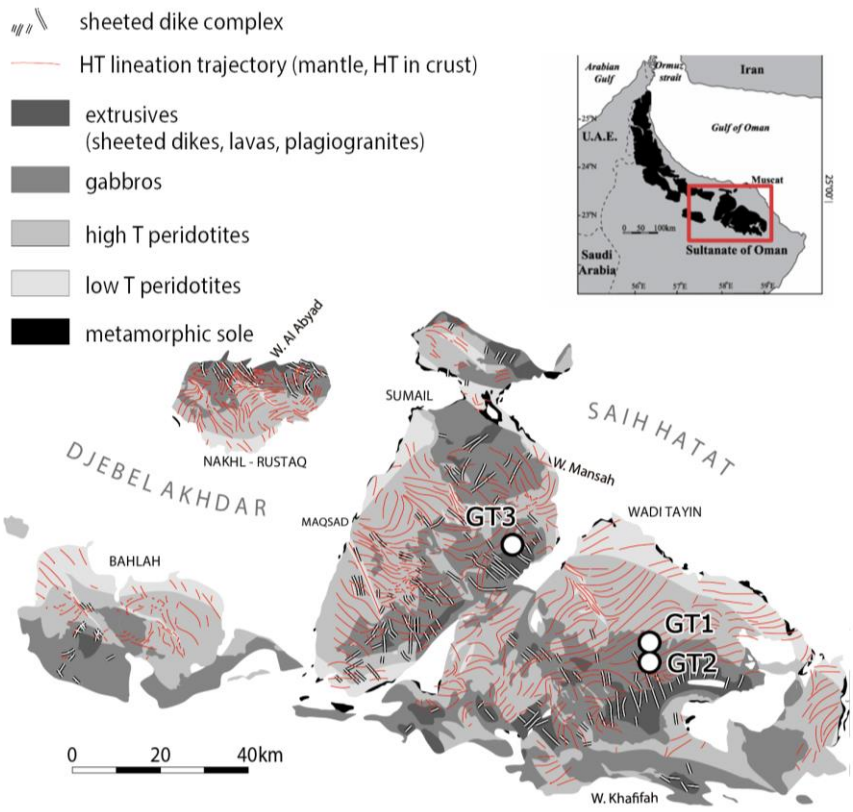

Figure 7.1 – Geological map of the southern massifs of the Oman ophiolite, showing the drill site locations of the Oman Drilling Project (modified from Nicolas et al. (2000).

I Scientific Party of OmanDP for two months aboard the Japanese drillship *Chikyū* where I worked on palaeomagnetic measurements and analyses on all three holes. The *Chikyū* laboratories were used to describe and analyse the OmanDP cores using its state of the art facilities, while the ship was in port in Japan, as part of a unique collaboration between ICDP and the International Ocean Discovery Program. This chapter covers the most important findings from the proceedings chapters written aboard the ship, as well as post-cruise analysis. Data were jointly acquired by Louise Koornneef, Jessica Till, Andrew Horst and Yoichi Usui (the Phase I palaeomagnetic team for OmanDP), and hence the content of this chapter should be considered to be jointly owned with shared intellectual property rights. Palaeomagnetic analysis and susceptibility results are described per hole, as well

as observations about the magnetic mineralogy through petrography and Curie temperature determinations. Because borehole imagery was available for holes GT1 and GT2, we applied a reorientation to the demagnetization results, rotating the initially unoriented drill cores back to their in situ orientation.

Figure 7.2 – Photographs taken at drill site GT3, showing the drill rig cores in the foreground that are ready to be packed, a group of Phase I scientists describing cores, and the core scanner.

7.2 – Remanent magnetizations

Due to a malfunctioning SQUID on the *Chikyū* shipboard long-core cryogenic magnetometer, palaeomagnetic measurements were exclusively made on discrete samples for holes GT1, GT2, and GT3 using a Natsuhara Giken SMD-88 fluxgate spinner magnetometer. Measurements of remanence magnetizations were made on a total of 656 discrete 20 mm-sided cubic samples that were taken from the working-half cores of the three holes, covering roughly 1200 metres in

cumulative length of layered, foliated, and varitextured gabbros, and dykes. A quarter of these samples were thermally demagnetised and the remaining samples were demagnetised using a stepwise increasing alternating field in order to isolate the characteristic remanent magnetization (ChRM) direction by the use of principal component analysis (PCA).

Discrete samples taken by the OmanDP Physical Properties team were subjected to overnight heating at 105°C (a requirement for moisture and density analysis), after which they were subjected to alternating field demagnetization. In order to compare the results of thermal demagnetization and alternating field demagnetization, we sampled directly next to the samples of the physical properties team. The resulting NRM directions and intensities of these sister samples are very similar (Figure 7.3), from which we conclude that low-

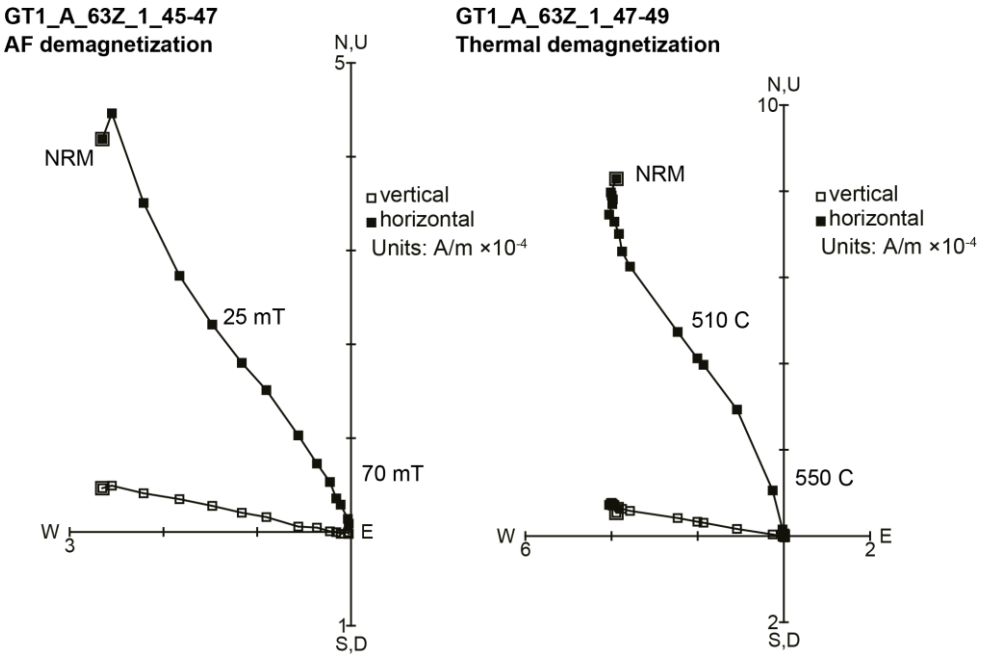

Figure 7.3 – Zijderveld diagrams of those sister samples that were subjected to alternating field and thermal demagnetization. Note the similarity between the demagnetization paths.

temperature laboratory heating did not significantly affect the magnetic mineralogy or remanence.

7.2.1 – Remanence results for OmanDP Hole GT1

OmanDP Hole GT1 entirely recovered layered gabbros from the Wadi Gideah locality, and discrete samples were mostly taken from olivine gabbros with some samples taken from cataclastic zones. Natural remanent magnetization (NRM) intensities vary between 8.8 $x10^{-4}$ A/m for a sample taken from a cataclastic zone to 10.7 A/m for samples taken from a zone with a high modal abundance of olivine (Figure 7.4). The mean intensity of all samples is 0.51 A/m. All reported inclinations for GT1 are presented in the core coordinate reference frame, and because the hole was drilled vertically inclinations are the same as in the geographic reference frame. Declination data are also in the core reference frame, but cores were not azimuthally oriented during drilling and individual core pieces were free to rotate in the core barrel so declination data are initially unconstrained in the geographic reference frame.

Samples subjected to thermal demagnetization were nearly entirely demagnetised by 600°C with the sharpest changes in intensity happening either between 510-530°C or 550-580°C (Figure 7.5a-b). In only a few samples the remanence directions varied slightly between these two unblocking temperature ranges (e.g. 16Z-02, Figure 7.5a), suggesting the presence of overlapping components with similar unblocking temperatures. The component with the highest unblocking temperature was interpreted as the ChRM.

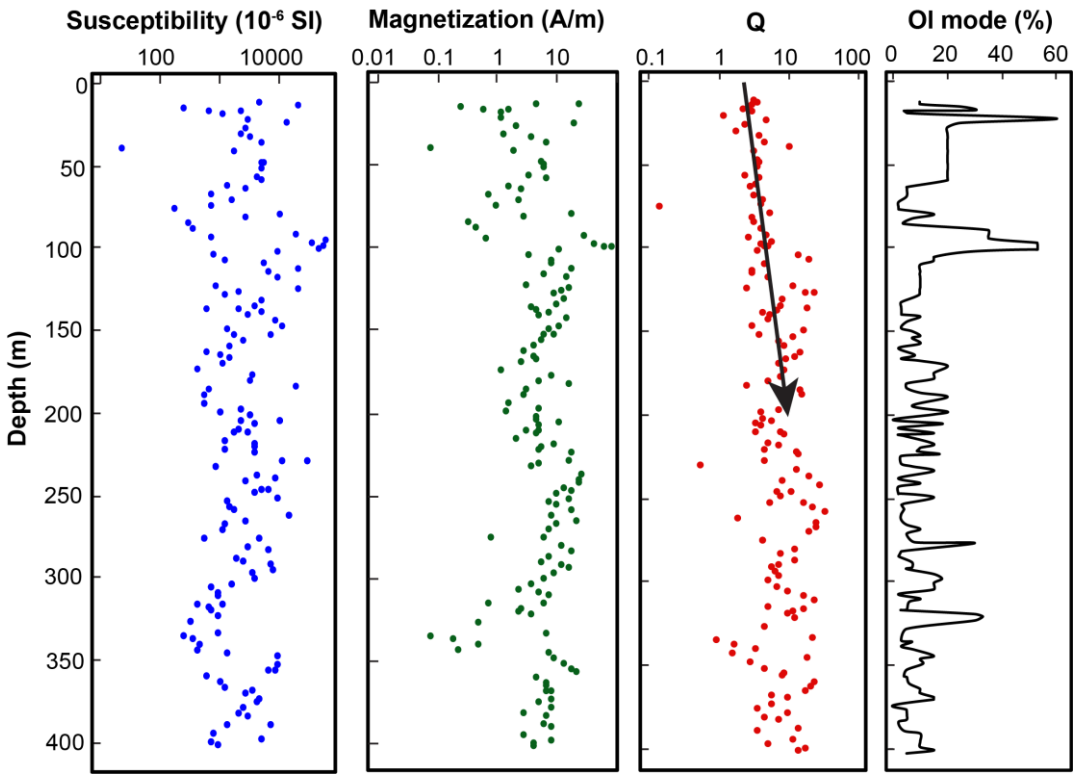

Figure 7.4 – Downhole plots of (left to right) bulk susceptibility, NRM intensity, Königsberger values (Q), and the olivine mode (%) for hole GT1.

Alternating field demagnetization provided very similar results to thermally demagnetised specimens (Figure 7.3), including changes in remanence directions up to high fields (Figure 7.5c-d) indicating that these two methods have isolated the same remanence components. Large low-coercivity components are absent in samples from Hole GT1, suggesting that the cores are not significantly affected by drilling-induced overprints. The median destructive field (MDF) ranges between 11 and 54 mT with a mean MDF of 25 mT.

7.2.2 – Remanence results for OmanDP Hole GT2

OmanDP Hole GT2 covers samples from the foliated gabbros down to the layered gabbros in the Wadi Gideah locality. Because this hole was drilled with a 60° plunge, any magnetic inclinations in this section are reported in core

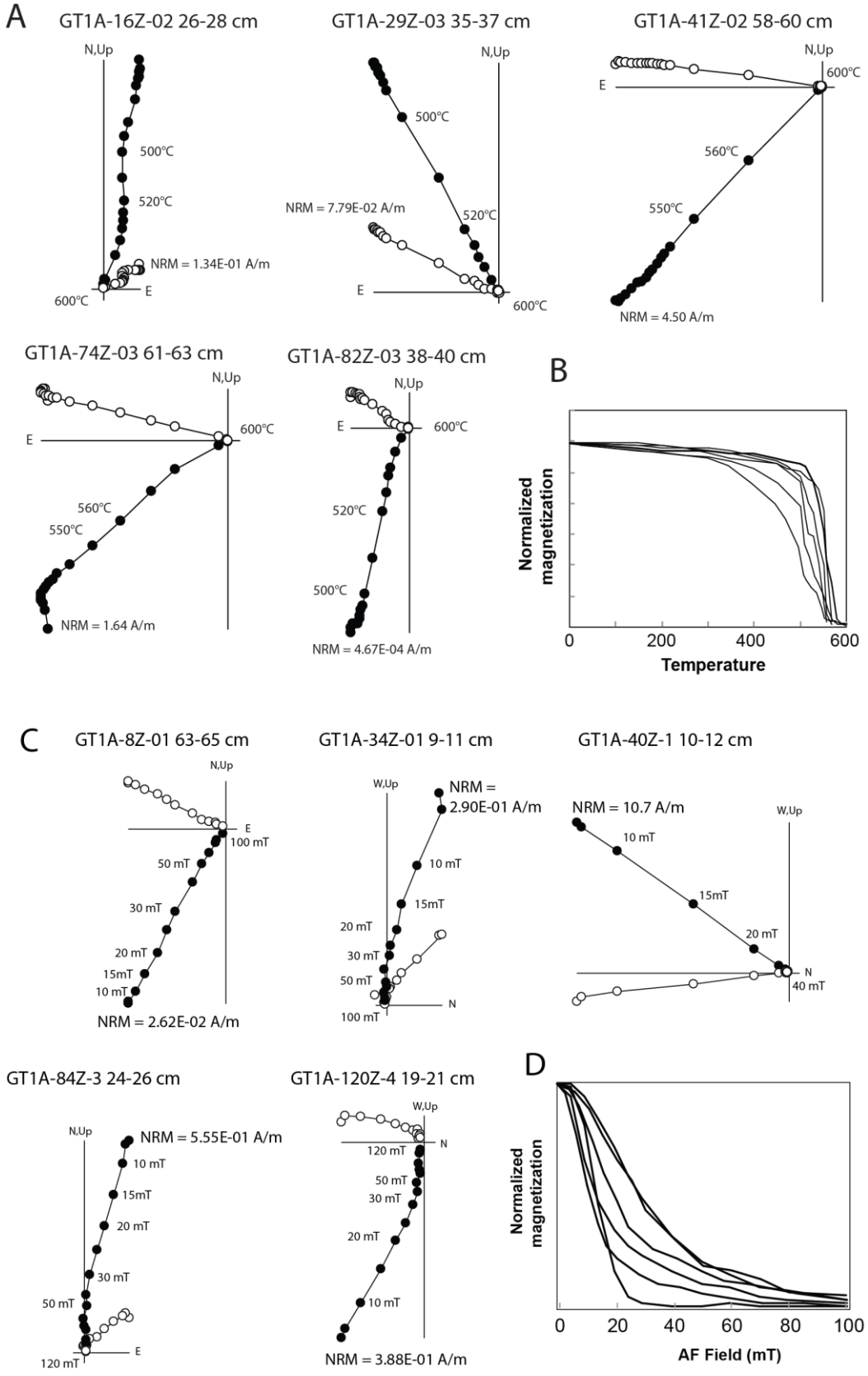

Figure 7.5 – Hole GT1: (a+c) Representative Zijderveld diagrams displaying behaviour of magnetic remanence directions during thermal demagnetization and alternating field demagnetization. (b+d) Normalised intensity curves as a function of temperature (b) and applied field (d).

coordinates that do not transfer to geographic coordinates. Core reorientation will later be applied that restores the samples to a geographic reference frame.

NRM intensities vary from 6.6 x10^{-3} A/m to 6.9 A/m with a mean intensity of 0.11 A/m (Figure 7.6). Thermal demagnetization results are very similar to those of Hole GT1, where most samples are demagnetised by 600°C with major decreases in remanence happening between 500-580°C (Figure 7.7a-b). The majority of samples only show minor changes in magnetization up to 475°C, however some samples also show minor decreases in magnetization at 350°C (example in Figure 7.7a, 94Z-3). The component with the highest unblocking temperature was chosen as the ChRM.

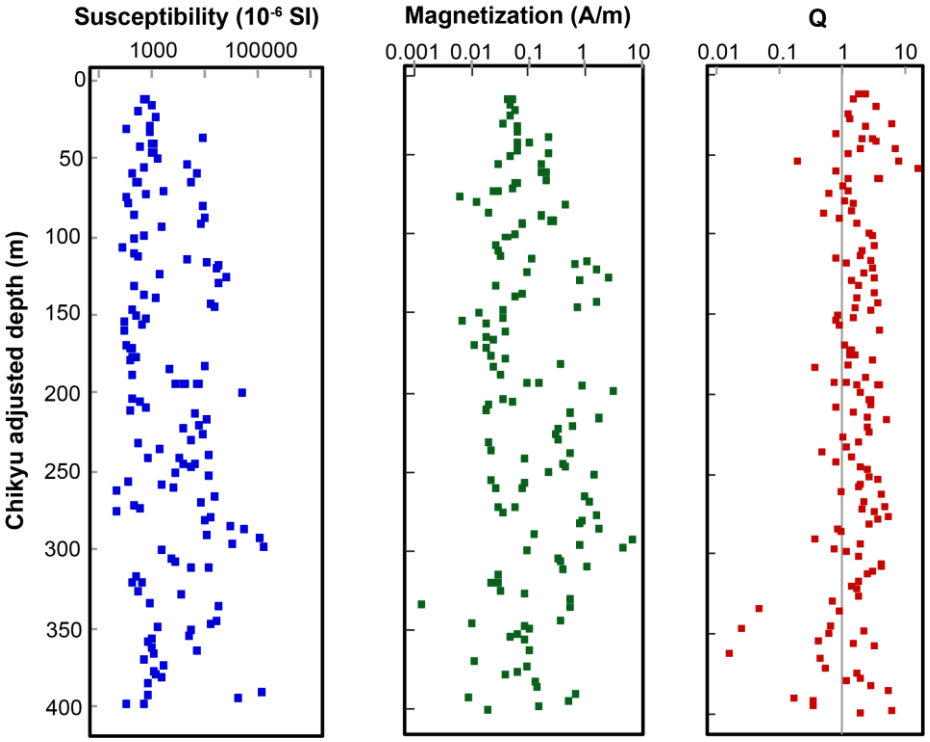

Figure 7.6 – Downhole plots of (left to right) bulk susceptibility, NRM intensity, Königsberger values (Q) for hole GT2.

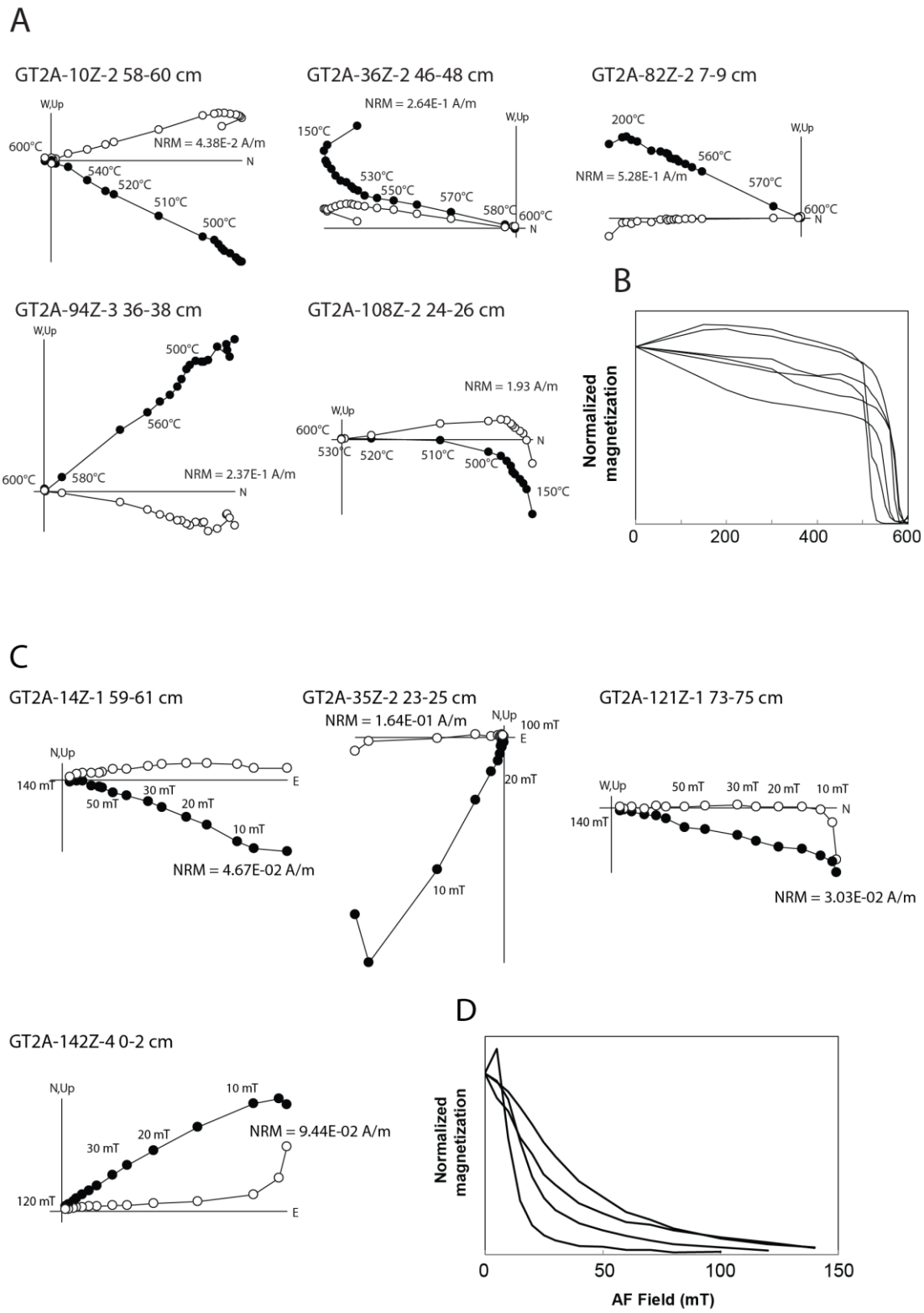

Figure 7.7 – Hole GT2: (a+c) Representative Zijderveld diagrams displaying behaviour of magnetic remanence directions during thermal demagnetization and alternating field demagnetization. (b+d) Normalised intensity curves as a function of temperature (b) and applied field (d).

Alternating field demagnetization was as effective as thermal demagnetization at removing the majority of magnetization, however some samples still retained some of their remanence even after applying the maximum field of 180 mT that the AF demagnetizer could produce (Figure 7.7c-d). The MDF ranges more widely than in Hole GT1 with values between 5 and 75 mT but has a similar mean MDF of 23 mT.

7.2.3 – Remanence results for OmanDP Hole GT3

OmanDP Hole GT3 was drilled at a different locality to GT1 and GT2 at Wadi Abdah and covers samples from sheeted dykes at the top down to varitextured gabbros. Whereas borehole logging data and imagery were available for Holes GT1 and GT2, it is absent for Hole GT3, and therefore all magnetic inclinations for Hole GT3 are reported in the core reference frame (the hole was drilled vertically).

NRM intensities vary from 6.2 $x10^{-4}$ A/m to 5.6 A/m with a mean intensity of 5.7 $x10^{-2}$ A/m, significantly lower than GT1 and GT2 (Figure 7.8). NRM intensities vary with depth from lower intensities at the top (sheeted dykes) to higher values at the bottom (varitextured gabbros).

Similar to both Holes GT1 and GT2, samples were entirely demagnetised by 600°C with the most significant decreases in magnetization happening between 500-580 °C and with some samples showing minor decreases at 350 °C (Figure 7.9a-b). Alternating field treatment successfully demagnetizes most samples, but just like in Hole GT2 fails to remove all of the remanence at high

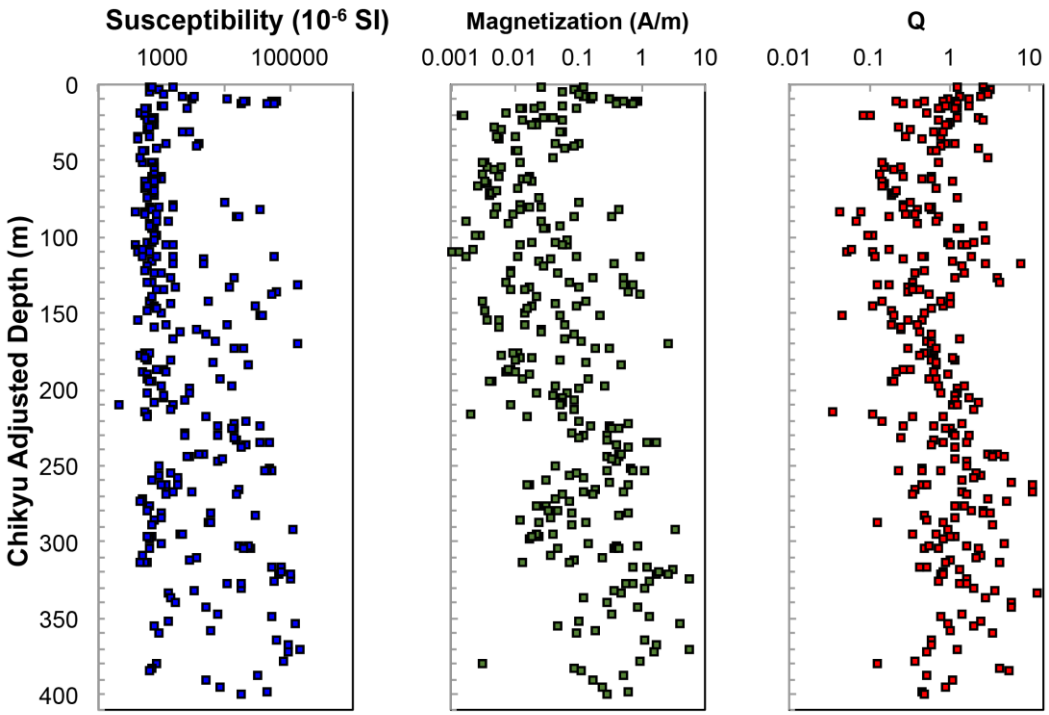

Figure 7.8 – Downhole plots of (left to right) bulk susceptibility, NRM intensity, Königsberger values (Q) for hole GT3.

field steps (Figure 7.9c-d) and generally exhibited very noisy demagnetization results at field steps higher than 80 mT. The MDF vary between 2.3 and 63 mT, with a mean MDF of 29 mT.

7.2.4 – Interpretation of remanence results

The distributions of both the NRM and ChRM inclinations in discrete samples from Holes GT1 to GT3 are shown in Figure 7.10, which combines ChRM data from thermal and alternating field experiments.

The majority of both the NRM and ChRM vectors for Hole GT1 have shallow, negative inclinations with only a few samples showing positive inclinations (Figure 7.10a-b – GT1). For Hole GT2 the NRM and ChRM orientations

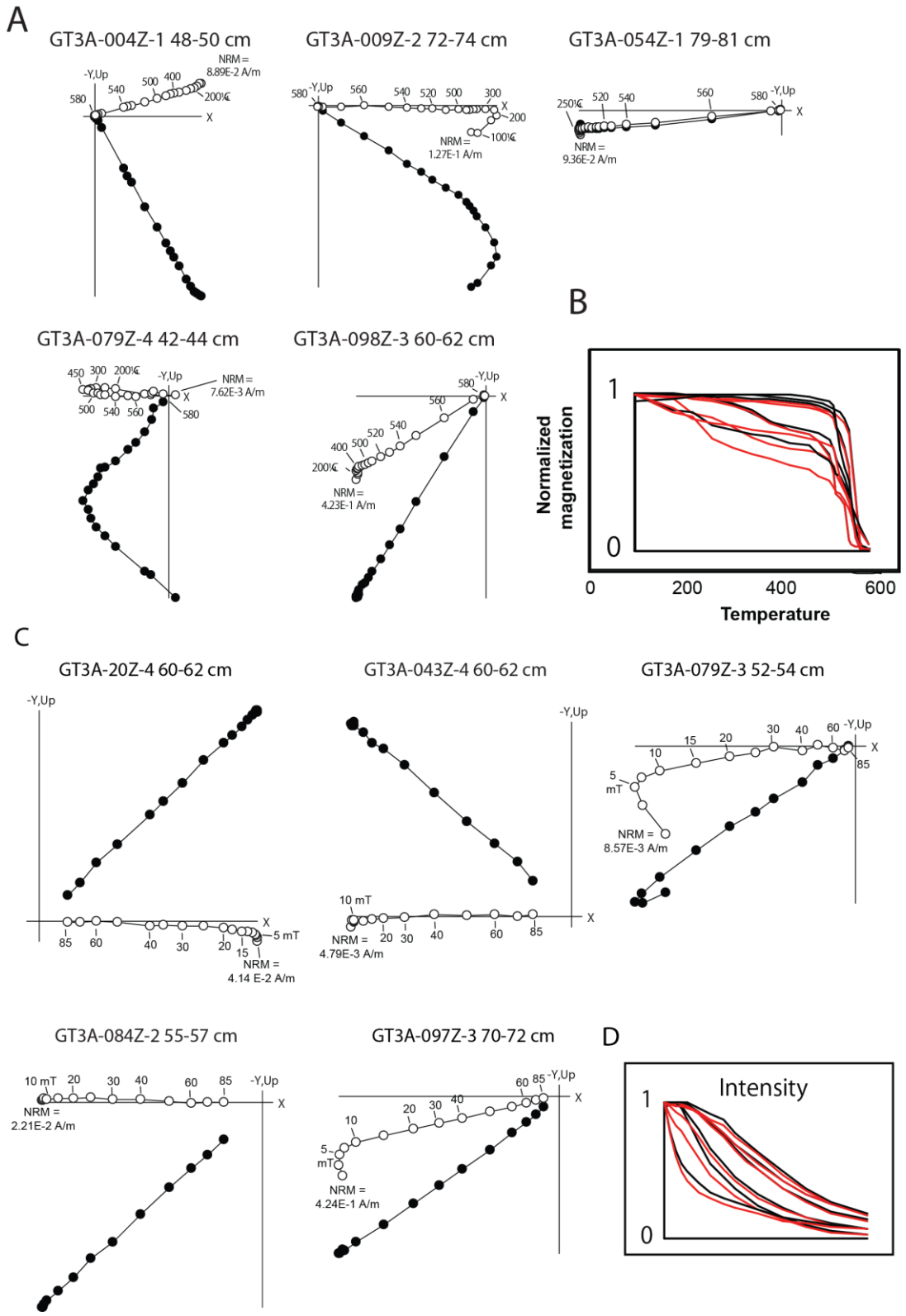

Figure 7.9 – Hole GT3: (a+c) Representative Zijderveld diagrams displaying behaviour of magnetic remanence directions during thermal demagnetization and alternating field demagnetization. (b+d) Normalised intensity curves as a function of temperature (b) and applied field (d).

vary with depth, changing from negative and shallow inclinations at the top of the hole to sub-horizontal inclinations around 200-250 m and to positive inclinations at the bottom. The NRM inclinations appear to be more scattered at the bottom of the hole than the ChRM inclinations (Figure 7.10 – GT2). Hole GT3 shows consistently low positive NRM and ChRM inclinations from the top to the bottom of the hole, which become more scattered from 75 m downward (Figure 7.10 – GT3) with moderate to steep inclinations.

NRM and ChRM inclinations in the upper half of Holes GT1 and GT2 are similar, despite the different orientations of the holes (Hole GT1 was drilled vertically, Hole GT2 was drilled at a 60° plunge). Hole GT2 was purposely drilled perpendicular to the orientation of the layered gabbros at that location, so that the trend of Hole GT2 is perpendicular to the palaeomagnetic remanence declination that was observed in outcrop samples from the same area (Luyendyk and Day, 1982; Weiler et al., 2000). Therefore, no significant difference in magnetic inclination angles is apparent in the Hole GT2 core reference frame.

Mean inclinations were calculated using the maximum likelihood method of Arason and Levi (2010) and are presented in Table 7.1.

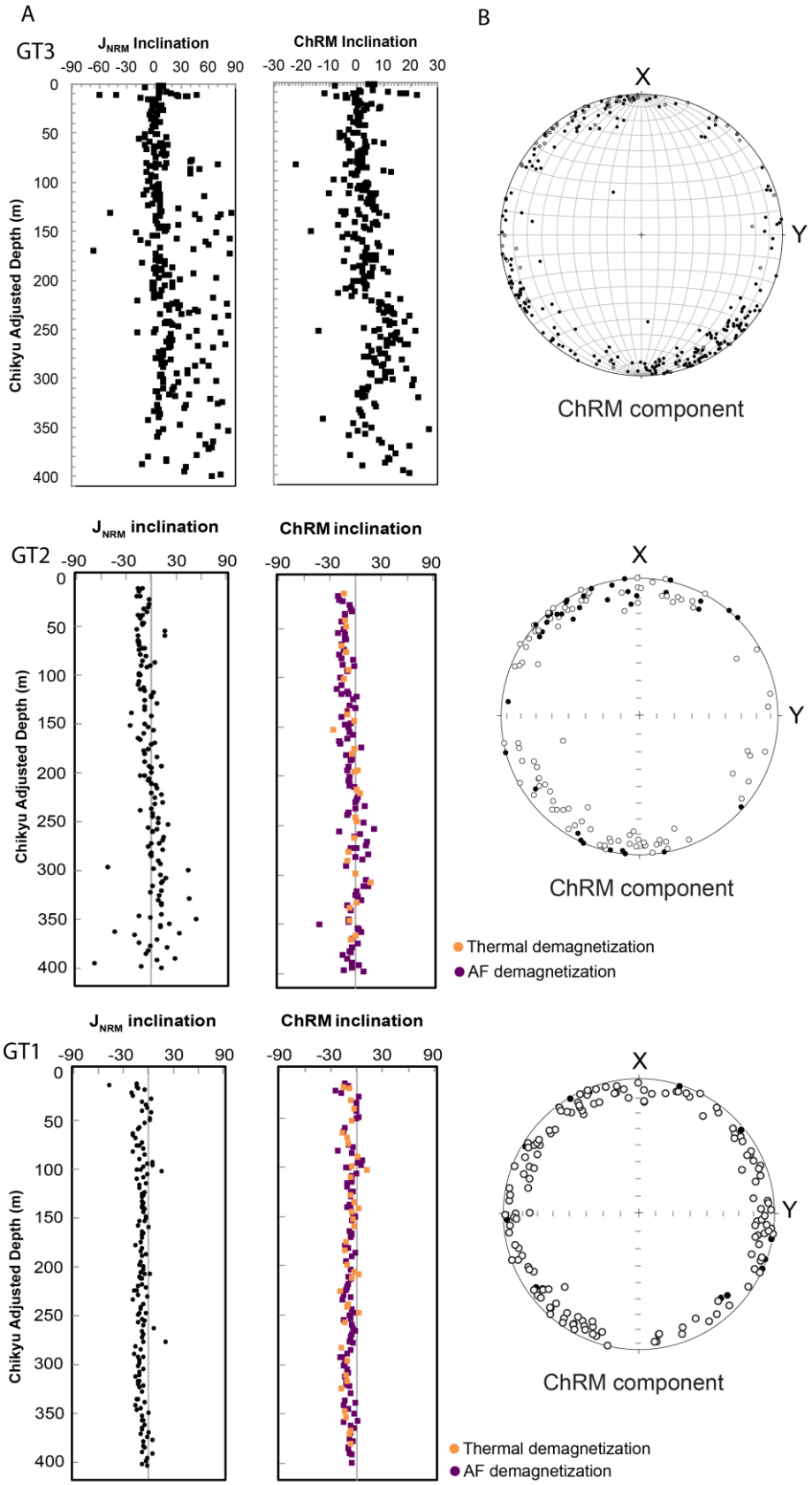

Figure 7.10 – (a) Downhole plots of NRM and ChRM inclinations determined from principal component analysis for the three holes. (b) Stereographic projections of remanence component orientations identified by principal component analysis. Solid black dots represent lower hemisphere directions, open dots represent the upper hemisphere directions.

Table 7.1 - Inclination-only statistics after Arason and Levi (2010). N = number of samples, Mean Inc = mean inclination, k = precision parameter, α95 = radius of 95% confidence, θ = angular standard deviation.

	Arason and Levi (2010)				
	N	**Mean Inc**	**k**	**α95**	**θ**
GT1					
ChRM	147	-7.28	98.01	1.18	8.17
NRM	147	-6.6	71.01	1.39	9.6
GT2					
ChRM	137	-5.62	36.1	2.03	13.48
NRM	151	-1.98	14.98	3.07	20.99
GT3					
ChRM	286	5.00	54.56	1.14	10.96
NRM	277	17.84	5.16	4.14	36.16

Similar low inclinations are found for Holes GT1 and GT2 for the ChRM (-7.3° and -5.6° respectively), the values of which are similar to those reported from outcrop investigations of previous studies (Weiler, 2000; Morris et al., 2016; van Hinsbergen et al., 2019) as well as results from this study (see Chapter 5), that find positive inclinations after applying a tilt correction. The ophiolitic complex at Wadi Gideah is considered to be tilted by 20° to the south/southeast (160°) according to the mapped field structures of the crust-mantle transition, as well as the orientation of layered gabbros from the sampled area. It is therefore possible that the negative inclinations measured in the Hole GT1 and Hole GT2 samples would revert to shallow positive inclinations after applying a tilt correction.

The inclination results for Hole GT3 are similar to Holes GT1 and GT2, showing a shallow positive inclination for the ChRM of 5.0° (Table 7.1). These inclinations are similar to inclinations reported from previous studies (Weiler, 2000; Morris et al., 2016; van Hinsbergen et al., 2019) as well as results from this study (see Chapter 5).

7.3 – Magnetic susceptibility and its anisotropy

7.3.1 – Bulk magnetic susceptibility

The downhole profiles of bulk magnetic susceptibility and the Königsberger ratios (*Q*) for OmanDP Holes GT1, GT2, and GT3 can be found in Figures 7.4, 7.6, and 7.8 respectively. In all three holes, the downhole profiles of bulk magnetic susceptibility and NRM intensity (magnetization in A/m) are similar, suggesting that the variation seen in the NRM intensity is controlled by the concentration of magnetic minerals rather than differences in grain size and mineralogy.

The majority of samples from Hole GT1 exhibit Königsberger ratios higher than 1 (Figure 7.4) with a mean ratio of 6.3, indicating that remanent magnetization dominates over induced magnetization. A downhole trend of increasing Königsberger values suggests that there may be some changes in the magnetic grain size or mineralogy through the core.

Whereas most samples from Hole GT2 also exhibit Königsberger ratios higher than 1 with a mean of 1.8, a small but significant proportion of samples fall below 1 (Figure 7.6). This indicates that induced magnetization has a greater contribution to the total magnetization in Hole GT2 than in Hole GT1. From 300 m downhole an increasing number of samples with a small Königsberger value is found, suggesting either a change in grain size distribution or a change in the magnetic mineralogy at the bottom of the hole.

The mean Königsberger value for Hole GT3 is 0.73, with approximately 60% of the samples having a value lower than 1 (Figure 7.8). This indicates that induced magnetization is predominant in the net magnetization of the rocks in this hole. From 200 m downwards a shift to larger Königsberger values can be seen, indicating that remanent magnetization is more dominant in the magnetization at the lower half of the hole, suggesting a shift in either grain size distribution or magnetic mineralogy down the hole. This seems likely as from 200 m downwards a change in lithology is seen in the hole from dykes to varitextured gabbros.

7.3.2 – Anisotropy of magnetic susceptibility

Anisotropy of magnetic susceptibility (AMS) was measured for all discrete samples from Holes GT1, GT2, and GT3 prior to demagnetization to characterise the magnetic fabrics present in the samples. The results can be seen in Figures 7.11 through 7.13; all anisotropy orientations are shown in a core reference frame. Throughout the three holes specimen magnetic fabric shapes vary widely from strongly prolate (T = -0.97) to strongly oblate (T = 0.95).

Samples in the upper 150 m of Hole GT1 tend to be oblate, whereas any samples below are mainly prolate (Figure 7.11a). When looking at the shape parameter T vs. the anisotropy degree P' however it appears that most samples are triaxial in shape (Figure 7.11c). A correlation between the anisotropy intensity and bulk susceptibility can also be seen (Figure 7.11b), which indicates that samples containing a greater quantity of magnetic particles also tend to be more

anisotropic, which may in turn reflect a strong preferred orientation of secondary magnetite during growth in altered olivine grains (see section 7.3.1). K_{max} orientations can be seen as consistently shallow (Figure 7.11d) whereas the K_{min} orientations are clustered near the core axes; this defines a near-horizontal magnetic foliation.

Samples from Hole GT2 tend to be mostly triaxial in shape (Figure 7.12c) and show a similar correlation between the anisotropy intensity and bulk susceptibility as found in Hole GT1. K_{min} orientations, the poles to magnetic foliation, are scattered around an axis that is sub-parallel to the core axis (Figure 7.12d). K_{max} orientations represent magnetic lineations that exhibit plunges between 0 and 82° with a mean plunge of 22° through the hole. At 150 m depth an abrupt change in the inclination angles can be seen (Figure 7.12a) that coincides with a major fault zone found in the hole.

The variability in the anisotropy degree in Hole GT3 has a much smaller range than in Holes GT1 and GT2 (Figure 7.13a-b) and is triaxial in character (Figure 7.13a-c). K_{max} and K_{min} orientations appear to be highly scattered (Figure 7.13d), however K_{max} axes (representing magnetic lineations) display a skewed distribution trending more towards lower plunges with a mean value of 29°. Plunges of both K_{max} and K_{min} vary widely from 0 to 90° and are scattered with a nearly uniform distribution.

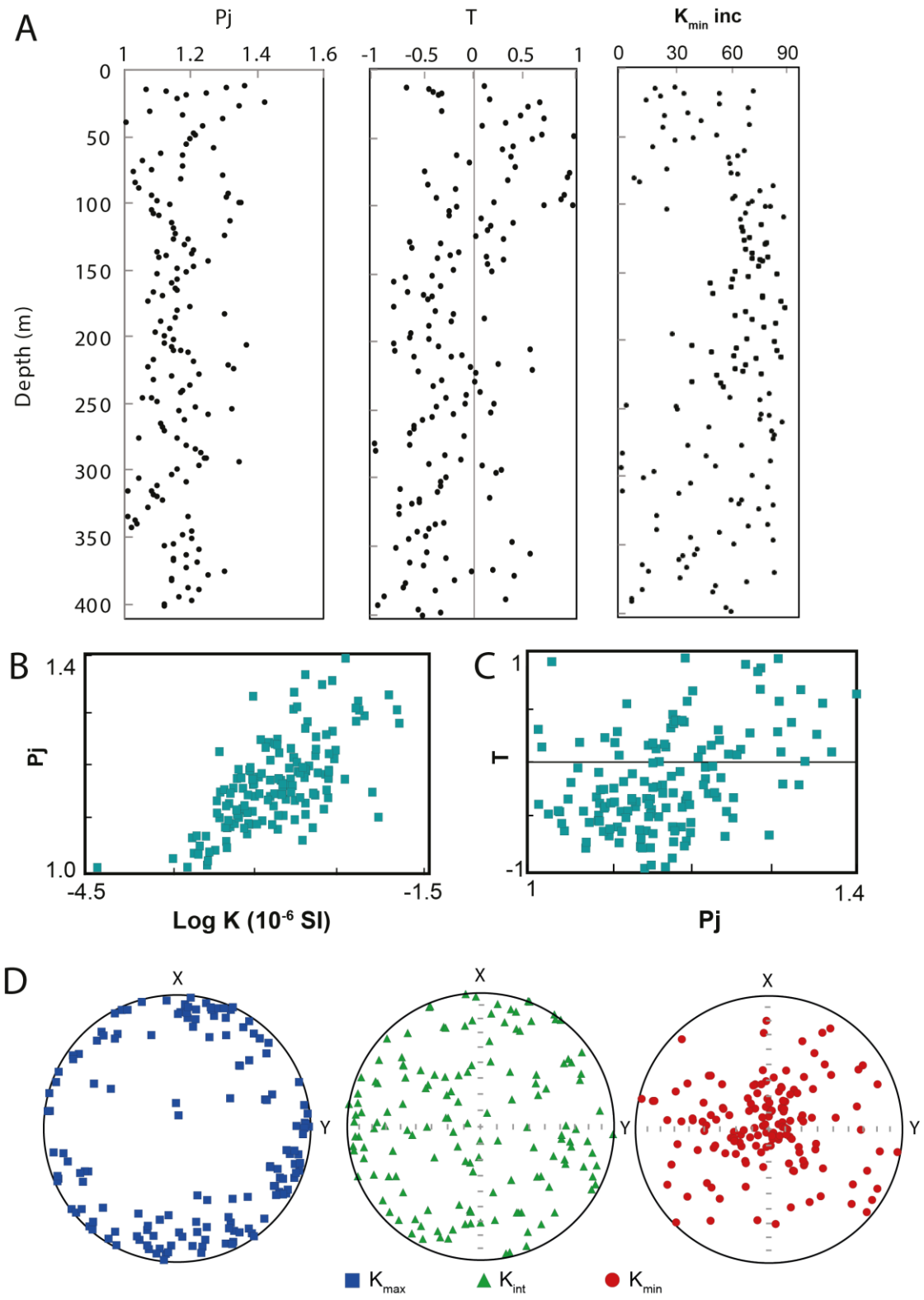

Figure 7.11 – GT1: (a) Downhole plots of magnetic anisotropy intensity (P'), shape (T), and K_{min} orientation. (b) Anisotropy degree against bulk susceptibility. (c) Shape parameter against anisotropy degree. (d) Stereographic projections of magnetic anisotropy principal axes plotted on the lower hemisphere in a core reference frame.

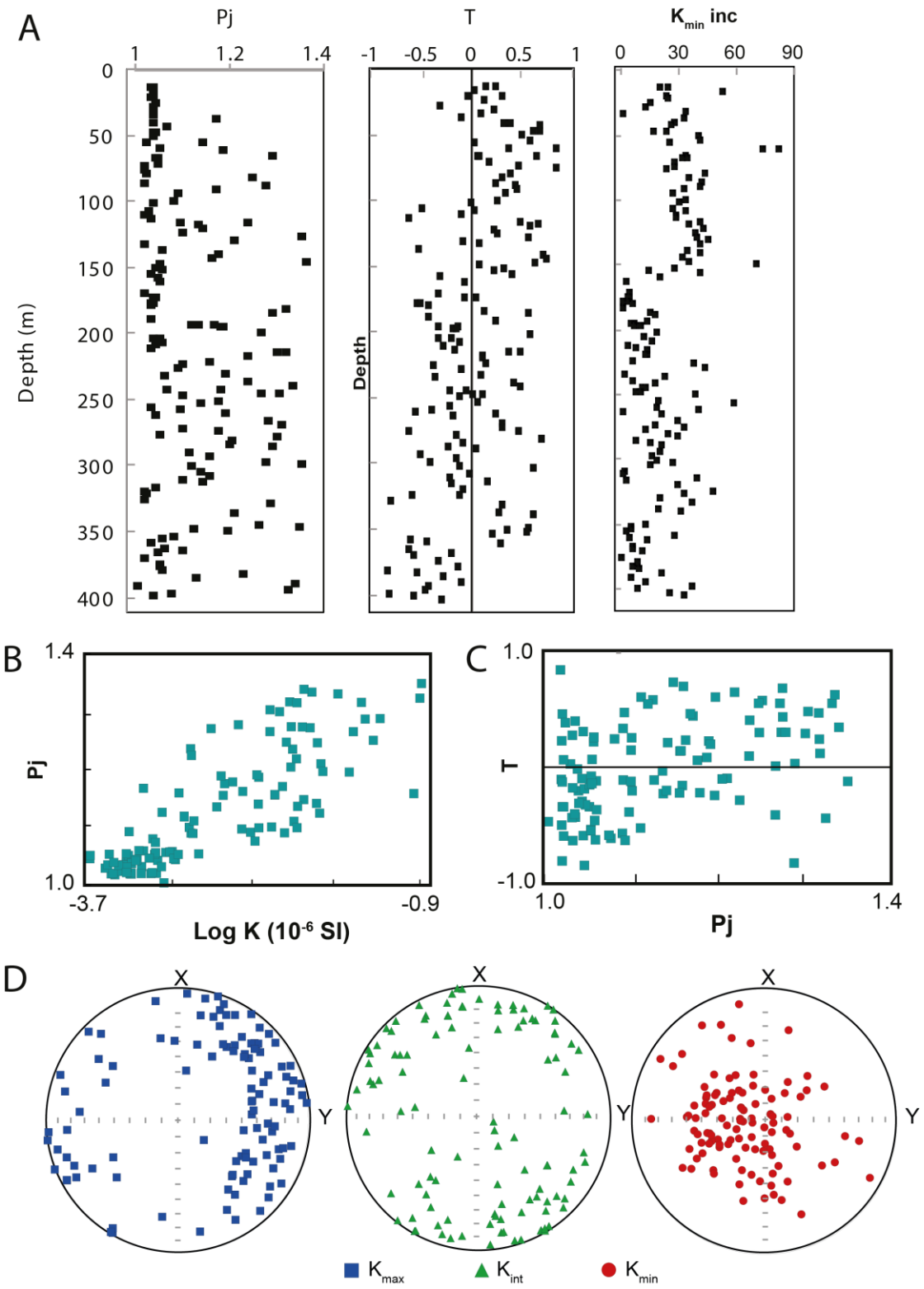

Figure 7.12 – GT2: (a) Downhole plots of magnetic anisotropy intensity (P'), shape (T), and K_{min} orientation. (b) Anisotropy degree against bulk susceptibility. (c) Shape parameter against anisotropy degree. (d) Stereographic projections of magnetic anisotropy principal axes plotted on the lower hemisphere in a core reference frame.

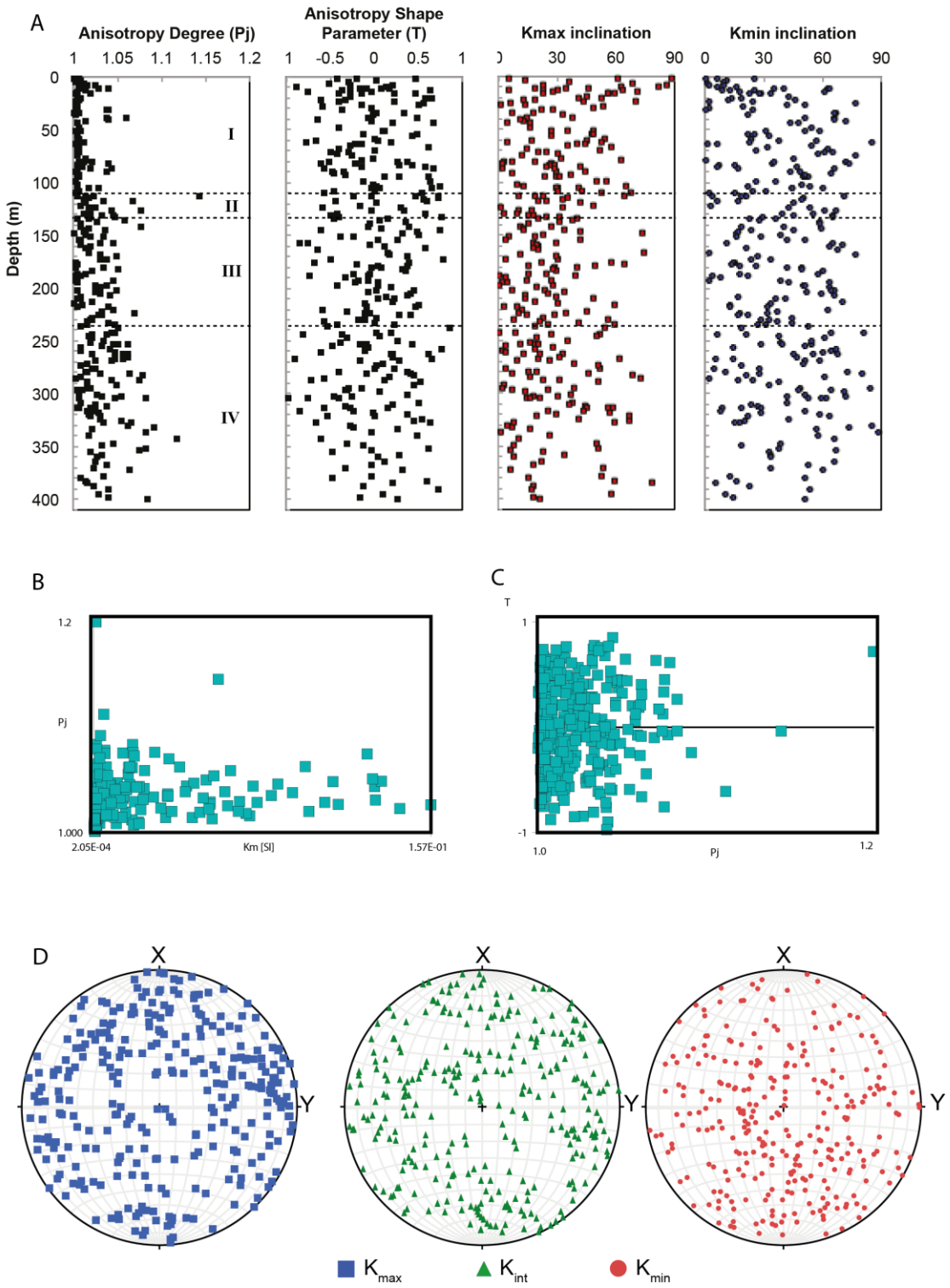

Figure 7.13 – GT3: (a) Downhole plots of magnetic anisotropy intensity (P'), shape (T), and K_{min} orientation. Dashed lines indicate encountered sequences: (I) Upper sheeted dyke sequence, (II) Upper gabbro seq., (III) Lower sheeted dyke seq., (IV) Lower gabbro seq. (b) Anisotropy degree against bulk susceptibility. (c) Shape parameter against anisotropy degree. (d) Stereographic projections of magnetic anisotropy principal axes plotted on the lower hemisphere in a core reference frame.

7.4 – Magnetic mineralogy

In all three holes, the high values of magnetic susceptibility (Figures 7.4, 7.6, 7.8), high coercivities around 100 mT, and high unblocking temperatures around 580°C (Figures 7.5, 7.7, 7.9) indicate that fine-grained magnetite is likely the dominant magnetic mineral in most of our samples. Lower unblocking temperatures around 500-530 °C may be the result of differences in the magnetic grain size or slight variations in magnetite composition, such as cation substitution or solid solutions with other spinel group phases (Moskowitz et al., 1998). Observations were made on a small number of representative thin sections in reflective light to help identify and understand the carrier of magnetic remanence in samples of holes GT1, GT2, and GT3.

7.4.1 – Petrography

Figure 7.14a-f shows a selection of reflected light microscopy observations made on samples from OmanDP Hole GT1 (layered gabbros). Opaque particles were identified in most samples that contain primary oxide minerals, often occurring together with yellow-coloured sulphides (pyrite) (Figure 7.14a). We also commonly find oxide occurrences in mesh-textured networks in altered olivine grains (Figure 7.14b-f). In addition, long strings or bands, which are likely magnetite or similar Fe-oxides, can be found as very fine isolated particles and even large oxide particles that may be aggregates of smaller grains (Figure 7.14d).

Figure 7.14g-j shows a selection of reflected light microscopy observations made on samples from OmanDP Hole GT2 (layered to foliated gabbro transition).

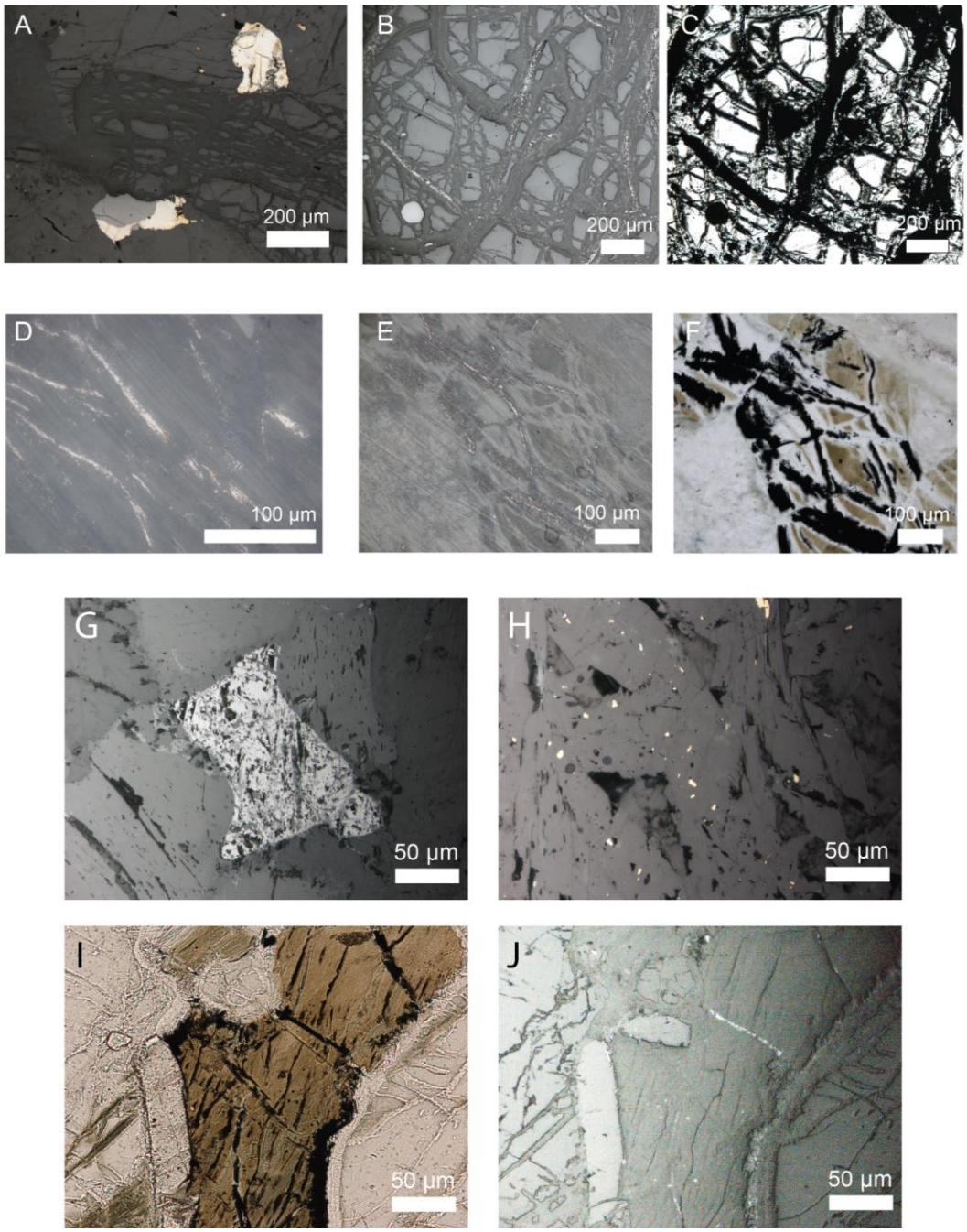

Figure 7.14 – Examples of: (a) Primary interstitial Fe-oxides occurring in association with Fe-sulphide minerals (reflected light), (b, d, e) Fine-grained oxides in altered olivine grains (reflected light), (c, f) Mesh texture of opaque phases in altered olivine grains (plane-polarised light), (g) Primary Fe-oxide grain containing a modified oxyexsolution texture (reflected light), (h) Pale yellow sulphide grains (reflected light), (i) Opaque mesh texture in an altered olivine grain (plane-polarised light), (j) Fine-grained oxides in the same region as shown in (i) (reflected light).

Large-scale opaque particles, interpreted as primary (titano)magnetite, are more abundant in Hole GT2 than in Hole GT1. Yellow sulphide minerals, interpreted as pyrrhotite based on their colour, were observed in several samples which may carry a small proportion of the magnetic remanence when it occurs in the ferromagnetic monoclinic form (Fe_7S_8). Drops in magnetization intensity around 350 °C found in thermally demagnetised samples are consistent with the Curie temperature of pyrrhotite at 320 °C. Just like in samples from Hole GT1, similar mesh textures of secondary opaque minerals are found within altered olivines in Hole GT2, which consist of fine-grained, elongated aggregations that could contribute to the well-defined magnetic anisotropy measured for Hole GT2 samples.

7.5 – Simple restoration of the AMS data to a palaeomagnetic reference frame

A first-order restoration of the AMS data to a palaeomagnetic reference frame was achieved by rotating corresponding specimen ChRMs to a consistent declination of 000° around the core axis. This approach ignores the effects of palaeosecular variation (that is known from the analysis presented in Chapter 5 to be significant in these sequences), but has often been adopted in the analysis of data from originally unoriented cores.

The results for OmanDP Holes GT1, GT2, and GT3 can be seen in the stereographic projections of Figure 7.15. After rotation, the AMS fabrics of Holes

GT1 and GT2 display a good clustering of the principal susceptibility directions with K_{min} axes clustering around the core axis and K_{max} axes clustering in two groups that dip shallowly in opposite directions, oriented parallel to the layering in the core (Figure 7.15a-d). These results are comparable to AMS results from our surface samples from Wadi Gideah (see section 4.5.6). In both holes we find abrupt changes in K_{max} and K_{min} which seem to switch their down-dip azimuth from +Y to –Y and vice versa, the most notable change happening at 150 m in Hole GT2. Absolute reorientation of each core using borehole imagery is required for further interpretation of these results (see section 7.6).

Simple rotation provides better clustering of principal AMS axes in GT3 than before (compare Figure 7.15e and 7.13). Results are shown in Figure 7.15e for the three sampled lithologies in Hole GT3; dyke interiors, dyke margins, and gabbros. To tell if the variations seen between the different lithologies are caused by changes in petrofabric orientations we would need a more detailed analysis. However, absolute reorientation (achieved for Holes GT1 and GT2) is not possible in the case of Hole GT3 as no downhole imagery and logging data is available for this hole.

A recent paper by Morris et al. (2019) presented AMS results from layered and foliated gabbros of Wadi Khafifah, a site just west of Holes GT1 and GT2. Our reoriented AMS results show similar results to those of Morris et al. (2019), who found an ENE-WSW, trending, subhorizontal orientation for the K_{max} axes. As also reported

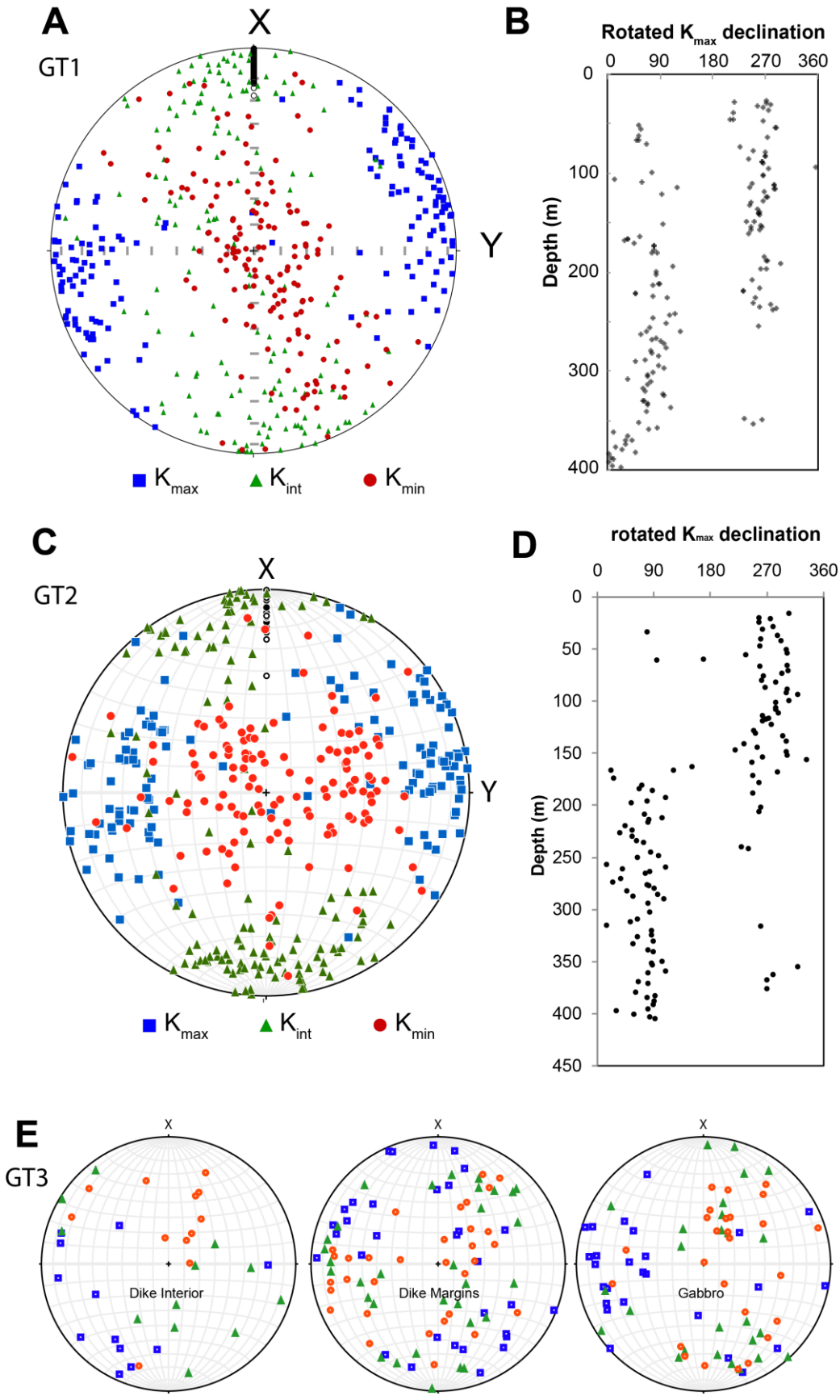

Figure 7.15 – (a, c, e) Stereographic projections of magnetic anisotropy orientations after azimuthal rotation of ChRM declinations around the core axis to a reference palaeomagnetic declination of 000°. (b, d) Downhole plots of rotated K_{max} declinations.

earlier in section 4.5.6, these AMS results show that the magnetic fabrics in the layered gabbros are aligned parallel to the measured layering in the gabbros, and their K_{max} axes follow the same trend as the regional-scale magmatic flow away from an inferred spreading ridge (Figure 4.13). Another explanation is that this alignment is caused by postintrusive deformation of a melt-rich crystal mush resulting from mechanical coupling with the underlying mantle during spreading (Nicholas et al., 1994; Morris et al., 2019).

7.6 – Core reorientation using borehole imagery

As soon as cores are recovered in the field, a red line was drawn on the outside indicating the X direction of the core reference frame used to determine ChRM directions (section 7.2). Core pieces are re-aligned in the field wherever possible to create contiguous sections, however sometimes this is impossible e.g. due to parts of the cored being lost or too broken to reassemble confidently. The ChRM directions in the core reference frame can therefore show a wide variation of declinations as a result of core sections rotating relatively to each other during drilling.

When drilling of a hole is finished, borehole imagery can be obtained by lowering a camera into the hole. The camera not only takes a continuous image of the walls of the borehole, but also measures any change in borehole plunge and rotation of the camera itself. If no rotation happens, the camera stays locked in place and a line downwards on the image will always have the same direction "X". On the resulting unrolled borehole imagery, the left side of the borehole will

therefore be X = 0° and the right side will be X = 360° (if no rotation occurs) (Figure 7.16a).

Images of the unrolled borehole wall can then be aligned with unrolled scanned images of core sections, scanned in the field on a rotating scanning surface after the red line has been marked on the core (Figure 7.16b). By aligning structural features such as veins and fault/fracture lines in the core with the corresponding features in the oriented images we can restore contiguous core intervals to their initial orientation (Figure 7.17).

Figure 7.16 – (a) Example of a continuous borehole image. (b) Core section scans that have been aligned based on their red line and their features (veins and fractures).

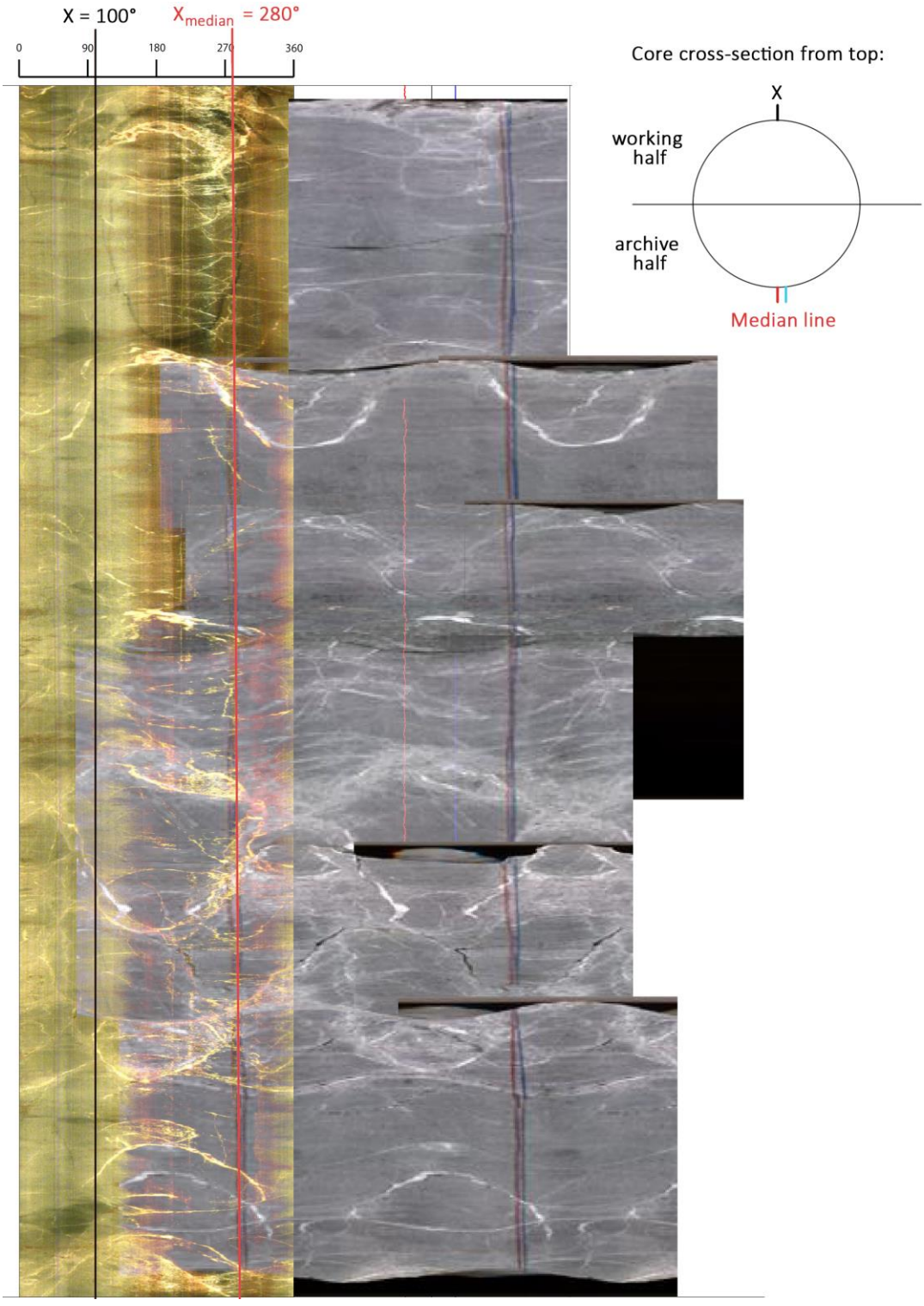

Figure 7.17 – Core sections are restored to their initial orientation by aligning features on borehole imagery, such as veins and fractures, with the features on mirrored core sections. We take away 180° from the drawn red lines on the core sections to find a 100° rotation of the core compared to the geographic reference frame of the borehole image.

The red line drawn on the core sections is always kept on the archive half of the core (cores are cut in half perpendicular to the red drawn line); therefore the reference frame for the working half of the core from which samples are taken, will be 180° different from the direction indicated by the red line. When mirrored unrolled cores and unrolled borehole imagery are aligned we should therefore add or subtract 180° from the position of the red line. The resulting X direction will then be in a geographic frame, and the amount of rotation required to align the core reference frame to the geographic reference frame can be added to the declination of our ChRMs.

Preliminary reorientation of Hole GT2 was carried out on 32 samples, resulting in reoriented ChRMs and AMS that are now in a true geographic reference frame. The results can be seen in Figure 7.18. As reorientation only affects the declinations of the ChRM, the inclinations stay the same as they were in the core reference frame (section 7.2).

The shallow, negative inclinations of the reoriented ChRM become positively oriented after a tilt correction of the gabbro layering (dip direction/dip = 065/33°) is applied. The reoriented declinations in Hole GT2 (Wadi Gideah) now show a northwest direction in geographic coordinates (Figure 7.18) that is similar to the direction found in our sites sampled at the surface of Wadi Gideah (Chapter 5). As discussed previously this north-western direction represents a remagnetization, and these reoriented core data demonstrate that this is therefore not an effect of surface weathering but affected the whole crust.

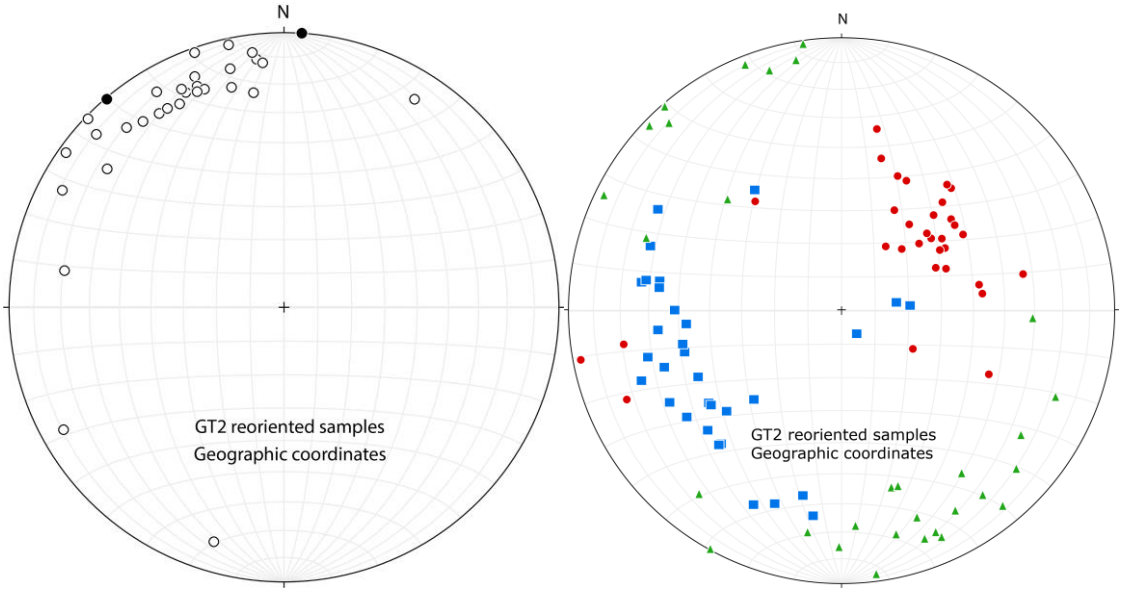

Figure 7.18 – (Left) Equal area stereographic projection of the GT2 ChRMs in a reoriented geographic reference frame. Open circles represent upper hemisphere, solid circles lower hemisphere. (Right) Equal area stereographic projection of the GT2 AMS data in a reoriented geographic reference frame. Blue squares represent K_{max}, green triangles represent K_{int}, red circles represent K_{min}.

When the AMS data are reoriented, K_{max} axes trend WSW-ENE, similar to results found by Morris et al. (2019) for the layered gabbros in the southern massifs. As previously explained in section 7.5, the magnetic lineation implied by the K_{max} orientation represent the regional-scale magmatic flow, either caused by the flow moving away from an inferred spreading ridge, or by deformation of melt-rich crystal mushes during spreading.

7.7 – Summary

OmanDP Holes GT1, GT2, and GT3 allow investigation of the relationships and processes in the dyke-gabbro transition zone down to the layered gabbros of the southern massifs of the Oman ophiolite, and palaeomagnetic analysis of the drill cores provides further characterization of the nature of the remagnetization

event that overprinted the original palaeomagnetic signal in these localities. Petrographic observations indicate that the primary carrier of magnetization in these rocks is (titano)magnetite, but that other minerals such as pyrrhotite might be carrying at least a part of the total magnetization. AMS measurements show that magnetic fabrics are well-defined in the layered and foliated gabbros of Wadi Gideah (likely following the orientation of the layering and foliation in the gabbros) but are less well-defined in the sheeted dykes and dyke rooting zone of Wadi Abdah. Finally, by reorienting cores for which borehole imagery is available, we were able to place the drill core ChRMs into a geographic reference frame, which confirmed that the ChRMs deeper into the ophiolite share similar magnetization directions to the ChRMs obtained from specimens sampled at the surface at the same localities. This provides further evidence that remagnetization in the southern massifs of the Oman ophiolite was a widespread event that affected rocks at depth, compatible with a fluid-related event that moved from the bottom of the ophiolite towards the top (Feinberg et al., 1999; Morris et al., 2016) during the obduction of the ophiolite onto the Arabian continent.

Chapter 8 – Conclusions

8.1 – Summary

The key aim of this study was to apply palaeomagnetic and other magnetic techniques to analyse systematically sampled sequences through the southern massifs of the Oman ophiolite in order to investigate the large-scale remagnetization event which obscured the original magnetic signal. Gaining a better understanding about the spatial and vertical scale of remagnetization, and particularly its upper limit, would provide information crucial to future geodynamic interpretations of palaeomagnetic data from Oman.

Systematic sampling of multiple sequences through the lower and upper crust of the Oman ophiolite, combined with drill core samples obtained from the Oman Drilling Project, provide the following key insights:

- Rock magnetic experiments suggest that the magnetic signal is carried by a variety magnetic minerals at our sampled localities. Magnetite with maximum unblocking temperatures of ~580°C is ubiquitous at all localities, but is accompanied by titanomagnetite and more rarely by pyrrhotite. Isothermal remanent magnetization experiments confirm these results, suggesting that SD to PSD (titano)magnetite is the dominant carrier of the magnetic signal everywhere but in Al Khadra, which shows evidence for MD titanomagnetite.
- Palaeomagnetic analysis in the Salahi massif (northern massifs), outside the inferred region of remagnetization, reveals SE-directed mean

directions in lower crustal layered gabbros. In agreement with previous workers, these magnetizations are inferred to represent primary magnetizations acquired during crustal accretion.

- NW-directed magnetizations are seen in all lithologies throughout the sampled sections in Wadi Abdah and Wadi Gideah in the southern massifs. Although these results are comparable with previously reported palaeomagnetic data from this region, this is the first time that these sections have been analysed along complete crustal transects. In agreement with Feinberg et al. (1999), Meyer (2015), and Morris et al. (2016), these NW-directed magnetizations are attributed to pervasive remagnetization of these sections of the ophiolite.
- Palaeomagnetic data from Wadi Abyad form a girdle distribution between previously reported NW-directed magnetizations at the bottom of the section (Meyer, 2015) to SE-directed magnetizations at the top (identified in sheeted dykes sampled in this study). These observations are best explained by remagnetization of the section from the base upwards, as previously proposed by Feinberg et al. (1999) and Morris et al. (2016). Forward modelling of progressive changes in demagnetization paths from the base to the top of the sequence in Wadi Abyad supports the hypothesis that remagnetization involved the acquisition of a grain-growth CRM or TCRM that decreased in intensity up-section, with complete replacement of original magnetizations at the base of the section, presence of intermediate directions resulting from overlapping unblocking

temperature spectra in the middle, and preservation of primary magnetizations in the topmost part of the section.

- The remagnetization event is inferred to relate to expulsion of orogenic fluids upwards through the ophiolite during its initial emplacement into the Arabian continental margin. A positive fold-test at the regional-scale indicates that this remagnetization took place before structural disruption of the Moho in the Campanian, related to the development of structural culminations in the basement beneath the ophiolite during continued convergence.
- Palaeomagnetic data from lavas and a cross-cutting dyke at Al Khadra reveals a NE-directed magnetization in the upper crust. These are interpreted as magnetizations that result from near complete overlap of NW remagnetised and SE original components of magnetization. However more sampling in this area would be needed to make a conclusive interpretation.
- Layered gabbros in the southern massifs of the Oman ophiolite have AMS fabrics that are parallel to the magmatic layering, with k_{max} axes forming a SW-oriented cluster in the southern massif (Wadi Gideah) and a SE-NW-oriented cluster in the northern massif (Salahi massif), comparable to results from other massifs recently reported by Meyer (2015) and Morris et al. (2019). The data are consistent with regional-scale magmatic lineations mapped across the ophiolite by Nicolas et al. (2000), suggesting

that the magnetic lineations in the sampled sites result from regional-scale magmatic flow away from the spreading ridge.

- Dykes from the dyke rooting zone and the sheeted dyke complex have AMS fabrics that are aligned with the orientation of the dykes. Variations in the plunges of the k_{max} axes suggest that magmatic flow in the dykes occurred either horizontally or vertically during intrusion.
- These magnetic fabric results suggest that the distribution and shape preferred orientations of newly formed ferromagnetic grains produced during remagnetization are largely controlled by pre-existing silicate petrofabrics.
- Net tectonic rotation analysis in the layered gabbros of the northern Salahi massif and the dykes of Wadi Abyad suggest 100-150° CW rotations around sub-vertical axes, consistent with regional-scale tectonic rotation models of Morris et al. (2016) and van Hinsbergen et al. (2019). This analysis restores the initial dyke strikes to NNE-SSW, consistent with a recent reconstruction of the ridge system reported by van Hinsbergen et al. (2019).
- End-member modelling and component analysis of the isothermal remanent magnetization (IRM) acquisition curves was applied to an ophiolite for the first time, to test whether this method can distinguish between rocks carrying primary and remagnetised remanences. When comparing localities side-by-side, the end-members of the Salahi massif (north, primary) and Wadi Gideah (south, remagnetised) are similar,

whereas the end-member composition of Wadi Abyad (varying from remagnetised at the bottom to primary at the top) looks different. We propose that the different end-member compositions in Wadi Abyad result from a prolonged cooling history related to the effects of a nearby propagating ridge during crustal accretion, which may have affected the (magnetic) mineral compositions and/or grain sizes.

The key outcomes of the analysis of cores of the Oman Drilling Project are similar to those from the sites sampled at the surface:

- (Titano)magnetite is found as the main carrier of magnetization in all three drill holes.
- After reorienting the cores into a geographic reference frame by using available borehole imagery, ChRMs deep into the ophiolite are found to share similar magnetization directions to the ChRMs observed at the surface. This provides evidence that remagnetization in the southern massifs of the Oman ophiolite was a wide-spread event that affected rocks at depth.

8.2 – Suggestions for further work

A number of aspects of this study could be taken further or improved by additional research:

- A systematic investigation of the geochemistry of the magnetite assemblages in the remagnetised and control sections of gabbros is required to further understand the nature of the fluid processes that cause remagnetization. The compositional variability of magnetite in response to ambient conditions during its formation has recently been recognised. Nadoll et al. (2014) recently proposed that trace element geochemistry may be able to distinguish between hydrothermally precipitated and primary magmatic magnetite (taking advantage of improved detection limits of techniques such as laser ablation inductively coupled mass spectrometry and electron microprobe analysis). They suggest that the main discriminator elements to use in such analyses are Mg, Al, Ti, V, Cr, Mn, Co, Ni, Zn and Ga, and propose that Ni/(Cr + Mn) vs Ti + V, Al + Mn vs Ti + V, and Sn/Ga discriminant plots may be able to fingerprint igneous versus hydrothermal magnetite. Applying these techniques to the Wadi Abyad section in particular would provide fresh insights into the process of remagnetization and an independent test of the conclusions of this study.
- The rock magnetic experiments conducted for this study are basic and should be complemented by more sophisticated analyses. No hysteresis measurements were performed, limiting the constraints that could be placed on magnetic grain sizes. A suite of first-order reversal curve (FORC) experiments (e.g. Muxworthy and Roberts, 2007) on specimens from the different localities would provide important information on magnetic

domain states and whether significant interactions occur between ferromagnetic grains.

- In addition, SEM-based observations on the major and trace element geochemistry of oxide and silicate phases in the sampled rocks and on preferred orientations of different phases using electron backscatter diffraction would complement both the rock magnetism and magnetic anisotropy data collected here, providing key information on the distribution and composition of oxide phases present in remagnetised and unremagnetised rocks.
- Inferences on dyke emplacement directions from the AMS data presented here are tentative. Robust analysis would require systematic sampling of opposing chilled margins of dykes in order to detect subtle crystal imbrications developed during initial intrusion (following the methodology of Staudigel et al., 1992).
- Further palaeomagnetic sampling across the dyke-gabbro transition zone in the vicinity of Wadi Abyad would potentially provide further information on the spatial variability of the vertical extent of remagnetization in this region that sits between the northern and southern massifs.
- The hypothesis that emplacement-related fluids were insufficient to result in remagnetization of the crust in the northern massifs should be tested by systematically sampling mantle sequences away from the basal thrust of the ophiolite. If these were found to carry stable NW-directed remanences (in contrast to the SE magnetizations seen in the overlying

crust) this would be a definitive test of this model. However, this may be complicated by the production of secondary magnetite during serpentinization of these rocks, which is known to be continuing at present (Kelemen et al., 2011) and was not restricted to the time of emplacement in the Late Cretaceous.

References

Aben, F.M., Dekkers, M.J., Bakker, R.R., van Hinsbergen, D.J.J., Zachariasse, W.J., Tate, G.W., McQuarrie, N., Harris, R., Duffy, B., 2014. Untangling inconsistent magnetic polarity records through an integrated rock magnetic analysis: A case study on Neogene sections in East Timor. *Geochemistry, Geophysics, Geosystems, 15, 2531-2554.*

Allerton, S., and Vine, F.J., 1987. Spreading structure of the Troodos ophiolite, Cyprus: Some paleomagnetic constraints. *Geology, 15, 7, 593-597.*

Allerton, S. and Vine, F. J., 1991. Spreading evolution of the Troodos ophiolite, Cyprus. *Geology, 19, 637-640.*

Alt, J.C., 1995. Subseafloor Processes in Mid-Ocean Ridge Hydrothermal Systems. *Geophysical Monograph 91, 85-114.*

Anonymous, 1972. Penrose field conference on ophiolites. *Geotimes, 17, 24-25.*

Arason, P. and Levi, S., 2010. Maximum likelihood solution for inclination-only data in paleomagnetism. *Geophysical Journal International, 182, 753-771.*

Boudier, F., Nicolas, A., Ildefonse, B. and Jousselin, D., 1997. EPR microplates, a model for the Oman Ophiolite. *Terra Nova, 9, 79-82.*

Butler, R.F., 1992. Paleomagnetism: magnetic domains to geologic terranes. *Blackwell Scientific Publications, Oxford, 319 p.*

Cannat, M., 1996. How thick is the magmatic crust at slow spreading oceanic ridges? *Journal of Geophysical Research, 101, 2847-2857.*

Collinson, D.W., 1983. Methods in rock magnetism and palaeomagnetism techniques and instrumentation. *Chapman and Hall Ltd, 503 p.*

Coogan, L.A., Jenkin, G.R.T., Wilson, R.N., 2002. Constraining the cooling rate of the lower oceanic crust: a new approach applied to the Oman ophiolite. *Earth and Planetary Science Letters, 199, 127-147.*

Cox, A., 1961. Anomalous remanent magnetization of basalt. *U.S. Geological Survey Bulletin, 1083-E, 131-160.*

Day, R., Fuller, M., Schmidt, V.A., 1977. Hysteresis properties of titanomagnetites: Grain-size and compositional dependence. *Physics of the Earth and Planetary Interiors, 13, 260-267.*

Deenen, M. H. L., Langereis, C. G., van Hinsbergen, D.J.J., Biggin, A.J., 2011. Geomagnetic secular variation and the statistics of palaeomagnetic directions. *Geophysical Journal International, 186, 509-520.*

Dekkers, M.J., 2012. End-member modelling as an aid to diagnose remagnetization: a brief review. *Geological Society, London, Special Publications, 371, 253-269.*

Dekkers, M.J., Heslop, D., Herrero-Bervera, E., Acton, G., Krasa, D., 2014. Insights into magmatic processes and hydrothermal alteration of in situ superfast spreading ocean crust at ODP/IODP site 1256 from a cluster analysis of rock magnetic properties. *Geochemistry, Geophysics, Geosystems, 15, 3430-3447.*

Dilek, Y., Furnes, H. and Shallo, M., 2007. Subduction zone ophiolite formation along the periphery of Mesozoic Gondwana. *Gondwana Research Focus, 11, 453-475.*

Dilek, Y. and Furnes, H., 2009. Structure and geochemistry of Tethyan ophiolites and their petrogenesis in subduction rollback systems. *Lithos, 113, 1-20.*

Dunlop, D.J., 1983. Viscous magnetization of .04-100 µm magnetites. *Geophysical Journal of the Research Astronomy Society, 74, 667-687.*

Dunlop, D. J and Özdemir, Ö, 1997. Rock Magnetism: Fundamentals and frontiers. *Cambridge University Press, 573 p.*

Egli, R., 2004. Characterization of Individual Rock Magnetic Components by Analysis of Remanence Curves, 1. Unmixing Natural Sediments. *Studia Geophysica et Geodaetica, 48, 391, 1573-1626.*

Elmore, R.D., Dulin, S., Engel, M.H., Parnell, J., 2006. Remagnetization and fluid flow in the Old Red Sandstone along the Great Glen Fault, Scotland. *Journal of Geochemical Exploration, 89, 96-99.*

Elmore, R.D., Foucher, J.L., Evans, M., Lewchuk, M., Cox, E., 2006. Remagnetization of the Tonoloway Formation and the Helderberg Group in the Central Appalachians: testing the origin of syntilting magnetizations. *Geophysical Journal International, 166, 1062-1076.*

Enkin, R. J., Osadetz, K. G., Baker, J., and Kisilevsky, D., 2000, Orogenic remagnetizations in the Front Ranges and Inner Foothills of the southern Canadian Cordillera: chemical harbinger and thermal handmaiden of Cordilleran deformation. *Geological Society of America Bulletin, 112, 929-92*.

Ernewein, M., Pflumio, C., Whitechurch, H., 1988. The death of an accretion zone as evidenced by the magmatic history of the Sumail ophiolite (Oman). *Tectonophysics, 151, 247-274.*

Feinberg, H., Horen, H., Michard, A., Saddiqi, O., 1999. Obduction-related remagnetization at the base of an ophiolite: Paleomagnetism of the Samail upper nappe lower sequence and of its continental substratum, southeast Oman Mountains. *Journal of Geophysical Research, 104, 17,703-17,714.*

Ferré, E.C., 2002. Theoretical models of intermediate and inverse AMS fabrics. *Geophysical Research Letters, 29, 7, 1-4.*

Fisher, R.A., 1953. Dispersion on a sphere. *Proceedings of the Royal Society of London, Ser. A 217, 295-305.*

Gass, I. G., 1968. Is the Troodos Massif of Cyprus a fragment of Mesozoic Oceanic floor*? Nature, 220, 39-42.*

Godard, M., Dautria, J-M. and Perrin, M., 2003. Geochemical variability of the Oman ophiolite lavas: Relationship with spatial distribution and paleomagnetic directions. *Geochemistry, Geophysical, Geosystems, 4, (6).*

Gong, Z., Dekkers, M.J., Heslop, D., Mullender, T.A.T., 2009. End-member modelling of isothermal remanent magnetization (IRM) acquisition curves: a novel approach to diagnose remagnetization. *Geophysical Journal International, 178, 693-701.*

Hacker, B.R., Mosenfelder, J.L., Gnos, E., 1996. Rapid emplacement of the Oman ophiolite: Thermal and geochronologic constraints. *Tectonics, 15, 1230-1247.*

Heslop, D., McIntosh, G., Dekkers, M.J., 2004. Using time- and temperature-dependent Preisach models to investigate the limitations of modelling isothermal remanent magnetization

acquisition curves with cumulative log Gaussian functions. *Geophysical Journal International, 157, 55-63.*

Heslop, D., and Dillon, M., 2007. Unmixing magnetic remanence curves without *a priori* knowledge. *Geophysical Journal International, 170, 556-566.*

Hopkinson, J., 1889. Magnetic and other physical properties of iron at a high temperature. *Philosophical Transactions of the Royal Society of London, 180, 443-465.*

Hopson, C. A., Coleman, R. G., Gregory, R. T., Pallister, J. S. and Bailey, E. H., 1981. Geologic Section Through the Samail Ophiolite and Associated Rocks Along a Muscat-Ibra Transect, Southeastern Oman Mountains. *Journal of Geophysical Research, 86 (B4), 2527-2544.*

Huang, W., Dupont-Nivet, G., Lippert, P.C., van Hinsbergen, D.J.J., Dekkers, M.J., Guo, Z., Waldrip, R., Li, X., Zhang, X., Liu, D., Kapp, P., 2015. Can a primary remanence be retrieved from partially remagnetized Eocene volcanic rocks in the Nanmulin Basin (southern Tibet) to date the India-Asia collision? *Geochemistry, Geophysics, Geosystems, 120, 42-66.*

Huang, W., Dupont-Nivet, G., Lippert, P.C., van Hinsbergen, D.J.J., Dekkers, M.J., Waldrip, R., Ganerød, M., Li, X., Guo, Z., Kapp, P., 2015. What was the Paleogene latitude of the Lhasa terrane? A reassessment of the geochronology and paleomagnetism of Linzizong volcanic rocks (Linzhou basin, Tibet). *Geochemistry, Geophysics, Geosystems, 34, 594-622.*

Huang, W., van Hinsbergen, D.J.J., Dekkers, M.J., Garzanti, E., Dupont-Nivet, G., Lippert, P.C., Li, X., Maffione, M., Langereis, C.G., Hu, X., Guo, Z., Kapp, P., 2015. Paleolatitudes of the Tibetan Himalaya from primary and secondary magnetizations of Jurassic to Lower Cretaceous sedimentary rocks. *Geochemistry, Geophysics, Geosystems, 16, 77-100.*

Inwood, J., Morris, A., Anderson, M. W. and Robertson, A. H. F., 2009. Neotethyan intraoceanic microplate rotation and variations in spreading axis orientation: Palaeomagnetic evidence from the Hatay ophiolite (southern Turkey). *Earth and Planetary Science Letters, 280, 105-117.*

Jelínek, V., Kropáček, V., 1978. Statistical processing of anisotropy of magnetic susceptibility measured on groups of specimens. *Studia Geophysica et Geodaetica, 22, 50–62.*

Juteau, T. Beurrier, M. Dahl, R. and Nehlig, P., 1988. Segmentation at a fossil spreading axis: The plutonic sequence of the Wadi Haymiliyah area (Haylayn Block, Sumail Nappe. Oman). *Tectonophysics, 151, 167-197.*

Kelemen, P. B., Matter, J., Streit, E. E., Rudge, J. F., Curry, W. B. and Blusztajn, J., 2011. Rates and mechanisms of mineral carbonation in peridotite: natural processes and recipes for enhanced, in situ CO2 capture and storage. *Annual Review of Earth and Planetary Sciences, 39, 545-576.*

Kirschvink, J.L., 1980. The least-squares line and plane and the analysis of palaeomagnetic data. *Geophysical Journal International, 62, 699-718.*

Koppers, A. A. P, Escutia, C., Inagaki, F., Pälike, H., Saffer, D. M. and Thomas, D., 2019. Special Issue on Scientific Ocean Drilling: Looking to the Future. *Oceanography, 32 (1).*

Kruiver, P.P., Dekkers, M.J., Heslop, D., 2001. Quantification of magnetic coercivity components by the analysis of acquisition curves of isothermal remanent magnetisation. *Earth and Planetary Science Letters, 189, 269-276.*

Kruiver, P.P., and Passier, H.F., 2001. Coercivity analysis of magnetic phases in sapropel S1 related to variations in redox conditions, including an investigation of the S ratio. *Geochemistry, Geophysics, Geosystems, 2 (12).*

Larson, R.L., Searle, R.C., Kleinrock, M.C., Schouten, H., Bird, R.T., Naar, D.F., Rusby, R.I., Hooft, E.E., Lasthiotakis, H., 1992. Roller-bearing tectonic evolution of the Juan Fernandez microplate. *Nature, 356, 571-576.*

Lenz, E., 1834. Ueber die Bestimmung der Richtung der durch elektodynamische Vertheilung erregten galvanischen Ströme. *Annalen der Physik und Chemie, 107 (31), 483-494.*

Lippard, S.J., Shelton, A.W., Gass, I.G., 1986. The ophiolite of Northern Oman. *London, 178 p.*

Lowrie, W., 1990. Identification of ferromagnetic minerals in a rock by coercivity and unblocking temperature properties. *Geophysics Research Letters, 17, 159-162.*

Luyendyk, B.P., Laws, B.R., Day, R., and Collinson, T.B., 1982. Paleomagnetism of the Samail ophiolite, Oman: 1. The sheeted dike complex at Ibra. *Journal of Geophysical Research, 87, 10,883-10,902.*

Luyendyk, B.P., and Day, R., 1982. Paleomagnetism of the Samail ophiolite, Oman: 2. The Wadi Kadir gabbro section. *Journal of Geophysical Research, 87, 10,903-10,917.*

MacLeod, C.J. & Rothery, D.A., 1992. Ridge axial segmentation in the Oman ophiolite: evidence from along-strike variations in the sheeted dyke complex. *In: Parson, L.M., Murton, B.J. & Browning, P., (eds.) Ophiolites and their Modern Oceanic Analogues. Special Publications Geological Society London 60, 39-63.*

MacLeod, C.J., and Yaouancq, G., 2000. A fossil melt lens in the Oman ophiolite: Implications for30 magma chamber processes at fast spreading ridges. *Earth and Planetary Science Letters, 176, 357-373.*

MacLeod, C.J., Carlut, J., Escartín, J., Horen, H., Morris, A., 2011. Quantitative constraint on footwall rotations at the 15°45'N oceanic core complex, Mid-Atlantic Ridge: Implications for oceanic detachment fault processes. *Geochemistry, Geophysics, Geosystems, 12, 5, 1-29.*

MacLeod, C. J., Lissenberg, C. J. and Bibby, L. E., 2013. "Moist MORB" axial magmatism in the Oman ophiolite: The evidence against a mid-ocean ridge origin. *Geology, 41, 459-462.*

Maffione, M., van Hinsbergen, D.J.J., Koornneef, L.M.T., Guilmette, C., Hodges, K., Borneman, N., Huang, W., Ding, L., Kapp, P., 2015. Forearc hyperextension dismembered the south Tibetan ophiolites. *Geology, 43, 6, 475-478.*

McClelland-Brown, E., 1982. Discrimination of TRM and CRM by blocking-temperature spectrum analysis. *Physics of the Earth and Planetary Interiors, 30, 405-414.*

McElhinny, M.W., 1964. Statistical significance of the fold test in paleomagnetism. *Geophysical Journal of the Royal Astronomical Society, 8, 338-340.*

McFadden, P.L. and Jones, D.L., 1981. The fold test in paleomagnetism. *Geophysical Journal of the Royal Astronomical Society, 67, 53-58.*

McFadden, P.L., McElhinny, M.W., 1988. The combined analysis of remagnetization circles and direct observations in palaeomagnetism. *Earth and Planetary Science Letter, 87, 161-172.*

Meijers, M.J., van Hinsbergen, D.J.J., Dekkers, M.J., Altıner, D., Kaymakcı, N., Langereis, C.G., 2010. Pervasive Palaeogene remagnetization of the Central Taurides fold-and-thrust belt (southern Turkey) and implications for rotations in the Isparta Angle. *Geophysical Journal International, 184, 1090-1112.*

Meyer, M.C., 2015. Magnetic fabric, palaeomagnetic and structural investigation of the accretion of lower oceanic crust using ophiolitic analogues. *[Ph.D. thesis]: Plymouth, UK, University of Plymouth, 305 p.*

Moores, E. M. and Vine, F. J., 1971. The Troodos Massif, Cyprus and other ophiolites as oceanic crust: evaluation and implications. *Philosophical Transactions of the Royal Society of London, A, 268, 443-466.*

Morris, A., Creer, K. M. and Robertson, A. H. F., 1990, Palaeomagnetic evidence for clockwise tectonic rotations related to dextral shear along the Southern Troodos Transform Fault, Cyprus. *Earth and Planetary Science Letters, 99, 250-262.*

Morris, A., Anderson, M.W., Robertson, A.H.F., 1998. Multiple tectonic rotations and transform tectonism in an intraoceanic suture zone, SW Cyprus. *Tectonophysics, 299, 229-253.*

Morris, A. and Anderson, M. W., 2002, Palaeomagnetic results from the Baër-Bassit ophiolite of northern Syria and their implication for fold tests in sheeted dyke terrains. *Physics and Chemistry of the Earth, 27, 1215-1222.*

Morris, A., Anderson, M. W., Robertson, A. H. F. and Al-Riyami, K., 2002, Extreme tectonic rotations within an eastern Mediterranean ophiolite (Baër-Bassit, Syria). *Earth and Planetary Science Letters, 202, 247-261.*

Morris, A., 2003, A palaeomagnetic and rock magnetic glossary. *Tectonophysics, 377, 211-228.*

Morris, A., Meyer, M., Anderson, M.W., MacLeod, C.J., 2016. Clockwise rotation of the entire Oman ophiolite occurred in a suprasubduction zone setting. *Geology, 44, 12, 1055-1058.*

Morris, A., Anderson, M.W., Omer, A., Maffione, M., van Hinsbergen, D.J.J., 2017. Rapid fore-arc extension and detachment-mode spreading following subduction initiation. *Earth and Planetary Science Letters, 478, 76-88.*

Morris, A., Meyer, M., Anderson, M.W., MacLeod, C.J., 2019. What do variable magnetic fabrics in gabbros of the Oman ophiolite reveal about lower oceanic crustal magmatism at fast spreading ridges? *Geology, 47, 275-278.*

Muxworthy, A. R. and Roberts, A. P., 2007. First-order reversal curve (FORC) diagrams. *In: Gubbins, D. and Herrero-Bervera, E. (eds.), Encyclopedia of Geomagnetism ad Paleomagnetism, Springer, 266-272.*

Nadoll, P., Angerer, T., Mauk, J. L., French, D. and Walshe, J., 2014. The chemistry of hydrothermal magnetite: a review. *Ore Geology Reviews, 61, 1-32.*

Néel, L., 1955. Some theoretical aspects of rock magnetism. *Advanced Physics, 4, 191-242.*

Nicolas, A., Ceuleneer, G., Boudier, F., Misseri, M., 1988. Structural mapping in the Oman ophiolites: Mantle diapirism along an oceanic ridge. *Tectonophysics, 151, 27-56.*

Nicolas, A., 1989. Structures in Ophiolites and Dynamics of Oceanic lithosphere. *Kluwer, Dordrecht, 367 p.*

Nicolas & Boudier 1995. Mapping oceanic ridge segments in Oman ophiolite. *Journal of Geophysical Research, 100 (B4), 6179-6197.*

Nicolas, A., Boudier, F., Ildefonse, B., Ball, E., 2000. Accretion of Oman and United Arab Emirates ophiolite – Discussion of a new structural map. *Marine Geophysical Researches, 21, 147-180.*

Nicolas A., Ildefonse, B., Boudier, F., Lenoir, X., Ismail, W.B., 2000. Dike distribution in the Oman-United Arab Emirates ophiolite. *Marine Geophysical Researches, 21, 269-287.*

Nicolas, A. and Boudier, F., 2003. Where ophiolites come from and what they tell us. In Dilek, Y. and Newcomb, S. (eds.), Ophiolite concept and the evolution of geological thought. *Geological Society of America Special Paper, 373, 137-152.*

Nicolas, A., Boudier, F., Koepke, J., France, L., Ildefonse, B. and Mevel, C., 2008. Root zone of the sheeted dike complex in the Oman ophiolite. *Geochemistry, Geophysical, Geosystems, 9 (5).*

Pallister, J.S., and Hopson, C.A., 1981. Samail Ophiolite plutonic suite: Field relations, phase variations, cryptic variation and layering, and a model of a spreading ridge magma chamber. *Journal of Geophysical Research, 86, 2593-2644.*

Pastor-Galán, D., Dekkers, M.J., Gutiérrez-Alonso, G., Brouwer, D., Groenewegen, T., Krijgsman, W., Fernández-Lozano, J., Yenes, M., Álvarez-Lobato, F., 2016. Paleomagnetism of the Central Iberian curve's putative hinge: Too many oroclines in the Iberian Variscides. *Gondwana Research, 39, 96-113.*

Pearce, J. A. and Robinson, P. T., 2009. The Troodos ophiolitic complex probably formed in a subduction initiation, slab edge setting. *Gondwana Research, 18, 60-81.*

Perrin, M., Prevot, M., Bruere, F., 1994. Rotation of the Oman ophiolite and initial location of the ridge in the hotspot reference frame. *Tectonophysics, 229, 31-42.*

Perrin, M., Plenier, G., Dautria, J-M., Cocuaud, E., Prévot, M., 2000. Rotation of the Semail ophiolite (Oman): Additional Paleomagnetic data from the volcanic sequence. *Marine Geophysical Research, 21, 181-194.*

Petrovský, E. and Kapička, A., 2006. On determination of the Curie point from thermomagnetic curves. *Journal of Geophysical Research, 111, 1-10.*

Piper, J.D.A., 1987. Palaeomagnetism and the continental crust. *Open University Press, 434 p.*

Pullaiah, G., Irving, E., Buchan, K.L., Dunlop, D.J., 1975. Magnetization changes caused by burial and uplift. *Earth and Planetary Science Letters, 28, 2, 133-143.*

Reuber, I., Nehlig, P. & Juteau, T., 1991. Axial segmentation at a fossil oceanic spreading centre in the Haylayn Block (Semail Nappe, Oman): off-axis mantle diapir and advancing ridge tip. *Journal of Geodynamics, 13 (2-4), 253-278.*

Rioux, M., Bowring, S., Kelemen, P., Gordon, S., Miller, R. and Dudás, F., 2013. Tectonic development of the Samail ophiolite: High-precision U-Pb zircon geochronology and Sm-Nd isotopic constraints on crustal growth and emplacement. *Journal of Geophysical Research: Solid Earth, 118 (5).*

Rioux, M., Garber, J., Bauer, A., Bowring, S., Searle, M., Kelemen, P., Hacker, B., 2016. Synchronous formation of the metamorphic sole and igneous crust of the Semail ophiolite: New constraints on the tectonic evolution during ophiolite formation from high-precision U-Pb zircon geochronology. *Earth and Planetary Science Letters, 451, 185-195.*

Robertson, A., 2004. Development of concepts concerning the genesis and emplacement of Tethyan ophiolite in the Eastern Mediterranean and Oman regions. *Earth Science Reviews, 66, 331-387.*

Rowan, C.J., Roberts, A.P., 2006. Magnetite dissolution, diachronous greigite formation, and secondary magnetizations from pyrite oxidation: Unravelling complex magnetizations in

Neogene marine sediments from New Zealand. *Earth and Planetary Science Letters, 241, 119-137.*

Rowan, C.J., Roberts, A.P., 2008. Widespread remagnetizations and a new view of Neogene tectonic rotations within the Australia-Pacific plate boundary zone, New Zealand. *Journal of Geophysical Research, 113, B3, 1-22.*

Searle, M. and Cox, J., 1999. Tectonic setting, origin, and obduction of the Oman ophiolite. *Geological Society of America Bulletin, 111 (1), 104-122.*

Searle, M.P., Cox, J., 2002. Subduction zone metamorphism during formation and emplacement of the Semail ophiolite in the Oman Mountains. *Geological Magazine, 139, 241-255.*

Searle, M.P., Warren, C.J., Waters, D.J., Parrish, R.R., 2004. Structural evolution, metamorphism and restoration of the Arabian continental margin, Saih Hatat region, Oman Mountains. *Journal of Structural Geology, 26, 451-473.*

Shelton, A.W., 1984. Geophysical studies on the northern Oman ophiolite. *[Ph.D. thesis] Milton Keynes, UK, The Open University, 353 p.*

Stacey, F.D., 1963. The physical theory of rock magnetism. *Advanced Physics, 12, 45-133.*

Stampfli, G. M., 2000. Tethyan oceans. *Geological Society, London, Special Publications, 173, 1-23.*

Stampfli, G. M. and Borel, G. D., 2002. A plate tectonic model for the Paleozoic and Mesozoic constrained by dynamic plate boundaries and restored synthetic oceanic isochrones. *Earth and Planetary Science Letters, 196, 17-33.*

Staudigel, H., Gee, J., Tauxe, L. & Varga, R. J., 1992. Shallow intrusive directions of intrusive dikes in the Troodos ophiolite: anisotropy of magnetic susceptibility and structural data. *Geology, 20, 841–844.*

Tarling, D. H., 1983. Palaeomagnetism: Principles and applications in geology, geophysics, and archaeology. *Chapman and Hall, London, 379 p.*

Tarling, D. H. and Hrouda, F., 1993. Magnetic anisotropy of rocks. *Chapman and Hall, London, 217 p.*

Tauxe, L. and Watson, G. S., 1994. The fold test: an eigen analysis approach. *Earth and Planetary Science Letters, 122, 331-341.*

Tauxe, L., 2010. Essentials of paleomagnetism. *University of California Press, 489 p.*

Thomas, V., Pozzi, J. P. and Nicolas, A., 1988. Paleomagnetic results from Oman ophiolites related to their emplacement. *Tectonophysics, 151, 297-321.*

Tilton, G. R., Hopson, C. A. and Wright, J. E., 1981. Uranium-lead ages of the Samail ophiolite, Oman, with applications to Tethyan ocean ridge tectonics. *Journal of Geophysical Research, 86 (B4), 2763-2775.*

van Hinsbergen, D.J.J., Dekkers, M.J., Koç, A., 2010. Testing Miocene Remagnetization of Bey Dağları: Timing and Amount of Neogene Rotations in SW Turkey. *Turkish Journal of Earth Sciences, 19, 123-156.*

van Hinsbergen, D.J.J., Maffione, M., Koornneef, L.M.T., Guilmette, C., 2019. Kinematic and paleomagnetic restoration of the Semail Ophiolite (Oman) reveals subduction initiation along an ancient Neotethyan fracture zone. *Earth and Planetary Science Letters 518, 183-196.*

VanTongeren, J.A., Kelemen, P.B., Hanghøj, K., 2008. Cooling rates in the lower crust of the Oman ophiolite: Ca in olivine, revisited. *Earth and Planetary Science Letters, 267, 69-82.*

Vine, F. J., 1966. Spreading of the Ocean Floor: New Evidence. *Science, 154 (3755), 1405-1415.*

Weiler, P.D., 2000. Differential rotations in the Oman Ophiolite: Paleomagnetic evidence from the southern massifs. *Marine Geophysical Researches, 21, 195-210.*

Weltje, G.J., 1997. End-Member Modeling of Compositional Data: Numerical-Statistical Algorithms for Solving the Explicit Mixing Problem. *Mathematical Geology, 29, 4, 503-549.*

Yaouancq, G. and MacLeod, C. J., 2000. Petrofabric Investigation of Gabbros from the Oman Ophiolite: Comparison between AMS and Rock Fabric. *Marine Geophysical Researches, 21, 289-305.*

Zijderveld, J.D.A., 1967. AC demagnetisation of rocks: Analysis of results. In: Methods in Paleomagnetism, *Elsevier, edited by D.W. Collinson et al., 254-268.*